

**First observation of the simultaneous
production of a W boson and two photons in
proton-proton collisions.**

Alessandro Ambler

Department of Physics
McGill University
Montréal, Québec, Canada

May 2024

A thesis submitted to McGill University in partial fulfillment of the
requirements of the degree of Doctor of Philosophy

©Alessandro Ambler 2024

Abstract

This thesis presents the first observation of the production of a W boson in association with two photons in proton-proton collisions. Processes involving the simultaneous production of three gauge bosons in proton-proton collisions are extremely rare, some of which have yet to be experimentally observed. The production rate of these final states is directly sensitive to new physics phenomena that could manifest themselves at lower energies as anomalous quartic gauge couplings. As such, the study of these types of processes provide an important test of the Standard Model of particle physics. The measurement presented in this thesis is based on 140 fb^{-1} of proton-proton collision data at a center of mass energy of 13 TeV collected between 2015 and 2018 by the ATLAS detector at the Large Hadron Collider. Events compatible with a W boson decaying to an electron or a muon with its associated neutrino were selected. Data-driven techniques were developed to estimate the reducible backgrounds arising from misreconstructed objects. Contributions from irreducible background sources were estimated using simulated data. An expected and observed statistical significance for the $pp \rightarrow W\gamma\gamma$ process of 5.6σ is obtained, constituting the first observation of the process. The effects of the detector acceptance and efficiency on the number of observed signal events is corrected for using simulation to obtain an inclusive fiducial cross section measurement for $W(\rightarrow e\nu_e)\gamma\gamma$ and $W(\rightarrow \mu\nu_\mu)\gamma\gamma$ events of $\sigma_{\text{fid}} = 13.8 \pm 1.1(\text{stat}) \pm_{-2.0}^{+2.1}(\text{syst}) \pm 0.1(\text{lumi}) \text{ fb}$, in good agreement with the leading Standard Model predictions.

Abrégé

Cette thèse présente la première observation de la production d'un boson W en association avec deux photons dans des collisions proton-proton. Les processus impliquant la production simultanée de trois bosons de jauge dans des collisions proton-proton sont extrêmement rares, certains n'ayant pas encore été observés expérimentalement. Le taux de production de ces états finals est directement sensible à de nouveaux phénomènes physiques qui pourraient se manifester à des énergies plus basses sous la forme de couplages quadratiques de jauge anormaux. En tant que tel, l'étude de ces types de processus constitue un test important du Modèle Standard de la physique des particules. La mesure présentée dans cette thèse est basée sur 140 fb^{-1} de données de collisions proton-proton à une énergie de centre de masse de 13 TeV collectées entre 2015 et 2018 par le détecteur ATLAS au Grand Collisionneur de Hadrons. Les événements compatibles avec la désintégration d'un boson W en un électron ou un muon avec son neutrino correspondant ont été sélectionnés. Des techniques basées sur les données ont été développées pour estimer les arrière-plans réductibles résultant d'objets mal reconstruits. Les contributions d'arrière-plans irréductibles ont été estimées à l'aide de données simulées. Une signification statistique attendue et observée pour le processus $pp \rightarrow W\gamma\gamma$ de 5.6σ est obtenue, constituant la première observation du processus. Les effets de l'acceptance et de l'efficacité du détecteur sur le nombre d'événements de signal observés sont corrigés en simulation pour obtenir une mesure inclusive de la section efficace fiduciaire pour les événements $W(\rightarrow e\nu_e)\gamma\gamma$ et $W(\rightarrow \mu\nu_\mu)\gamma\gamma$ de $\sigma_{\text{fid}} = 13.8 \pm 1.1(\text{stat}) \pm_{-2.0}^{+2.1}(\text{syst}) \pm$

0.1(lumi) fb, en bon accord avec les prédictions de pointe du Modèle Standard.

Acknowledgements

I would not have been able to complete this thesis without the help of a great many people. If I forgot to mention you here, know that I am still grateful for your help and support.

First and above all, I want to express my deepest gratitude to my supervisor, Professor Brigitte Vachon, whose unwavering guidance, encouragement, and support have been invaluable throughout the journey of this thesis, especially during the pandemic. To say that this thesis would not have been possible without her would be an understatement.

I also would like thank Professor Heather Russell for her mentorship and guidance as leader of the $W\gamma\gamma$ analysis team. This measurement and this thesis are both deeply indebted to her incredible patience and expertise.

Many thanks also go to Dr. Auriane Canesse, who worked alongside me on this analysis, and to Dr. Tony Kwan, not only for his help on the analysis, but also for letting me help out in the McGill lab to get me out of my apartment in the thick of the pandemic.

I would also like to extend my gratitude to all of the members of the ATLAS McGill group for their support and feedback throughout the years. That includes Professors François Corriveau and Andreas Warburton, postdocs Raphael, Xingguo, Jona, Steffen, and Andrée, and students John, Lia, Sebastien, Benoit, and Anabelle.

Thank you Laura for sharing all of those much needed coffee breaks with me in the final stretch of writing this thesis.

Special thanks also go to Shreya for her long conversations and amazing home cooked

meals, and Matteo for being such a lovely office mate.

Thank you Kevin and Dan for your friendship and camaraderie throughout the years, I'm looking forward to many more.

Thank you to all of the friends I made during my year at CERN who made it much more difficult for me to leave than I would have ever thought.

Last but not least, thank you to my friends and family for your support and encouragement through the best and the worst of it, and to Murphy, who will be forever missed.

Author's Contributions

The ATLAS collaboration is one of the largest collaborative efforts in science, with approximately 6000 members spread across 182 institutions in 42 countries. The construction, operation, and maintenance of the ATLAS detector and the processing and analysis of its data is the work of many thousands of physicists, engineers, technicians, students, and support staff spanning many years. These include hundreds of scientists who develop and maintain the software tools used in the measurement presented in this thesis.

The data analysis presented in this thesis is however the work of a smaller team, with two PhD students, the author Alessandro Ambler and Dr. Auriane Canesse, one post-doctoral student, Dr. Tony Kwan, and two professors, Prof. Heather Russell who led the analysis team and Prof. Brigitte Vachon, the author's supervisor. Every member of the analysis team contributed to the development and validation of the analysis strategy, the analysis software framework, and the analysis methods.

This thesis presents the first observation of the production of a W boson in association with two jets in proton-proton collision, making it an original and distinct contribution to scientific knowledge.

In the following bullet points, a brief summary of the author's contributions and those of the other analysis team member is given for each chapter.

- Chapter 1 : The author motivates the measurement and gives an overview the contents of the thesis.

-
- Chapter 2 : The author presents an overview of the theoretical background necessary for the reader to understand the work presented in the thesis. This chapter also includes a review of the relevant literature in the field of particle physics to motivate the measurement presented in the thesis.
 - Chapter 3 : The author gives an overview of the experimental techniques and infrastructure used to produce and record the data used in this thesis. This includes an overview of the Large Hadron Collider (LHC) and the ATLAS detector which were built and operated by thousands of scientists. The author has contributed to the development and simulation of upgrade electronics for the ATLAS Liquid Argon Calorimeter which will be used in future data-taking runs [1]. The author also contributed to the monitoring of the ATLAS Calorimeter in the control room during data-taking.
 - Chapter 4 : The author describes the algorithms used to reconstruct and identify the particles recorded by the ATLAS detector. These algorithms were developed by members of the ATLAS collaboration.
 - Chapter 5 : The author presents the analysis strategy and the event selection used to define the measurement phase space. This work was done by the author in collaboration with the other members of the analysis team.
 - Chapter 6 : The author describes the various techniques developed to estimate the signal and background contributions. Signal simulation samples were generated by the author using the MadGraph simulation framework. The other signal and background simulation samples were studied and validated by the author and the other analysis team members. The background estimation technique for jets misidentified as photons was developed by Dr. Auriane Canesse and Prof. Heather Russell. The background estimation techniques for electrons misidentified as photons

and jets misidentified as leptons were developed by the author. The background estimation technique for photons originating from pileup vertices was developed by Prof. Heather Russell.

- Chapter 7 : The experimental and theoretical systematic uncertainties presented in this chapter are developed by specialized working groups within the ATLAS Collaboration. Their implementation and validation within the analysis framework was done by the author, Prof. Heather Russell, Dr. Auriane Canesse, Dr. Tony Kwan.
- Chapter 8 : The author presents the statistical model used for the measurement of the significance and fiducial cross section of the process presented in this thesis. It was developed by the author, Dr. Auriane Canesse, Dr. Tony Kwan.
- Chapter 9 : The author presents the results of the significance and fiducial cross section measurements.
- Chapter 10 : The author summarizes the results of the thesis and provides insight into future developments related to the measurement. This includes future uses of the measurement and possible improvements to its precision.

Contents

1	Introduction	1
2	The Standard Model of Particle Physics	4
2.1	Overview	4
2.1.1	Fermions	7
2.1.2	Bosons	7
2.1.3	Mathematical Formulation of the Standard Model	8
2.2	Quantum Electrodynamics	10
2.3	Quantum Chromodynamics	11
2.3.1	Quantum Chromodynamics at Hadron Colliders	11
2.4	Electroweak Symmetry Breaking	16
2.5	Beyond the Standard Model	17
2.5.1	Effective Field Theories	22
2.6	The $pp \rightarrow W\gamma\gamma$ Process	23
2.7	Motivation	24
3	Experimental Setup	26
3.1	The Large Hadron Collider	26
3.2	The ATLAS Detector	32
3.2.1	The Inner Detector	38

3.2.2	The Calorimeter	42
3.2.3	The Muon Spectrometer	46
3.2.4	Luminosity Measurement	50
3.2.5	Trigger and Data Acquisition	51
4	Object Reconstruction, Identification, and Isolation	53
4.1	Intermediate Objects	53
4.1.1	Inner Detector Tracks	54
4.1.2	Vertices	56
4.1.3	Calorimeter Clusters	56
4.2	Electrons	57
4.2.1	Electron Reconstruction	58
4.2.2	Electron Identification	61
4.2.3	Electron Isolation	61
4.3	Photons	63
4.3.1	Photon Reconstruction	64
4.3.2	Photon Identification	66
4.3.3	Photon Isolation	66
4.4	Muons	67
4.4.1	Muon Reconstruction	69
4.4.2	Muon Identification	70
4.4.3	Muon Isolation	71
4.5	Jets	72
4.5.1	Jet Reconstruction	72
4.5.2	b-Jets	74
4.6	Missing Transverse Energy	75

5	Event Selection	79
5.1	Analysis Strategy	79
5.1.1	Blinding Strategy	82
5.2	Trigger Selection	82
5.2.1	Signal Region	83
5.2.2	Control Region	83
5.3	Object Selection	84
5.3.1	Electrons	85
5.3.2	Photons	86
5.3.3	Muons	86
5.3.4	Jets	88
5.4	Event Selection	88
6	Background Estimation	95
6.1	Simulation of Proton-Proton Collisions	96
6.1.1	Simulation Samples	99
6.2	Background from Multiboson Production	101
6.3	Background from Top Quark Production	101
6.4	Background from Jets Misidentified as Photons	102
6.5	Background from Electrons Misidentified as Photons	114
6.5.1	Fake Factor Method	115
6.5.2	Fake Rate Estimate	116
6.5.3	Fake Rate Application	120
6.5.4	Validation	124
6.5.5	Systematic Uncertainties	129
6.5.6	Signal and Control Region Estimates	134
6.6	Background from Jets Misidentified as Leptons	136

6.6.1	Fake Factor Method	137
6.6.2	Fake Rate	138
6.6.3	Fake Rate Application	141
6.6.4	Validation	141
6.6.5	Systematic Uncertainties	143
6.6.6	Signal Region Estimate	147
6.7	Background from Pileup	148
6.8	Summary	151
7	Systematic Uncertainties	154
7.1	Experimental Uncertainties	155
7.1.1	Energy Scale and Resolution	155
7.1.2	Efficiencies	158
7.1.3	Luminosity	162
7.2	Theoretical Uncertainties	163
7.2.1	Parton Distribution Functions	164
7.2.2	Strong Coupling Constant	164
7.2.3	Renormalization and Factorization Scales	164
7.3	Summary of Uncertainties	165
8	Statistical Model	166
8.1	Signal Significance Extraction	166
8.2	Fiducial Cross Section	171
9	Results	179
10	Summary and Outlook	189
	Bibliography	192

List of Abbreviations	210
List of Figures	215
List of Tables	217

Chapter 1

Introduction

Particle physics is the study of elementary particles and the forces that govern their interactions. The Standard Model of particle physics is a mathematical framework that describes these fundamental constituents of matter and how they interact. The theory stands as one of the most successful and rigorously tested theories in modern physics, having been shown to be in excellent agreement with experimental observations. Its predictive power culminated in the discovery of the Higgs boson in 2012 by the ATLAS and CMS experiments at the Large Hadron Collider [2, 3]. There are, however, several indications that the Standard Model of particle physics is not a complete theory. These include the fact that the Standard Model does not account for gravity, one of the fundamental forces of nature, nor does it provide an answer to the question of dark matter, which makes up a significant portion of the universe's mass.

One way to search for potential new physics phenomena that could provide insights towards a new model of particle physics is to test the limitations of the Standard Model in high energy particle collisions. With the aim of achieving this goal, the Large Hadron Collider collides protons together at unprecedented energies to create rare processes that can be used to probe our understanding of the universe. Particles created from these collisions are

identified and their properties are measured using complex experimental apparatuses such as the ATLAS detector. The resulting data can then be used to search for signatures of new and interesting physics. This includes the extremely rare simultaneous production of three electroweak gauge bosons, the mediators of the electromagnetic and weak nuclear forces, in proton-proton collisions. One such process, the production of a W boson in association with two photons, is predicted to be more than 4000 times rarer than the production of a Higgs boson at the Large Hadron Collider. Importantly, the production rate for this process is entirely determined by the Standard Model. As such, any deviations from predictions would hint at new physics, making the study of the $pp \rightarrow W\gamma\gamma$ process an ideal candidate to test our knowledge of the Standard Model and potentially constrain models that predict new physics phenomena.

To search for events compatible with the $pp \rightarrow W\gamma\gamma$ process, a set of selection criteria is established based on the measured properties of objects reconstructed by the detector. In addition to signal events, several background processes are expected to contribute to the selected data. These include irreducible backgrounds from processes with the same detector signatures as the signal process, which are estimated using simulated data. In addition, there are several reducible backgrounds arising from misidentified objects in the detector. These are typically poorly modelled in simulation and are estimated using data-driven techniques.

A statistical model is built from the expected and observed data and their respective uncertainties. The model is then used to determine the statistical significance of the measurement, which is a measure of the probability that the observed data is due to a statistical fluctuation of the background estimate in the absence of any signal. In order to reveal the true underlying physics of the particle collisions, the detector acceptance and efficiency are disentangled from the data in a process called unfolding. The unfolded data is used to measure the production rate of the $pp \rightarrow W\gamma\gamma$ process, which is then compared with Standard Model predictions. This measurement will be extended in the future to constrain theories describing new physics phenomena beyond the Standard Model.

The thesis is structured as follows. An overview of the Standard Model of particle physics and its limitations is presented in Chapter 2. A description of the experimental setup of the Large Hadron Collider and the ATLAS detector is given in Chapter 3. A summary of the reconstruction algorithms used to identify and measure the outgoing particles from the proton-proton collisions is given in Chapter 4. The event selection requirements for the measurement presented in this thesis are described in Chapter 5. The signal and background estimates in the measurement signal region are detailed in Chapter 6. The experimental and theoretical systematic uncertainties considered in the measurement are summarized in Chapter 7. The statistical model used to extract the significance and the production rate of the measurement is presented in Chapter 8. The expected and observed significance and the measured production rate are presented in Chapter 9. Finally, a summary of the results, the significance of the presented work, and possible future avenues to further study the $W\gamma\gamma$ process are presented in Chapter 10.

Chapter 2

The Standard Model of Particle Physics

The Standard Model (SM) of particle physics is the current theoretical framework used to describe the properties of all known elementary particles and the forces that govern their interactions, with the exception of gravity. This chapter presents a general overview of the theoretical concepts relevant to the motivation and understanding of the $pp \rightarrow W\gamma\gamma$ measurement methods and results. Included is also a discussion of the shortcomings of the Standard Model as well as a compelling model-independent way to parameterize the physics beyond the Standard Model to which the $W\gamma\gamma$ measurement presented in this thesis is sensitive. A large part of the content provided in this chapter is based on References [4, 5, 6], which delve much deeper into the mathematics of the theory.

2.1 Overview

Particle physics is the study of subatomic particles and the forces that govern them, which are themselves mediated by subatomic particles. These elementary point-like particles include the quarks which form the neutrons and protons of the atomic nucleus, which, together with

electrons, form the atoms which make up matter. Electrons are bound to atomic nuclei via the electromagnetic force which is mediated by elementary particles called photons. The quarks inside neutrons and protons are bound together by the strong nuclear force, which is mediated by gluons. These are, to the best of our knowledge, the smallest building blocks of observable matter. However, they are only one small piece of the puzzle. Subatomic particle physics is mathematically described by the Standard Model, a relativistic quantum-mechanical theory in which particles are described as being the excitations of quantum fields. These fields have several quantum mechanical properties which include the specific charges related to the forces with which they can interact, such as the familiar electrical charge associated to the electromagnetic force. In addition, every particle has an associated spin, which can be thought of as a form of intrinsic angular momentum. In quantum mechanics, spin is quantized and its total value can take on either half integer values for fermionic fields or integer values for bosonic fields. Fermions are the particles that make up matter, while the gauge bosons are the particles that communicate or mediate the fundamental forces. There is another type of boson, the Higgs boson, which is understood to arise from spontaneous symmetry breaking of the unified electromagnetic and weak nuclear forces, called the electroweak force. This so-called Higgs mechanism gives rise to the masses of the fermions and the gauge bosons of the weak nuclear force. This is discussed in more detail in Section 2.4. An overview of the elementary particles that make up the Standard Model and their properties is shown in Figure 2.1.

Note that in this thesis, units of energy, and more precisely electronvolts (eV), will be used when referring to the mass, energy, and momentum of particles. This follows the natural units convention used in particle physics whereby $c = \hbar = 1$.

QUARKS	Mass: 2.2* Charge: 2/3 Spin: 1/2	1,270 2/3 1/2	173,100 2/3 1/2	GAUGE BOSONS (VECTOR BOSONS)	0 0 1	SCALAR BOSONS	125,180
							
	4.7 -1/3 1/2	96 -1/3 1/2	4,180 -1/3 1/2		0 0 1		
LEPTONS	0.511 -1 1/2	105.66 -1 1/2	1,776.8 -1 1/2	GAUGE BOSONS (VECTOR BOSONS)	91,188 0 1	SCALAR BOSONS	
							
	<0.00000012 0 1/2	<0.00000012 0 1/2	<0.00000012 0 1/2		80,379 +/-1 1		
							

Figure 2.1: Summary of the elementary particles that make up the Standard Model and their properties [7]. Fermions are split into the quarks (blue) and leptons (grey), and bosons are split into the gauge bosons (orange) and the Higgs boson (yellow). The three generations of leptons are shown in three columns starting with the first generation in the leftmost column. The mass (in units of MeV), electric charge, and spin of each particle are also listed.

2.1.1 Fermions

Matter is composed of spin- $\frac{1}{2}$ fermions of which there are two types, leptons and quarks. Leptons and quarks can be further classified into three generations of pairs. The first generation of leptons consists of the electron, which interacts via the electromagnetic and weak forces, and the electron neutrino, which interacts only via the weak force. The pairing of an electrically charged lepton with its associated neutral neutrino is replicated with the muon and tau lepton making up the second and third generations, respectively. Neutrinos are the lightest massive particles in the Standard Model. Only upper and lower bounds currently exist on their masses, and their mass hierarchy is also not yet fully determined [8]. The other type of fermion, quarks, interact via the electromagnetic, weak, and strong forces. The first generation of quarks is comprised of the up and down quarks, followed by the charm and strange quarks in the second generation, and the top and bottom quarks in the third. Leptons and quarks of the first generation are the lightest fermions and therefore cannot decay to any lower mass fermion. As a result, these are the particles that make up ordinary stable matter in the universe.

For every elementary matter particle, there exists an associated anti-particle with the same mass but with opposite charges. For example, the electron has an electric charge of -1, while the anti-electron, called positron, has the same mass as the electron but has an electric charge of +1. Throughout this thesis, references to a specific type of particle will implicitly refer to both the particle and its associated anti-particle unless otherwise stated.

2.1.2 Bosons

Matter particles interact with each other via the fundamental forces of nature, which are mediated by the spin-1 gauge bosons. The electromagnetic force is mediated by the massless photon, the weak nuclear force is mediated by the massive W^\pm and Z^0 bosons, and the strong force is mediated by the massless gluons. These gauge bosons interact with

particles that carry the charges of their respective forces. Particles that interact via the electromagnetic force carry either positive or negative electric charge. Particles that interact via the strong force carry colour charge, referred to as red, green or blue (or anti-red, anti-green, and anti-blue in the case of anti-particles). As described in the next section, particles can undergo weak interactions according to their values of weak hypercharge and weak isospin. In addition, the W^\pm boson is electrically charged and thus interacts via the electromagnetic force. Furthermore gluons themselves carry colour charge, which leads to several interesting experimentally observable consequences as will be discussed in Section 2.3.

The final type of observed elementary boson is the massive Higgs boson, which is a spin-0 scalar boson arising from the symmetry breaking of the electroweak force, the unified electromagnetic and weak forces. The Higgs mechanism is what gives rise to the masses of the fermions and the W^\pm and Z^0 bosons. As such, it is hypothesised that the Higgs boson interacts with all massive particles of the Standard Model, including itself, with the exception of neutrinos which do not get their masses from the Higgs mechanism.

2.1.3 Mathematical Formulation of the Standard Model

The Standard Model is a relativistic quantum field theory. Particles are represented as operators on a Hilbert space which create and annihilate excitations of a quantum field. The Standard Model Lagrangian is a function of these operators and their space-time derivatives, or, in other words, of the position and velocity of the particles that make up the theory. The action, which is the integral of the Lagrangian density over space-time, is minimized according to Hamilton's principle of least action, leading to the Euler-Lagrange equations which describe the dynamics of the system [4]. The Lagrangian formalism of the Standard Model includes certain properties common to all generic quantum field theories, including space-time symmetry through Lorentz invariance, internal symmetries through

gauge invariance, as well as causality and locality. In accordance with Noether's theorem [9], every continuous symmetry of the Lagrangian of a system implies a conservation law. For example, invariance under translation, rotation, and time leads to the conservation of momentum, angular momentum, and energy, respectively. These conservation rules are a consequence of the Lorentz invariance of the Standard Model Lagrangian. Invariance of operators in a Lagrangian under local gauge transformation leads to the conservation of a charge. For example, the $U(1)_{\text{EM}}$ symmetry in Quantum Electrodynamics (QED) leads to the conservation of the electric charge.

The fields of the Standard Model transform under the local gauge symmetries of the $SU(3)_c \times SU(2)_L \times U(1)_Y$ group. The conserved charges of these groups are the hypercharge Y for $U(1)_Y$, the weak isospin T for $SU(2)_L$, and colour charge c for $SU(3)_c$. The $SU(3)_c$ gauge group describes the symmetries of Quantum Chromodynamics (QCD), the theory of the strong force discussed in Section 2.3. The $U(1)_Y \times SU(2)_L$ gauge group represents the symmetries of the electroweak force discussed in Section 2.4. The subscript L indicates that only left-handed fermions (or right-handed anti-fermions) transform under the $SU(2)_L$ group, meaning that left-handed fermions transform as weak isodoublets while right-handed fermions transform as weak isosinglets (and vice versa for anti-fermions). The familiar electric charge Q is related to hypercharge Y and weak isospin T through the Gell-Mann-Nishijima relation $Q = \frac{1}{2}Y + T_3$ [10, 11], where T_3 represents the third component of the weak isospin. Given the field content of the Standard Model previously described, the possible set of interactions between particles arise from the most general set of mathematically consistent, or renormalizable, interactions.

The Standard Model Lagrangian contains 19 free parameters that must be measured experimentally in order to realize the predictive power of the theory. These include parameters such as the masses of the fermions and bosons, the matrix elements describing the mixing between the three generations of quarks and its phase, and the vacuum expectation value of the Higgs field.

So-called *Feynman diagrams* are used to graphically represent the complex integrals that must be evaluated to calculate the probability amplitudes for the possible interactions allowed in the Standard Model. While Feynman diagrams represent a uniquely intuitive way to visualize particle interactions in quantum field theories, they also provide a prescription (called *Feynman rules*) to be followed in order to calculate the interaction probabilities. The Feynman rules of a quantum field theory associate a term for each incoming and outgoing line to conserve energy, momentum, and spin, a term for each internal line corresponding to the virtual particle's propagator, and a term for each interaction vertex. Feynman diagrams represent perturbative corrections to the scattering amplitudes of a given process. As such, every possible diagram constructed from the possible vertices of the theory contributes to the calculation. However, in the perturbative regime where the coupling strengths of the interactions are small, diagrams with more interaction vertices contribute less to the total amplitude. As such, the value of a scattering amplitude can be approximated by cutting off the calculation at a given order in the perturbative expansion, which is equivalent to ignoring Feynman diagrams beyond a certain number of vertices.

2.2 Quantum Electrodynamics

The first part of the Standard Model to be formalized was the theory of Quantum Electrodynamics (QED), which was spearheaded by Paul Dirac [12]. This is the theory of electromagnetism which describes the dynamics of electrons and photons. All of the possible Feynman diagrams of this theory are formed from the simple vertex shown in Figure 2.2, which couples a photon to two electrons (or an electron and a positron).

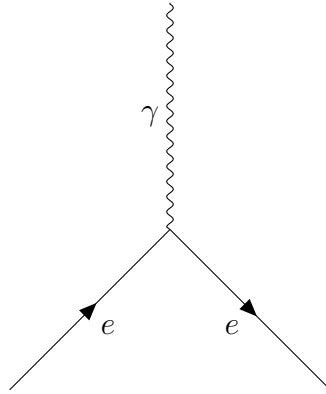


Figure 2.2: Feynman diagram representing the interaction vertex associated with Quantum Electrodynamics whereby one photon couples to two electrons or an electron and positron.

2.3 Quantum Chromodynamics

The theory of the strong force is called Quantum Chromodynamics (QCD) referring to the representation of its fundamental charges as colours. The non-Abelian (or non-commutative) $SU(3)_c$ gauge group has 8 generators, giving a total of 8 mediating gluons which carry combinations of the three colour and three anti-colour charges. All particles that couple to gluons and thus interact via the strong force carry colour charge. The fact that gluons carry the charge of the force they mediate leads to several interesting properties, including the self coupling of gluons. The possible interaction vertices of Quantum Chromodynamics are shown in Figure 2.3. The allowed interaction vertices include a vertex coupling two same-flavour quarks to a gluon, and two vertices where gluons self-interact via a triple or quartic gauge couplings.

2.3.1 Quantum Chromodynamics at Hadron Colliders

Due to the fact that gluons carry colour charge, the strength of the strong force increases with the distance between two colour charges. This leads to a phenomenon called confinement, whereby only colourless bound states can exist in isolation. In high energy collisions, quark

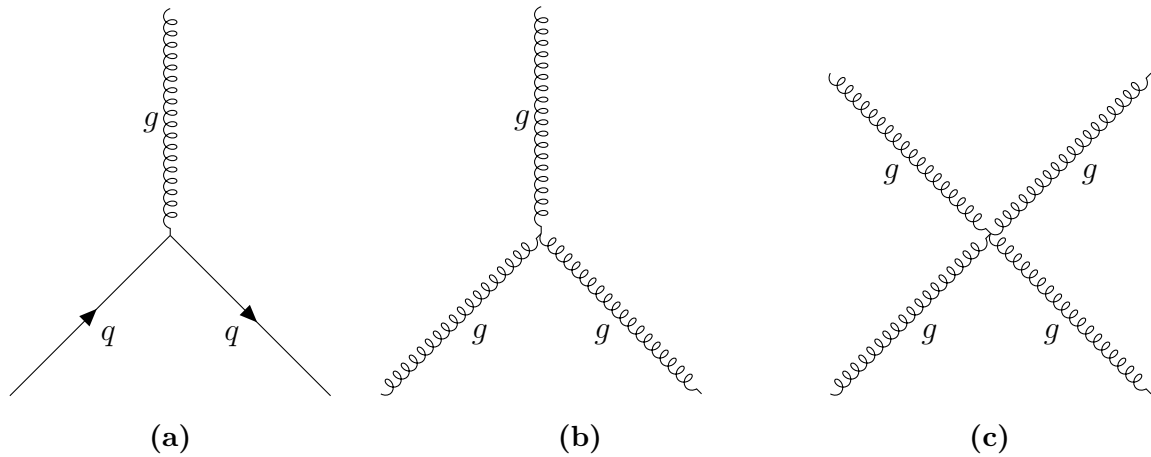


Figure 2.3: Feynman diagrams representing the interaction vertices associated to Quantum Chromodynamics, whereby (a) a gluon couples to two same-flavour quarks, (b) three gluons directly couple to each other, and (c) four gluons directly couple to each other.

and anti-quark pairs produced in isolation either come together to form a colourless bound state, or quark anti-quark pairs are spontaneously created from vacuum to bind with the initial particles and form lower energy colourless bound states. The latter phenomenon occurs due to the large energy density in the gluon field between the quark anti-quark pair. This phenomenon also happens to gluons produced in high energy collisions due to the fact that they also carry colour charge. The process of forming colourless bound states is called hadronization. Hadronization results in the formation of hadronic jets made up of many collimated colourless bound states of quarks whose kinematic properties are correlated to those of the initial quark or gluon. These colourless bound states of quarks, called hadrons, can be made of two or three quarks, called mesons and baryons, respectively. In addition, hadrons with four or five quarks have been observed in recent years [13], called tetraquarks and pentaquarks, respectively. Conversely, at small distances and large energies, like those probed in proton-proton collisions at the LHC, the value of the strong coupling decreases and quarks behave as free particles. This phenomenon is called asymptotic freedom.

In high energy collisions, not only are the valence quarks of the colliding hadrons

probed, but also the gluons that bind them together, as well as the quark anti-quark pairs spontaneously created from these gluons, called sea quarks. In fact, the mass of the proton, approximately 938 MeV, is much heavier than the sum of masses of its three valence quarks (two up quarks and one down quark), which make up only approximately 1% of the proton's mass. The rest comes from the binding energy between the valence quarks.

In the proton, the valence quarks, gluons, and sea quarks are called partons. The composition of the proton is described using Parton Distribution Functions (PDFs). These represent the probability that a quark or gluon is probed, for a given momentum transfer, as a function of the fraction of the proton's momentum carried by the parton. Since the interactions between the quarks and gluons inside a proton are at low energies, Parton Distribution Functions cannot be calculated from perturbative Quantum Chromodynamics and must be determined experimentally. However, Parton Distribution Functions can be evolved to different energy scales using perturbative Quantum Chromodynamics via the Dokshitzer–Gribov–Lipatov–Altarelli–Parisi (DGLAP) evolution equations [14, 15, 16]. An example set of Parton Distribution Functions used to simulate some of the data used in this thesis is shown in Figure 2.4.

When two partons interact inelastically in a proton-proton collision, a process called the *hard scatter*, new particles are created from the energy of the interaction. These inelastic collisions are the main processes of interest in the context of this thesis. The remaining partons not involved in the hard scatter, as well as additional protons in the same proton bunches, can also interact with each other, forming the underlying event. The incoming partons and outgoing quarks and gluons can also radiate additional quarks or gluons in processes called initial and final state radiation. As this process unfurls, the initial and radiated quarks and gluons are left with progressively less and less energy until they reach the energy scale at which the value of the strong coupling is large enough that the phenomenon of hadronization takes over. The various phenomena at play in proton-proton collisions are schematically depicted in Figure 2.5.

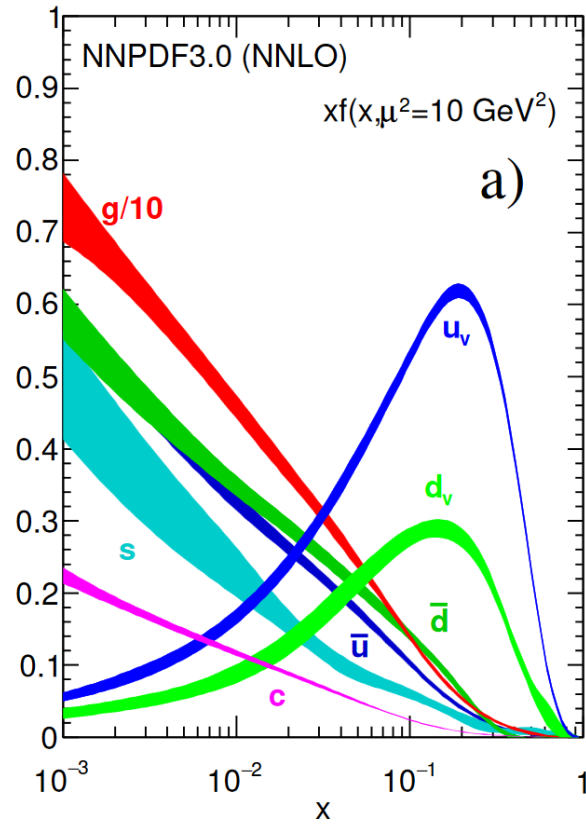


Figure 2.4: Example Parton Distribution Function from the NNPDF group [8, 17]. The x -axis represents the fraction x of the total proton energy carried by the parton while the y -axis represents the value of the parton distribution function $f(x)$ multiplied by x .

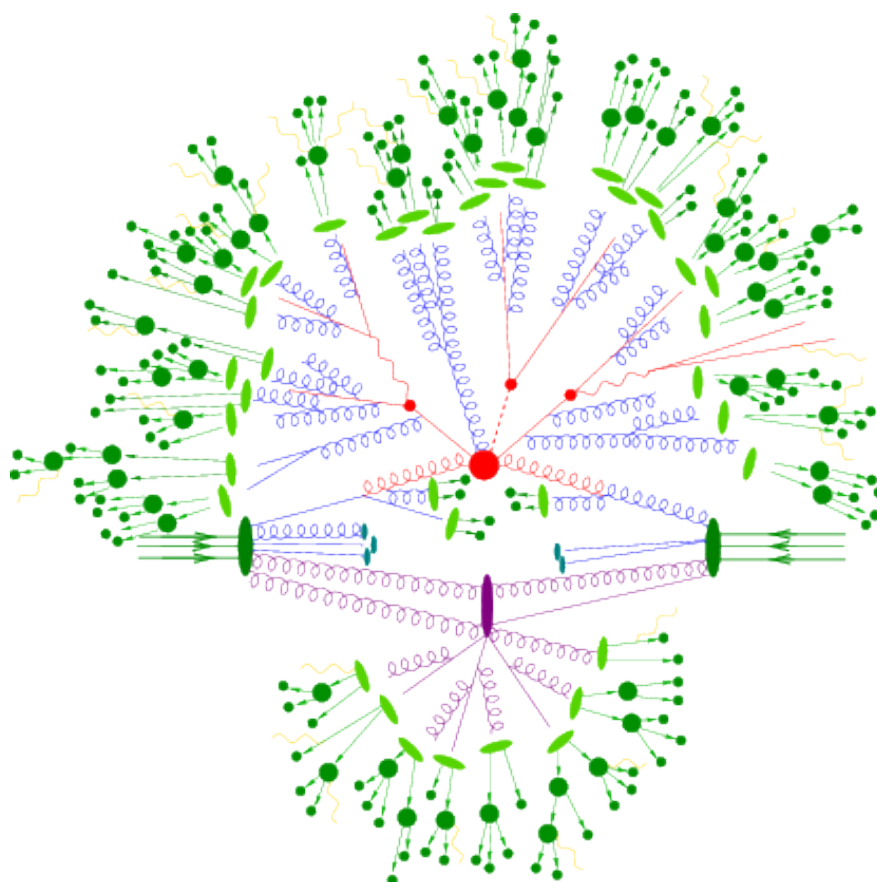


Figure 2.5: Schematic diagram representing the different components of a proton-proton collision [18]. The hard scatter is shown in red, the contributions from the underlying event are shown in purple, initial and final state radiation are shown in blue, the hadronization process is shown in light green, and colourless bound states of quarks are shown in dark green.

2.4 Electroweak Symmetry Breaking

At energies higher than the energy scale of the weak interaction, represented by the masses of the W^\pm and Z bosons (approximately 100 GeV), the electromagnetic and weak forces become indistinguishable and are described by a common electroweak force. This force is represented by the $SU(2)_L \times U(1)_Y$ symmetry group of the Standard Model. The $SU(2)_L$ group has the conserved charge of weak isospin and is mediated by three massless gauge bosons, labeled W_1 , W_2 , and W_3 . The $U(1)_Y$ group is associated with hypercharge and is mediated by one massless gauge boson, labeled B . Explicit mass terms for the gauge bosons and fermions are forbidden in the Standard Model Lagrangian by the $SU(2)_L \times U(1)_Y$ local gauge invariance.

At energies well below the electroweak energy scale, spontaneous symmetry breaking occurs through the introduction of a isospin doublet of complex scalar fields ϕ in the Standard Model Lagrangian. This field has a potential $V(\phi)$ with an unstable critical point at the origin and thus a ground state which breaks its rotational symmetry, as shown in Figure 2.6. The energy of this non-zero ground state is called the Higgs vacuum expectation value (v.e.v.). With the exception of the neutrinos, fermions acquire mass through Yukawa couplings to the Higgs vacuum expectation value. The W_1 and W_2 bosons combine to form the massive W^\pm bosons, and the W_3 and B bosons combine to form the massive Z^0 boson and the massless photon via the weak mixing angle, θ_w , which also relates the mass of the W boson to the Z boson. Finally, a massive spin-0 scalar boson is left called the Higgs boson.

The electroweak symmetry breaking mechanism results in the electroweak force manifesting itself at lower energies as the familiar weak and electromagnetic forces. It is important to note that the $U(1)_{EM}$ symmetry of the electromagnetic force is distinct from the $U(1)_Y$ symmetry group; it is a subgroup of the electroweak $SU(2)_L \times U(1)_Y$ symmetry group. The allowed interaction vertices of the electroweak theory are shown in Figure 2.7. These include the vertices responsible for flavour-changing charged currents whereby a W

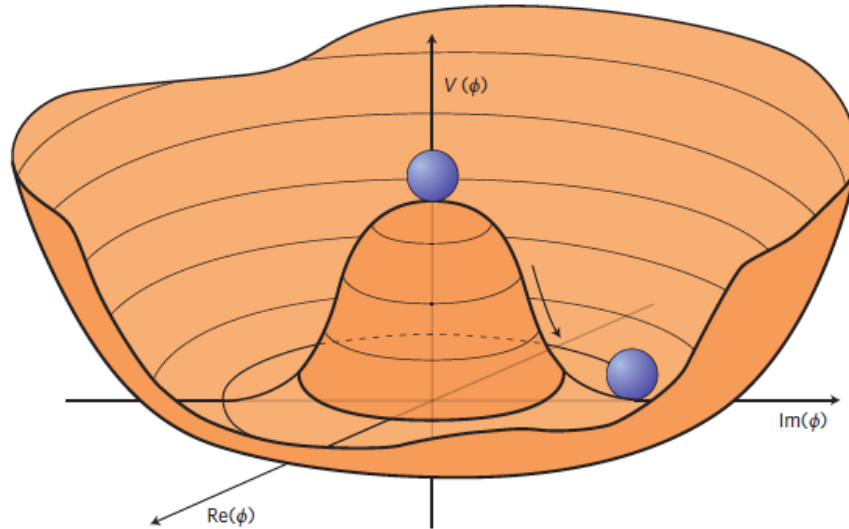


Figure 2.6: Sketch of the Higgs field potential $V(\phi)$ showing the degenerate vacuum states responsible for the spontaneous symmetry breaking of the electroweak force [19].

boson couples to a charged lepton and its neutral neutrino counterpart, or couples two different flavours of quarks. Quark flavour mixing is described by the Cabibbo–Kobayashi–Maskawa (CKM) matrix [20, 21] which mixes the different flavours of quarks. This occurs due to the fact that the quark mass eigenstates do not correspond to their flavour eigenstates. In addition, there exist triple and quartic gauge coupling vertices which couple directly three or four of the electroweak gauge bosons. Electroweak interaction vertices which include the Higgs boson are shown in Figure 2.8, which couple the Higgs boson to two fermions, to two vector bosons, or to itself and gauge bosons through various triple and quartic vertices.

2.5 Beyond the Standard Model

The Standard Model has been extremely successful, both in its excellent agreement with experimental data and through its predictive power. For example, Figure 2.9 shows a

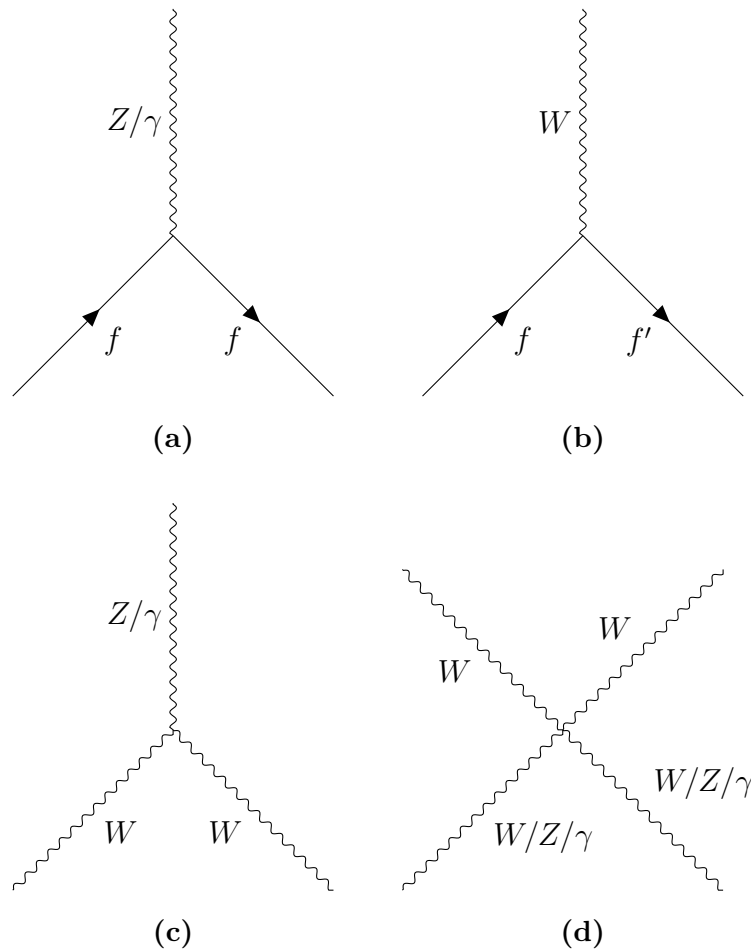


Figure 2.7: Feynman diagrams representing interaction vertices associated to electroweak theory whereby (a) a photon / Z boson couples to two same flavour fermions, (b) a W boson couples to two different flavour fermions, (c) a photon / Z boson couples to two W bosons, and (d) four gauge bosons couple directly to one another forming a quartic $WWWW$, $WWZZ$, $WWZ\gamma$, or $WW\gamma\gamma$ vertex.

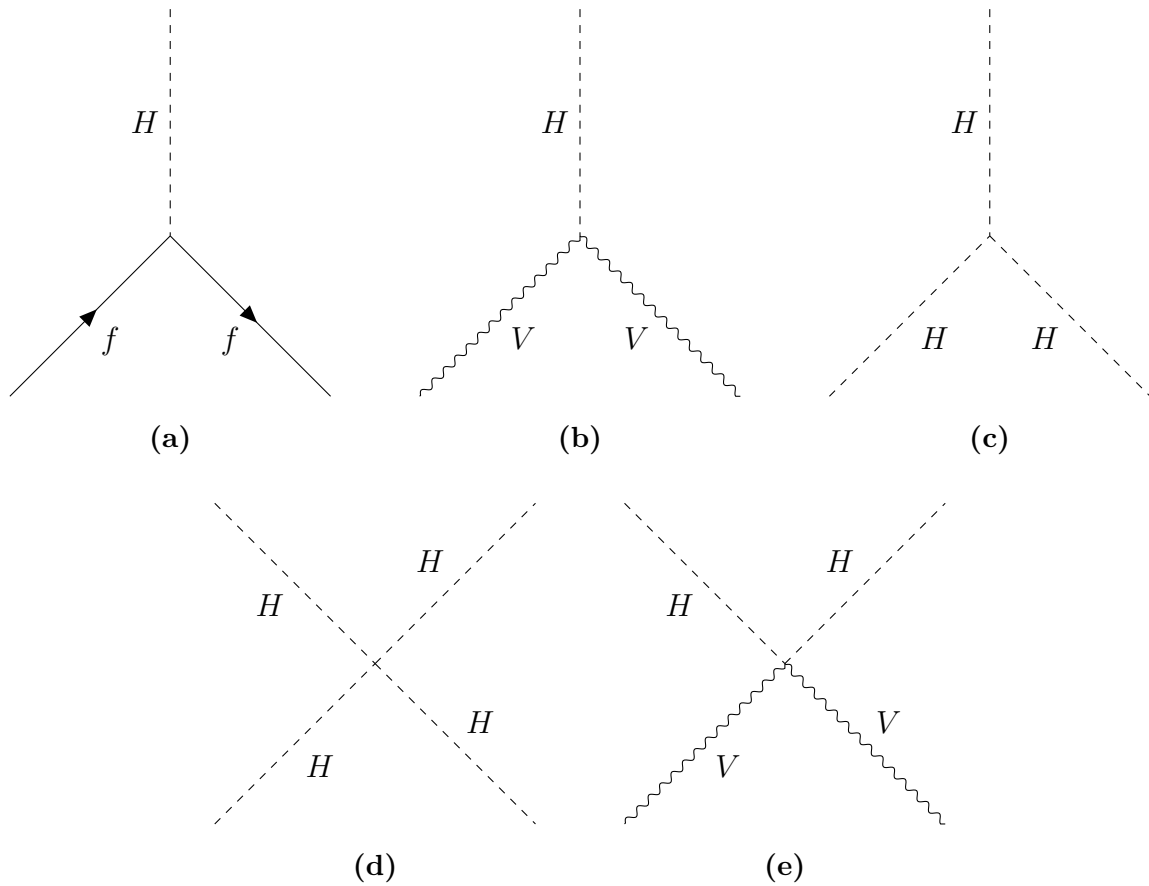


Figure 2.8: Feynman diagrams representing interaction vertices associated to the Higgs boson whereby (a) a Higgs boson couples to two same-flavour fermions, (b) a Higgs boson couples to two massive gauge bosons of the same type ($V = Z$ or W), (c) three Higgs bosons couple directly together, (d) four Higgs bosons couple directly together, and (e) two Higgs bosons couple to two massive gauge bosons of the same type.

comparison between measured and predicted production cross sections for a large number of processes studied using the ATLAS detector. Standard Model predictions agree with a wide range of physics processes over cross sections spanning more than 14 orders of magnitude. In addition, the Standard Model predicted the existence of several particles before their discovery through experiment, including the W and Z bosons in 1983 [22, 23], the top quark in 1995 [24, 25], and Higgs boson in 2012 [2, 3].

There are, however, several indications that the Standard Model is an incomplete theory. One of the fundamental forces of nature, gravity, and its description through Einstein's general relativity, has yet to be reconciled with quantum mechanics and thus is not described by the Standard Model. In addition, the matter described by the Standard Model only makes up an estimated 5% of the energy content of the universe, as inferred through cosmological observations [8]. Dark matter, a form of matter hypothesized to exist through its gravitational effects observed on astrophysical and cosmological scales, is thought to make up approximately 25% of the energy content of the universe. The remaining 70% is made up of dark energy, which is responsible for the accelerating expansion of the universe. There is evidence that neutrinos have a non-zero mass due to the observation of neutrino oscillation [27], implying that their flavour and mass eigenstates are not the same. However, using only renormalizable interactions and the minimal field content of the Standard Model, neutrinos do not acquire mass through the Higgs mechanism [4]. As such, currently, the Standard Model does not contain any mechanism by which neutrinos could acquire mass. The Standard Model also does not have a mechanism to explain the observed matter anti-matter asymmetry in the universe. In fact, even the Charge-Parity (CP) violating phase of the CKM matrix in Quantum Chromodynamics seems to be unnaturally small, requiring so-called *fine tuning* of the Standard Model theory's parameters [4]. Another fine tuning issue is the apparent hierarchy problem stemming from the huge energy scale difference between the electroweak scale at about 100 GeV and the Planck scale at around 10^{19} GeV, requiring a fine tuning of the radiative

corrections to the Higgs bare mass [28]. These and other unanswered questions all point towards the existence of new physics phenomena beyond those described by the Standard Model.

2.5.1 Effective Field Theories

Since the nature of new physics phenomena beyond those described by the Standard Model is unknown, one particularly powerful approach to modelling possible deviations from Standard Model predictions is the use of Effective Field Theories (EFTs). The historical development of the mathematical description of β -decays illustrates well the power of this approach. Fermi's theory of β -decays was in fact an Effective Field Theory which parametrized the then unknown electroweak theory by directly coupling the neutron, proton, electron, and anti-electron neutrino in a single vertex, as shown in Figure 2.10(a) [4]. This type of interaction is described by a dimension-6 operator which leads to interaction probabilities beyond unity at high energies, thereby violating unitarity. At higher energies (or smaller distances), the W boson becomes resolvable and the Standard Model describes β -decay by two renormalizable dimension-4 vertices as shown in Figure 2.10(b).

Fermi's theory of beta decay illustrates how by using an Effective Field Theory approach, the effects of unknown physics phenomena can be parameterized in a model independent way by adding operators to the Standard Model Lagrangian (\mathcal{L}_{SM}). These additional terms go beyond the set of renormalizable operators of dimension $n = 4$ already present in the Standard Model. These additional non-renormalizable terms in the Lagrangian parameterize the effects of new physics at an unknown energy scale Λ through higher dimension operators \mathcal{O}_n . The new Standard Model Effective Field Theory (SMEFT) Lagrangian becomes:

$$\mathcal{L}_{\text{SMEFT}} = \mathcal{L}_{\text{SM}} + \sum_{n=5}^{\infty} \frac{f_n}{\Lambda^{n-4}} \mathcal{O}_n, \quad (2.1)$$

where f_n represents dimensionless coupling coefficients. These additional terms include

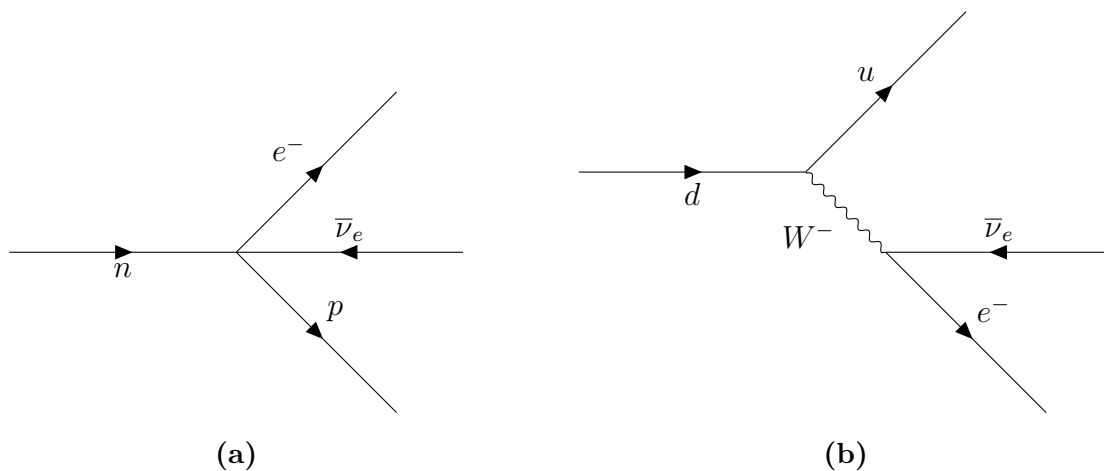


Figure 2.10: Feynman diagrams for (a) Fermi's effective interaction and (b) the Standard Model diagram for β -decay.

so-called anomalous Triple and Quartic Gauge Couplings (aTGC and aQGC, respectively) which couple directly three or four of the electroweak gauge bosons and correspond to dimension-6 and dimension-8 operators, respectively. These couplings increase the cross section and affect the kinematics of processes sensitive to triple and quartic couplings between the electroweak gauge bosons. Cross section measurements of different processes that are sensitive to these couplings can be used to measure or set constraints on the coupling coefficients f_n of these higher dimension operators. While the $pp \rightarrow W\gamma\gamma$ process is sensitive to both aTGCs and aQGCs, diboson final states are much more sensitive to aTGCs, making triboson final states in proton-proton collisions, such as $pp \rightarrow W\gamma\gamma$, ideal candidates for setting limits on aQGCs [29, 30].

2.6 The $pp \rightarrow W\gamma\gamma$ Process

A few representative Feynman diagrams of the $pp \rightarrow W\gamma\gamma$ process are shown in Figure 2.11. These include Feynman diagrams in which the photons are produced via $WW\gamma$ triple and $WW\gamma\gamma$ quartic gauge coupling vertices. These diagrams are sensitive to aTGC and aQGC

operators, as described in the previous section. In addition, Feynman diagrams in which the photons are produced via initial or final state radiation off of the initial or final state partons, respectively, can also contribute. Finally, both photons can also be produced through the decay of a Higgs boson, though this diagram is considered to be a source of background in the context of this analysis.

2.7 Motivation

The observation and measurement of the production cross section of triboson final states are important tests of the Standard Model and are complementary to other measurements at the LHC. The production of three electroweak gauge bosons in proton-proton collisions is extremely rare, with the production of a $W\gamma\gamma$ event being more than 4000 times rarer than the production of a Higgs boson. Some of these triboson production processes are only now becoming accessible for the first time with the latest data from the LHC. Triboson production processes that have recently been observed for the first time include the $WW\gamma$ [31] and the $WZ\gamma$ [32] processes, as well as the $W\gamma\gamma$ [33] process presented in this thesis. Other triboson final states such as the $ZZ\gamma$ and ZZZ processes remain elusive. In addition, the $W\gamma\gamma$ process will be background to the $WH(\rightarrow\gamma\gamma)$ process which could become accessible with more data from the LHC, underlining the importance of understanding the $W\gamma\gamma$ final state. Finally, triboson processes are directly sensitive to the structure of the electroweak triple and quartic gauge vertices, which are completely determined by the Standard Model. As such, any deviations from predictions would be a sign of new physics. In the absence of any statistically significant deviation, measurements of triboson production cross sections can be used to set constraints on anomalous Triple and Quartic Gauge Coupling operators in the context of an Effective Field Theory approach as described in Section 2.5.1. As such, the first observation of the $pp \rightarrow W\gamma\gamma$ process presented in this thesis opens up new directions of scientific inquiries.

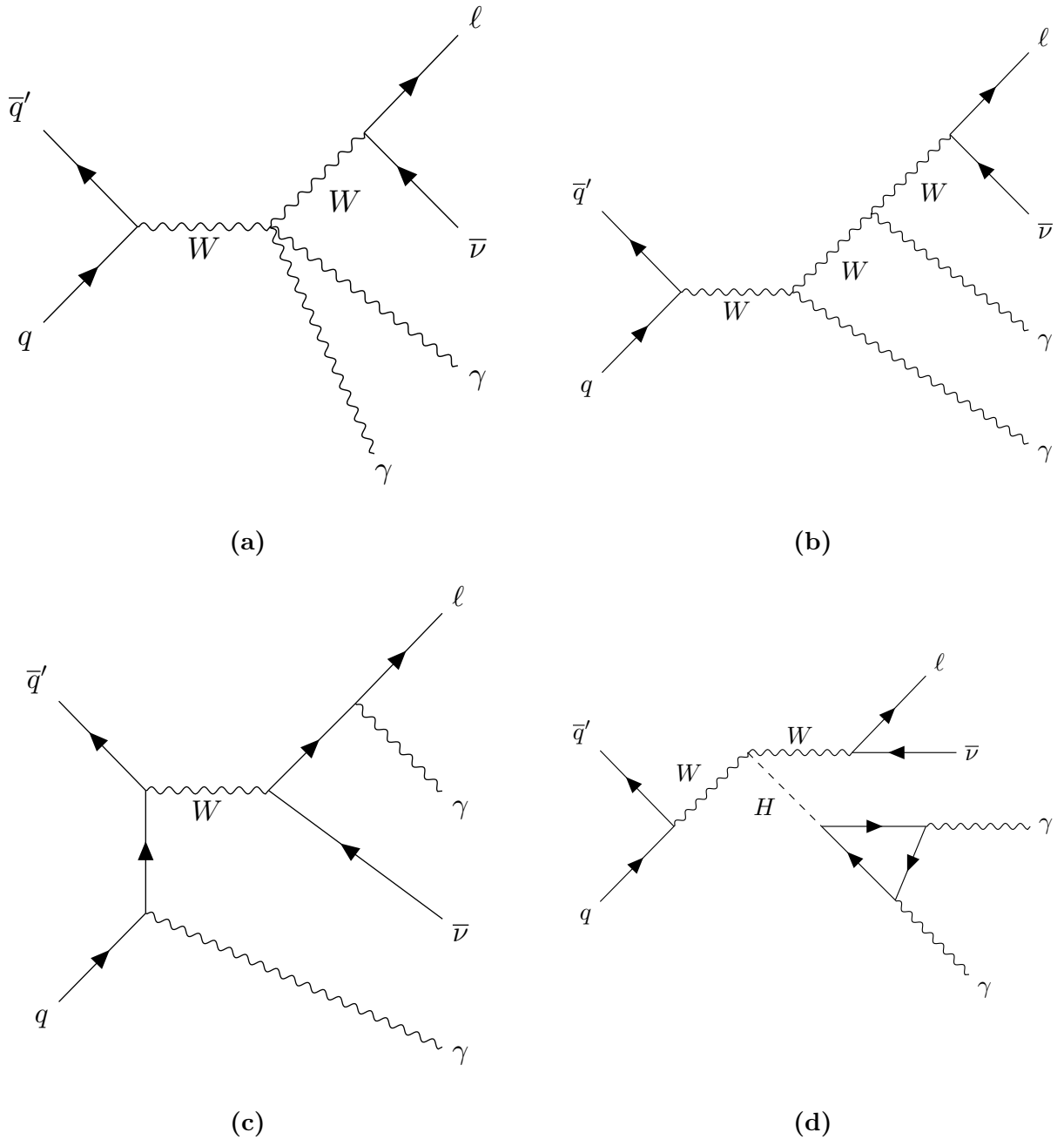


Figure 2.11: Representative sample of Feynman diagrams contributing to the $pp \rightarrow W\gamma\gamma$ process. These include diagrams in which the photons are produced via (a) a $WW\gamma\gamma$ quartic gauge coupling, (b) two $WW\gamma$ triple gauge couplings, (c) both initial and final state radiation, (d) or the decay of a Higgs boson.

Chapter 3

Experimental Setup

In this chapter, an overview of the experimental setup used to collect the data used in this thesis is given. The data was collected by the ATLAS detector at the Large Hadron Collider (LHC) located at the Conseil Européen pour la Recherche Nucléaire (CERN). These two principal components of the experimental setup, the collider and detector, are described in this chapter given their configuration over the course of the data taking period from 2015 to 2018. A more detailed description of the LHC and the ATLAS detector can be found in References [34] and [35], respectively.

3.1 The Large Hadron Collider

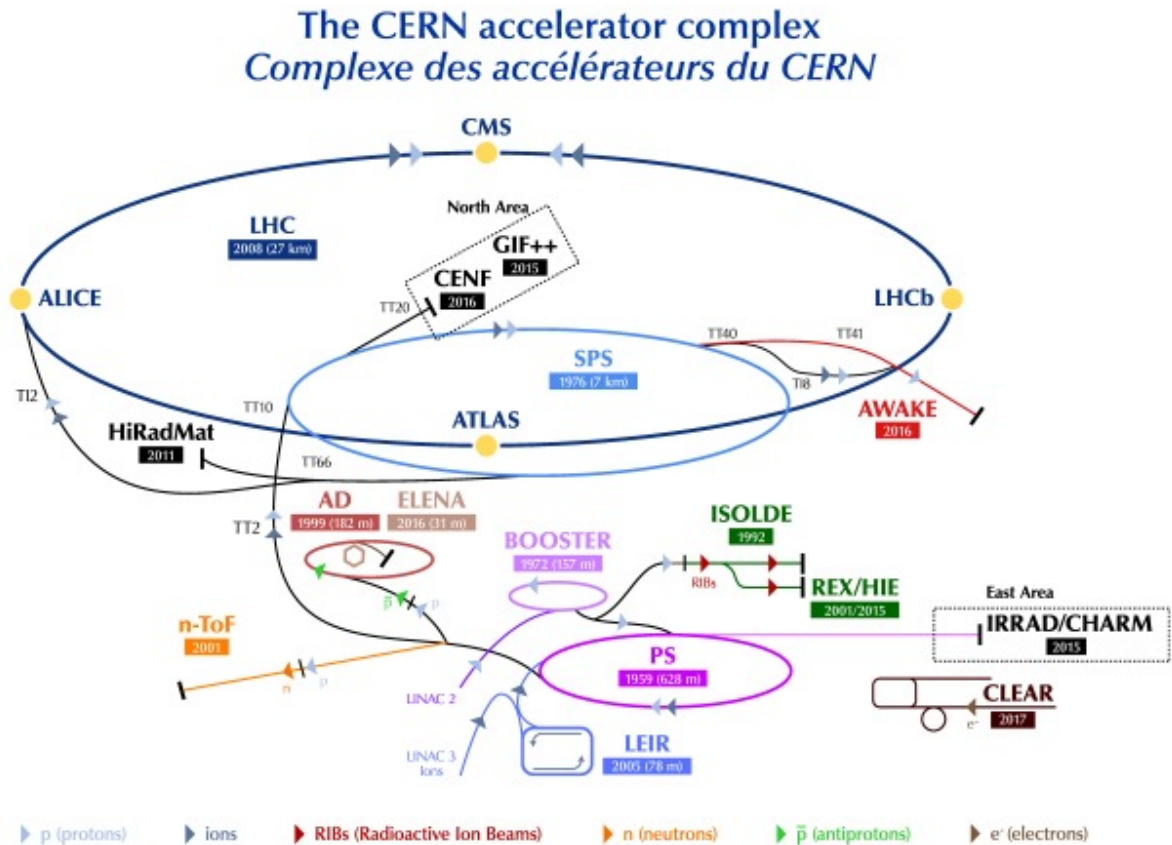
The Large Hadron Collider is a particle accelerator located at the CERN laboratory, which straddles the border between Switzerland and France near the city of Geneva, Switzerland. It is designed to collide bunches of protons together at four interaction points corresponding to the locations at which the four main detectors are placed, ATLAS [35], CMS [36], ALICE [37], and LHCb [38], as can be seen in Figure 3.1.

The collider is located in a tunnel approximately 100 m underground that has a circumference of 27 km. It consists of two parallel beam-lines held at ultrahigh vacuum

(approximately 10^{-10} to 10^{-11} mbar of pressure) through which two counter-rotating proton beams travel at speeds very close to the speed of light. During the Run 2 data taking period from 2015 to 2018, protons were collided at a center of mass energy of 13 TeV, the highest center of mass energy achieved in a laboratory at that point.

The LHC provides the last stage of acceleration in a long chain of accelerators. At the beginning of the chain, electrons are stripped from a hydrogen gas by an electric field and the remaining protons are accelerated inside the Linear Accelerator 2 (LINAC2), after which they are injected into the Booster. Here, the protons are accelerated to an energy of 1.4 GeV for injection into the Proton Synchrotron (PS) where they are further accelerated to 26 GeV. They are then injected into the Super Proton Synchrotron (SPS) and accelerated up to 450 GeV before being injected into the LHC. During the Run 2 data taking period, the proton beams inside the LHC were each accelerated to 6.5 TeV in order to achieve the final collision center of mass energy of 13 TeV.

In the Large Hadron Collider, the protons are accelerated by 16 superconducting Radio Frequency (RF) cavities, 8 per beam, that each provide a 400 MHz oscillating electric field with amplitudes ranging from 8 MV to 16 MV. In addition to accelerating the protons from 450 GeV to 6.5 TeV, these Radio Frequency cavities are responsible for keeping the protons in bunches and spaced 25 ns apart, giving the Large Hadron Collider its bunch crossing (BC) frequency of 40 MHz. In reality, not every possible RF bucket is filled with a proton bunch due to certain technical limitations of various systems along the acceleration path of the protons. Of the 3564 RF buckets inside the LHC, only 2808 are filled. The filled bunches follow patterns called filling schemes, where sequential filled bunches are called bunch trains. Trains end in a number of RF buckets deliberately left empty corresponding to $\approx 3 \mu\text{s}$ along the circumference of the LHC. These empty RF buckets make up the abort gap that provides enough time for magnets to be turned on to safely direct the beams into the beam dump. In so doing, the proton beams are redirected and ejected into an external absorber material. The time between the injection of protons into the Large Hadron Collider beam and the



LHC - Large Hadron Collider // SPS - Super Proton Synchrotron // PS - Proton Synchrotron // AD - Antiproton Decelerator // CLEAR - CERN Linear Electron Accelerator for Research // AWAKE - Advanced WAKEfield Experiment // ISOLDE - Isotope Separator OnLine // REX/HIE - Radioactive EXperiment/High Intensity and Energy ISOLDE // LEIR - Low Energy Ion Ring // LINAC - LINear ACcelerator // n-ToF - Neutrons Time Of Flight // HiRadMat - High-Radiation to Materials // CHARM - Cern High energy AcceleraTOR Mixed field facility // IRRAD - proton IRRADIation facility // GIF++ - Gamma Irradiation Facility // CENF - CERN Neutrino platform

Figure 3.1: Schematic diagram of the CERN accelerator complex [39].

ejection of the beams into the beam dump is called a fill.

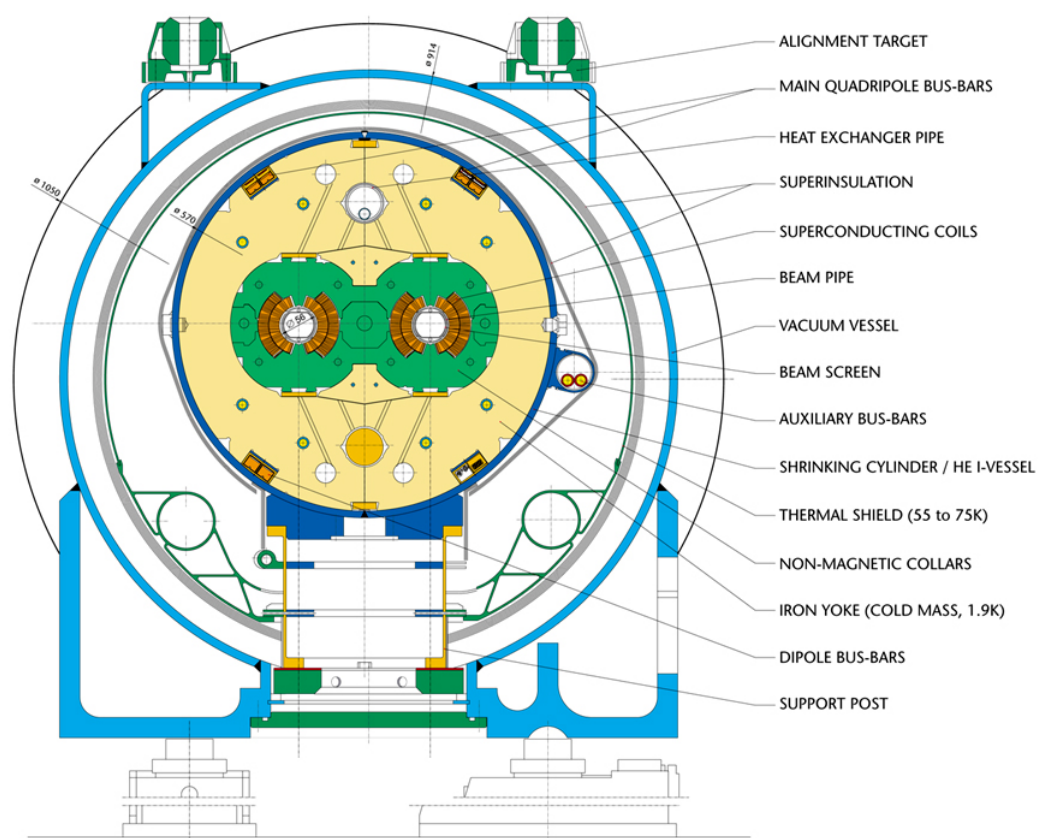
The LHC is equipped with almost 10,000 superconducting magnets that are used to steer and focus the proton beams within the beam pipes and at the interaction points along the circumference of the LHC. These superconducting magnets are held at a temperature below 2 K using superfluid helium-4 (^4He) in order to achieve magnetic fields above 8 T. There are 1232 dipole magnets and 450 quadrupole magnets used to bend and focus the proton beams, respectively. Figure 3.2 shows a diagram of the transverse cross section of an LHC dipole magnet. In addition, there are several thousand corrector magnets used to account for imperfections in the field geometry as well as injection and kicker magnets at the beam injection and extraction points.

At the start of an LHC fill, protons are injected until each proton bunch contains approximately 1.2×10^{11} protons. Then, the protons are accelerated to 6.5 GeV and collisions can begin. Due to the gradual drop in beam intensity from the protons interacting and the bunches subsequently emptying, a point is reached at which it becomes more advantageous to dump the beams and begin a new fill instead of collecting data at a reduced number of interactions per bunch crossing. The number of interactions per bunch crossing as a function of time is measured using the instantaneous luminosity \mathcal{L} . This can be calculated in terms of the beam parameters with the following equation [8]:

$$\mathcal{L} = f_{\text{coll}} \frac{n_1 n_2}{4\pi \sigma_x^* \sigma_y^*} \mathcal{F}, \quad (3.1)$$

where f_{coll} is the revolution frequency of the LHC, 40 MHz, n_1 and n_2 are the number of protons in the colliding bunches, σ_x^* and σ_y^* are a measure of the vertical and horizontal Root Mean Square (RMS) of the spatial spread of the bunches at the interaction point, and finally \mathcal{F} is a geometric factor meant to account for the crossing angle, finite bunch length, and various dynamic effects. Instantaneous luminosity has units of interactions per area per second (typically expressed in units of $\text{cm}^{-2}\text{s}^{-1}$).

LHC DIPOLE : STANDARD CROSS-SECTION



CERN AC/DI/MM - HE107 - 30 04 1999

Figure 3.2: Schematic diagram of the transverse cross section of an LHC dipole magnet [40].

The probability for a certain process to occur is proportional to the so-called production cross section of the process. The cross section is a quantity that has units of area, given in terms of barns, where $1 \text{ b} = 10^{-28} \text{ m}^2$.

At the Large Hadron Collider, the instantaneous luminosity can also be defined in terms of the total proton-proton cross section σ_{pp} , and the number of proton-proton interactions per second $\frac{dN}{dt}$:

$$\mathcal{L} = \frac{1}{\sigma_{pp}} \frac{dN}{dt}. \quad (3.2)$$

The instantaneous luminosity is also related to the number of interactions per bunch crossing μ through the following relation:

$$\mu = \sigma_{pp} \Delta t_{BC} \mathcal{L}, \quad (3.3)$$

where Δt_{BC} is the time between bunch crossings, which is 25 ns at the LHC. During the Run 2 data taking period, the average number of proton-proton interactions per bunch crossing $\langle \mu \rangle$ was approximately 34, although the number of interactions per bunch cross can vary greatly over the course of a data taking period as shown in Figure 3.3.

The integrated luminosity L is a measure of the amount of proton-proton collision data collected. It is calculated as the integral of the instantaneous luminosity over the period of time over which data was collected:

$$L = \int \mathcal{L} dt, \quad (3.4)$$

expressed in units of inverse barns. The work presented in this thesis is based on the analysis of 140 fb^{-1} of proton-proton collision data recorded by the ATLAS detector [42].

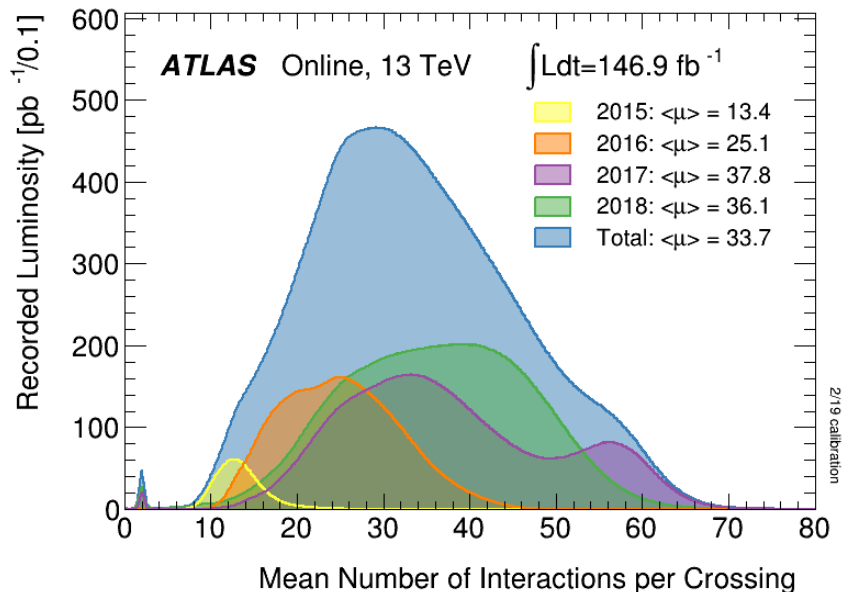


Figure 3.3: Distribution of the mean number of interactions per bunch crossing (μ) during the Large Hadron Collider Run 2 data taking period [41].

3.2 The ATLAS Detector

The ATLAS detector is a multi-purpose detector of 44 m in length and 25 m in height, weighing almost 7 000 tonnes. It was designed to discover the Higgs boson, search for new physics beyond the Standard Model, and make precision measurements of Standard Model parameters and processes. Its various subsystems are designed to identify and reconstruct electrons, photons, muons, and hadronic jets produced in the proton-proton collisions, as well as infer the presence of neutrinos through the missing energy in the transverse plane perpendicular to the collision axis (E_T^{miss}). To achieve this, the ATLAS detector consists of several sub-detectors layered around the interaction point. A schematic diagram of the ATLAS detector and its subsystems is shown in Figure 3.4. Moving radially outwards from the center of the detector, the ATLAS sub-detectors are the Inner Detector, the Electromagnetic Calorimeter, the Hadronic Calorimeter, and finally the Muon

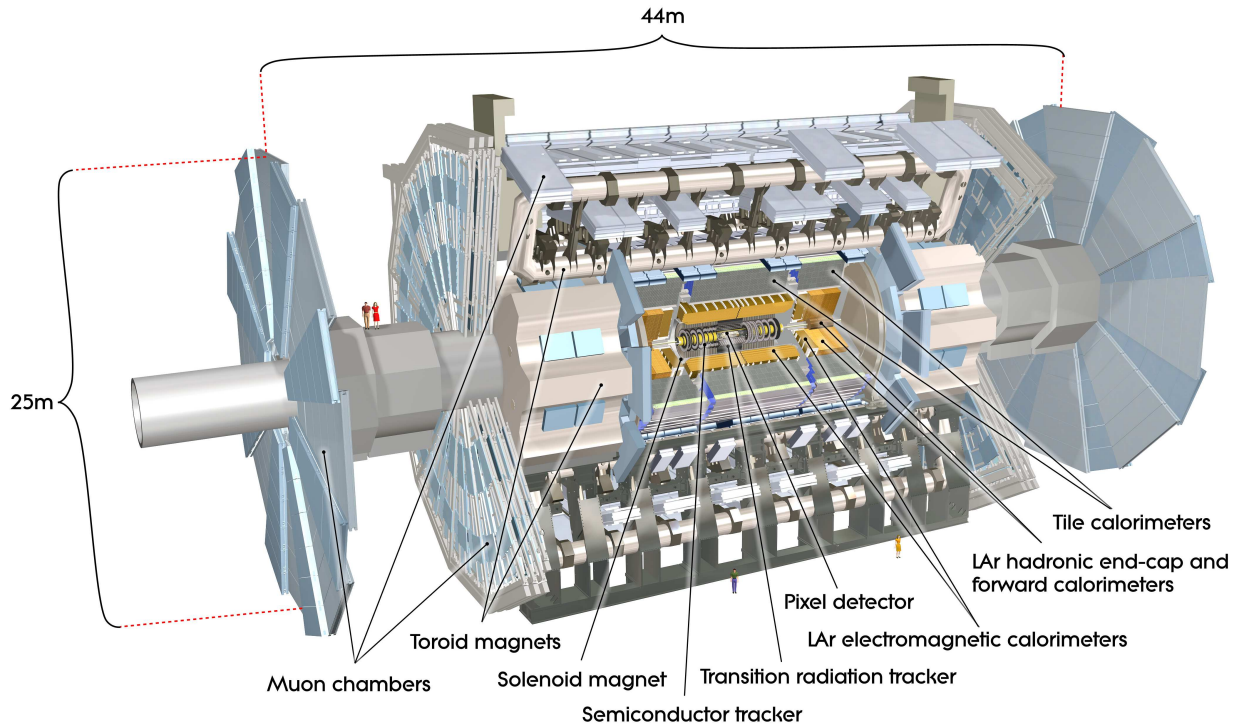


Figure 3.4: Schematic diagram of the ATLAS detector and its sub-detectors [35]. The Pixel Detector, Semiconductor Tracker, and Transition Radiation Tracker are part of the Inner Detector, while the Tile, Liquid Argon Electromagnetic, Hadronic End-Cap and Forward Calorimeters make up the calorimeter system. The muon chambers make up the Muon Spectrometer. The solenoid and toroid magnets make up the magnet system.

Spectrometer. An important part of the ATLAS detector's design is the magnet system, which is comprised of a solenoid magnet which surrounds the Inner Detector and toroid magnets outside the calorimeter systems and embedded within the Muon Spectrometer. The magnet system provides a strong magnetic field that bends the trajectories of charged particles in both the Inner Detector and Muon Spectrometer, allowing for the reconstruction of their momentum. The sub-detectors are arranged in three distinct regions, a cylindrical barrel region sandwiched between two wheel-shaped end-cap regions.

The coordinate system used in this thesis is defined with the origin at the interaction

point at the center of the detector. A right-handed coordinate system is used where the x -axis points towards the center of the LHC ring and the y -axis points upwards. The z -axis is defined by the direction of the beam pipe and is thus parallel to the axis of the proton-proton collisions, while the $x - y$ plane defines the transverse plane. The azimuthal ϕ angle is measured around the z -axis in the $x - y$ plane starting from the positive x -axis and the polar angle θ is measured from the positive z -axis. The ATLAS detector is constructed to have an approximate ϕ symmetry and mirror symmetry at $z = 0$, dividing the detector into an A ($z > 0$) and a C ($z < 0$) side. Pseudorapidity is related to the polar angle θ by:

$$\eta = -\ln \left(\tan \left(\frac{\theta}{2} \right) \right). \quad (3.5)$$

Pseudorapidity is a particularly useful quantity in particle physics because it is a good approximation of a particle's rapidity in the limit that the particle's mass is zero or its momentum is much larger than its mass. Rapidity is given by the equation:

$$y = \frac{1}{2} \ln \left(\frac{E + p_z}{E - p_z} \right), \quad (3.6)$$

where E is the particle's energy and p_z is its momentum component along the z -axis. Rapidity is also a useful quantity because differences in rapidity are invariant under boosts (or rotation-free Lorentz transformations) in the direction of the z -axis, making the number of particles produced in collisions constant as a function of rapidity. In addition, another important variable in the kinematic description of proton-proton collisions is the Lorentz-invariant angular distance:

$$\Delta R = \sqrt{(\Delta\eta)^2 + (\Delta\theta)^2}, \quad (3.7)$$

used to describe either the angular separation between particles or the lateral particle shower sizes in the ATLAS detector.

Particle detection and identification in ATLAS relies on both tracking and calorimetry. Tracking refers to the reconstruction of the trajectories of charged particles based on the recorded position of energy deposits in the multiple layers of the detector subsystems. These reconstructed trajectories are referred to as tracks. The bending of the charged particle's trajectory through the solenoid and toroid magnet systems is then used to resolve its momentum p , which is related to the particle's electric charge q , the bending radius of its trajectory r , and the strength of the magnetic field B through the relation $p = qrB$. Calorimetry consists in the measurement of the energy of a particle. In the ATLAS detector, calorimetry relies on fully containing the cascades of particles produced by neutral or charged particles within the calorimeter sub-detectors. These cascades of secondary particles inside the calorimeter volume are called particle showers. There are two types of particle showers, electromagnetic and hadronic showers.

Electromagnetic showers are initiated by high energy electrons, positrons, or photons interacting with the detector material. Due to the high energies of the particles produced in the proton-proton collisions, photons interact with matter primarily through electron-positron pair production, while electrons and positrons primarily interact by emitting photons through bremsstrahlung [8]. When a high energy electron, positron, or photon interacts with the calorimeter system, the combination of these two processes results in a cascade of electrons, positrons, and photons. This showering process continues until all the particles in the shower have lost enough energy to no longer interact through the aforementioned processes, at which point the shower is considered fully contained. The incident particle's energy is inferred by measuring the total energy deposited during the showering process. The radiation length for particles interacting electromagnetically is defined as the mean distance the particle must travel to lose $1/e$ of its energy and it depends on the atomic weight A and number Z of the detector material as $\propto A/Z^2 \ln(183 Z^{-1/3})$ [43].

Hadronic showers are much more complex as they can proceed through the

electromagnetic, weak, and strong interactions of the incident particles with the detector material. As such, in addition to electrons, positrons, and photons, hadronic showers may contain many other different types of particles. These include muons, which at these energies deposit only a very small amount of their energy through ionization, neutrinos, which typically don't interact at all with the detector due to the fact that they only interact through the weak force, and hadrons, which can interact and lose energy through nuclear interactions with the detector material. This means that a significant fraction of a hadronic shower's energy is not measured and must be accounted for through a calibration of the detector's response. The mean free path between two inelastic nuclear interactions, the co-called *nuclear interaction length*, scales as $\propto A^{1/3}$ and thus, in most materials, is much longer than the radiation length. For this reason, hadronic showers are typically initiated after, and penetrate deeper, than electromagnetic showers in a given material [43]. As such, in the ATLAS detector, the Hadronic Calorimeter surrounds the Electromagnetic Calorimeter, allowing for discrimination between particle showers purely electromagnetic in nature and those that contain both electromagnetic and hadronic components.

Figure 3.5 shows a schematic representation of how each type of particle of interest interacts with every ATLAS sub-detector. The information from all sub-detectors is combined to identify the type of particle based on its unique signature. Muons deposit very little of their energy in the detector and make it all the way through the detector volume. This is due to the fact that muons are over 200 times more massive than electrons and the energy loss through bremsstrahlung, the main electromagnetic mechanism through which massive charged particles lose energy in the detector, is inversely proportional to the square of the mass of the particle [43]. As such, muons do not tend to initiate electromagnetic showers in the calorimeters and are identified and reconstructed by the energy that they deposit through ionization in the different layers of the Inner Detector and the Muon Spectrometer. This information is used to reconstruct their tracks. Photons, since they

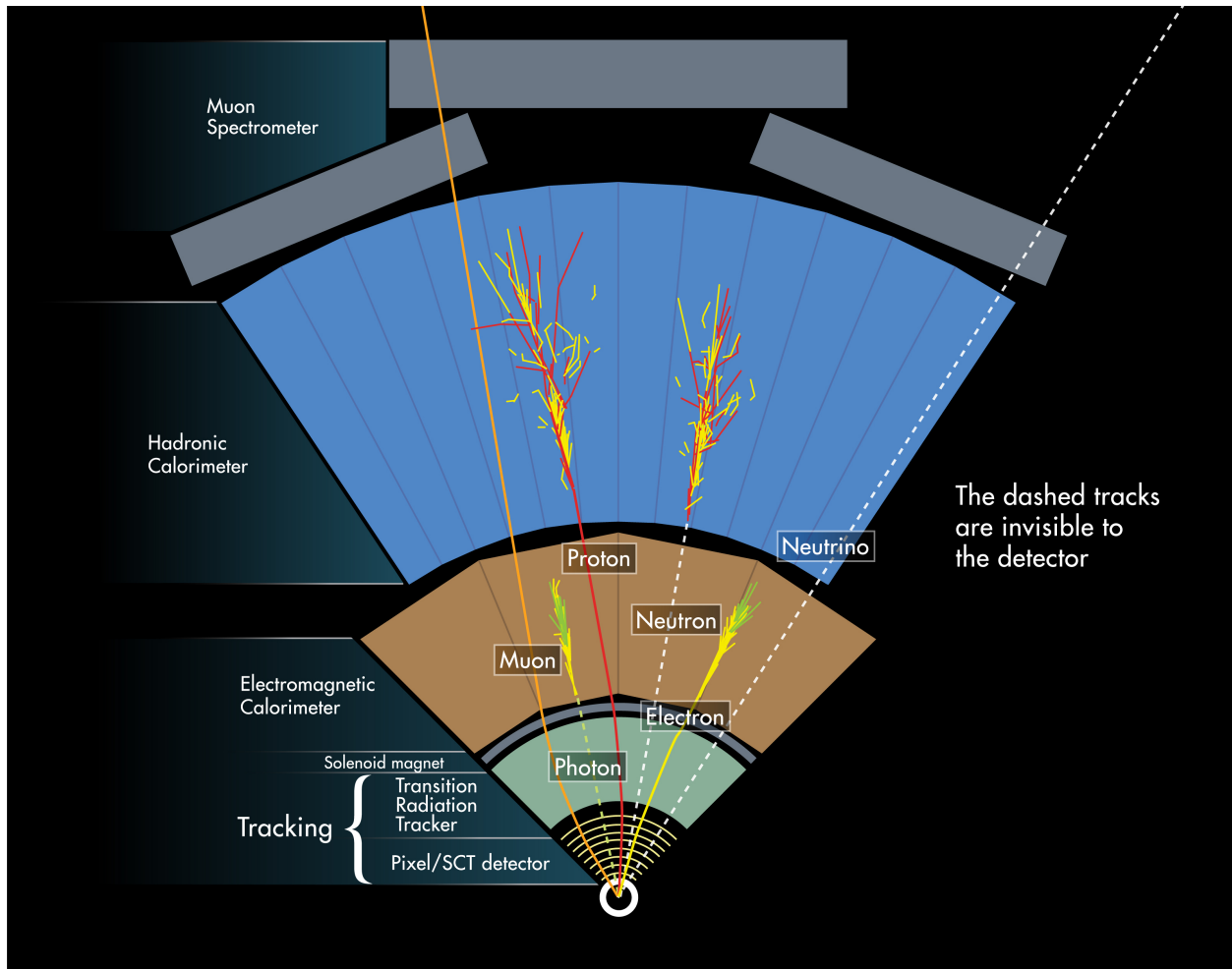


Figure 3.5: Schematic diagram showing how different types of particles interact with each subsystem of the ATLAS detector [44]. By combining information from all subsystems, it is possible to identify the types of the particles produced in a proton-proton collision.

carry no electric charge, leave no tracks in the Inner Detector, and deposit most of their energy in the Electromagnetic Calorimeter. There is a caveat here for photon to electron/positron pair conversions in the Inner Detector, where they appear as two charged particle tracks consistent with coming from a massless particle. However, due to inefficiencies in the Inner Detector and the actual location of the conversion, only one track might be reconstructed. As such, more complex identification algorithms are employed to distinguish between electrons and converted photons as discussed in Section 4.3. Hadronic jets from charged hadrons like protons leave tracks in the Inner Detector and deposit most of their energy in the Hadronic Calorimeter which is designed to fully contain them. Hadronic jets from neutral hadrons like the neutron are similar to jets from charged hadrons but don't leave any tracks in the Inner Detector. Electrons leave tracks in the Inner Detector and deposit most of their energy in the Electromagnetic Calorimeter. Finally, neutrinos don't interact with the detector at all but appear as the missing transverse energy that would be required to balance the vector sum of all other momenta reconstructed from a proton-proton interaction.

3.2.1 The Inner Detector

The Inner Detector, shown in Figure 3.6, is the sub-detector located closest to the interaction point [45, 46]. Its radial dimension ranges from approximately 3 cm from the beam axis to almost 1.1 meters away, and covers the pseudorapidity range of $|\eta| < 2.5$. The Inner Detector is used to measure the trajectories of charged particles, to aid in identifying electrons with $|\eta| < 2.0$, and to provide interaction point, or vertex, reconstruction capabilities. It is comprised of three detector technologies which are, moving radially outwards from the beam line, the silicon Pixel Detector, the Semiconductor Tracker (SCT), and the Transition Radiation Tracker (TRT). The entire Inner Detector volume is immersed in a 2 T axial magnetic field in the transverse plane provided by the solenoid magnet system, shown in

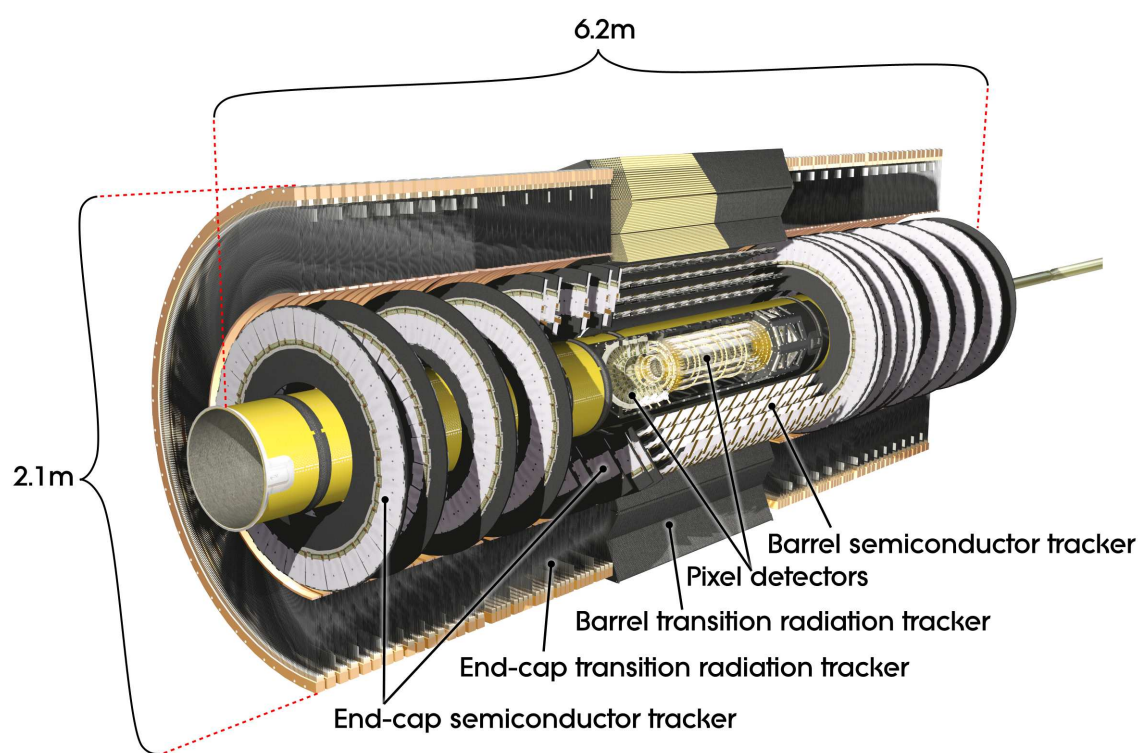


Figure 3.6: Schematic diagram of the ATLAS Inner Detector [35]. It is made up of three detector technologies: the Pixel Detector, Silicon Tracker, and Transition Radiation Tracker.

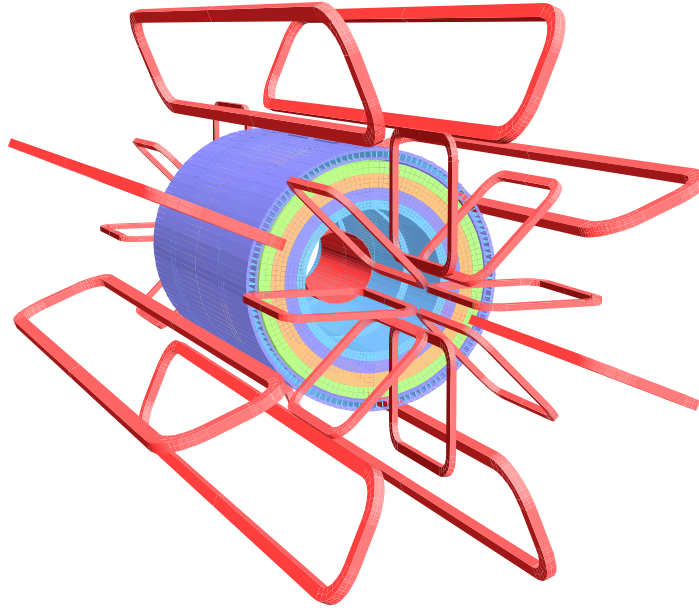


Figure 3.7: Schematic diagram of the ATLAS solenoid and toroid magnet systems [35]. The magnetic field lines produced by the solenoid magnet system are in the z direction and reach a magnitude of up to 2 T, while the magnetic field lines produced by the toroid magnet system are in the ϕ direction in the $x - y$ plane and reach a magnitude of up to 1 T.

Figure 3.7. A schematic diagram of the Inner Detector layers in the barrel region is shown in Figure 3.8.

The Pixel and Semiconductor Tracker detectors are based on silicon semiconductor sensors. When charged particles interact with the detector medium, electron-hole pairs are produced. A voltage difference within the bulk of the sensors creates an electric field which causes the ionization charges to drift. This creates a change in the electric field and induces a current in the readout electronics.

The Pixel Detector consists of four layers of pixelated silicon sensors with pixel sizes $50 \times 250 \mu\text{m}^2$ in the first layer and $50 \times 400 \mu\text{m}^2$ in the remaining three layers, corresponding to a total area of about 1.9 m^2 for over 92 million pixels [47, 48]. The Pixel Detector achieves an intrinsic spatial resolution of $10 \mu\text{m}$ in the $R - \phi$ plane and $115 \mu\text{m}$ along the z -axis.

The Semiconductor Tracker is comprised of 6 million silicon strip sensors over 6 barrel layers and 9 layers in each end-cap. The strips are $285 \mu\text{m}$ wide and 6 cm long with an $80 \mu\text{m}$ pitch. The Semiconductor Tracker achieves an intrinsic spatial resolution of $17 \mu\text{m}$ in the $R - \phi$ plane and $580 \mu\text{m}$ along the z -axis.

The Transition Radiation Tracker is based on the principle of transition radiation whereby, due to a rapid change in electric field, a charged particle radiates photons at the boundary between two mediums with different dielectric constants. The intensity of the radiation is logarithmically proportional to the Lorentz factor of the particle [43]. The Transition Radiation Tracker is made up of 300 000 thin-walled drift tubes, called "straws", of 4 mm in diameter and filled with a mixture of Xe, CO₂, and O₂. Each straw holds a $30 \mu\text{m}$ gold-plated tungsten wire at its center which is kept at ground while the walls are held at -1.5 kV. Incident charged particles ionize the gas inside the tubes. The ionization charges then drift in the electric field and produce secondary ionizations of the gaseous medium. These moving charges induce a current in the readout electronics which is proportional to the energy of the initial ionizing radiation. Each tube thus acts as a proportional counter. The energy deposits the different layers of the Transition Radiation Tracker can then be used to reconstruct the trajectories of charged particles. In addition, the volume between the straws is filled with a material designed to induce transition radiation from incident charged particles. The amount of transition radiation produced is related to the incident particle's Lorentz factor $\gamma = \frac{E}{m}$, where E is the particle's energy and m its mass. The transition radiation is absorbed by the gas inside the straws, producing additional ionization charges. As such, the Transition Radiation Tracker can be used for particle identification, namely to discriminate electrons from pions due to the large discrepancy in their masses (approximately 511 KeV for electrons versus approximately 140 MeV for the charged pion). The barrel region contains 76 layers of 144 cm long straws that are arranged parallel to the beam axis while the end-cap region contains 160 layers of 76 cm long straws that are perpendicular to the beam axis. The straws provide an intrinsic

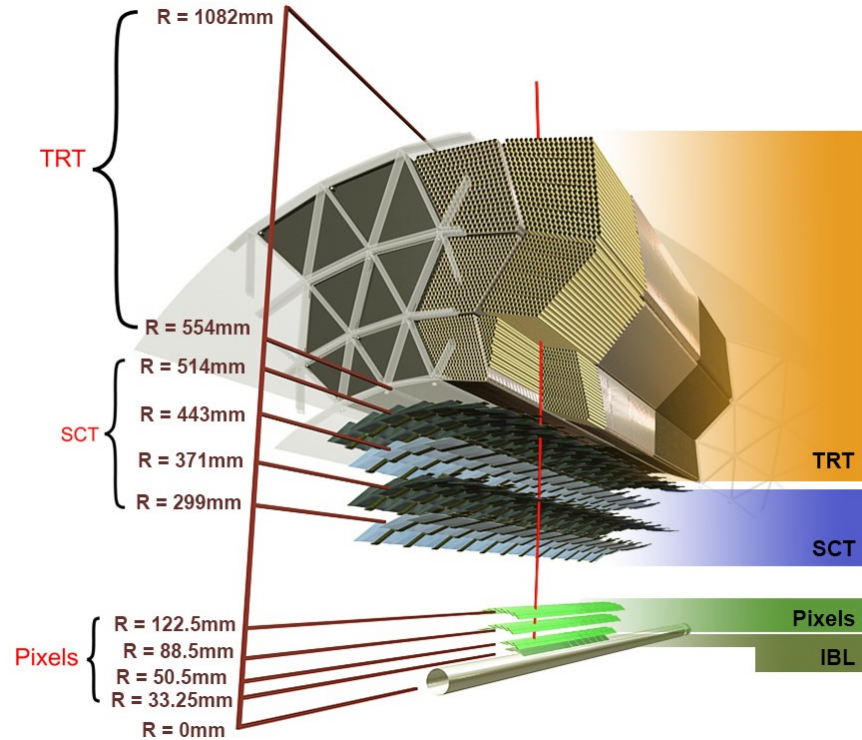


Figure 3.8: Schematic diagram showing the multiple layers of each of the Inner Detector sub-detectors in the barrel region with their distances from the beam-line [49]. The Inner Detector is made up of three detector technologies; the Pixel Detector (Pixels), Silicon Tracker (SCT), and Transition Radiation Tracker (TRT).

spatial resolution of up to $130\ \mu\text{m}$ in the $R - \phi$ plane in the barrel region and $130\ \mu\text{m}$ in the z -axis in the end-cap region.

3.2.2 The Calorimeter

There are two main calorimeter subsystems, the Electromagnetic Calorimeter which measures the energy of electrons and photons, and the Hadronic Calorimeter which measures the energy of hadronic jets from either quarks or gluons. Each subsystem must provide enough material to fully contain the particle showers induced by electrons,

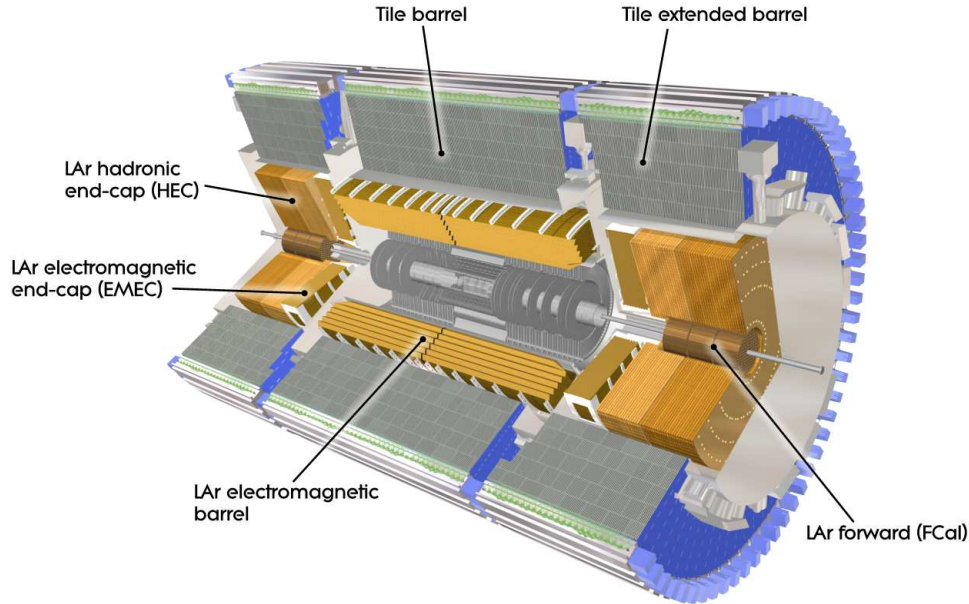


Figure 3.9: Schematic diagram of the ATLAS calorimeter system [35].

photons, and hadronic jets originating from the proton-proton collision. To achieve an accurate measure of the particle's energy, it is important that their showers be fully contained and not leak through to the Muon Spectrometer. Calorimetry in ATLAS relies on incident particles inducing either electromagnetic showers or hadronic showers, depending on the type of incident particle. Both are very different and inform the design of each respective calorimetry system. The calorimeter system, shown in Figure 3.9, is made up of the Liquid Argon (LAr) and Tile Calorimeters and covers a range of up to $|\eta| < 4.9$, surrounding the Inner Detector in the barrel and end-cap regions. All of the sub-detectors of the calorimeter system are sampling calorimeters, meaning that the amount and spatial distribution of energy deposited by the electromagnetic and hadronic showers are sampled longitudinally. There are two main detection techniques used in the ATLAS calorimeters, one based on ionization and the other based on scintillation.

The calorimeter system based on ionization uses liquid argon (LAr) as its active

material which is interspersed with absorber material [50]. The absorber material induces electromagnetic or hadronic showers from incident particles, thus creating secondary particles which ionize the liquid argon. The liquid argon layers are segmented into cells defined by the layout of the readout electrodes. Cells are held in an electric field and instrumented such that the ionization charges moving in the gap induce a current in the electrodes which is then read out. This is the principle behind the Electromagnetic Barrel (EMB), the Electromagnetic End-Cap (EMEC), the Hadronic End-Cap (HEC), and the Forward Calorimeter (FCal). The Electromagnetic Barrel and Electromagnetic End-Cap absorber material is lead. Each has three layers in addition to a pre-sampler, covering the ranges $|\eta| < 1.475$ and $1.375 < |\eta| < 3.2$, respectively, with a gap between $1.37 < |\eta| < 1.52$ for cabling for the Inner Detector. The pre-sampler is used to correct for the energy lost by particles upstream of the calorimeter system [51]. Each layer has a different granularity in $\eta - \phi$, with the first layer having the finest granularity to ensure good photon identification and π^0 rejection. The barrel region corresponding, to the region of $|\eta| < 2.5$, has finer granularity to match the Inner Detector acceptance and provide good electron and photon reconstruction capabilities. The lead absorber and liquid argon volumes in the Electromagnetic Barrel and Electromagnetic End-Cap are arranged in an accordion structure to ensure full ϕ coverage. An example of this accordion structure in the Electromagnetic Barrel is shown in Figure 3.10. The Hadronic End-Cap covers the range $1.7 < |\eta| < 3.2$, has four sensing layers, and uses copper as its absorber material. The Forward Calorimeter covers the range $3.1 < |\eta| < 4.9$. It uses copper in its first layer as an absorber material which is optimised to measure the energy deposited by electromagnetic showers. Tungsten is used as its absorber material in its two outer layers which are optimized to measure the energy from hadronic showers. The Electromagnetic Barrel and Electromagnetic End-Cap make up the barrel and end-cap sections of the Electromagnetic Calorimeter while the Hadronic End-Cap and Forward Calorimeter make up the end-cap sections of the Hadronic Calorimeter. The total thickness of the Electromagnetic

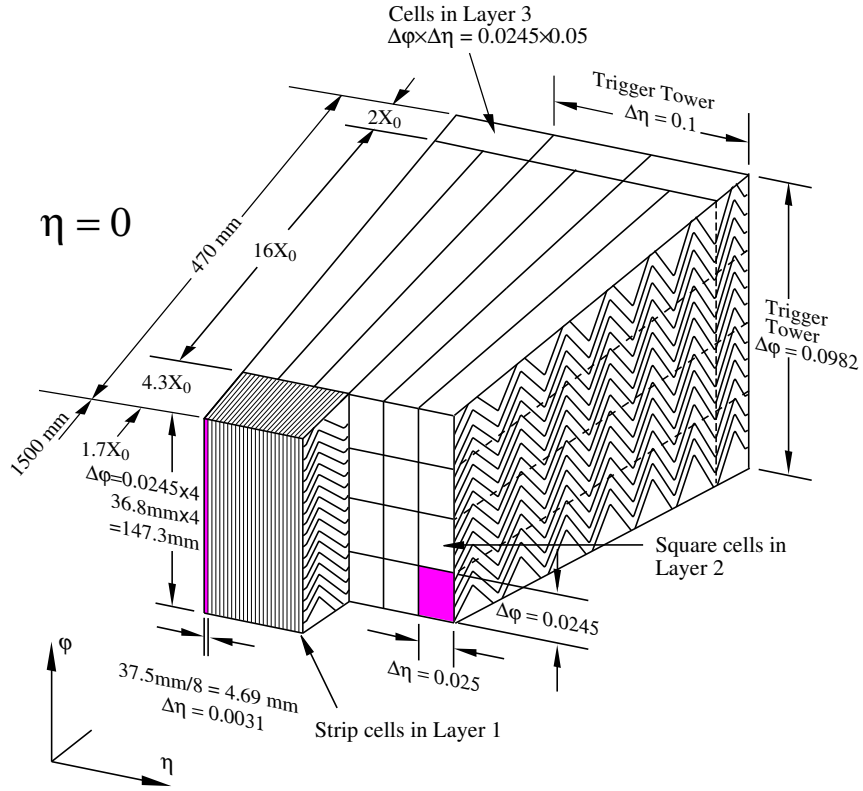


Figure 3.10: Schematic diagram of the Electromagnetic Barrel layers and their segmentation in $\eta - \phi$ [35].

Calorimeter corresponds to more than 22(24) radiation lengths and approximately 9.7(10) interaction lengths in the barrel (end-cap) region. The total thickness of the Forward Calorimeter is approximately 200 radiation lengths and 9.9 interaction lengths, while the Hadronic End-Cap's total thickness is approximately 100 radiation lengths and 9.7 interaction lengths.

The scintillating Tile Calorimeter makes up the barrel portion of the Hadronic Calorimeter, covering the range $|\eta| < 1.7$ [52]. The Tile Calorimeter uses steel as an absorber material to induce particle showers and a polystyrene plastic as the scintillating material which absorbs the energy from the secondary charged particles and re-emits it as ultraviolet light. The light is then guided through wavelength shifting fibers to

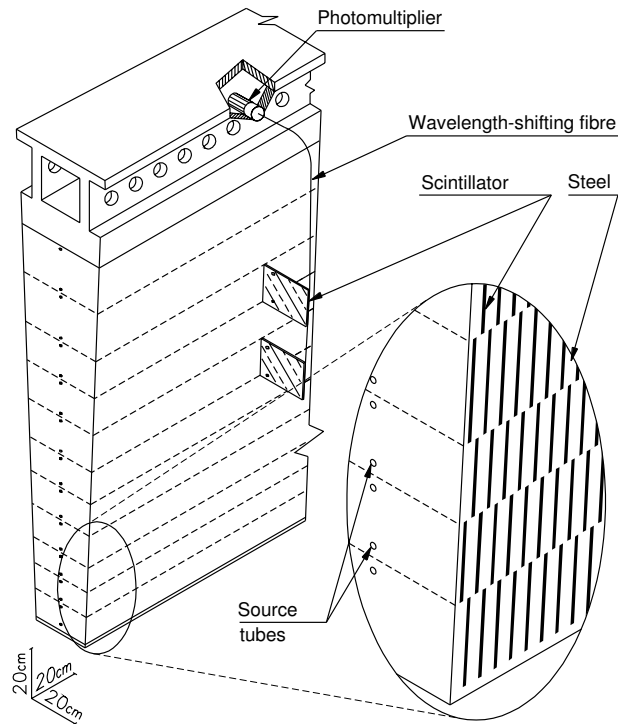


Figure 3.11: Schematic diagram of the Tile Calorimeter optical readout [35].

photomultiplier tubes (PMTs) which convert the photons to current. A schematic diagram of the optical readout of the Tile Calorimeter is shown in Figure 3.11.

3.2.3 The Muon Spectrometer

A schematic diagram of the Muon Spectrometer is shown in Figure 3.12. It provides trajectory and, together with the Inner Detector and the magnet system, momentum and electric charge measurements for muons [53]. The Muon Spectrometer is the outermost subsystem of the ATLAS detector. Muons produced in proton-proton collisions behave as Minimum Ionizing Particles (MIPs) due to their relatively large mass. As such, they don't lose a lot of their energy through ionization, making them the only type of elementary particle other than neutrinos that make it all the way through the detector. The Muon

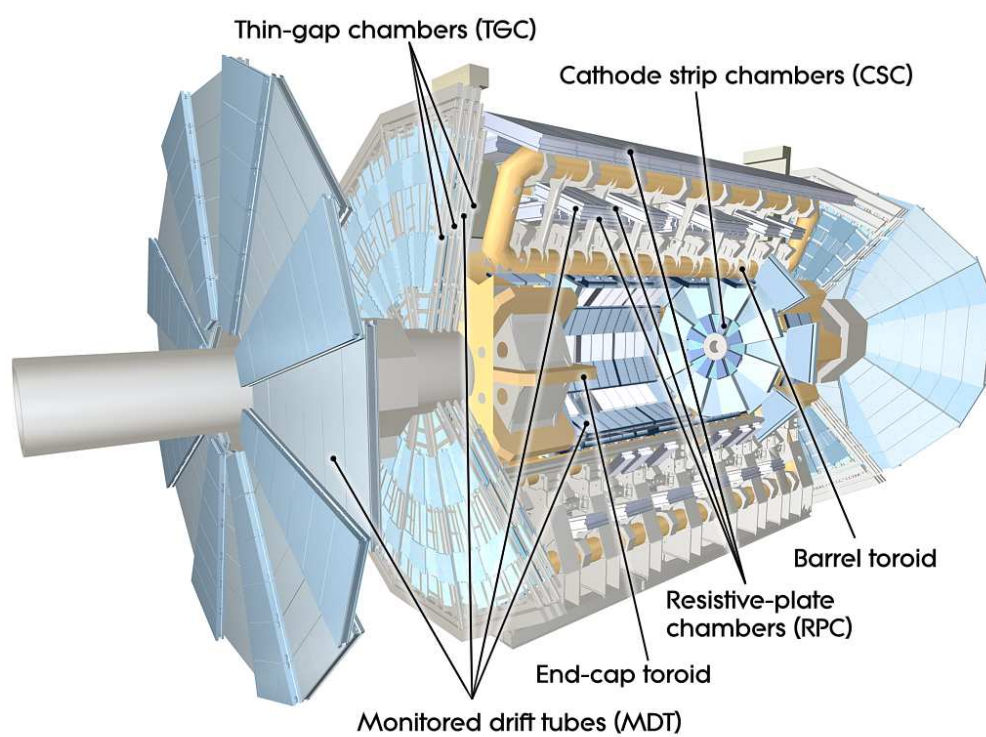


Figure 3.12: Schematic diagram of the ATLAS Muon Spectrometer [35].

Spectrometer covers a pseudorapidity range of $|\eta| < 2.7$ and is made up of the Monitored Drift Tubes (MDTs), Cathode Strip Chambers (CSCs), Resistive Plate Chambers (RPCs), and Thin Gap Chambers (TGCs). All of these sub-detectors are different types of gaseous ionization chambers. The passage of a charged particle such as a muon ionizes the gas, producing charges that are then accelerated by an electric field, thereby inducing a current in the readout electronics.

Precision reconstruction of a muon's trajectory is done by the Monitored Drift Tubes in the pseudorapidity range $|\eta| < 2.7$. These are arranged in chambers with three to eight layers of drift tubes which are 30 mm in diameter, made of aluminum, and containing a tungsten-rhenium anode wire of 50 μm in diameter. These tubes are filled with a gas mixture of 93% Argon and 7% CO_2 , which was selected for its good ageing properties. The gas in the tubes is held at a pressure of 3 bar and contains a small amount of water to improve high voltage stability. A spatial resolution of 35 μm per chamber is achieved while providing up to 20 measurements of a muon's energy deposits along its trajectory in both the barrel and end-cap regions.

The Cathode Strip Chambers add additional layers of tracking in the inner forward region of $2.0 < |\eta| < 2.7$. Due to the higher flux of particles in the forward region, the Cathode Strip Chambers are needed in order to provide higher rate and better timing resolution capabilities. Cathode Strip Chambers are planar multi-wire proportional chambers filled with a gas mixture of 80% Argon and 20% CO_2 . The chambers contain radially oriented gold-plated tungsten anode wires of 30 μm in diameter. Cathode strips are placed orthogonal to the wires and are read out, providing 40 μm resolution in the plane perpendicular to the transverse plane (the bending plane) and 5 mm in the transverse plane. The Cathode Strip Chambers provide up to 4 hits per muon track.

The Resistive Plate Chambers and Thin Gap Chambers provide fast tracking information to the trigger system described in Section 3.2.5 in the pseudorapidity regions covering $|\eta| < 1.07$ and $1.07 < |\eta| < 2.7$, respectively. These detectors must have a fast response as well

as good timing and spatial resolution for the trigger system. In addition, they must be able to operate at a high hit efficiency in a very high particle flux environment. Resistive Plate Chambers are gaseous parallel plate detectors instrumented with readout strips of 25 to 35 mm in pitch. The Resistive Plate Chambers are located in the barrel regions and has of three layers, one on either side of the middle layer of Monitored Drift Tubes, and one outside the final Monitored Drift Tube layer. Each of the Resistive Plate Chamber layers has two volumes of gas. Each volume consists of two parallel graphite coated electrodes held 2 mm apart. The gas volumes are filled with a gas mixture of 94.7% $C_2H_2F_4$, 5% Iso- C_4H_{10} , and 0.3% SF_6 . Readout strips are placed orthogonally to each other on either side of the gas volume. A spacial resolution of 10 mm per chamber in the bending plane and a timing resolution of 7 ns per chamber is achieved. The Resistive Plate Chambers provide up to 6 hits per muon track.

In addition to triggering, the Thin Gap Chambers provide an additional measurement of the ϕ coordinate of a muon's trajectory in the end-cap regions. The Thin Gap Chambers operate as multiwire chambers instrumented with copper strips and pad electrodes on either side of the 2.8 mm thick gas volume. Anode wires with a pitch of 1.8 mm sit in the gaps and are held at a voltage of 3.1 kV. The gas consists of a mixture of CO_2 and n- C_5H_{12} (n-pentane). The Thin Gap Chambers achieve a spacial resolution of 3-7 mm in ϕ and a timing resolution of 4 ns. The Thin Gap Chamber system is able to provide up to 9 hits per muon track.

The trajectories of muons are bent by the toroidal magnetic field of 1 T in the barrel region covering $|\eta| < 1.4$ and 0.5 T in the end-cap region covering $1.6 < |\eta| < 2.7$. The Toroid magnet system is shown alongside the solenoid magnet system in Figure 3.7 and it provides a magnetic field pointing in the ϕ direction along the $x - y$ plane.

3.2.4 Luminosity Measurement

Most analyses using ATLAS data rely on a precise measurement of the integrated luminosity delivered to the detector by the LHC. The detectors and methodology used to calculate the Run 2 integrated luminosity are described in [42]. The main detector used to measure the luminosity is the Luminosity Cherenkov Integrating Detector 2 (LUCID2) [54] forward detector placed close to the beam line ± 17 m away from the interaction point on either side of the ATLAS detector. Each LUCID2 detector contains 16 photomultiplier tubes with quartz windows coated with ^{207}Bi radioactive sources that provide a calibration signal. The detection principle of the LUCID2 detectors is Cherenkov radiation, whereby a charged particle travelling faster than the speed of light in a given medium, in this case quartz, emits radiation. The effect is similar to the phenomenon of a sonic boom created when an object breaches the speed of sound in a given medium. The resulting Cherenkov radiation is collected and read out by the photomultiplier tubes.

The integrated luminosity recorded by the ATLAS detector is often slightly smaller than the total luminosity delivered by the LHC. This is due to effects such as readout dead-time during data taking and possible technical problems. Data recorded by ATLAS is deemed "Good for Physics" only when all ATLAS subsystems are fully operational. Over the LHC Run 2 data taking period, this corresponds to a measured integrated luminosity of 140 fb^{-1} with an uncertainty of 0.83% [42]. The integrated luminosity that was delivered by the Large Hadron Collider, recorded by ATLAS, and identified as "Good for Physics", is shown in Figure 3.13.

In addition to the integrated luminosity, the instantaneous luminosity, and the related mean number of proton-proton interactions per bunch crossing, are important due to their relation to the amount of pileup present during data taking. The mean number of proton-proton interactions per bunch crossing as measured by the ATLAS detector over Run 2 is shown in Figure 3.3. Pileup refers to the overlapping of signals from different proton-proton

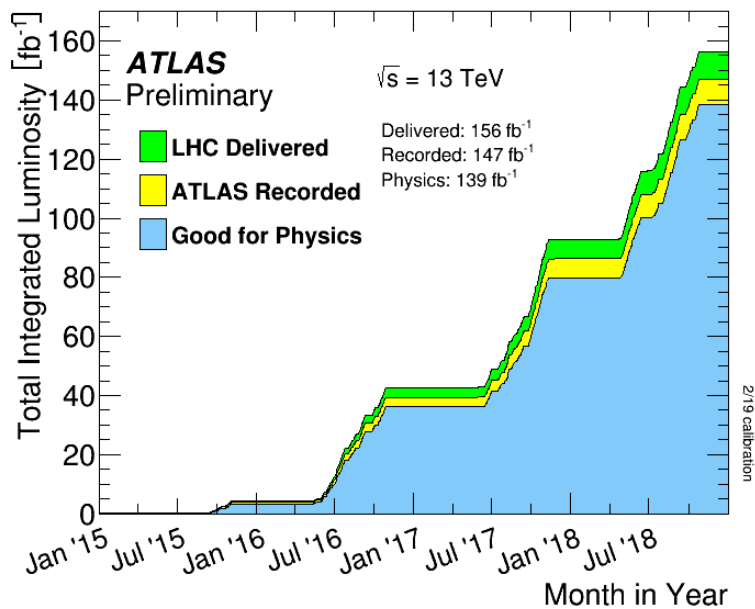


Figure 3.13: Integrated luminosity delivered by the LHC, recorded by the ATLAS detector, and subsequently considered of sufficiently good quality for use in physics analyses over the course of the Run 2 data taking period [41].

interactions both in the same bunch crossing (called in-time pileup), and from different bunch crossings (called out-of-time pileup). Out-of-time pileup occurs because some sub-detectors have response times that are much longer than the 25 ns bunch crossing period, leading to the overlapping of signals in the readout electronics. Knowledge of the pileup conditions are used to properly calibrate the response of multiple sub-detectors and to improve the energy resolution of reconstructed physics objects.

3.2.5 Trigger and Data Acquisition

The Trigger and Data Acquisition (TDAQ) system is dedicated to the processing, selection, and storage of events recorded by the ATLAS detector for offline analyses such as the one presented in the thesis. An event corresponds to the information recorded for a specific

bunch crossing. With 40 millions bunch crossings per second and an average event size of approximately 1 MB during Run 2, the bandwidth and amount of storage that would be required to read out and store the information from every collision is not technically feasible. To address this challenge, a two level trigger system is used to successively reduce the rate at which events are read out and recorded. The first level selects interesting events using a subset of the detector information and simplified object reconstruction. The second level uses more detector information and more complex event processing. The trigger system as used during the LHC Run 2 is described in Reference [55].

The Level 1 (L1) trigger system is implemented in hardware [56]. Custom electronics and Field Programmable Gate Arrays (FPGAs) are used to read out and process detector signals from the Calorimeter and the Muon Spectrometer systems at a reduced granularity. This information is processed and used to consider events based on the number, type, and kinematic properties of the coarsely reconstructed physics objects. The L1 trigger decision to keep an event and process it further is done within a latency of $2.5 \mu\text{s}$. The L1 trigger selection criteria are tuned to reduce the LHC collision rate of 40 MHz to an event rate of approximately 100 kHz.

Once the L1 trigger selects an event for further processing, data from all sub-detectors is sent to a large computing farm hosting the High Level Trigger (HLT) [57]. Here, more computationally intensive reconstruction algorithms are used. The HLT software is based on the Athena [58, 59] software used for offline analyses and data processing. Selection criteria based on the fully reconstructed event is used to reduce the final event rate to approximately 1.2 kHz, corresponding to about 1.2 GB/s of data being recorded and sent to permanent storage. Events are processed with a latency of a few hundred milliseconds by the HLT, after which the full detector readout is sent for permanent storage on tape at a Tier-0 [60] computing facility.

Chapter 4

Object Reconstruction, Identification, and Isolation

This chapter details how the raw signals from the different ATLAS sub-detectors are interpreted and combined to reconstruct the secondary particles produced in proton-proton collisions. This includes the algorithms and quality criteria used to identify the different types of particles as well as quantify their level of isolation from other objects in the same event.

4.1 Intermediate Objects

The first step in the reconstruction of particles produced in proton-proton collisions consists in the reconstruction of objects referred to as *tracks*, *vertices*, and *calorimeter clusters*. The algorithms used to reconstruct each of these types of objects are described below.

4.1.1 Inner Detector Tracks

A track refers to the reconstructed three-dimensional trajectory of a charged particle. These trajectories are reconstructed based on the hit patterns in the multiple layers of the ATLAS sub-detectors. Inner Detector tracks are made from hits in the silicon detectors [61] and extended to the Transition Radiation Tracker [62]. The procedure for forming Inner Detector tracks begins in the Pixel Detector and Semiconductor Tracker. Here, the ionization charge produced by a single interaction of a charged particle with the detector material can be collected on multiple adjacent readout pixels or strips in a given layer. Clusters are formed from raw hits using an algorithm that groups adjacent pixel and strip readout channels above a certain threshold within a sub-detector sensor. From these hit clusters, three dimensional space-points are formed which represent the location where charged particles interacted with the detector. The next step is to reconstruct so-called *track seeds* made of three separate space-points from different layers compatible with the trajectory of a charged particle. Track purity is improved by first considering track seeds from regions of the Inner Detector with the best spatial resolution that satisfy quality criteria on the particle's transverse momentum and distance of closest approach of its trajectory to the z -axis. The distance of closest approach of a track to the z -axis is called the impact parameter (d_0) which is schematically shown in Figure 4.1. An additional space-point compatible with the trajectory estimated from the track seed is then required. Then, a combinatorial Kalman filter [63] is used to build tracks from seeds by searching for additional nearby space points compatible with the estimated seed trajectory. An ambiguity solving algorithm is employed to resolve hit clusters used in multiple tracks by scoring tracks based on the sub-detector spatial resolution, expected hit cluster multiplicity, the track p_T , and the χ^2 of the track fit, with gaps in the layers along the track reducing the score. The ambiguity solving algorithm then determines to which track clusters that are assigned to multiple track candidates should belong using an iterative procedure. Candidate tracks must then pass some basic quality cuts including $p_T > 400$ MeV,

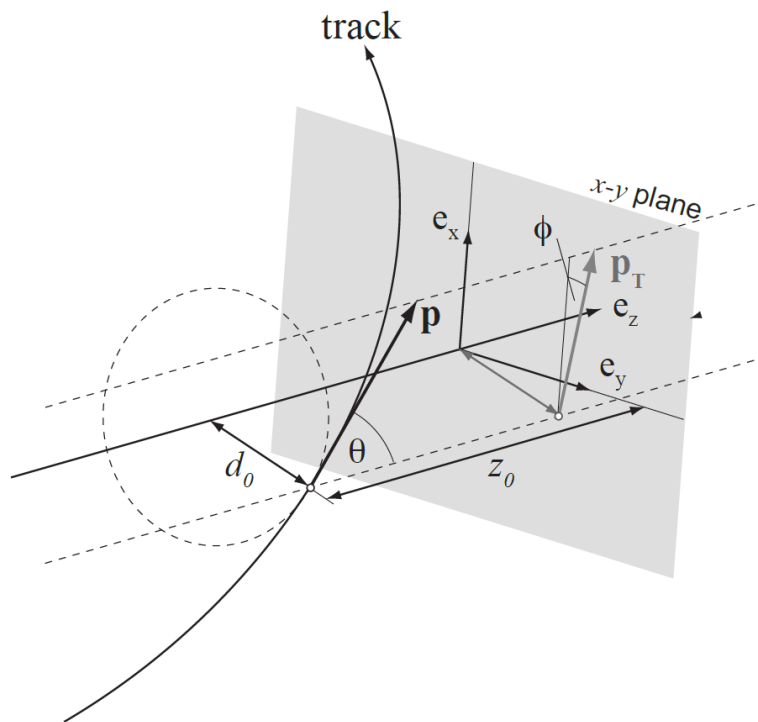


Figure 4.1: Schematic diagram of a track's parameters [64].

$|\eta| < 2.5$, requiring a minimum of 7 hit clusters in the Pixel Detector and Semiconductor Tracker, and additional requirements on the track impact parameter, cluster multiplicity, and number of missing clusters along the reconstructed trajectory. Tracks are then fit using all available parameters of the candidate track, with the position and uncertainty of each cluster determined by Neural Networks (NNs).

In a final step, candidate tracks are extended to the Transition Radiation Tracker by matching the hit coordinates in the Transition Radiation Tracker to the extrapolated track candidate. A fit is performed to check for compatibility of the additional hits with the track candidate while taking into account possible additional weighing and grouping of Transition Radiation Tracker hits as described in [62].

The final outcome of the track reconstruction algorithm is a set of charged particle trajectories defined by the parameters schematically represented in Figure 4.1.

4.1.2 Vertices

The reconstructed vertex of a particle interaction refers to the reconstructed three-dimensional point in space where the particle interaction or collision occurred. Since multiple proton-proton interactions can occur in a given bunch crossing, it is important that reconstructed particles be associated to the correct vertex. Vertices are reconstructed by grouping high quality tracks [65] according to their point of origin. The vertex reconstruction procedure is done in two steps, starting with vertex finding and followed by vertex fitting [66]. The vertex finding starts with the definition of an initial seed position. Then, using the seed vertex position and the reconstructed charged particle tracks, a fit is done to find the most likely vertex position. The initial seed vertex is then replaced with the recomputed vertex and the fit is performed again, with less weight assigned to the least compatible tracks. This is repeated iteratively until the final vertex position is defined, after which the incompatible tracks can be used to determine the next vertex.

The outcome of this reconstructed step is several vertex positions associated to a single bunch crossing. The so-called *primary vertex* is then defined as the vertex with the highest sum of its associated track p_T . The other secondary vertices are referred to as pileup vertices.

4.1.3 Calorimeter Clusters

A calorimeter cluster corresponds to a grouping of nearby calorimeter cells with measured energy deposits in a region of the calorimeter system. Two types of algorithms are used to reconstruct calorimeter clusters. The first is the sliding-window algorithm [67] used mainly for reconstructing electromagnetic showers from particles which do not interact hadronically. The second algorithm is used to reconstruct so-called *topological clusters* [68] that are mainly used to reconstruct the hadronic showers associated with hadronic jets.

The sliding-window algorithm uses as input so-called calorimeter *towers* formed by summing the energies deposited in all the layers of the Electromagnetic Calorimeter in a

given $\eta \times \phi = 0.025 \times 0.025$ region. This angular area corresponds to the granularity of the second layer of the Electromagnetic Calorimeter. This angular area gives a total of 200×256 towers. The sliding-window is formed from 3×5 towers in $\eta \times \phi$ and is moved step-wise to cover the full calorimeter in search of seed-clusters with a total transverse energy of more than 2.5 GeV. If two seed-clusters fall within $\Delta\eta \times \Delta\phi = 5 \times 9$ towers, a single seed cluster is selected based on the properties and distribution of the measured transverse energy in the calorimeter cells within each cluster.

Topological clusters are formed using both the $\eta \times \phi$ segmentation and the different layers of the calorimeter system. Topological seed-clusters are formed by cells with a measured absolute energy of at least four times the standard deviation of the total noise in that cell. The total noise includes both the noise from the detector electronics and the noise from in- and out-of-time pileup. The cluster is then expanded from the initial calorimeter cell by adding all adjacent cells with absolute energies at least two times higher than their respective total noise. When this step is done, all immediate neighboring calorimeter cells are added to the cluster. In a final step, some topological clusters with two or more local energy maxima are split in two. Electromagnetic and hadronic showers tend to deposit different amounts of energy in the calorimeter relative to their total energy. Therefore, a local energy scale correction is applied to each cluster based on a classification of the cluster as either being part of a hadronic or electromagnetic shower and its location inside the calorimeter.

4.2 Electrons

A schematic drawing of the path of an electron through the various ATLAS sub-detectors is shown in Figure 4.2. The signatures of electrons and photons in the Electromagnetic Calorimeter share many similarities due to the nature of the electromagnetic showers both types of particle produce. In addition, photons can convert into an electron and positron pair, leaving tracks in the Inner Detector. Converted photons and electrons thus also share many

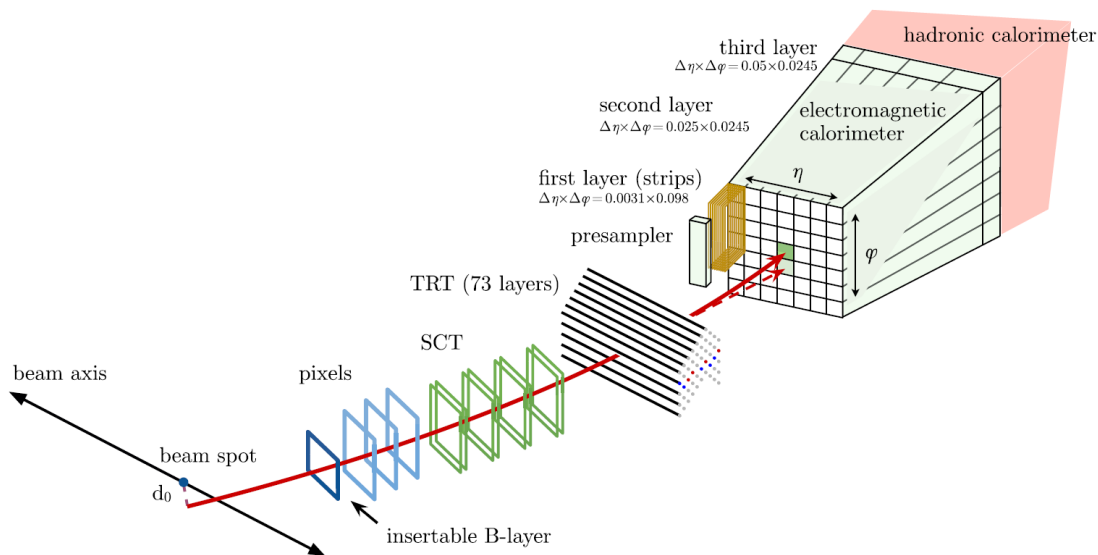


Figure 4.2: Schematic drawing of the path of an electron in the ATLAS detector [69]. A typical electron signature consists of hits in the Pixel Detector, Semiconductor Tracker (SCT), and Transition Radiation Tracker (TRT), forming a track that points to a reconstructed sliding-window cluster in the Electromagnetic Calorimeter.

similarities in terms of their signatures in the Inner Detector. As such, the reconstruction of electrons and photons proceeds in parallel.

4.2.1 Electron Reconstruction

The electron reconstruction procedure adds an additional step to the track reconstruction described in Section 4.1.1. For tracks that are loosely matched in $\eta \times \phi$ to an electromagnetic sliding-window cluster and with at least four silicon hits, an additional fitting procedure is done to account for energy loss from charged particles in the detector material and non-linear effects relating to bremsstrahlung radiation [69]. These tracks are refit with a Gaussian-Sum Filter (GSF) [70]. The algorithm is based on a generalization of the Kalman filter [63], which accounts for experimental uncertainties modelled by a sum of Gaussian functions. This fitting procedure accounts for radiative energy loss through the silicon tracker which

can affect the trajectory of electrons in the Inner Detector by lowering their momentum and increasing their curvature in the magnetic field.

These GSF-track candidates are then geometrically matched to sliding-window clusters. If multiple tracks are matched to a cluster, a track is selected by an algorithm which takes into account several properties of the track and cluster. Some of the properties considered include the angular distance of the extrapolated track to the cluster energy barycenter in the second layer of the Electromagnetic Calorimeter, and the number of hits in the silicon detector layers. If the candidate track can be matched to a secondary vertex and has no hits in the Pixel Detector, it is classified as a converted photon candidate. Otherwise, candidate tracks are considered as electron candidates. An additional classification step is done to determine if the object should still be considered as a potential converted photon candidate using the object's kinematic and reconstructed track properties. This is done to ensure high converted photon reconstruction efficiency.

In a final step, the sliding-window cluster is extended to 3×7 towers in the barrel region and 5×5 towers in the end-cap region. The energy of the updated cluster is calibrated using Z boson decays to electron-positron pairs in data and simulated samples using a multivariate regression algorithm [71]. The efficiency to reconstruct electrons as a function of electron E_T is shown in Figure 4.3. It can be seen that the electron reconstruction efficiency increases as a function of electron E_T . For electron candidates with a transverse energy $E_T > 15$ GeV and a track with at least one pixel hit and seven silicon hits, the reconstruction efficiency varies from about 97% to 99%. The evaluation of the electron reconstruction, identification, and isolation performance is done using data and simulated samples of J/ψ mesons and Z bosons decaying to electron positron pairs. These events are used because they provide a very high purity sample of electrons.

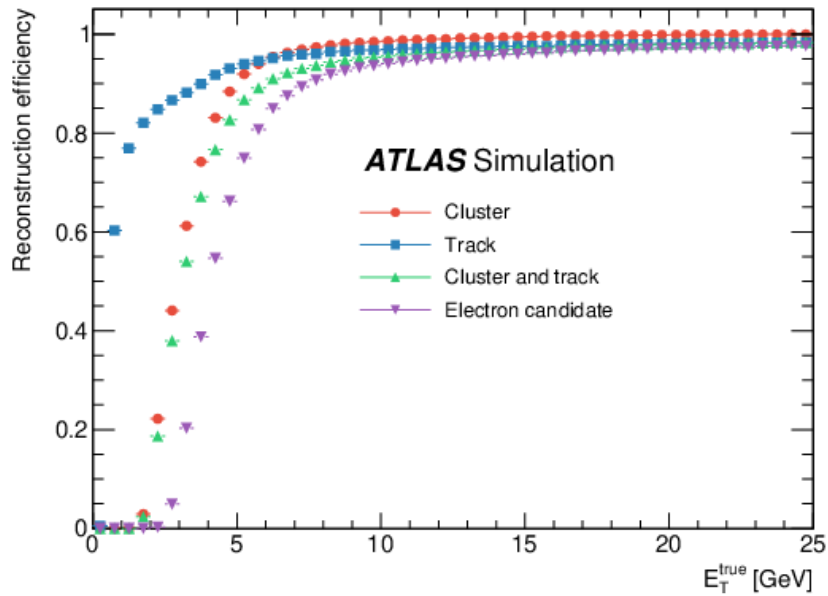


Figure 4.3: Electron reconstruction efficiency as a function of electron E_T [72]. The efficiencies to reconstruct clusters, tracks, and cluster and track combinations produced by electrons are also shown.

4.2.2 Electron Identification

Identification refers to the final classification of a reconstructed object in the ATLAS detector. Electron candidates are required to pass a likelihood (LH) based identification with multiple working points corresponding to different signal and background selection efficiencies [69]. A higher signal efficiency comes at the cost of a lower ability to reject background. The likelihood function is based on measurements from the tracking system, the calorimeter, and a combination of both, to achieve a good discrimination between electrons and sources of backgrounds. The variables used in the likelihood function include quantities such as the ratio of the transverse energy deposited in the Hadronic Calorimeter and the Electromagnetic Calorimeter ($R_{had} = \frac{E_T^{had}}{E_T}$) and the ratio of the energy difference between the two highest local maxima of the electron cluster and their sum ($E_{ratio} = \frac{E_{max,1}^{S1} - E_{max,2}^{S1}}{E_{max,1}^{S1} + E_{max,2}^{S1}}$). Many of these variables are shared with the identification algorithm used for photons shown in Figure 4.6. There are three main operating points for the electron identification algorithm, called *Loose*, *Medium*, and *Tight*. These working points have identification efficiencies of 93%, 88%, and 80%, respectively, for electrons with $E_T = 40$ GeV. The *Medium* identification working point was selected for the analysis in order to retain the highest selection efficiency compatible with the trigger identification criteria described in Section 5.2.

4.2.3 Electron Isolation

Isolation is a way of quantifying how separated a certain object is from other objects in the detector. Having well separated objects ensures that they have well defined kinematic properties and that there is no overlap or ambiguities in their identification. Hadronic jets and the decays of heavy quarks which are misidentified as prompt electrons, photons, or muons tend to be less well isolated in the detector when compared to prompt electrons, photons, and muons produced in the hard scatter. This can be quantified by summing the transverse momentum of tracks and the transverse energy of clusters within a certain

radius $\Delta R = \sqrt{\Delta\eta^2 + \Delta\phi^2}$ of the candidate object while excluding the tracks and clusters associated with candidate itself. There are two types of isolation for electrons: calorimeter-based isolation and track-based isolation.

Calorimeter-based isolation energy, E_T^{iso} , is calculated using topological clusters due to their robustness against energy deposits from pileup. Figure 4.4 shows a schematic diagram illustrating how calorimeter-based isolation energy is calculated. The energy from the sliding-window calorimeter cluster is subtracted from the energy sum of topological calorimeter clusters within a cone ΔR around the electron. Possible leakage of electron energy outside of its associated sliding-window cluster is accounted for using correction factors derived from simulated samples of single electrons with no additional pileup activity. Contributions from energy deposits within the cone of ΔR originating from pileup and the underlying event are also accounted for using a data-driven method that estimates the ambient energy density [73].

Track-based isolation momentum, p_T^{iso} , is calculated by summing the transverse momentum of tracks within a cone ΔR of the candidate electron's track, excluding the electron's track itself. Unlike the calorimeter-based isolation energy calculation, track-based isolation is calculated inside a cone with a variable radius $\Delta R = \min\left(\frac{10 \text{ GeV}}{p_T[\text{GeV}]}, R_{\text{max}}\right)$. This allows for narrower cone sizes than the ones used for calorimeter-based isolation, which is afforded by the finer segmentation of the Inner Detector. The tracks that enter the track-based isolation momentum calculation are required to have $p_T > 1 \text{ GeV}$ and $|\eta| < 2.5$, as well as satisfy some basic quality requirements optimised using muons in simulated $t\bar{t}$ samples. In order to suppress background from pileup, an additional requirement is placed on the track's longitudinal impact parameter z_0 . Additional tracks from the candidate electron emitting bremsstrahlung radiation are subtracted by removing tracks that fall within $\Delta\eta \times \Delta\phi = 0.05 \times 0.1$ of the candidate electron's calorimeter cluster.

The analysis presented in this thesis requires electrons to satisfy a calorimeter-based isolation of $E_T^{\text{iso}}|_{\Delta R=0.2}/E_T < 0.06$ and a track-based isolation of $p_T^{\text{iso}}|_{R_{\text{max}}=0.2}/p_T < 0.06$.

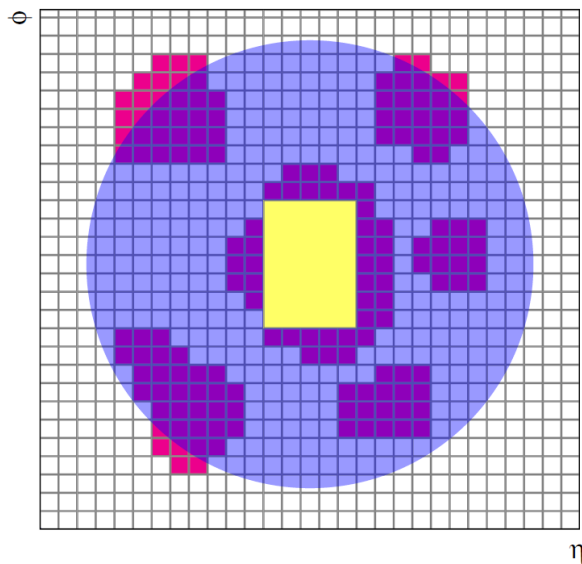


Figure 4.4: Schematic of the electron calorimeter-based isolation energy calculation [69]. The grid corresponds to calorimeter cells in the $\eta - \phi$ plane. The central yellow area corresponds to the sliding-window calorimeter cluster area, while the red cells indicate energy deposits associated to topological clusters. The circular blue-shaded area corresponds to the radius of the cone used to calculate the isolation energy.

The overall isolation efficiency for this working point starts at approximately 95% at a low average number of interactions per bunch cross of $\langle \mu \rangle \approx 10$ and decreases to approximately 85% at $\langle \mu \rangle \approx 80$ [72].

4.3 Photons

Photons are reconstructed using sliding-window clusters in the Electromagnetic Calorimeter and tracks in the Inner Detector for converted photon. Up to 60% of photons will undergo conversion before reaching the calorimeter system depending on the photon's pseudorapidity [74, 35]. Reconstructed photons are then required to satisfy a cut-based identification criteria and a calorimeter-based isolation energy cut.

4.3.1 Photon Reconstruction

The photon reconstruction procedure uses the same GSF re-fitted tracks implemented in the electron reconstruction. An additional step of vertex reconstruction is done to identify secondary vertices from photon conversions using a set of loosely matched tracks [75]. Two-track vertices are formed as well as single track vertices from tracks with no hits in the innermost layers of the Inner Detector. The electron identification capabilities of the Transition Radiation Tracker described in Section 3.2.1 are used to increase the purity of tracks originating from electrons. If multiple conversion vertices are associated to a single electromagnetic cluster, the most likely one is selected based on the number of tracks, their location in the Inner Detector, and the opening angle between the tracks for two-track vertices.

Sliding-window calorimeter clusters with neither a conversion vertex nor associated tracks are categorized as unconverted photon candidates and clusters matched to a conversion vertex are categorized as converted photon candidates. If a converted photon candidate is also reconstructed as an electron, an arbitration procedure is done which takes into account the track hit, momentum, and energy properties of the reconstructed object. The converted photon reconstruction efficiency is estimated in data and using simulated $Z \rightarrow \mu\mu\gamma$ events. For photons with $E_T > 20$ GeV, the reconstruction efficiency varies from 75% to 65% for pileup values of $\mu \approx 0$ to $\mu \approx 60$ respectively. The reconstruction efficiency for converted photons as a function of photon E_T is shown in Figure 4.5. It can be seen that the converted photon reconstruction efficiency is relatively flat as a function of photon E_T , except at the lowest values of photon E_T where it decreases slightly. The energy of photon calorimeter clusters is calibrated using simulation-based and data-driven techniques, and is done separately for converted and unconverted photons [71].

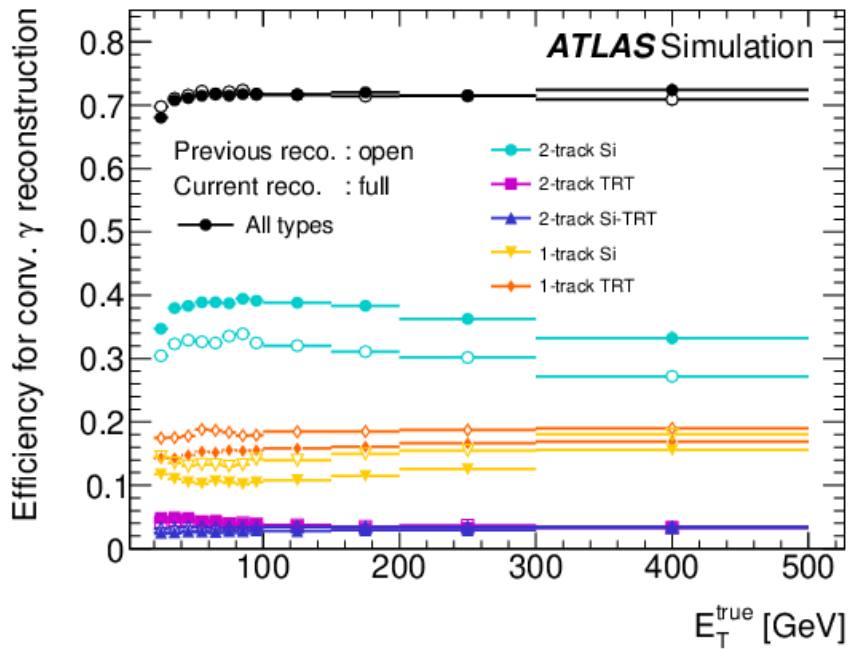


Figure 4.5: Efficiency to reconstruct converted photons as a function of true photon E_T [72]. In addition, the contribution to the total reconstruction efficiency of converted photons with associated tracks having varying numbers of hits in the Silicon and Transition Radiation Trackers is shown (Si and TRT respectively). The solid and open markers correspond to the efficiency achieved using the most recent version of the photon reconstruction software and the previous version, respectively.

4.3.2 Photon Identification

Photons are required to pass a set of identification criteria to help discriminate against two main sources of background. The first comes from misidentified hadronic jets which deposit a lot of their energy in the Electromagnetic Calorimeter. The second source of background comes from non-prompt photons from the decay of neutral hadrons inside jets such as the decay of neutral pions ($\pi^0 \rightarrow \gamma\gamma$). The signature of photons from neutral pion decays is characterized by two local maxima in the first layer of the Electromagnetic Calorimeter. Photon identification relies on calorimeter-based variables similar to those used for the electron identification procedure. However, the photon identification algorithm is cut-based instead of likelihood-based. The variables used in photon identification describe the lateral and longitudinal shower development, the amount of energy leakage into the Hadronic Calorimeter, and the energy distribution inside of clusters. These variables are illustrated in Figure 4.6. Different cuts applied to these calorimeter-based variables define two photon identification working points called *Loose* and *Tight* [75]. The *Tight* identification selection is used in the $W\gamma\gamma$ signal region maximize signal purity. The *Tight* identification efficiency is optimized separately for converted and unconverted photons and is tuned as a function of photon E_T and $|\eta|$. The efficiency of the *Tight* photon identification working point as a function of photon E_T is shown for unconverted and converted photons separately in Figure 4.7. It can be seen that the photon identification efficiency increases as a function of photon E_T , and that the identification efficiency for converted photons is generally higher than for unconverted photons at high photon E_T .

4.3.3 Photon Isolation

Photons are required to be isolated to further discriminate against background from misidentified hadronic jets and non-prompt photons from neutral hadron decays. The photon calorimeter-based isolation E_T^{iso} is calculated using topological calorimeter clusters

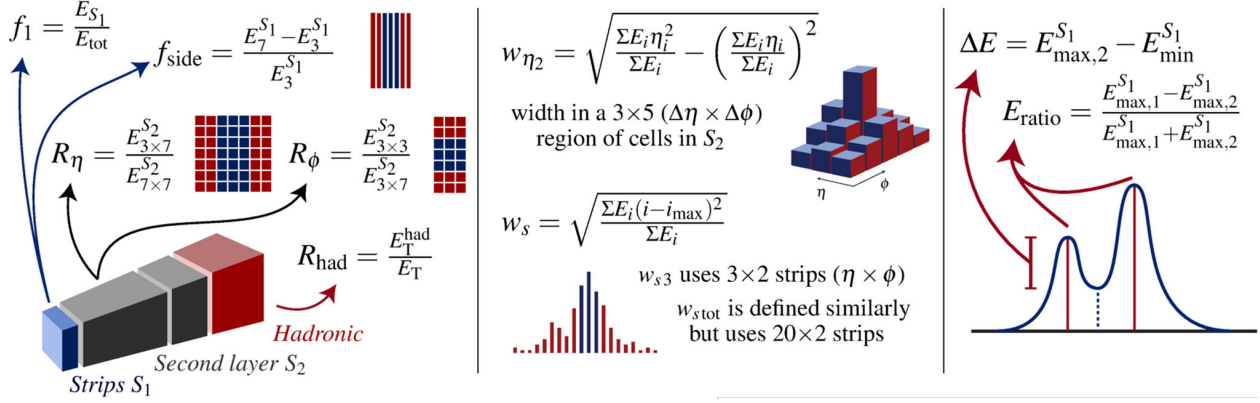


Figure 4.6: Schematic depiction of the different calorimeter-based variables used for photon identification [76]. These includes variables that describe the longitudinal shower development (left), the lateral (transverse) shower shape (middle), and the distribution of energy measured within the cluster (right).

in the same way as it is done for electrons. The isolation working point used in this thesis is the so-called *Calorimeter-Only Tight* working point with $E_T^{\text{iso}}|_{\Delta R < 0.4} < 2.45 \text{ GeV} + 0.022 \cdot E_T$. This working point is optimized to reduce the background from jets misidentified as photons, the largest source of background in the analysis. The photon isolation efficiency for this working point ranges from approximately 65 to 75% for photons with $E_T = 20 \text{ GeV}$ to approximately 92 to 98% for photons with $E_T = 1 \text{ TeV}$ [72].

4.4 Muons

Muons are reconstructed using tracks in the Inner Detector that are matched to tracks in the Muon Spectrometer. Reconstructed muons are additionally required to satisfy an identification criteria and a track-based momentum isolation cut.

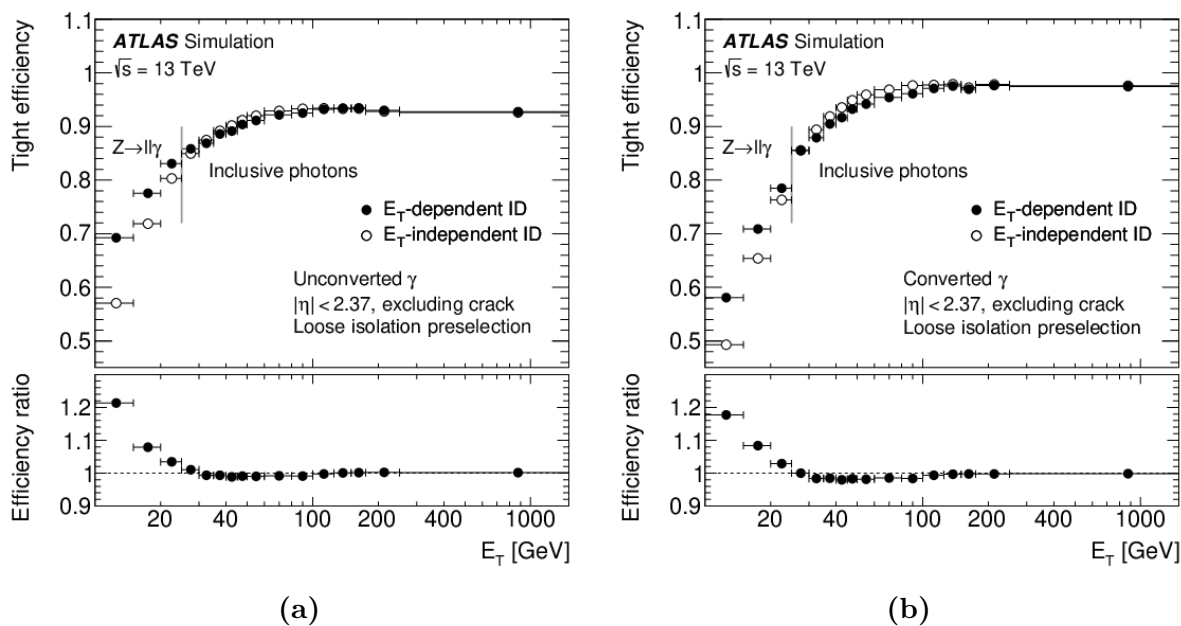


Figure 4.7: The *Tight* photon identification efficiency for (a) unconverted and (b) converted prompt photons as a function of photon E_T [72]. The identification efficiency is estimated from a sample of $Z \rightarrow \ell\ell\gamma$ events at low E_T and inclusive photons at high E_T . The bottom panels show the ratio of the efficiencies from the E_T -dependent and E_T -independent identification criteria points.

4.4.1 Muon Reconstruction

Muons are first reconstructed in the Muon Spectrometer and then combined with tracks in the Inner Detector [77]. Segments in the chambers of the Muon Spectrometer are formed from hit patterns with loose compatibility requirements. The segments are then used as seeds for an algorithm which combines them to form tracks. Tracks are formed with at least two segments which must satisfy basic quality criteria based on variables such as the number of associated hits and their goodness-of-fit. Tracks in the barrel/end-cap transition region of the Muon Spectrometer can be formed by a single high-quality segment. An overlap removal algorithm is employed to re-assign segments shared between multiple tracks to at most two tracks. This is done to keep the efficiency for reconstructing close-by muons high. A χ^2 fit is performed to assess the quality of the tracks reconstructed in the Muon Spectrometer. This is done iteratively while removing hits not compatible with the reconstructed track and recovering additional hits consistent with the extrapolated track.

Four different algorithms are used to reconstruct muon candidates. So-called *combined muons* are formed using a global fit based on information from the hits from tracks in the Inner Detector and Muon Spectrometer. This type of muon candidate has the highest purity. *Segment-tagged* muons are constructed by extrapolating from tracks in the Inner Detector to single layer segments in the Muon Spectrometer in order to increase the reconstruction efficiency for muons with low p_T or with trajectories in areas of the Muon Spectrometer with reduced acceptance. *Extrapolated* muons are formed from good quality tracks in the Muon Spectrometer which loosely point towards the interaction point. This category of muon candidate increases the reconstruction efficiency in the $2.5 < |\eta| < 2.7$ pseudorapidity region not covered by the Inner Detector. Finally, *calorimeter tagged* muon candidates are defined as tracks in the Inner Detector that are matched to energy deposits in the calorimeter that are consistent with a Minimum Ionizing Particle. This type of muon candidate has the lowest purity but nevertheless increases the overall muon reconstruction efficiency in the $|\eta| < 0.1$

pseudorapidity region where the Muon Spectrometer acceptance is reduced due to cabling and instrumentation. Overlap between different types of muon candidates sharing an Inner Detector track is resolved by preferentially assigning the muon candidate to the muon type with the highest purity. Overlap between muons of different types sharing a track in the Muon Spectrometer is resolved by selecting the muon candidate with the best quality track.

4.4.2 Muon Identification

Muon identification criteria are used to distinguish between prompt muons from the hard scatter and non-prompt muons originating from hadron decays. Because non-prompt muons from hadron decays originate from a displaced secondary vertex, their reconstructed tracks have larger longitudinal impact parameters. In addition, they typically have worse track quality and poorer compatibility between the momentum measurements of their associated tracks in the Inner Detector and their tracks in the Muon Spectrometer. The muon identification criteria is cut-based and uses variables that quantify the difference in track characteristics between the Inner Detector and Muon Spectrometer. In addition, the quality of the combined tracks is used, including the χ^2 of the combined fit and the hit/hole multiplicities in various layers of the tracking sub-detectors. Four identification working points, *Loose*, *Medium*, *Tight*, and *High- p_T* , provide various prompt and non-prompt muon efficiencies. For muons with $20 \text{ GeV} < p_T < 100 \text{ GeV}$, the prompt and non-prompt muon identification efficiencies range from 96.7% and 0.53%, respectively, for *Loose* muons, and 78.1% and 0.26%, respectively, for *High- p_T* muons. The *Medium* working point is used in the measurement presented in this thesis in order to maximize the muon identification efficiency while being compatible with single muon triggers described in Section 5.2 used to estimate the non-prompt muon background described in Section 6.6. The *Medium* identification selection has a prompt muon selection efficiency of 95.5% and a non-prompt muon selection efficiency of 0.38% [77].

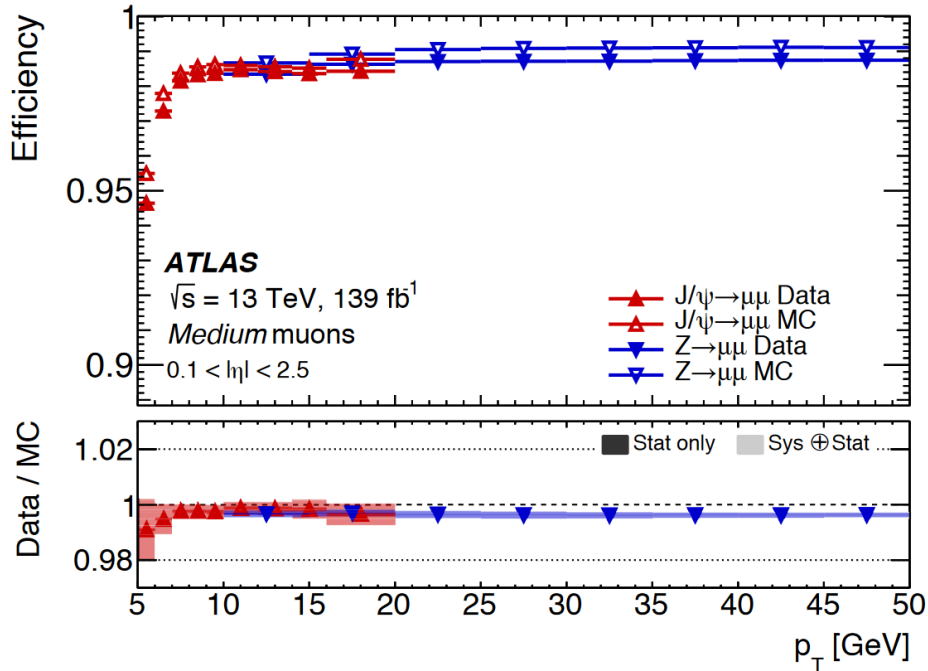


Figure 4.8: Combined muon reconstruction and identification efficiency for the *Medium* identification working point as a function of muon p_T [78]. Efficiencies are measured using J/Ψ and Z decays to two muons and compared in data and simulation (MC). Error bars show the statistical uncertainty. The bottom panel displays the ratio of the observed and expected efficiencies with statistical and systematic uncertainties.

Figure 4.8 shows the combined reconstruction and identification efficiencies for muons passing the *Medium* identification working point as a function of muon p_T . It can be seen that the combined muon reconstruction and identification efficiency is relatively flat for muons above $p_T \gtrsim 10$ GeV.

4.4.3 Muon Isolation

Prompt muons are usually isolated from other particles produced in proton-proton collisions, as opposed to muons originating from the semi-leptonic decays of charged hadrons. Like electrons, muons have a track-based isolation momentum p_T^{iso} and a

calorimeter-based isolation energy E_T^{iso} which are calculated using the algorithms described in Section 4.2.3. For the analysis presented in this thesis, muons are required to satisfy a calorimeter-based isolation energy cut of $E_T^{\text{iso}}|_{\Delta R=0.2}/E_T < 0.15$ and a track-based isolation momentum cut of $p_T^{\text{iso}}|_{R_{\text{max}}=0.3}/p_T < 0.04$. The muon isolation efficiency at this working point is approximately 85% for muons with $p_T \approx 25$ GeV and close to 100% for muons with $p_T \gtrsim 100$ GeV, as measure in $Z \rightarrow \mu\mu$ events [77].

4.5 Jets

Although jets are not explicitly required as part of the $W\gamma\gamma$ selection criteria, they are often present in the event final state due to initial or final state radiation off of the interacting partons of the colliding protons. In addition, as will be shown in Chapter 6, the reconstruction of jets is important because it provides additional information that can be used to suppress an important source of background. It is in this context that jets are used as input to the b -tagging algorithm described in Section 4.5.2. Jets are reconstructed using algorithms that take advantage of their conical shape in the detector. The algorithms used to reconstruct jets must maintain consistent and stable results in the presence of collinear emission of particles and the emission of low energy (or infrared) radiation.

4.5.1 Jet Reconstruction

Hadronic jets are reconstructed using topological clusters and Inner Detector tracks. The particle-flow algorithm [79] is employed to combine momentum and energy measurements of tracks and calorimeter clusters in order to avoid double-counting. This is done by matching good quality tracks to topological clusters based on the cluster energy barycenter. In order to calculate the transverse momentum associated to a track based on its curvature, the mass of the charged particle needs to be known. Since charged pions are estimated to make up

two thirds of all visible energy deposited by hadronic jets in the calorimeter, it is assumed that all tracks are made by charged pions. This approximation also provides an estimate of the expected energy deposited by the tracks in the calorimeter cells. The estimated energy deposited by individual charged particles in the topological cluster is subtracted cell-by-cell from the topological cluster itself, excluding tracks from candidate electrons and muons. Since a single charged particle can deposit energy in multiple topological clusters, the statistical significance between the energy of the topological cluster and the expected energy deposited by the charged particle is used to determine if additional topological clusters should be associated to the track. Below a certain threshold of statistical significance, all topological clusters within $\Delta R = 0.2$ are matched to the charged particle's track. If the remaining energy of a topological cluster is consistent with a statistical fluctuation of the amount of energy deposited by a single charged particle, the cluster is removed and not considered as input to the jet reconstruction algorithm described below. The outcome of the particle-flow algorithm is a set of tracks and calorimeter clusters with overlaps removed between the momentum measurements made in the Inner Detector and the energy measurements made in the calorimeter system.

The collection of tracks and clusters from the particle-flow algorithm that are matched to the primary vertex are used as input to the anti- k_t jet finding algorithm [80]. In this algorithm, the four-vector of the clusters and tracks are added together pairwise based on the following metric:

$$d_{ij} = \min\left(\frac{1}{p_{T,i}^2}, \frac{1}{p_{T,j}^2}\right) \frac{\Delta R_{ij}^2}{R^2} \quad (4.1)$$

using a radius parameter of $R = 0.4$. Here, d_{ij} is computed between two objects i and j , where $\Delta R_{ij} = \sqrt{(y_i - y_j)^2 + (\phi_i - \phi_j)^2}$ is the angular separation between the two objects defined in terms of their azimuthal angle and rapidity (instead of pseudorapidity). The metric d_{ij} is analogous to a distance and ensures that nearby low energy objects are combined with high

energy objects before being combined with each other, resulting in conically shaped jets.

Before the jet energy calibration is done, the average energy from in- and out-of-time pileup is first removed based on the jet's angular size and the overall p_T density of the event [73]. Then, the jet energy scale is calibrated using the simulated samples of different physics processes. Differences between simulation and data are accounted for *in situ* with a correction factor calculated using well-measured reference objects such as the Z boson [81]. In order to suppress the reconstruction of jets originating from pileup, a multivariate discriminant called the jet-vertex-tagger (JVT) is used. This discriminant is based on the properties of all the tracks in the event, those associated to the primary vertex, and those associated to the jet [82].

4.5.2 b-Jets

Hadronic jets originating from b -quarks have several kinematic properties that can be exploited for their identification. Since many physics processes result in the production of b -jets, b -tagging can be useful to increase the purity these types events. Processes with top quarks constitute an important background to the $W\gamma\gamma$ process due to the fact that top quarks nearly always decay to a b -quark and a W boson [8]. As such, b -tagging in the context of the $pp \rightarrow W\gamma\gamma$ measurement can be used to reduce the background from processes involving top quarks in their final state. Figure 4.9 highlights the typical kinematic properties of b -jets used to distinguish them from jets originating from light flavour quarks. Hadrons containing b -quarks typically decay within the detector acceptance, leading to jets with larger impact parameters, higher invariant masses, higher track multiplicities, and unique fragmentation properties.

The b -tagging algorithm used in this measurement starts with the output from several low-level algorithms which are then combined into a Neural Network-based classification. The first two low level algorithms are called IP2D and IP3D [83] and use the impact

parameters of tracks associated to jets as inputs to form likelihood-based discriminants. A secondary vertex finding algorithm called SV1 [84] iterates over all tracks associated to the jet and attempts to reconstruct a single displaced vertex associated to the jet. Finally, a topological multi-vertex algorithm, JETFITTER [85], uses the topological structure of b -hadron decays to reconstruct its full decay chain using a modified Kalman filter [63]. The outputs from these low-level algorithms are then used as inputs to a deep feed-forward Neural Network called DL1 [86] which outputs the probabilities for a jet to be a b -jet, a c -jet, or a light-flavour jet. The working point for the DL1 algorithm used in this thesis has an efficiency to select b -jets of 77% and a rejection factor for c -jets and light-flavour jets of one in 4.9 and one in 130, respectively [86].

4.6 Missing Transverse Energy

Though the initial momentum fraction carried by the interacting partons in a proton-proton collision is unknown, the sum of the transverse momentum of all of the particles produced in the interaction should be zero. Thus, after taking into account detector acceptance and inefficiencies, any transverse momentum imbalance observed in the detector is interpreted as resulting from the presence in the event of one or more particles that did not interact with the detector, such as a neutrino. The $W\gamma\gamma$ leptonic final states used in the analysis presented in this thesis include the production of a neutrino. As such, the amount of missing transverse momentum in an event is an important quantity to infer the presence of neutrinos. Missing transverse momentum is reconstructed from the calibrated electrons, muons, jets, and tracks not associated to physics objects but still associated to the primary vertex. The transverse missing momentum vector is calculated from the negative vector sum of the transverse momenta of all aforementioned objects [87]. Prior to this vector sum, algorithms are employed to resolve any ambiguities between energy measurements associated to jets, photons, electrons, and muons. In addition, before

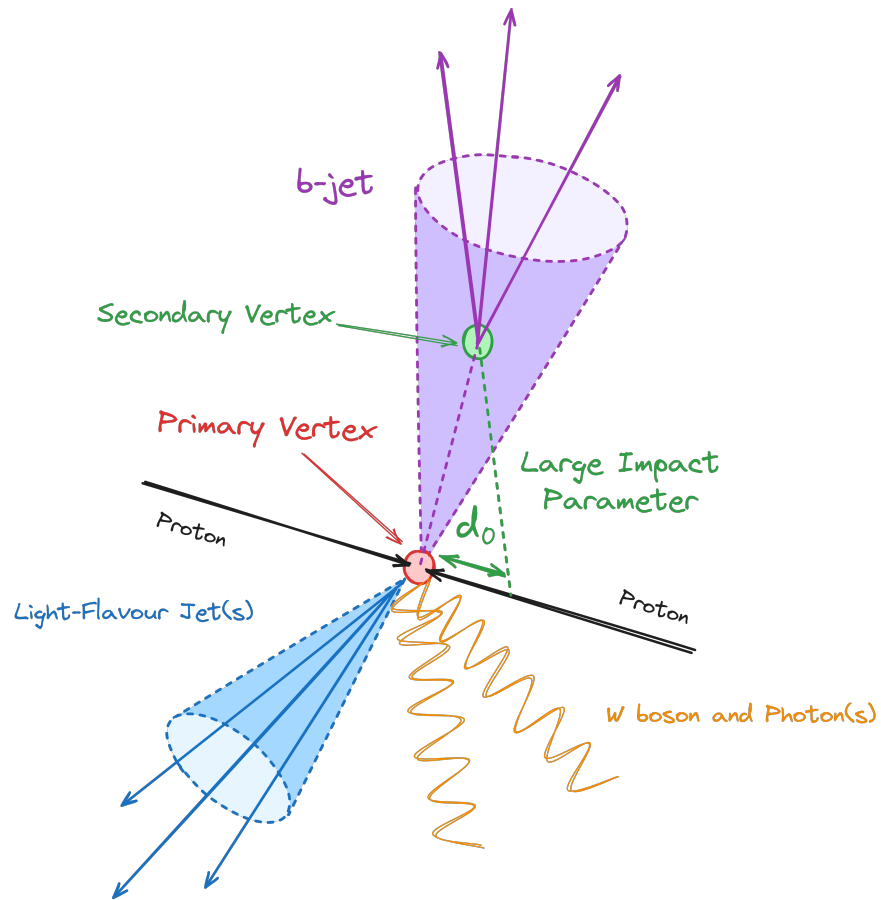


Figure 4.9: Schematic diagram highlighting the differences in the kinematic properties of a b -jet and jets originating from light-flavour quarks.

objects can be used to calculate the missing transverse momentum, an overlap removal procedure is applied to remove any remaining possible double-counting of physics objects. The overlap removal algorithm proceeds as follows, in the order given:

- Electrons that share an Inner Detector track with a muon are removed.
- Photons within $\Delta R = 0.4$ of an electron or muon are removed.
- Jets within $\Delta R = 0.2$ of an electron are removed.
- Electrons within $\Delta R = 0.4$ of a jet are removed.
- Jets within $\Delta R = 0.2$ of a muon are removed.
- Photons and muons within $\Delta R = 0.4$ of any remaining jets are removed.

A negative vector sum of the p_T of the remaining objects originating from the primary vertex is done to obtain the missing transverse momentum.

By common convention, in the rest of this thesis, missing transverse momentum is referred to as missing transverse energy (E_T^{miss}). The missing transverse energy resolution as a function of true missing transverse energy is shown in Figure 4.10 for $W(\rightarrow e\nu)$, $W(\rightarrow \mu\nu)$, and $t\bar{t}$ events from MC simulation. It can be seen that the E_T^{miss} resolution is generally better for $W \rightarrow \ell\nu$ events than for $t\bar{t}$ events. The E_T^{miss} calculation for $W \rightarrow \ell\nu$ events between $25 \text{ GeV} \lesssim p_T \lesssim 50 \text{ GeV}$ is dominated by the lepton p_T contribution, leading to an overall better resolution.

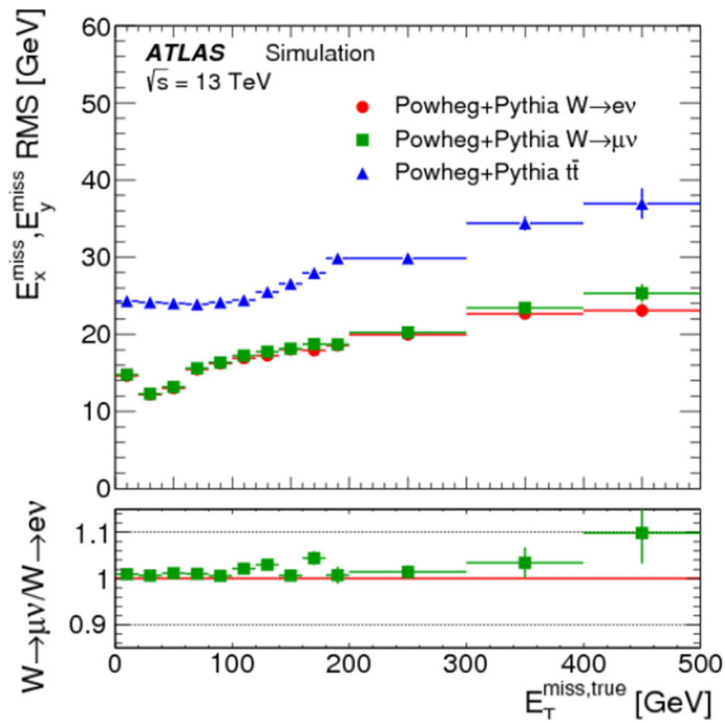


Figure 4.10: The missing transverse energy resolution along both the x and y axes as a function of the true missing transverse energy in simulated $W \rightarrow e\nu$, $W \rightarrow \mu\nu$, and $t\bar{t}$ events [88].

Chapter 5

Event Selection

In this chapter, an overview of the $pp \rightarrow W\gamma\gamma$ analysis strategy is first presented. Then, the selection requirements used to construct the region of phase space used to measure the $W\gamma\gamma$ statistical significance and production cross section are presented.

5.1 Analysis Strategy

The final states of interest in the $pp \rightarrow W\gamma\gamma$ measurements are those resulting from the electron and muon decay modes of the W boson, $W(\rightarrow e\nu_e)$ and $W(\rightarrow \mu\nu_\mu)$. The electron and muon channels are combined in order to provide enough events for the data-driven background estimation method for jets misidentified as photons described in Section 6.4. Though the leptonic decay branching ratio of the W boson is smaller than its hadronic decay branching ratio, the leptonic decay channels are much cleaner and offer better background discrimination than the hadronic decay channels. The tau decay channel of the W boson is not considered part of the signal except for events in which the tau decays to an electron or a muon accompanied by a neutrino, though these events represent only an estimated 2.4% of events in the analysis signal region. Tau leptons are challenging to reconstruct since, due to their mass and lifetime, they decay within the volume of the detector into multiple decay

channels, 65% of the time hadronically and 35% of the time leptonically [89]. Tau leptons in the ATLAS detector are typically reconstructed using their hadronic final states. Due to their complex signatures, tau leptons decaying hadronically are easily misidentified and prone to background contamination from hadronic jets. Therefore, in the analysis presented in this thesis, the tau decay channel of the W boson in which the tau decays hadronically are considered background. The measurement of the $pp \rightarrow W\gamma\gamma$ process presented in this thesis is inclusive of hadronic jets since they can be radiated by the initial state or final state partons. In summary, the final states of interest for the observation of the $pp \rightarrow W\gamma\gamma$ process are those consisting of one electron or one muon, at least two photons, and some missing transverse energy.

The first step in the event selection in both data and simulation is the set of trigger requirements. From the events in the subset of events that are deemed *good for physics* that pass the trigger selection, the event selection is defined based on fully reconstructed objects to create multiple regions where the signal and background processes can be estimated.

The Signal Region (SR) refers to a specific set of requirements that define the phase space in which the final fits to extract the $pp \rightarrow W\gamma\gamma$ significance and cross section are performed. In addition, several Control Regions (CRs) and Validations Regions (VRs) are used to estimate and validate different sources of background as described in Chapter 6. Both control and validation regions are typically designed to preferentially select a specific background while being orthogonal to each other (or mutually exclusive). Events in a CR are typically used to estimate a parameter required for a specific background estimation method. The background estimation method is then validated by comparing the number of predicted and observed events in a VR. The VR is typically kinematically more similar in terms of its definition to the SR than the CR is.

A diagram of the steps involved in the selection of both data and simulated events is shown in Figure 5.1. The final event selection is made from the proton-proton collisions that were recorded by the ATLAS detector at 13 TeV during the Run 2 data taking period

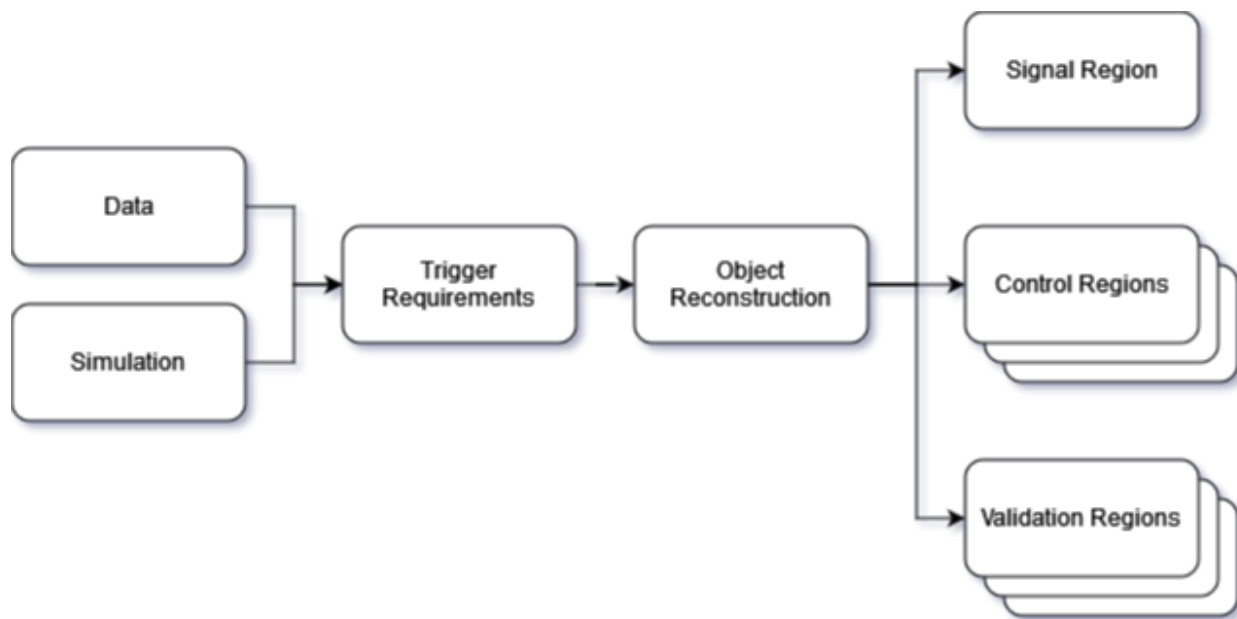


Figure 5.1: Diagram summarizing the process of selecting events from both data and simulation.

from 2015 to 2018. In addition, these collisions must pass the minimum requirements in order to be considered *good for physics* as described in Section 3.2.4. Furthermore, events must pass the trigger requirements described in Section 5.2. Objects in these events are then reconstructed using the algorithms described in Chapter 4 and required to pass the selections presented in Section 5.3. Finally, different event selections are defined to create multiple regions of phase space where the number of signal and background events can be estimated. The event selection for the analysis SR is detailed in Section 5.4.

There are several control and validation regions used to estimate the backgrounds crucial to the $pp \rightarrow W\gamma\gamma$ measurement. These backgrounds include the misidentified and non-prompt photon background (called $j \rightarrow \gamma$ background), the misidentified and non-prompt lepton background (called $j \rightarrow \ell$ background), the background from electrons misidentified as photons background (called $e \rightarrow \gamma$ background), the background from events with a top quark in their final state (called top quark background), and the background from events

in which one or both photons come from a pileup vertex (called pileup background). These sources backgrounds and the control and validation regions used to estimate them are detailed in Chapter 6. In addition, the systematic uncertainties relating to the object reconstruction and event simulation are discussed in Chapter 7. The statistical model and procedures used to extract the $pp \rightarrow W\gamma\gamma$ statistical significance and the measured cross section are described in Chapter 8.

5.1.1 Blinding Strategy

In order to avoid any bias, data in some regions of phase space were blinded (or deliberately not looked at) during the development and design of the analysis. The SR and any other control or validation region where signal events are estimated to make up more than 10% of events were kept entirely blinded, such as the VR used for the $j \rightarrow \mu$ background estimate. For the development of the data-driven $j \rightarrow \gamma$ background estimate, the dominant source of background, only half of data in the relevant CRs was used. The $pp \rightarrow W\gamma\gamma$ analysis was performed on the full unblinded dataset after it had undergone a thorough peer review process within the ATLAS collaboration. As such, the observed (unblinded) results will be shown along side the expected (blinded) results.

5.2 Trigger Selection

The first step in the selection of events of interest is the trigger selection. As described in Chapter 3.2.5, only a small fraction of all proton-proton collisions are recorded. Interesting collisions that are relevant to the ATLAS physics program are selected using a menu of different triggers. The triggers used to select events for the various signal, control, and validation regions are chosen to select for events with the desired physics objects while having the lowest possible thresholds to maximize signal efficiency.

Multiple sets of triggers are used for the electron and muon channels as well as for the various signal, control, and validation regions. These are based on the L1 and HLT electron, muon, and photon triggers used in Run 2 which are described in detail in References [90, 91]. These trigger requirements are applied both in data and in simulation. Knowledge of the efficiency at which events pass the trigger requirements is crucial for obtaining a cross section measurement and for the comparison of data with simulated samples. Correction factors are used in simulation to account for modelling differences in the trigger efficiencies between data and simulation and are calculated using $Z \rightarrow ee$ and $Z \rightarrow \mu\mu$ events.

5.2.1 Signal Region

The SR triggers require the reconstruction of one lepton and two photons in the event. In the muon channel, a trigger requiring one muon with $p_T > 20$ GeV and two photons passing *Loose* identification with $p_T > 10$ GeV was used for the full Run 2 period. In the electron channel, all triggers required one electron passing *Medium* identification and two photons passing *Loose* identification. The electron and photon p_T thresholds changed throughout the data taking period based on the data taking conditions and physics program. In 2015 and 2016, the electron p_T threshold was $p_T > 20$ GeV and the photon thresholds were $p_T > 10$ GeV, while in 2017 and 2018 the thresholds were $p_T > 24$ GeV and $p_T > 12$ GeV, respectively.

5.2.2 Control Region

The triggers used in the various control and validation regions are often, and unless indicated otherwise, the same as those used in SR. However, a number of CRs used to estimate the $e \rightarrow \gamma$ and $j \rightarrow \ell$ background sources require a dedicated set of triggers for reasons that will be described in Sections 6.5 and 6.6, respectively. These CRs are constructed using events satisfying a combination of single lepton and di-lepton trigger requirements.

The single lepton triggers require one reconstructed lepton satisfying an identification cut and passing a minimum p_T threshold. The identification working points and minimum p_T thresholds changed throughout the Run 2 data taking period. In 2015, the electron (muon) was required to satisfy $p_T > 20$ GeV ($p_T > 24$ GeV) and pass the *Medium (Loose)* identification working point. From 2016 to 2018, the electron (muon) was required to satisfy $p_T > 26$ GeV ($p_T > 26$ GeV) and pass the *Tight (Medium)* identification working point. Additional triggers with higher p_T thresholds were used to maintain a high trigger efficiency at high lepton p_T .

Two dilepton trigger requirements were used which remained the same throughout all of Run 2. One requiring two electrons with $p_T > 17$ GeV and passing the *Loose* identification requirements, and one requiring a muon with $p_T > 14$ GeV and an electron with $p_T > 17$ GeV passing the *Loose* identification requirements.

5.3 Object Selection

The second step in the selection process consists in defining quality criteria that individual reconstructed objects must satisfy. The objects and variables used to define the event selection in this section and the next build off of the reconstructed objects described in Section 4. Three categories of object qualities called *Preselect*, *Baseline* and *Signal* are defined using progressively more stringent requirements. The *Signal* requirements for an object are inclusive of the *Baseline* requirements which are themselves inclusive of the *Preselect* requirements. These categories are used to define the selection criteria aimed at rejecting background events and constructing various regions of phase space. *Signal* objects are used to construct the SR while *Baseline* objects that are not *Signal* objects can be used to construct orthogonal CRs. The inclusivity of an object's selection criteria is typically limited by the trigger selection. In other words, identification requirements cannot be less stringent than the ones used to define the trigger requirements. In addition, a slightly

Object	<i>Preselect</i>	<i>Baseline</i>	<i>Signal</i>
Electrons	$p_T > 6 \text{ GeV}$ $ z_0 \cdot \sin(\theta) < 0.5 \text{ mm}$ $ \eta < 2.47$	pass <i>Preselect</i> $p_T > 25 \text{ GeV}$ <i>Medium</i> identification excluding $1.37 < \eta < 1.52$	pass <i>Baseline</i> $E_T^{\text{iso}} _{\Delta R=0.2} / E_T < 0.06$ $p_T^{\text{iso}} _{R_{\text{max}}=0.2} / p_T < 0.06$ $ \sigma_{d_0} < 5$
Muons	$p_T > 6 \text{ GeV}$ $ z_0 \cdot \sin(\theta) < 0.5 \text{ mm}$ $ \eta < 2.4$ <i>Medium</i> identification	pass <i>Preselect</i> $p_T > 25 \text{ GeV}$	pass <i>Baseline</i> $E_T^{\text{iso}} _{\Delta R=0.2} / E_T < 0.15$ $p_T^{\text{iso}} _{R_{\text{max}}=0.3} / p_T < 0.04$ $ \sigma_{d_0} < 3$
Photons		$p_T > 20 \text{ GeV}$ $ \eta < 2.37$ excluding $1.37 < \eta < 1.52$ <i>Tight</i> identification	pass <i>Baseline</i> $E_T^{\text{iso}} _{\Delta R=0.4} - 0.022 \cdot E_T < 2.45 \text{ GeV}$
Jets			$p_T > 20 \text{ GeV}$ $ \eta < 4.5$ JVT > 0.5 for jets with $20 < p_T < 60 \text{ GeV}$ and $ \eta < 2.4$

Table 5.1: Summary of the *Preselect*, *Baseline*, and *Signal* selection requirements for electrons, muons, and jets. *Signal* objects are inclusive of *Baseline* objects which are inclusive of *Preselect* objects.

higher p_T threshold is preferred for the reconstructed versus trigger object counterparts to ensure the full trigger efficiency. The object selection requirements used in this analysis are summarized in Table 5.1 and described in the following subsections.

5.3.1 Electrons

Preselect electrons are required to satisfy $p_T > 6 \text{ GeV}$, $|\eta| < 2.47$, $|z_0 \cdot \sin(\theta)| < 0.5 \text{ mm}$, and satisfy the *Loose* electron identification requirements described in Section 4.2.2. *Baseline* electrons are required to additionally satisfy $p_T > 25 \text{ GeV}$, $|\eta| < 2.47$ excluding the uninstrumented calorimeter region between $1.37 < |\eta| < 1.52$, and to satisfy the *Medium* electron identification requirements. Finally, *Signal* electrons are required to satisfy $|\sigma_{d_0}| < 5$ and be isolated by requiring that they satisfy a calorimeter-based isolation energy requirement of $E_T^{\text{iso}} / E_T < 0.06$ calculated within $\Delta R < 0.2$ and a track-based isolation momentum requirement of $p_T^{\text{iso}} / p_T < 0.06$ calculated using the variable radius cone described in Section 4.2.3 with $R_{\text{max}} = 0.2$.

5.3.2 Photons

There are no *Preselect* photons. *Baseline* photons are required to satisfy $p_T > 20$ GeV and $|\eta| < 2.37$ excluding the uninstrumented calorimeter region between $1.37 < |\eta| < 1.52$. In addition, *Signal* photons are required to pass the *Tight* photon identification working point described in Section 4.3.2 and the *Calorimeter-Only Tight* isolation working points described in Section 4.3.3.

For the purpose of estimating background contributions originating from misidentified photons, several additional photon identification working points are defined. These *LoosePrime* (LP) working points called LP2, LP3, LP4, and LP5 are constructed by selecting photons that fail at least one of 2, 3, 4, or 5 criteria used to define the *Tight* photon identification working point [75]. The subset of cuts that are required/allowed to fail for each of the LP working points is summarized in Table 5.2. All other cuts defining the *Tight* working point are required to be satisfied by the LP working points [72]. These LP photon identification categories are by construction orthogonal to the *Tight* working point.

5.3.3 Muons

Preselect muons are required to satisfy $p_T > 6$ GeV, $|\eta| < 2.4$, $|z_0 \cdot \sin(\theta)| < 0.5$ mm, and pass the *Medium* muon identification working point described in Section 4.4.2. *Baseline* muons are further required to satisfy $p_T > 25$ GeV. *Signal* muons are additionally required to satisfy $|\sigma_{d_0}| < 3$ and be isolated. The isolation requirement on the calorimeter-based isolation energy is $E_T^{\text{iso}}/E_T < 0.15$ and is calculated within $\Delta R < 0.2$, while the track-based isolation momentum requirement is $p_T^{\text{iso}}/p_T < 0.04$ and is calculated using the variable radius cone with $R_{\text{max}} = 0.3$.

Variable	Description	LP5	LP4	LP3	LP2	<i>Tight</i>
w_{s3}	Lateral shower width in a 3-cell window around the highest-energy cell					x
f_{side}	Energy fraction outside core of three central cells within seven cells surrounding the highest-energy cell divided by the energy inside the same three central cells					x
ΔE_S	Energy difference between the second-highest energy cell and smallest energy cell found between the first and second-highest energy cells				x	x
E_{ratio}	Ratio of the energy difference between the first and second-highest energy deposit to their sum			x	x	x
w_{stot}	Total lateral shower width		x	x	x	x

Table 5.2: Summary of the *Loose Prime* (LP) and *Tight* identification working points used in the analysis. An "x" indicates the requirements each working point has to pass. Each LP working point is required to fail at least one of the other variables. This is a non-exhaustive list of the photon identification requirements, showing only those that are allowed/required to fail to create the various LP working points [72].

5.3.4 Jets

There are no *Preselect* or *Baseline* jets. *Signal* jets are required to satisfy $p_T > 20$ GeV and $|\eta| < 4.5$. In order to suppress pileup jets, *Signal* jets satisfying $20 < p_T < 60$ GeV and $|\eta| < 2.4$ must also satisfy $JVT > 0.5$ as described in Section 4.5. The DL1 *b*-tagging algorithm at the 77% efficiency working point, as described in Section 4.5.2, is applied to *Signal* jets with $|\eta| < 2.5$. This is used to reject events containing a jet likely originating from a *b*-quark in order to suppress background events that have a top quark in their final state.

5.4 Event Selection

The final step in the event selection is to define a set of criteria based on the kinematic properties of the reconstructed objects. The event selection presented in this section is designed to achieve a relatively good signal efficiency and background rejection to form the SR. The SR is formed by requiring at least two *Signal* photons and exactly one *Signal* lepton. The two photons are ensured to be well-separated from each other and the lepton by requiring $\Delta R_{\gamma\gamma} > 0.4$ and $\Delta R_{\ell\gamma} > 0.4$. In order to select for events compatible with the presence of a leptonically decaying *W* boson, events must satisfy $E_T^{\text{miss}} > 25$ GeV and $m_T^W > 40$ GeV, where m_T^W is formed using the missing transverse energy E_T^{miss} , the lepton p_T^ℓ , and their azimuthal separation $\Delta\phi$:

$$m_T^W = \sqrt{2p_T^\ell E_T^{\text{miss}}(1 - \cos \Delta\phi)}. \quad (5.1)$$

In order to suppress background events with a *Z* boson or two *W* bosons, events containing an additional *Preselect* same-flavour lepton or an additional opposite-flavour *Baseline* lepton are rejected. Events with one or more *b*-tagged *Signal* jet are also rejected in order to suppress background events from processes with a top quark in their final state.

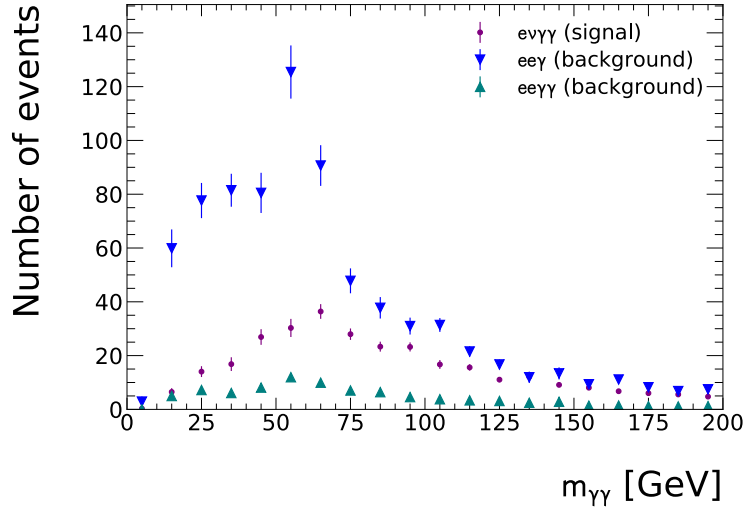


Figure 5.2: Diphoton invariant mass $m_{\gamma\gamma}$ in the Signal Region before the $Z\gamma$ veto requirement in the electron channel for $e\nu\gamma\gamma$ (signal), $ee\gamma$, and $ee\gamma\gamma$ simulated events.

A large fraction of the events selected with the requirements described above originate from the $Z\gamma$ and $Z\gamma\gamma$ processes as shown in Figure 5.2. These background events are selected due to electrons being misidentified as photons and/or electrons failing to be reconstructed due to limited detector acceptance and reconstruction efficiencies.

In order to discriminate between signal events and this type of background, several kinematic variables are formed. These include the combined invariant mass of the lepton and two photons ($m_{\ell\gamma\gamma}$), the invariant mass of the highest p_T photon and the lepton ($m_{\ell\gamma_1}$), the invariant mass of the second highest p_T photon and the lepton ($m_{\ell\gamma_2}$), and the combined transverse momentum of the lepton and two photons ($p_{T,\ell\gamma\gamma}$). Simulated $e\nu\gamma\gamma$ signal events and simulated background $ee\gamma$ and $ee\gamma\gamma$ events are used to optimise the cut values on each of these variables. The value of the cut was chosen as the value at which the number of $e\nu\gamma\gamma$ signal events selected is larger than the total number of $ee\gamma + ee\gamma\gamma$ background events. The resulting cut values are $81 \text{ GeV} < m_{\ell\gamma_1}, m_{\ell\gamma_2}, m_{\ell\gamma\gamma} < 100 \text{ GeV}$ and $p_{T,\ell\gamma\gamma} > 30 \text{ GeV}$. The impact of each individual cut is shown in Figure 5.3.

Signal Region
= 1 <i>Signal</i> lepton and ≥ 2 <i>Signal</i> photons $\Delta R_{\gamma\gamma} > 0.4, \Delta R_{l\gamma} > 0.4$ $E_{\text{T}}^{\text{miss}} > 25$ and $m_{\text{T}}^W > 40$ GeV No additional <i>Preselect</i> same-flavour lepton No additional opposite-flavour <i>Baseline</i> lepton <i>Z</i> γ veto cuts: $p_{\text{T}}^{\ell\gamma\gamma} > 30$ GeV, and $81 \text{ GeV} < m_{\ell\gamma_1}, m_{\ell\gamma_2} < 100$ GeV <i>b</i> -jet veto on jets with $p_{\text{T}} > 20$ GeV and $ \eta < 2.5$ JVT > 0.5 for jets with $20 < p_{\text{T}} < 60$ GeV and $ \eta < 2.4$

Table 5.3: Summary of the Signal Region selection criteria.

Though the $Z\gamma$ veto is meant to suppress $Z\gamma$ and $Z\gamma\gamma$ events in the electron channel, the cuts are applied to both the electron and muon channels in order to enable their combination in the estimation of the $j \rightarrow \gamma$ background as described in Section 6.4.

The selection requirements used to define the SR are summarized in Table 5.3. In addition, a cutflow is presented in Figure 5.4 showing the number of events selected from the events that are *good for physics* to the full SR selection after all cuts are applied. Figures 5.5 and 5.6 show event displays of candidate signal events in the electron and muon decay channels of the $W\gamma\gamma$ process, respectively.

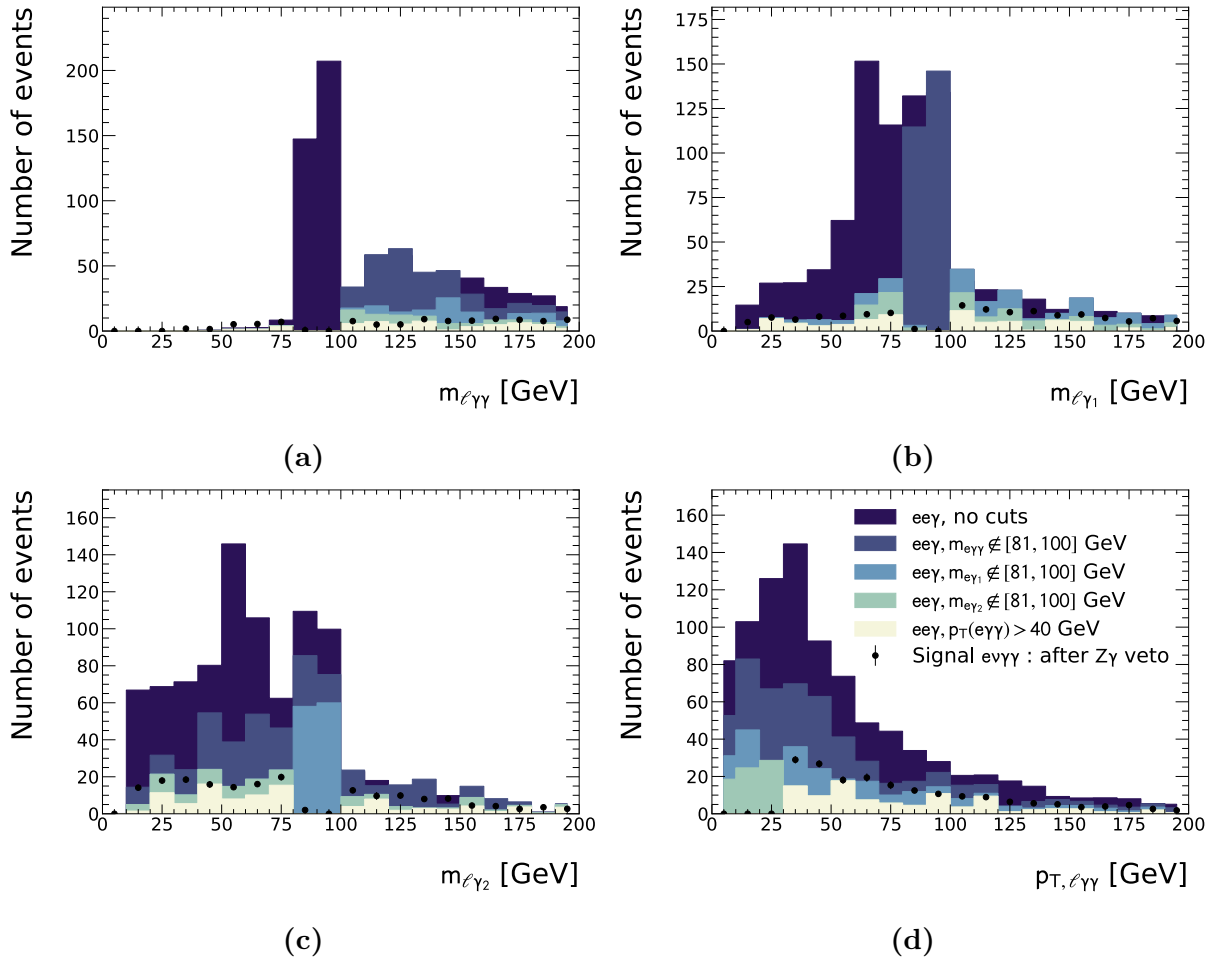


Figure 5.3: Distributions of kinematic variables (a) $m_{\ell\gamma\gamma}$, (b) $m_{\ell\gamma_1}$, (c) $m_{\ell\gamma_2}$, and (d) $p_{T,\ell\gamma\gamma}$ obtained using simulated $e\nu\gamma\gamma$ signal events and $ee\gamma$ and $ee\gamma\gamma$ background events. Each lighter shade is the result of the application of an additional $Z\gamma$ veto requirements in the order that they appear in the legend. The expected number of $e\nu\gamma\gamma$ signal events is shown with all four $Z\gamma$ veto cuts applied as the black circular markers.

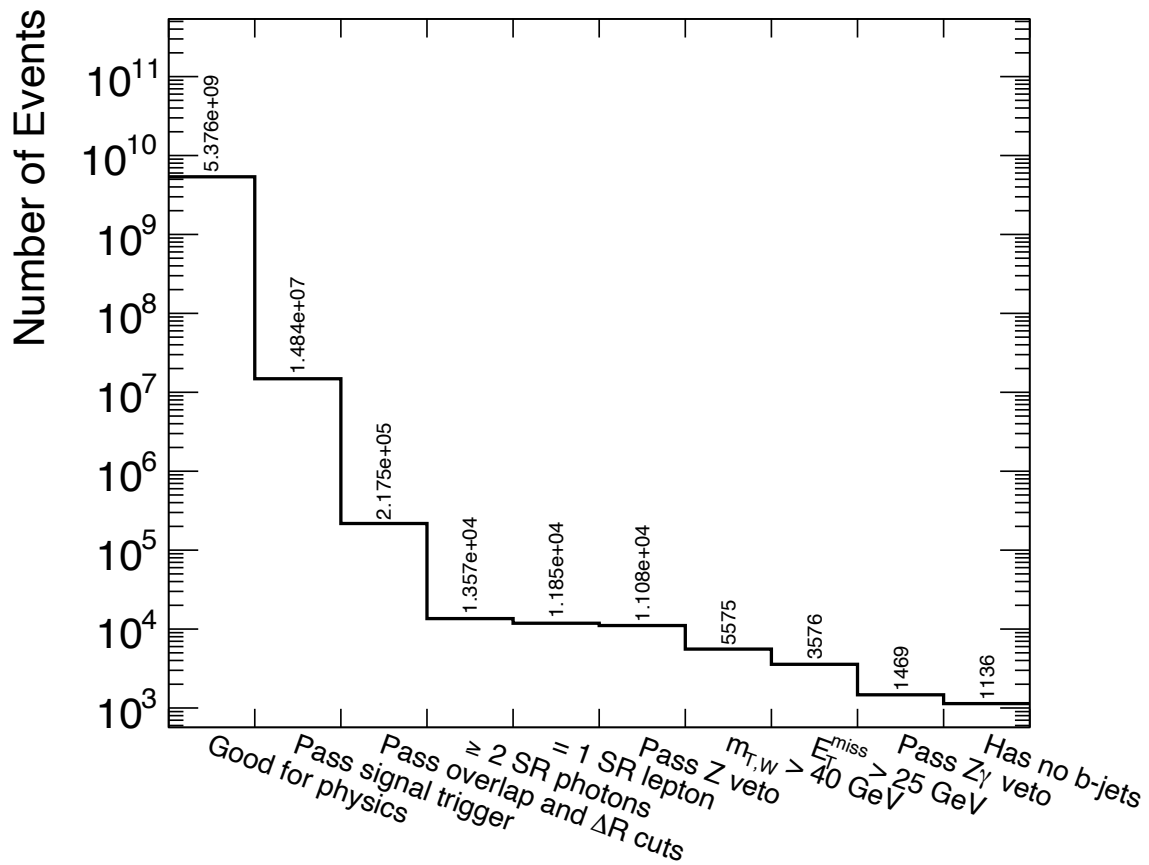


Figure 5.4: Number of events selected after sequentially applying the different requirements of the event selection defining the Signal Region (SR).

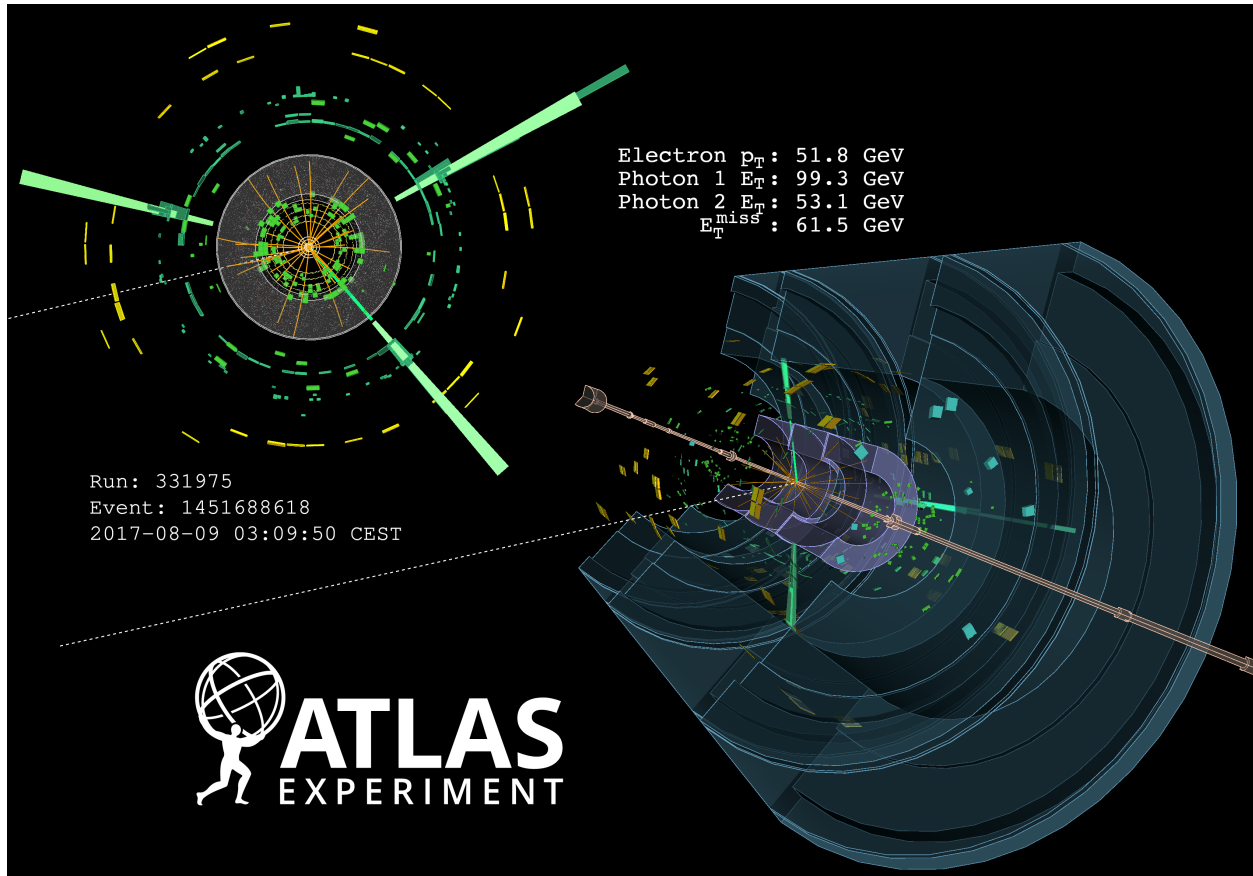


Figure 5.5: Display of a candidate $W(\rightarrow e\nu)\gamma\gamma$ event from proton-proton collisions recorded by the ATLAS detector with LHC stable beams at a center of mass collision energy of 13 TeV. Orange lines indicate tracks in the Inner Detector with transverse momentum above 2 GeV. The coloured boxes indicate energy deposits in calorimeter cells with transverse energies above 250 MeV in the liquid argon Electromagnetic Calorimeter (green), 250 MeV in the Tile Calorimeter (yellow), and 800 MeV in the Hadronic Endcap Calorimeter (cyan). The longer light green boxes indicate calorimeter energy clusters which are either associated with a green track in the Inner Detector for the reconstructed electron, or not in the cases of the two reconstructed photons. The dashed white line indicates the missing transverse energy. No jet has been reconstructed with transverse momentum above 20 GeV.

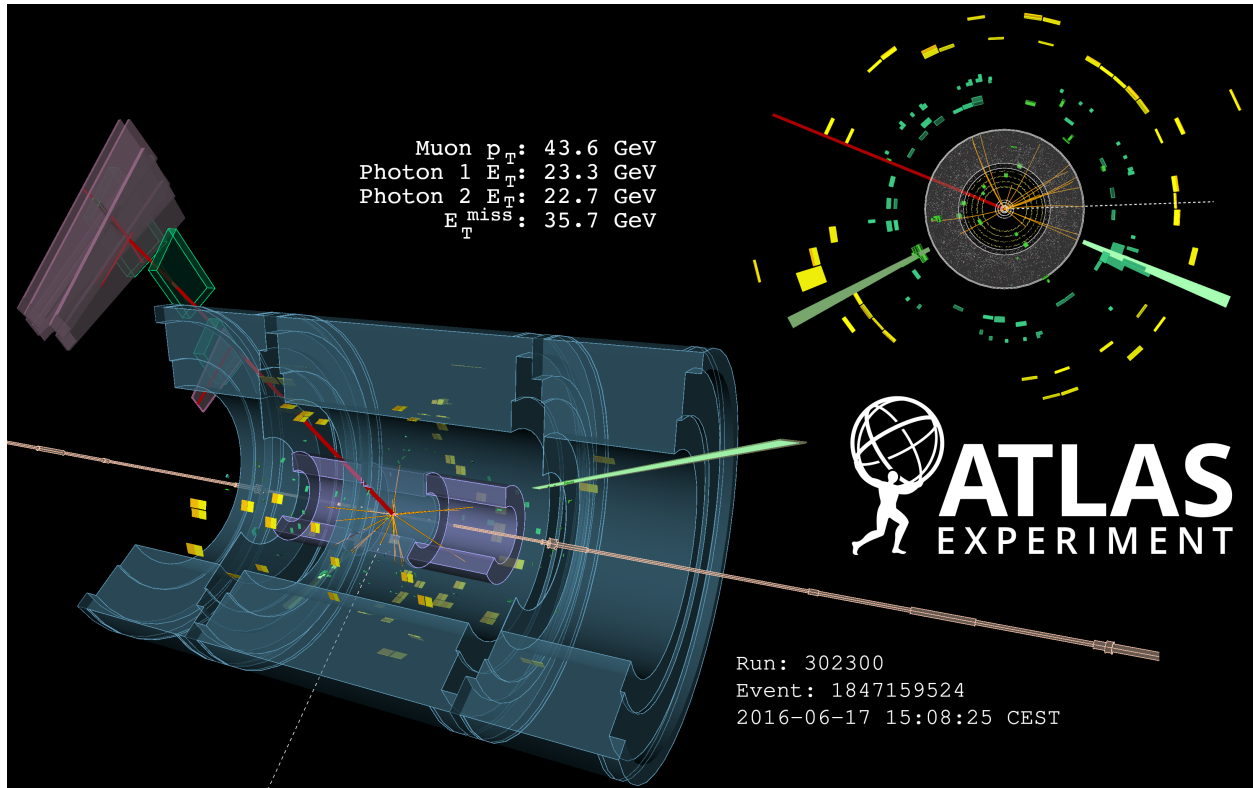


Figure 5.6: Display of a candidate $W(\rightarrow \mu\nu)\gamma\gamma$ event from proton-proton collisions recorded by the ATLAS detector with LHC stable beams at a center of mass collision energy of 13 TeV. Orange lines indicate tracks in the Inner Detector with transverse momentum above 2 GeV. The coloured boxes indicate energy deposits in calorimeter cells with transverse energies above 250 MeV in the liquid argon Electromagnetic Calorimeter (green), 250 MeV in the Tile Calorimeter (yellow), and 800 MeV in the Hadronic Endcap Calorimeter (cyan). The longer light green boxes indicate calorimeter energy clusters associated to the two reconstructed photons while the red line indicates the track of the reconstructed muon. The dashed white line indicates the missing transverse energy. No jet has been reconstructed with transverse momentum above 20 GeV.

Chapter 6

Background Estimation

The results presented in this thesis rely on the precise determination of the number of signal and background events expected to be selected in the Signal Region (SR). The techniques used to estimate the expected number of events from signal and different background sources are presented in this chapter. Since all of the background estimation techniques rely in some way on simulated event samples, the first section of the chapter describes the different steps involved in simulating the possible outcomes of proton-proton collisions. The following sections then present the methods developed to estimate the number of events expected from different sources of background.

The different sources of background events can be classified into two categories: irreducible backgrounds originating from physics processes producing the same types of objects with similar kinematic properties as those expected from signal events, and reducible backgrounds originating from events with misidentified objects. Irreducible background sources include physics processes resulting in the production of multiple bosons and the production of top quarks, both described in Section 6.2 and Section 6.3, respectively. Contributions from reducible background sources originating from the misidentification of physics objects are estimated using data-driven methods as described

in Sections 6.4 to 6.7. A summary of the different sources of background is given in Section 6.8.

6.1 Simulation of Proton-Proton Collisions

The simulation of proton-proton collisions is done in multiple steps involving different software packages. These steps are summarized below. A more detailed description can be found in the papers associated to the individual simulation packages used to simulate the signal and background samples described in Section 6.1.1. A more general overview is given in Reference [92]. Several simulation steps involve the use of Monte Carlo (MC) methods to sample underlying probability distributions or to perform numerical integration.

The first simulation step involves the sampling of Parton Distribution Functions (PDFs). As explained in Section 2.3.1, PDFs describe the probability for each type of parton inside the proton to interact in a given hard scatter process as a function of the fraction of the total proton momentum carried by the parton. The PDFs cannot be calculated from first principle as they describe physics phenomena in the non-perturbative regime of QCD. They are determined by fitting empirical models to an ensemble of measurements at varying energy scales. In the simulation of proton-proton collisions, the energy scale at which PDFs are sampled is called the factorization scale [8]. The simulated event samples described later use different sets of PDFs. These differ in the empirical models used to parameterize the non-perturbative effects and the ensemble of measurements used in their fit to data. The outcome of this first simulation step is the determination of the types of the interacting partons and the momentum fractions they carry from their respective proton's total momentum.

The second simulation step consists in the calculation of the so-called *matrix element* of the simulated physics process. The matrix element describes the transition probability between an initial and final state for a given interaction. The calculation is done at a given order in perturbative QCD. Leading Order (LO) matrix element calculations only include

Feynman diagrams with the minimal number of electroweak and QCD vertices required to produce the final state particles of interest. Next-to Leading Order (NLO) matrix element calculations further include all of the Feynman diagrams with an additional vertex that produce the final state particles of interest. In the context of this thesis, NLO calculations specifically refer to additional QCD vertices unless otherwise stated. This essentially corresponds to adding terms of higher powers of the strong coupling constant in the perturbative expansion of the matrix element. Due to the finite order of these perturbative calculations, the resulting matrix element estimate depends on the value of the strong coupling constant at a specific energy scale called the renormalization scale [8]. The exact choice of both the factorization and renormalization scales used in the simulation of proton-proton collisions is somewhat arbitrary and unphysical. As such, an uncertainty on the simulated event distributions is assigned to the choice of these scales by varying their values in a procedure described in Section 7.2.3.

To improve the accuracy of the simulation, radiative corrections are applied to the fixed order matrix element calculations in order to approximate the missing higher order contributions. These radiative corrections model the probability of an initial or final state parton to radiate a gluon or split into two or more partons. This so-called *parton showering* process proceeds until the energy of the partons fall below the factorization scale. At this energy, colour confinement comes into play and hadronization occurs. To avoid any double counting, the parton showering process must be properly matched to the fixed order matrix element calculations in order to account for radiated quarks and gluons already simulated in the hard scatter.

The hadronization portion of the simulation parameterizes the formation of hadronic jets after the parton showering process. In this regime, as the strong coupling constant becomes larger, non-perturbative QCD takes over, and the phenomenon of colour confinement emerges whereby partons form colourless bound states called hadrons. Different hadronization models exist such as the *cluster* [93] and the *string* [94] models. This part of the event simulation

is also responsible for the modeling of the decays of unstable hadrons.

The next step in the simulation chain consists in the simulation of the interactions of the particles produced in the proton-proton collisions with the detector material. This includes the simulation of the particle showers that are produced by the interactions of the final state photons, electrons, and hadrons in the calorimeters and the simulation of the response of the readout electronics. This simulation step is done using a simulation software called Geant4 [95].

After the detector simulation, events are processed by the ATHENA [58, 59] reconstruction software in the same way as events in real data are processed. However, unlike events in real data, simulated events also have so-called *truth* information specifying the four-momentum vectors and types of all the particles created at the matrix element level before the parton shower, hadronization, and detector interactions are simulated. Using this truth information, particles misidentified by the reconstruction software can be labeled as such and properly identified in a procedure called *truth-matching*. This consists in matching the reconstructed object's properties to its corresponding truth particle at the matrix element level.

The final simulation step consists in adding the outcome of additional inelastic proton-proton collisions taking place simultaneously with the process of interest within a single bunch crossing. These additional collisions can create a measurable signature in the detector and contribute to each event as pileup. Proton-proton interactions contributing to pileup are generated separately from the physics processes of interest and then overlaid event by event. The number of these additional parton-parton interactions is related to the number of proton-proton collisions per bunch crossing which is Poisson distributed around the mean number of interactions per bunch crossing μ as described in Section 3.2.4. The distributions of the mean number of interactions per bunch crossing in simulated samples is re-weighted to closely match the measured distributions over the course of the Run 2 data taking period shown in Figure 3.3. In addition, the remnants of the interacting protons that produce the

hard scatter can sometimes interact leading to the production of additional particles from the same proton-proton collision. These additional particle interactions are simulated by the event generators along with the hard scatter of interest. Together, the pileup contributions and the additional particles from the remnants of the interacting protons form what is called the *underlying event*.

The event generators used for the matrix element calculations are MadGraph [96], POWHEG [97], and Sherpa [98] which uses the Comix [99], OpenLoop [100, 101], and Collier [102] libraries. The parton shower portion of the simulation for Sherpa samples is also done in Sherpa [103], while for the MadGraph and POWHEG samples the parton showering is done using Pythia 8 [104, 105]. The inelastic proton-proton interactions that are overlaid onto the hard scatter events are simulated using Pythia 8 and re-weighted to reproduce the pileup distributions measured in data.

6.1.1 Simulation Samples

The simulation samples use in the $W\gamma\gamma$ analysis are summarized in Table 6.1, along with the software packages used to generate each process, information on how many additional partons (gluons or quarks, labelled j) are simulated in the matrix element, at what order in QCD these additional diagrams are generated (LO or NLO), and the sample's k -factor and cross section. The k -factor refers to the ratio of the total NLO to LO cross section. This factor is applied as an overall normalization factor to LO event distributions in order to approximate NLO distributions.

While some simulation samples are directly used to estimate the expected number of events from a particular physics process in the SR, other simulation samples are used to estimate systematic uncertainties, to perform cross-checks, or to validate some of the data-driven methods used to estimate the reducible sources of background described later in this chapter.

Process	Generator	Order	k -factor	Cross Section (pb)
W$\gamma\gamma$ (signal)				
$W(\rightarrow \ell\nu)\gamma\gamma$	Sherpa 2.2.10	$0j$ NLO, $1,2j$ LO	1	6.2
$W(\rightarrow \ell\nu)\gamma\gamma$	MadGraph + Pythia 8	$0,1j$ NLO	1	4.4×10^{-1}
WH				
$W(\rightarrow \ell\nu)H(\rightarrow \gamma\gamma)j$	POWHEG + Pythia 8	NLO	1	3.2×10^{-3}
Z$\gamma\gamma$				
$Z(\rightarrow \ell\ell)\gamma\gamma$	Sherpa 2.2.10	$0j$ NLO, $1,2j$ LO	1	4.2
Wγ				
$W(\rightarrow \ell\nu)\gamma$	Sherpa 2.2.8	$0j$ NLO, $1,2j$ LO	1	1.1×10^3
$W(\rightarrow \ell\nu)\gamma$	MadGraph + Pythia 8	$0,1j$ NLO	1	5.4×10^1
Zγ				
$Z(\rightarrow \ell\ell)\gamma$	Sherpa 2.2.8	$0j$ NLO, $1,2j$ LO	1	3.0×10^2
$Z(\rightarrow \ell\ell)\gamma$	MadGraph + Pythia 8	$0,1j$ NLO	1	4.4×10^1
Top				
$t\bar{t}$	POWHEG + Pythia 8	LO	1.1397	6.4×10^1
$t\bar{t}\gamma$	MadGraph + Pythia 8	LO	1.16	4.6
tW	MadGraph + Pythia 8	LO	1	2.9×10^{-1}
$tW\gamma$	MadGraph + Pythia 8	LO	1	1.2×10^{-1}
$tq\gamma$	MadGraph + Pythia 8	NLO	1	1.1×10^{-1}
WWγ				
$W(\rightarrow \ell\nu)W(\rightarrow \ell'\nu')\gamma$	Sherpa 2.2.11	$0j$ NLO, $1,2j$ LO	1	4.4×10^{-1}
WZγ				
$\ell\nu\ell'\ell'\gamma$	Sherpa 2.2.11	$0j$ NLO, $1,2j$ LO	1	9.2×10^{-3}
Diboson				
$\ell\nu\ell'\nu' + \ell\nu\ell'\ell' + \ell\ell\ell'\ell'$	Sherpa 2.2.2	$0,1j$ NLO, $2,3j$ LO	1	1.9×10^1
Diphoton				
$\gamma\gamma$	Sherpa 2.2.4	$0,1j$ NLO, $2,3j$ LO	1	3.0×10^2
W + jets				
$W(\rightarrow \ell\nu)$	Sherpa 2.2.11	$0,1,2j$ NLO, $3,4,5j$ LO	1	4.4×10^4
Z + jets				
$Z(\ell\ell)$	Sherpa 2.2.10	$0,1,2j$ NLO, $3,4,5j$ LO	1	4.7×10^3

Table 6.1: Summary of the simulation samples used in the analysis, including the name of the event generator(s), the number of additional jets (where j represents either a gluon or a quark) generated in the hard scatter, the matrix element calculation order in QCD vertices, the k -factor associated to the sample, and its cross section.

6.2 Background from Multiboson Production

The production of multiple bosons in proton-proton collisions can lead to final states similar to those expected from the $W\gamma\gamma$ signal process. These types of background events represent approximately 7% of events in the SR. One example of such a process is the production of a W boson in association with a Higgs boson, where the W boson decays leptonically and the Higgs boson decays to a pair of photons ($pp \rightarrow W(\rightarrow \ell\nu)H(\rightarrow \gamma\gamma)$). The two other multiboson production processes also considered are the $pp \rightarrow WW\gamma$ and $pp \rightarrow Z\gamma\gamma$ processes. Events from the $pp \rightarrow WW\gamma$ process contribute as background in the SR when one of the leptons from a W boson decay is not reconstructed due to detector acceptance or inefficiencies and a photon is radiated from one of the initial or final state particles. Events from the $pp \rightarrow Z\gamma\gamma$ process contribute when a lepton from the decay of the Z boson is not reconstructed. The simulation samples for these three processes (WH , $WW\gamma$ and $Z\gamma\gamma$) are used to estimate the irreducible background contributions from multiboson production in the SR.

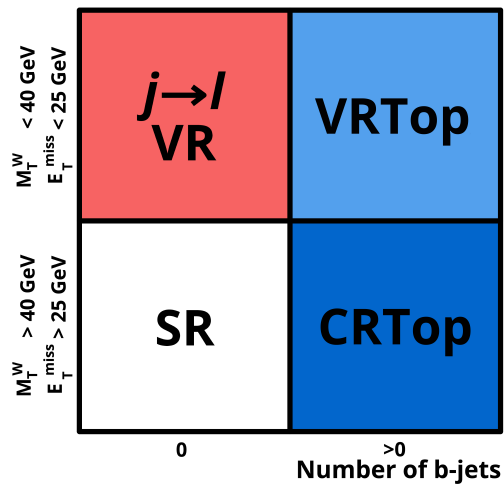
6.3 Background from Top Quark Production

The background from $t\bar{t}\gamma$, $tW\gamma$, and $tq\gamma$ events, referred to as the top quark background, represents approximately 3% of events in the SR. Since top quarks mostly decay to a W boson and a b -quark, these background events can mimic the signature of a $W\gamma\gamma$ event in the SR when additional photons are present in the final state due to initial or final state radiation. A significant fraction of these events is removed by requiring that events in the SR must not contain any b -tagged jet, as discussed in Section 5.4. The remaining contributions from background processes which include a top quark in their final state are estimated using simulated events. The $t\bar{t}\gamma$ contribution is normalized to data in a control region called CRTop to account for large uncertainties on the process's cross section. The

CRTop region is obtained by inverting the b -tagging requirement in the SR. A validation region, labelled VRTop, is formed by both requiring at least one b -tagged jet and inverting the $E_{\text{T}}^{\text{miss}}$ and m_{T}^W requirements of the SR definition. This VRTop region is used to validate the $t\bar{t}\gamma$ normalization obtained in CRTop. A schematic diagram of these regions of phase space in relation to the SR is shown in Figure 6.1. The normalization of the $t\bar{t}\gamma$ contribution in CRTop is left floating in the final fit used to extract the significance and fiducial cross section of the $W\gamma\gamma$ process in the SR as described in Section 8. The CRTop region is divided into three bins of leading photon p_{T} , while the VRTop region is made up of a single bin. The background from jets misidentified as photons ($j \rightarrow \gamma$) and electrons misidentified as photons ($e \rightarrow \gamma$) in the CRTop and VRTop regions are estimated using the data-driven methods described in Sections 6.4 and 6.5, respectively. The background from jets misidentified as leptons ($j \rightarrow \ell$) and the pileup background are found to be negligible in both of these regions. The remaining irreducible background contribution from multiboson processes in these two regions is estimated in simulation. The resulting estimated composition of the CRTop and VRTop regions is shown in Figure 6.2 prior to the $t\bar{t}\gamma$ event yield normalization to data in the CRTop region.

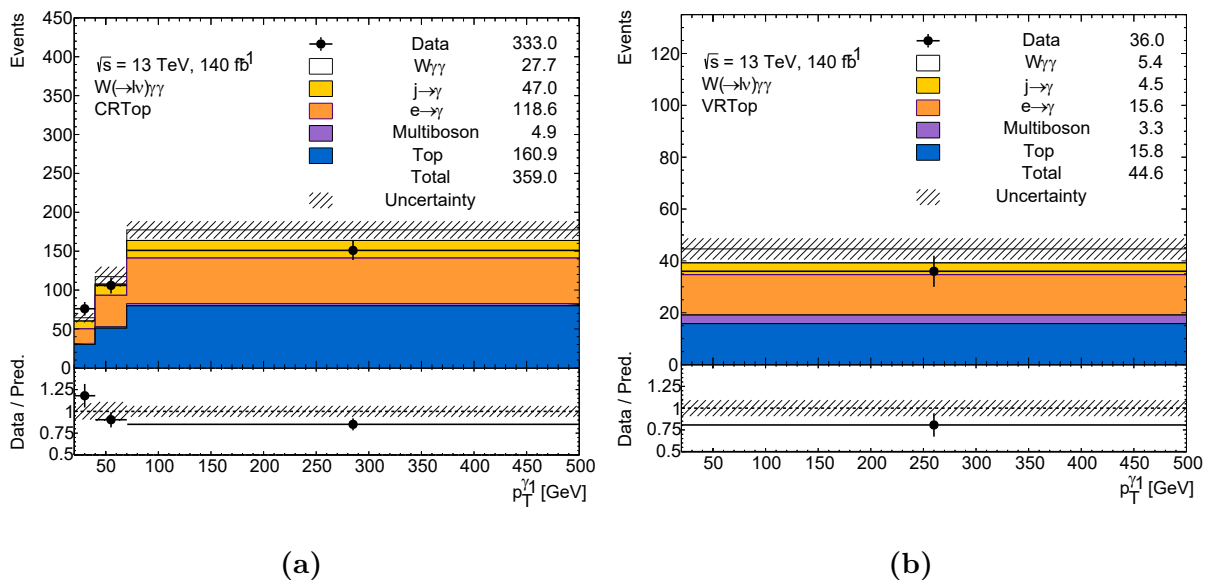
6.4 Background from Jets Misidentified as Photons

The background from hadronic jets and non-prompt photons from neutral hadron decays that are misidentified as prompt photons, called the $j \rightarrow \gamma$ background, represents the largest background in the SR. Despite the small jet misidentification rate, the large number of hadronic jets produced in collisions at the LHC results in this type of event making up a significant fraction of the total background in the SR. This background accounts for approximately 37% of events in the SR. Hadronic jets can be misidentified as photons when a jet deposits a large amount of its energy in the Electromagnetic Calorimeter and has no associated tracks in the Inner Detector due to detector inefficiencies and track mismatches.



(a)

Figure 6.1: Schematic diagram summarizing the CRTop and VRTop regions used to estimate and validate the $t\bar{t}\gamma$ normalization in relation to the Signal Region (SR) and the $j \rightarrow \ell$ Validation Region (VR).



(a)

(b)

Figure 6.2: Estimated composition of the CRTop and VRTop regions prior to the $t\bar{t}\gamma$ normalization to data in the CRTop region.

In addition, neutral hadrons such as π^0 and η mesons that are produced as part of the jet formation process can decay to photons. Though these photons are real, they do not originate directly from the hard scatter process. As such, they are referred to as non-prompt photons. Both of these types of background photons are usually surrounded by increased activity in the calorimeter and thus have different isolation energy distributions. These backgrounds are difficult to model in simulation due to the complexity of the hadronic jet interactions with the calorimeters and the large number of different processes that can contribute to the $j \rightarrow \gamma$ background. In addition, the low jet misidentification rate means that the number of events needed to be simulated in order to achieve a small enough statistical uncertainty is computationally prohibitive.

This background is estimated using a data-driven 2D template fit method based on the ones described in References [106] and [107]. The method relies on the difference between the isolation energy distributions of prompt photons and jets misidentified as photons ($j \rightarrow \gamma$). On average, given the additional hadronic activity surrounding jets misidentified as photons, these objects are expected to have larger values of isolation energy than prompt photons. Templates of isolation energy distributions for the leading and subleading prompt photons and leading and subleading $j \rightarrow \gamma$ fakes are constructed from fits in control regions that either enhance or suppress the contribution of the $j \rightarrow \gamma$ background. These control regions define different regions of phase space where either the leading, subleading, or both reconstructed photons are more likely to come from a jet misidentified as a photon. These three possible categories of events are symbolically referred to as γj , $j\gamma$, and jj events. A two-dimensional fit of the normalization of the isolation energy templates in data is performed in an extended SR to extract the number of $\gamma\gamma$, γj , $j\gamma$, and jj events in the SR.

Before discussing the details of the 2D template fit method, a simpler use of this method for estimating the background from jets misidentified as photons in events containing only one photon is first presented. In this case, the method proceeds by first constructing a phase space enhanced in jets misidentified as photons. This is achieved by selecting events

where the *Tight* photon identification working point is replaced by one of the *LoosePrime* (LP) working points described in Section 5.3.2. The photon isolation energy requirement is also removed to have access to the full distribution and its discrimination power. This control region with enhanced contributions from jets misidentified as photons is called CR_j . A template of the isolation energy distribution from jets misidentified as photons is obtained by fitting a Bukin function [108] to data in the CR_j region. This normalized template shape is referred to symbolically as $F_{L'}$, where the subscript L' refers to the *LoosePrime* photon identification working point used to define the CR_j region. The second template that is required is a normalized function describing the isolation energy distribution of prompt photons. Since the kinematic properties of prompt photons are well-modelled in simulation, simulated event samples are used to construct the prompt photon template. The prompt photon template, F_T , is obtained from simulated events satisfying the SR selection without the requirement on the photon isolation energy. This control region is called CR_γ . The isolation energy distribution of simulated prompt photons in CR_γ is fit to a double-sided Crystal Ball function [109] in order to obtain the normalized prompt photon template F_T . The isolation energy distribution of data events in CR_γ is then described as the sum of the normalized template shapes $F_{L'}$ and F_T , with associated normalization factors $w_{L'}$ and w_T determined by a fit to data in CR_γ . Figure 6.3 illustrates this step using toy data events generated from the sampling of the isolation energy distributions of simulated events. The normalization factors $w_{L'}$ and w_T provide an estimate of the number of jets misidentified as photons and the number of prompt photons, respectively, in the CR_γ region. The number of background events in the SR originating from jets misidentified as photons is obtained by integrating its isolation energy distribution $w_{L'}F_{L'}$ from $E_T^{\text{iso}} = -\infty$ to 2.45 GeV to recreate the isolation energy requirement of the SR. Finally, the impact on the estimated number of $j \rightarrow \gamma$ fakes from prompt photon leakage into the CR_j region used to construct the template shape of jets misidentified as photons is estimated using simulated events and corrected.

A conceptually analogous 2D template fit method is used to estimate the number of jets

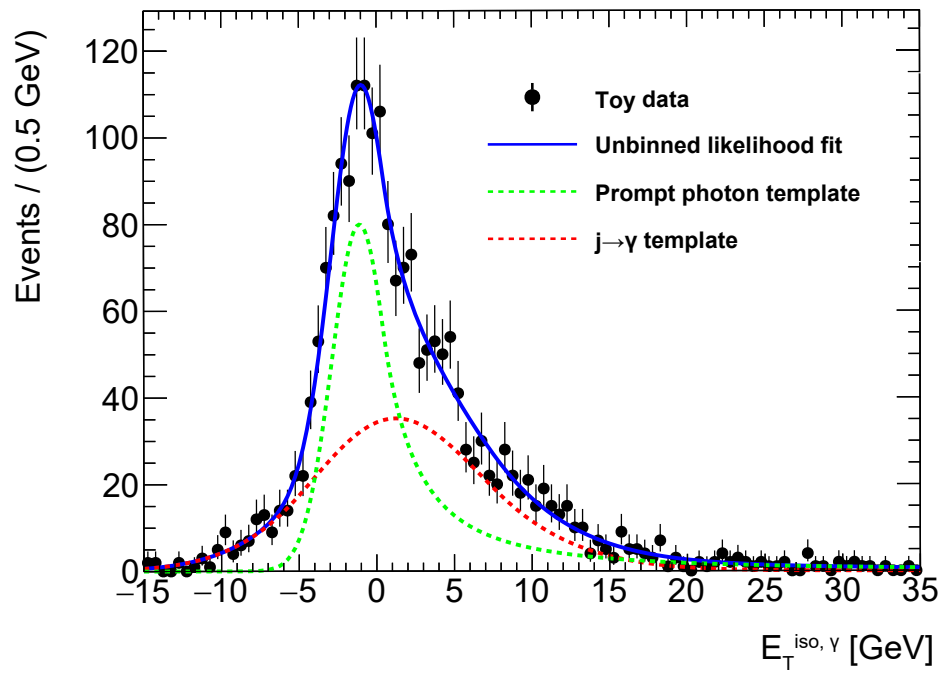


Figure 6.3: Example of a 1D template fit to toy data of the isolation energy (E_T^{iso}) distributions of prompt photons and jets misidentified as photons ($j \rightarrow \gamma$) in an extended Signal Region called $\text{CR}\gamma$. The toy data is generated by sampling distributions from simulated events.

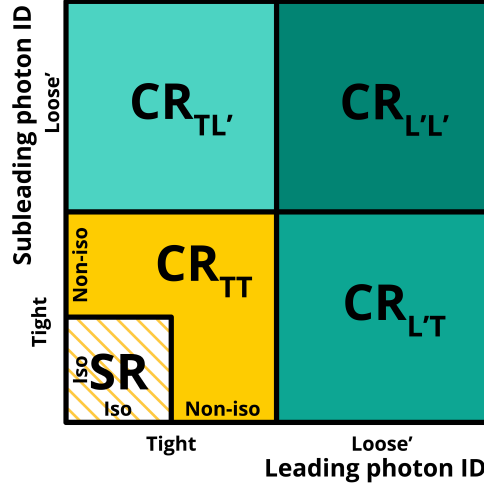


Figure 6.4: Schematic diagram of the control regions and their relation to the Signal Region (SR) used to fit the 2D template parameters in the $j \rightarrow \gamma$ background estimate. They are obtained by inverting the leading and subleading photon identification (ID) requirements and removing all photon isolation energy requirements.

misidentified as photons in the $W\gamma\gamma$ SR. The template fit method is extended to two dimensions in order to account for differences in isolation energy distributions between the leading and subleading photons, and to account for the different possible background contributions where only the leading photon, the subleading photon, or both photons are jets misidentified as photon. To achieve this, four orthogonal regions of phase space are defined based on the photon identification working points satisfied by the leading and subleading photons, and by removing the isolation energy requirement for all photons. A schematic diagram of these control regions and their relation to the SR is shown in Figure 6.4. Events belonging to control regions CR_{TT} , $CR_{TL'}$, $CR_{L'T}$, and $CR_{L'L'}$ are used to construct the normalized 2D isolation energy templates F_{TT} , F'_{TL} , $F_{L'T}$, and $F_{L'L'}$, respectively, where the subscript refers to the combination of photon identification working points satisfied by the leading photon and subleading photons.

Using simulated event samples it was found that the correlation between the isolation

energy distributions of the leading and subleading photons is below 10% in CR_{TT} , $CR_{TL'}$, and $CR_{L'T}$. As a result, the 2D isolation energy distribution templates for events belonging to each of these three control regions were constructed from the multiplication of the 1D distributions associated with the leading and subleading photon, i.e.:

$$\begin{aligned} CR_{TT} : F_{TT} &= F_{T_1} \times F_{T_2} \\ CR_{TL'} : F_{TL'} &= F_{T_1} \times F_{L'_2} \\ CR_{L'T} : F_{L'T} &= F_{L'_1} \times F_{T_2}, \end{aligned} \tag{6.1}$$

where F_{i_1} and F_{i_2} are the normalized templates for the leading and subleading photons, respectively, and i refers to either the *Tight* or *LoosePrime* photon isolation working points.

The F_{T_1} and F_{T_2} 1D templates are obtained by fitting a Bukin function to the isolation energy distributions of simulated $W\gamma\gamma$ signal events in the CR_{TT} region. The $F_{L'_1}$ and $F_{L'_2}$ 1D templates are obtained by fitting a double-sided Crystal Ball function to data in the $CR_{L'T}$ and $CR_{TL'}$ regions, respectively. All four 1D fits used to obtain the F_{T_1} , F_{T_2} , $F_{L'_1}$, and $F_{L'_2}$ 1D templates are shown in Figure 6.5.

Events belonging to the $CR_{L'L'}$ control region primarily originate from the production of a W boson accompanied by two or more jets. In this region of phase space, simulated events show a significant correlation between the leading and subleading photon isolation energy distributions of approximately 45%. This prevents the construction of a 2D template shape from the simple multiplication of two 1D templates. Instead, the $F_{L'L'}$ 2D template is directly obtained from a 2D fit to data in the $CR_{L'L'}$ region using an adaptive kernel density estimate [110] whereby each input data point is modelled by a Gaussian kernel. This properly accounts for correlations between the reconstructed leading and subleading photon isolation energy distributions.

All four 2D templates (F_{TT} , $F_{TL'}$, $F_{L'T}$, and $F_{L'L'}$) are shown in Figure 6.6. The 2D function describing the leading vs subleading photons isolation energy distribution in the

CR_{TT} region is then given by the sum of these four normalized 2D templates:

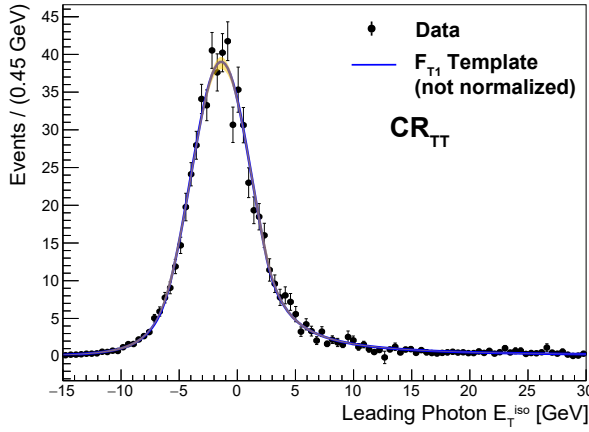
$$w_{tot} F_{tot} = w_{TT} F_{TT} + w_{TL'} F_{TL'} + w_{L'T} F_{L'T} + w_{L'L'} F_{L'L'}, \quad (6.2)$$

where w_{TT} , $w_{TL'}$, $w_{L'T}$, and $w_{L'L'}$ represent overall normalization factors for each of the four 2D templates. Values for the normalization factors are determined from an extended maximum likelihood fit to data in the CR_{TT} region. In the fitting procedure, all template parameters are allowed to float within the constraints provided by the statistical covariance matrices obtained when constructing the templates.

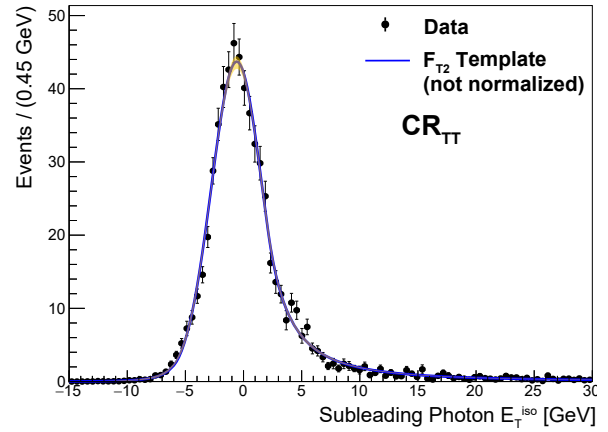
The statistical uncertainty on the fraction of events from prompt photons in the *LoosePrime* control regions is accounted for in the final estimate. In addition, a systematic uncertainty associated with the choice of *LoosePrime* working point is assigned by considering the template fit parameters for the LP2 and LP5 working points as 1σ up and down variations on the nominal fit parameters obtained using the LP4 photon identification working point. Since the $F_{L'_1}$ and $F_{L'_2}$ templates each have 4 parameters, the uncertainties on their combined parameters is given by an 8×8 covariance matrix. This covariance matrix includes both the statistical uncertainties on the parameters from their fits in the $\text{CR}_{L'T}$ and $\text{CR}_{TL'}$ regions and the additional uncertainties associated to the choice of LP working point. This covariance matrix is used to implement a multivariate Gaussian constraint on the 8 template parameters in the final 2D fit to data in the CR_{TT} region.

The 1D projections of the final 2D fits in the CR_{TT} region are shown in Figure 6.7. The final number of $j \rightarrow \gamma$ background events in the SR is obtained by integrating the 2D fitted functions describing the leading and subleading photon isolation energy from $E_T^{\text{iso}} = -\infty$ to 2.45 GeV. This is done to recreate the isolation energy requirement of the SR on both photons.

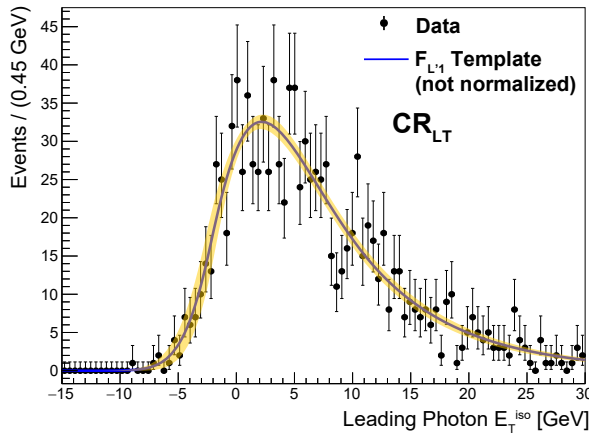
The estimated number of $j \rightarrow \ell$ background events is then corrected for the leakage of prompt photons into the $\text{CR}_{TL'}$, $\text{CR}_{L'T}$, and $\text{CR}_{L'L'}$ regions used to construct the $F_{TL'}$, $F_{L'T}$,



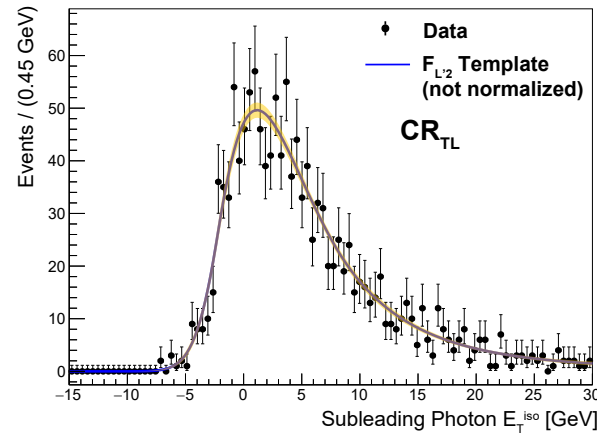
(a)



(b)



(c)



(d)

Figure 6.5: One-dimensional fits to the photon isolation energy distributions defining the (a) F_{T_1} , (b) F_{T_2} , (c) $F_{L'_1}$, and (d) $F_{L'_2}$ templates.

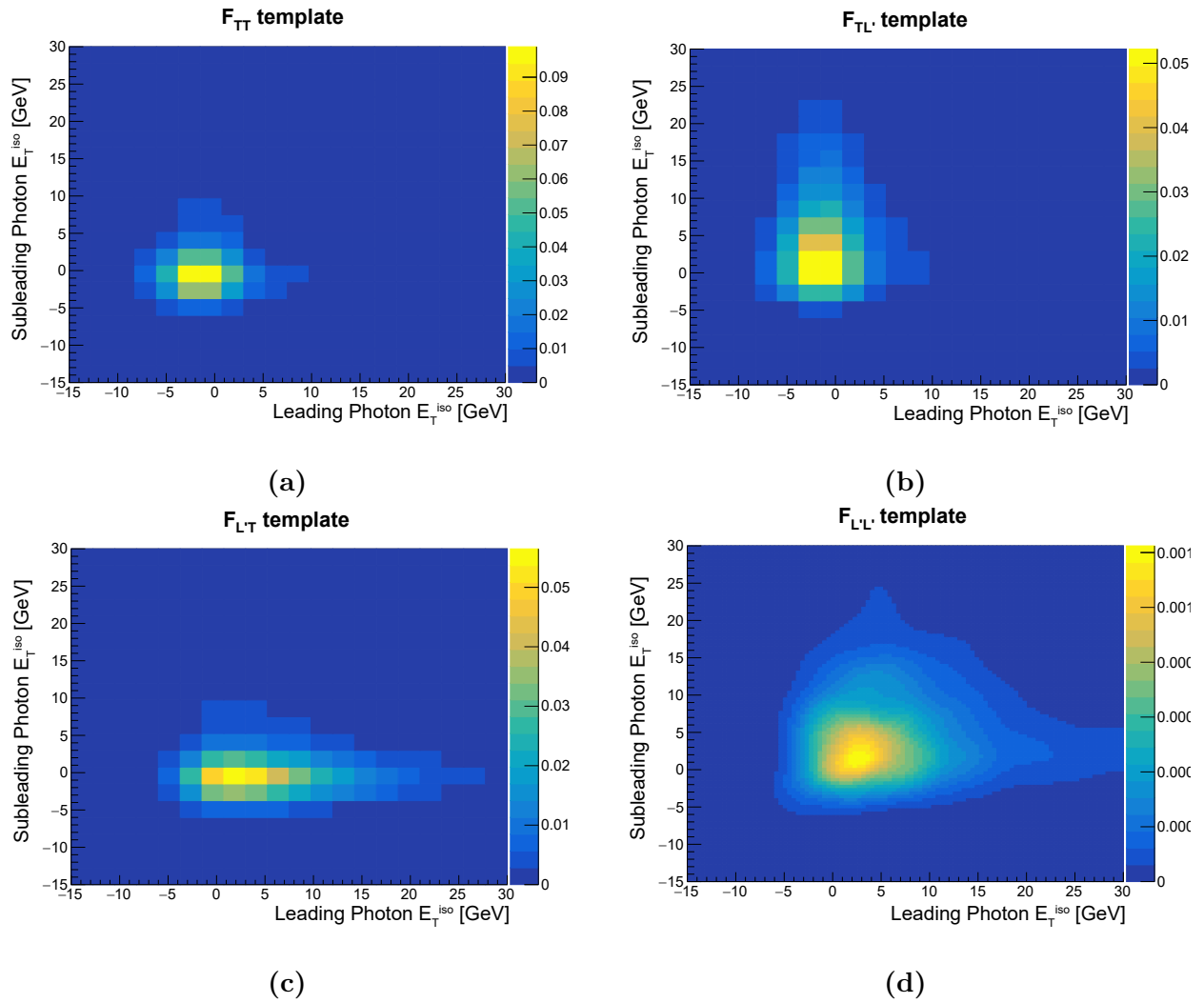


Figure 6.6: Two-dimensional photon isolation energy distributions of the (a) F_{TT} , (b) F_{TL} , (c) F_{LT} , and (d) F_{LL} templates.

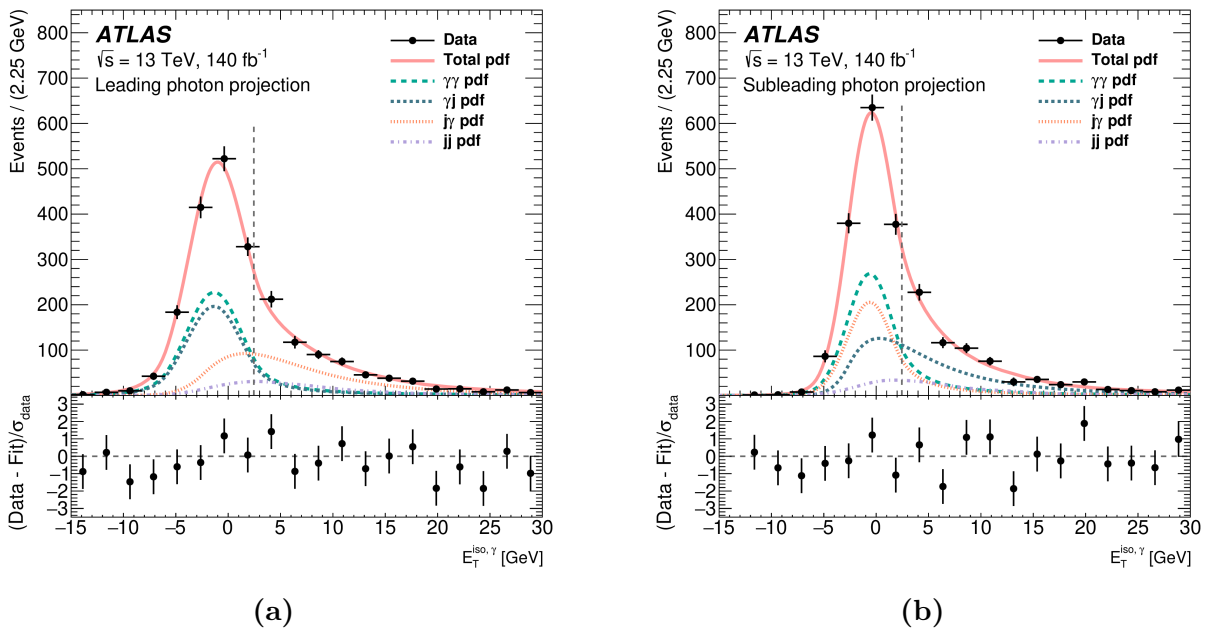


Figure 6.7: One-dimensional projections of the (a) leading and (b) subleading photon isolation energy distributions from the 2D template fit in the CR_{TT} region. The $\gamma\gamma$, $j\gamma$, γj , and jj pdf labels correspond to the weighted isolation energy templates. Error bars indicate the statistical uncertainty on the number of events in data.

and $F_{L'L'}$ templates. Truth information from simulated $W\gamma\gamma$ and $W\gamma + jets$ events is used to estimate the fraction of events originating from prompt photons in each of these control regions. The resulting leakage fractions are applied to the fitted normalization factors to obtain the corrected number of $\gamma\gamma$, γj , $j\gamma$, and jj events.

Since the uncertainty on the fitted normalization factors w_{TT} , $w_{TL'}$, $w_{L'T}$, and $w_{L'L'}$ are correlated, the final statistical uncertainty on the number of $j \rightarrow \gamma$ background events is obtained from the standard deviation of 10,000 trials generated from the sampling of the covariance matrix of the final 2D fit, the integration of the resulting functions, and the application of the signal leakage correction factors. The resulting total number of background events in the SR with at least one photon originating from a jet misidentified as a photon is 420 ± 48 .

An uncertainty due to the choice of adaptive kernel parameter, or bandwidth parameter, of $h = 1.4$ [110] was estimated by varying its value by $\pm 25\%$. This variation was found to have a negligible impact on the estimated number of $j \rightarrow \gamma$ background events. The experimental uncertainties described in Section 7 on the simulation samples used to obtain the F_{T_1} and F_{T_2} prompt photon isolation energy templates are also found to have a negligible impact on the number of estimated $j \rightarrow \gamma$ background events. Finally, the impact of the number of electrons misidentified as photons on the $j \rightarrow \gamma$ estimate was also studied. The $e \rightarrow \gamma$ background estimation method described in Section 6.5 was used in CR_{TT} . The resulting number of $e \rightarrow \gamma$ background events was subtracted from data before applying the 2D template fit method. The resulting impact on the $j \rightarrow \gamma$ estimate was found to be negligible, most likely due to the similarities between the electron and photon isolation energy distributions.

The 2D template fit estimate was done in two additional regions of phase space, the CRTop and VRTop regions. As described in Section 6.3, these regions are used to estimate and validate the background from processes resulting in the production of a top quark. The number of $j \rightarrow \gamma$ background events is estimated differentially in three bins of leading photon

p_T in the CRTop region, and in a single bin in the VRTop region. In these two regions, the smaller number of events in data required that a different approach be used to estimate the systematic uncertainty associated with the choice of the LP4 photon identification working point. The systematic uncertainty on the estimated number of $j \rightarrow \gamma$ background events in the CRTop and VRTop regions was taken as the difference in the estimated $j \rightarrow \gamma$ background yields in the SR obtained when using the LP2 and LP5 working points. This approach results in an overall systematic uncertainty of +18% and -13% on the estimated $j \rightarrow \gamma$ contributions in the CRTop and VRTop regions. The estimated $j \rightarrow \gamma$ background in the CRTop and VRTop regions are shown in Figure 6.2.

6.5 Background from Electrons Misidentified as Photons

The background from events containing an electron misidentified as a photon, also called the $e \rightarrow \gamma$ background, represents a large fraction of the background in the SR. It is comparable to the contribution from the $j \rightarrow \gamma$ background in the electron channel, and represents approximately 14% of events in the combined electron and muon channels of the SR. This source of background originates primarily from inefficiencies in track reconstruction and track matching to energy clusters in the Electromagnetic Calorimeter. Background events from electrons misidentified as photons primarily originate from $Z(\rightarrow ee)\gamma$ events in which one of the electrons from the Z boson decay is misidentified as a photon. The cuts developed for the $Z\gamma$ veto described in Section 5.4 are designed to significantly reduce this background, yet a relatively small amount of $e \rightarrow \gamma$ background events still contaminate the SR. Inverting the $Z\gamma$ veto cuts produces a region dominated by $e \rightarrow \gamma$ background events. In this region, the kinematic distributions of simulated events were found to significantly differ from data. In addition, the simulated estimates of the

$e \rightarrow \gamma$ background have large theoretical uncertainties (described in Section 7.2), reaching up to 50% in the SR. Therefore, a data-driven fake factor method is developed to estimate the background from electrons misidentified as photons.

6.5.1 Fake Factor Method

The data driven method used to estimate the $e \rightarrow \gamma$ fake contribution in the SR is based on a fake factor method described in Reference [75]. The method consists in measuring the electron to photon misidentification (or fake) rate in data and applying it to events in a CR analogous to the SR where one of the two selected photons is instead required to be an electron. The fake rate measurement requires the construction of two additional CRs, one enriched in prompt electrons and one enriched in electrons misidentified as photons. The fake rate is given by

$$F_{e \rightarrow \gamma} = \frac{N_{\gamma}^{\text{reco}} \epsilon_{\gamma}}{N_e^{\text{reco}} \epsilon_e} \quad (6.3)$$

where N_{γ}^{reco} and N_e^{reco} are the number of events in the regions of phase space enriched with electrons misidentified as photons and prompt electrons, respectively, and ϵ_{γ} and ϵ_e are the combined trigger, reconstruction, identification, and isolation efficiencies for the reconstructed electrons and photons in these regions, respectively. The $e \rightarrow \gamma$ fake rate is then applied to events in a control region where the SR selection is changed by replacing one of the reconstructed photons by an electron with similar p_T , isolation, and identification requirements.

Given that the $e \rightarrow \gamma$ fake rate depends on both the photon and electron efficiencies, the trigger and selection requirements used to define the electrons in the control regions used to calculate the $e \rightarrow \gamma$ fake rate must be identical to those used in the control region in which the fake rate is applied. Furthermore, the photon selection used to define the photon in the $e \rightarrow \gamma$ fake rate estimation region, the photon in the $e \rightarrow \gamma$ fake rate application region, and

the photons in the SR must match. The different control regions used in the estimate of the $e \rightarrow \gamma$ background are described in the following subsections.

6.5.2 Fake Rate Estimate

The $e \rightarrow \gamma$ fake rate is estimated using a so-called *tag and probe* method. This data-driven method is used to measure efficiencies based on the decay of known particle resonances. From this pair of decay products, one object is labelled as the *tag* and the other as the *probe*. The *tag* object is required to pass a more stringent set of requirements while the *probe* is selected using a less restrictive set of requirements. The *probe* objects are then used to estimate a selection efficiency.

The $e \rightarrow \gamma$ fake rate is estimated using $pp \rightarrow Z(\rightarrow ee)$ events. These events are selected by requiring either two reconstructed electrons or one reconstructed electron and one reconstructed photon with an invariant mass near the Z boson mass, around 91.2 GeV [8]. These two requirements form the $CRee$ and $CRe\gamma$ control regions. The $CRee$ region provides a high purity sample of prompt electrons while the $CRe\gamma$ control region provides a high purity sample of electrons misidentified as photons due to the large likelihood that the photon is a misidentified electron. These regions can then be used to estimate the $e \rightarrow \gamma$ fake rate. In both cases, a *tag* electron is required to satisfy and match to a single lepton trigger and have $p_T > 27.3$ GeV to ensure the full trigger efficiency. Events are then required to have one reconstructed *probe* object, either a reconstructed electron in $CRee$ or a reconstructed photon in $CRe\gamma$. In both regions, the identification working point for electrons is changed from *Medium* to *Tight* to match the single electron trigger identification requirement. The requirements for the *tag* and *probe* objects in both control regions is summarized in Table 6.2. Events are rejected if they contain an additional reconstructed *Baseline* electron or *Baseline* photon (as defined in Section 5.3) in order to avoid the ambiguity of which two objects originate from the Z boson decay and avoid

	CRee	CRe γ
<i>Tag</i>	<u>Electron</u> $p_T > 27.3$ GeV <i>Tight</i> Identification <i>Tight</i> Isolation $z_0 < 0.5$ & $ \sigma_{d_0} < 5$ $ \eta < 2.47$, excluding $1.37 < \eta < 1.52$ Matched to trigger electron	
<i>Probe</i>	<u>Electron</u> $p_T > 20$ GeV <i>Tight</i> Identification <i>Tight</i> Isolation $z_0 < 0.5$ & $ \sigma_{d_0} < 5$ $ \eta < 2.47$, excluding $1.37 < \eta < 1.52$ Matched to trigger electron	<u>Photon</u> $p_T > 20$ GeV <i>Tight</i> Identification <i>Calorimeter-Only Tight</i> Isolation $ \eta < 2.37$, excluding $1.37 < \eta < 1.52$ Matched to trigger photon
Event	One <i>tag</i> and one <i>probe</i> No additional <i>Baseline</i> leptons or photons Standard overlap removal	

Table 6.2: Table summarizing the object selection used to define the CRee and CRe γ control regions used to calculate the $e \rightarrow \gamma$ fake rate.

overlap with the control regions in which the $e \rightarrow \gamma$ fake rate is applied.

Events in the CRee and CRe γ control regions are further binned as a function of the *probe* object's p_T and $|\eta|$. This is done in order to account for detector effects and object kinematics in the $e \rightarrow \gamma$ fake rate. In each p_T and $|\eta|$ bin, a fit to the invariant mass distribution of the *tag* and *probe* is performed to estimate the number of events from Z boson decays. A Gaussian with a double-sided exponential [109] is used to describe the Z boson resonance while the contribution from other background processes is modeled by an exponential function. Examples of fitted distributions in CRee and CRe γ are shown in Figures 6.8 and 6.9, respectively.

In the CRee region, for events in which both reconstructed electrons satisfy both the *tag* and the *probe* criteria, both of the permutations of *tag* and *probe* electrons contribute to the $e \rightarrow \gamma$ fake rate calculation. Thus, each permutation is considered separately and both contribute the denominator of the $e \rightarrow \gamma$ fake rate calculation.

The number of events used to estimate the $e \rightarrow \gamma$ fake rate are obtained by integrating the

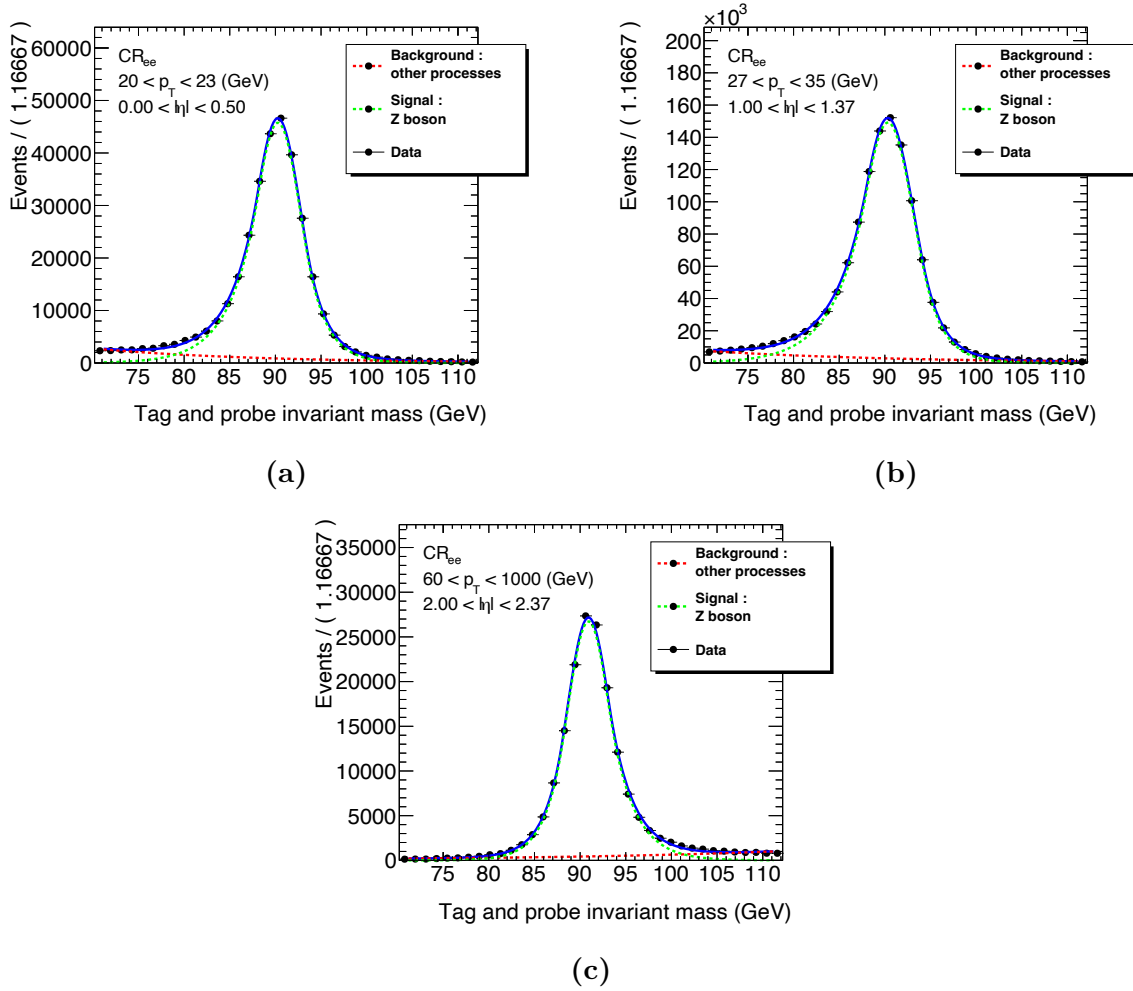


Figure 6.8: Distributions of the reconstructed invariant mass of the *tag* and *probe* electrons in three representative bins of the *probe* electron's p_T and $|\eta|$ in the CR_{ee} control region.

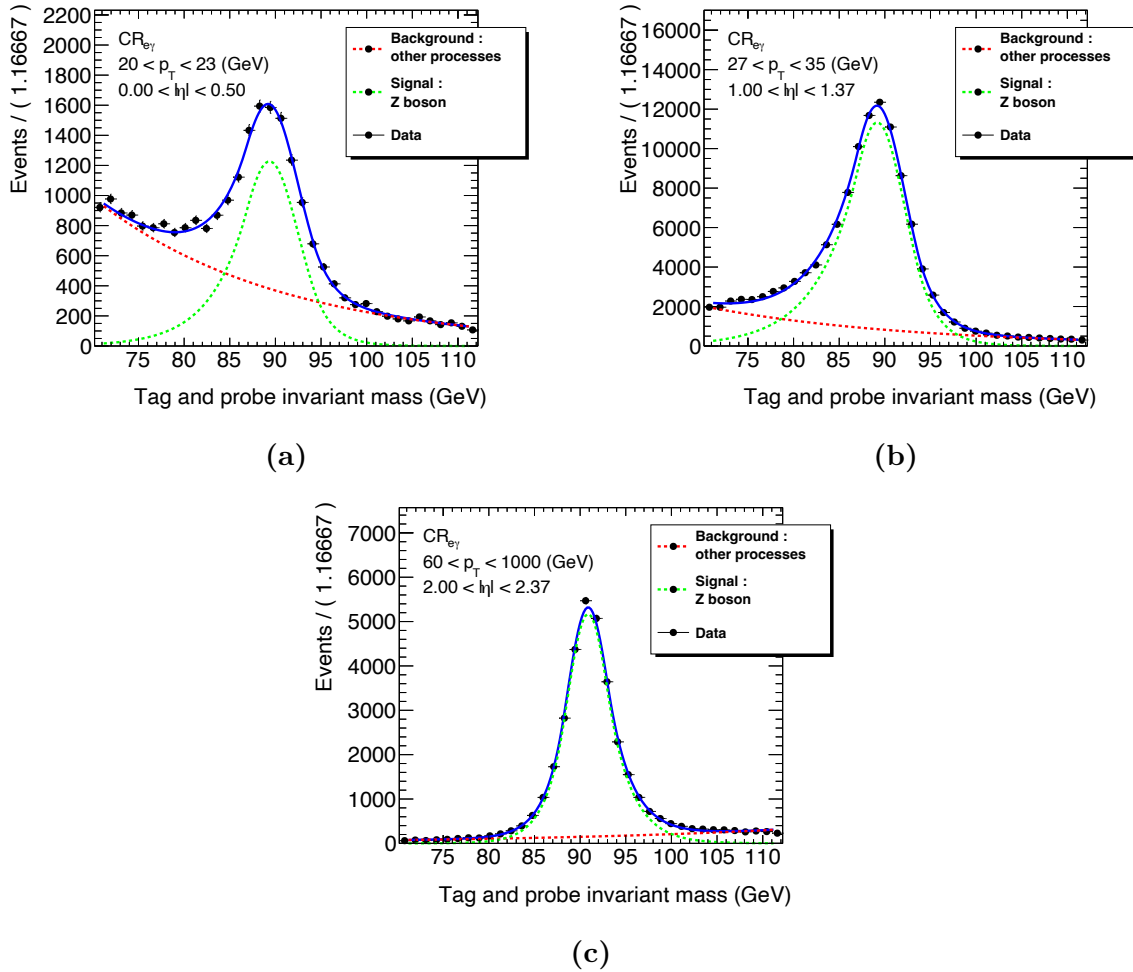


Figure 6.9: Distributions of the reconstructed invariant mass of the *tag* electron and *probe* photon in three representative bins of the *probe* photon's p_T and $|\eta|$ in the $CR_{e\gamma}$ control region.

fitted Z boson resonance function in a 10 GeV window around the Z mass with background from other processes subtracted. As shown schematically in Figure 6.10, the number of Z boson events in the CRee and $\text{CRe}\gamma$ control regions are used to construct the H_e and H_γ 2D histograms, respectively. The $e \rightarrow \gamma$ fake rate as a function of the *probe* object's p_T and $|\eta|$ is obtained by dividing the two histograms, $F_{e \rightarrow \gamma} = H_\gamma/H_e$. The final $e \rightarrow \gamma$ fake rate as a function of p_T and $|\eta|$ is shown in Figure 6.11 with statistical uncertainties from the fits.

6.5.3 Fake Rate Application

The number of background events in the SR from events in which an electron is misidentified as a photon is estimated by applying the measured $e \rightarrow \gamma$ fake rate to events belonging to a control region analogous to the SR but with one of the photons replaced with an electron. This additional electron is required to satisfy the same requirements as the *probe* electron in CRee shown in Table 6.2. In order to separately estimate the number of $e \rightarrow \gamma$ events in the electron and muon channels of the SR, two control regions are formed. The application region for the electron channel selects for two reconstructed electrons and one reconstructed photon, forming the $\text{CRee}\gamma$ region. The application region for the muon channel selects for a muon, an electron, and a photon, forming the $\text{CR}\mu e\gamma$ region. A schematic diagram of these fake rate application regions in relation to the SR is shown in Figure 6.12.

To estimate the number of $e \rightarrow \gamma$ events in the muon channel of the SR, events in the $\text{CR}\mu e\gamma$ region are weighted by the *probe* electron's corresponding $e \rightarrow \gamma$ fake rate according to its p_T and $|\eta|$.

Estimating the number of $e \rightarrow \gamma$ events in the electron channel of the SR requires some additional care. Some events in $\text{CRee}\gamma$ can have both electrons simultaneously satisfy the *Signal* and *probe* electron object definitions. In these events, two possible permutations must be considered, one in which the leading electron is the *probe* and one in which the subleading electron is the *probe*. Since both cannot be simultaneously misidentified as a photon, the

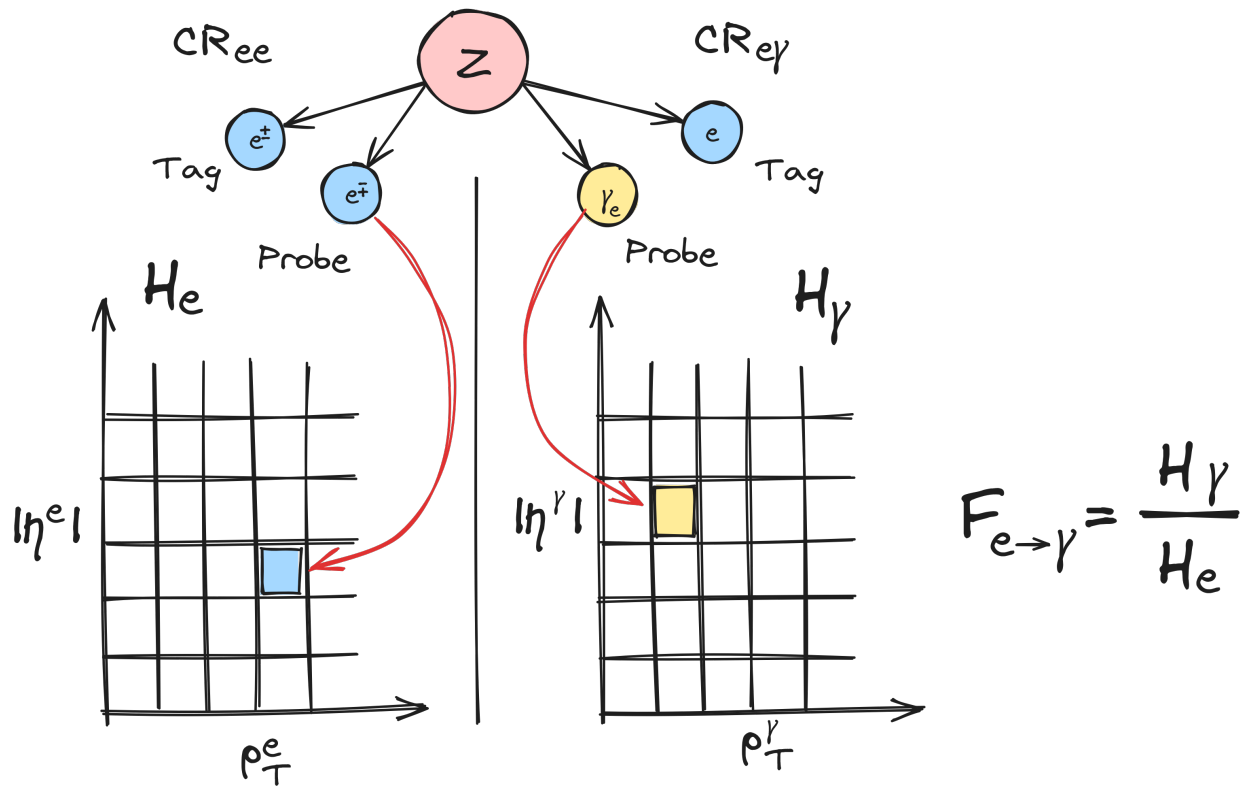


Figure 6.10: Schematic diagram describing the use of the *tag and probe* method to calculate the fraction of electrons misidentified as photons, $F_{e \rightarrow \gamma}$, as a function of the object transverse momentum and pseudorapidity. The $F_{e \rightarrow \gamma}$ fake rate is obtained by dividing the 2D histograms of the number of electrons misidentified as photons (H_γ) by the number of correctly identified electrons (H_e).

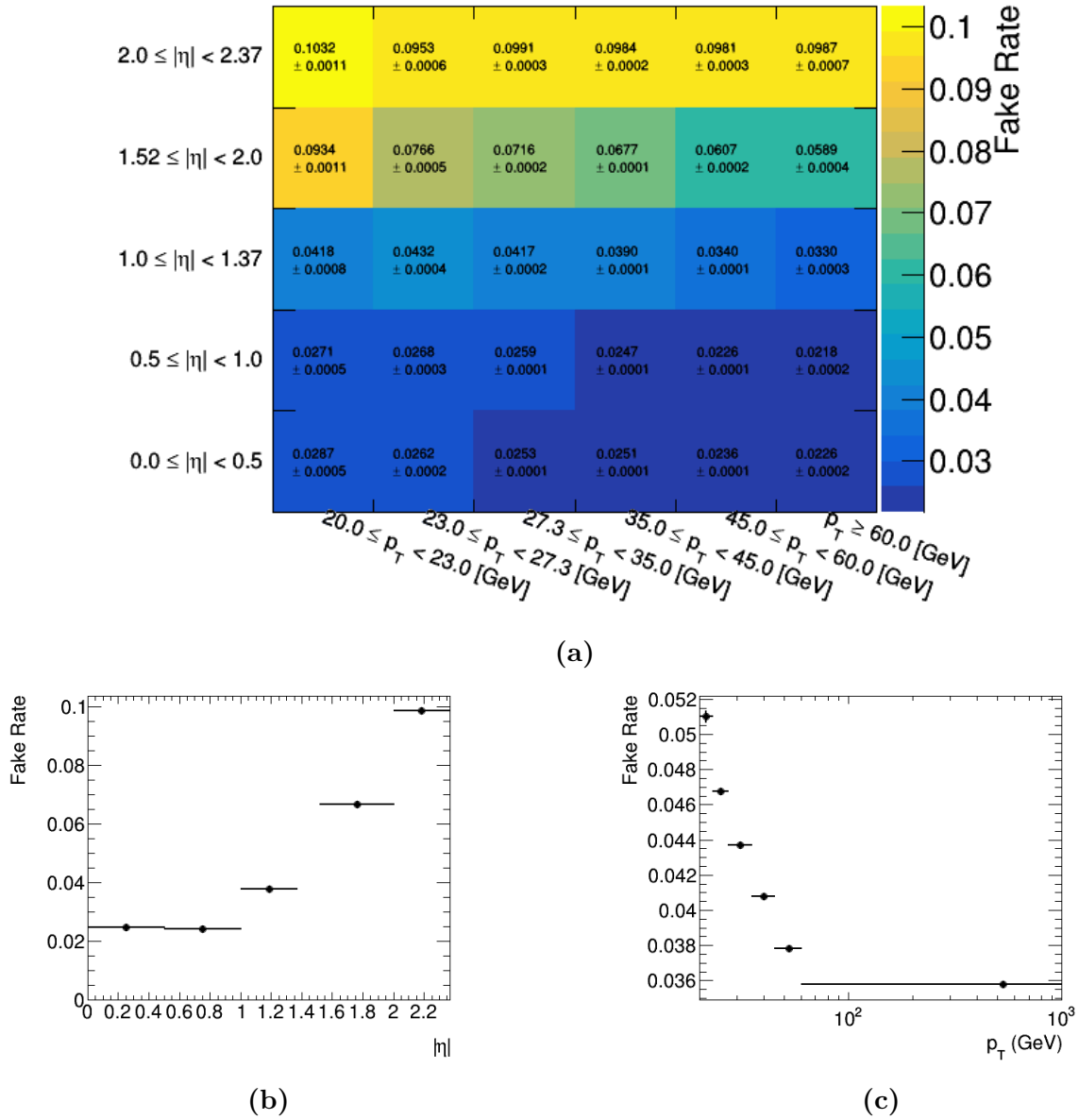
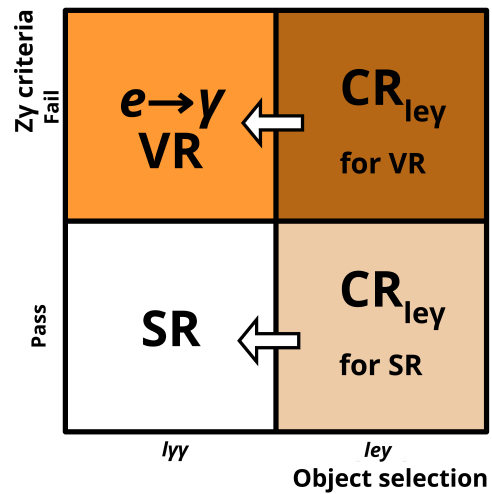


Figure 6.11: Nominal $e \rightarrow \gamma$ fake rate with statistical uncertainties as a function of p_T and $|\eta|$ in 2D and projected onto either axis.



(a)

Figure 6.12: Schematic diagram summarizing the $e \rightarrow \gamma$ background estimate's validation region (VR) in relation to the Signal Region (SR). Also shown is their respective $e \rightarrow \gamma$ fake rate application regions where one of the required photons from the $l\gamma\gamma$ selection in the signal and validation regions is substituted for an electron, creating an $le\gamma$ selection.

total probability for the event to contribute to the $e \rightarrow \gamma$ background is given by a logical exclusive *or* of the probabilities that each electron is separately misidentified as a photon.

To do this, the $e \rightarrow \gamma$ fake rate for each electron is converted to an efficiency using the relation:

$$\epsilon_i = \frac{F_i}{1 + F_i}, \quad (6.4)$$

where ϵ_i is the fake efficiency for electron i and F_i is its fake rate. The combined efficiency, accounting for either electron being misidentified as a photon in an event but not both simultaneously, is then:

$$\epsilon_{tot} = \epsilon_1 + \epsilon_2 - 2\epsilon_1\epsilon_2. \quad (6.5)$$

The total efficiency is then converted back to a fake rate using the relation:

$$F_{tot} = \frac{\epsilon_{tot}}{1 - \epsilon_{tot}}. \quad (6.6)$$

Any correlation between the two electron fake rates is neglected. Every event i in $CR_{ee\gamma}$ is given an event weight w_{ij} for each possible permutation j of the two electrons:

$$w_{ij} = \frac{F_{ij}}{\sum_j F_{ij}} F_i, \quad (6.7)$$

where F_i is the total fake rate of event i and F_{ij} is the fake rate associated to each possible permutation j of the two electrons in the event.

6.5.4 Validation

The validation of the $e \rightarrow \gamma$ fake factor method is done in two control regions enhanced in $e \rightarrow \gamma$ background events. The first is obtained by inverting the SR's $Z\gamma$ veto cuts which are designed to reduce the $e \rightarrow \gamma$ background in the SR. This region is called the $Z\gamma$ veto

region at high E_T^{miss} . To further reduce the contribution from events with a W boson, in addition to inverting the $Z\gamma$ veto cuts, both the m_T^W and E_T^{miss} cuts in the SR are inverted to form the $Z\gamma$ veto region at low E_T^{miss} . Figure 6.13 shows the truth-matched type of the reconstructed photon pair in simulation samples for the electron channels of the SR and the $Z\gamma$ regions at low and high E_T^{miss} .

Fake rate application regions for both $Z\gamma$ validation regions are formed in an analogous way to the SR's $\text{CR}e\gamma$ and $\text{CR}\mu e\gamma$ application regions. An estimate for the number of $e \rightarrow \gamma$ background events in the $Z\gamma$ validation regions is obtained by applying the $e \rightarrow \gamma$ fake rate to events in their respective application region. A schematic diagram of the $Z\gamma$ high E_T^{miss} validation region and its $e \rightarrow \gamma$ fake rate application region with respect to the SR and its application region is shown in Figure 6.12.

In order to validate the method, the $e \rightarrow \gamma$ estimates in each $Z\gamma$ validation region are added to the simulated estimates from other processes and compared to data. Events with two prompt photons are estimated directly from simulation. Background events from jets misidentified as photon are estimated using truth-matched simulated events which are then corrected using a scale factor. The scale factor is derived from the $j \rightarrow \gamma$ 2D template fit estimate in the SR (described in Section 6.4) divided by the $j \rightarrow \gamma$ estimate from truth-match simulated events in the SR. In the $j \rightarrow \gamma$ simulated events, events in which one reconstructed photon is a misidentified electron and one reconstructed photon is a misidentified jet are vetoed to avoid double counting with the $e \rightarrow \gamma$ fake factor estimate. Accounting for statistical uncertainties on the simulated $e \rightarrow \gamma$ events and statistical and systematic uncertainties on the $j \rightarrow \gamma$ estimate from the 2D template fit method, the scale factor on simulated $j \rightarrow \gamma$ events in the $Z\gamma$ validation regions is 2.5 ± 0.5 .

The differential validation of the $e \rightarrow \gamma$ estimate in leading photon p_T is shown in Figures 6.14 and 6.15 for the electron channels of the $Z\gamma$ veto region at high and low E_T^{miss} , respectively. The predicted leading photon p_T distributions are in good agreement with data in both validation regions. Table 6.3 shows the total estimated number of events in

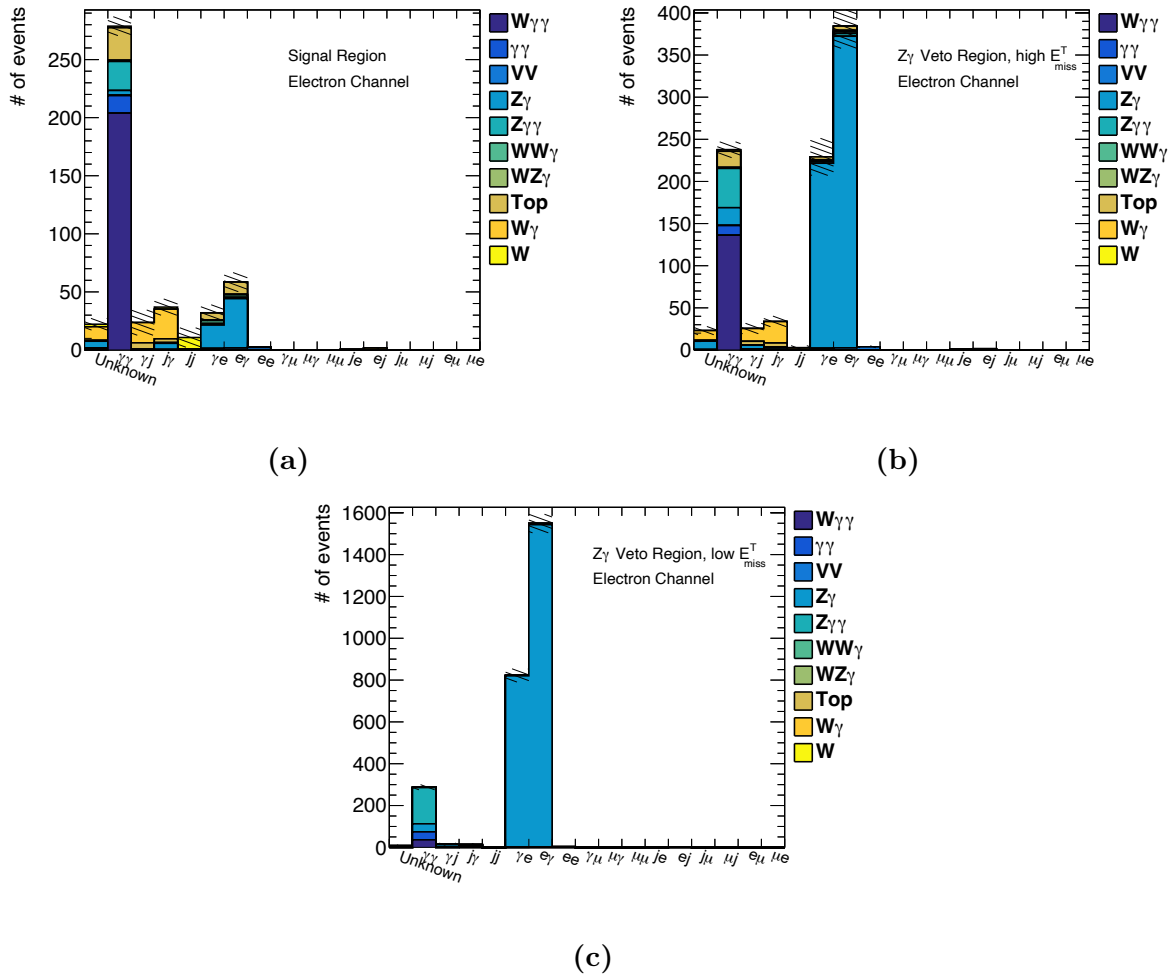


Figure 6.13: Truth-matched types of the reconstructed photon pair in the electron channel of (a) the $Z\gamma$ Veto Region at High E_T^{miss} , (b) the $Z\gamma$ Veto Region at Low E_T^{miss} , and (c) the Signal Region in simulated samples. The truth-matched types of the reconstructed leading and subleading photons are shown on the x -axis.

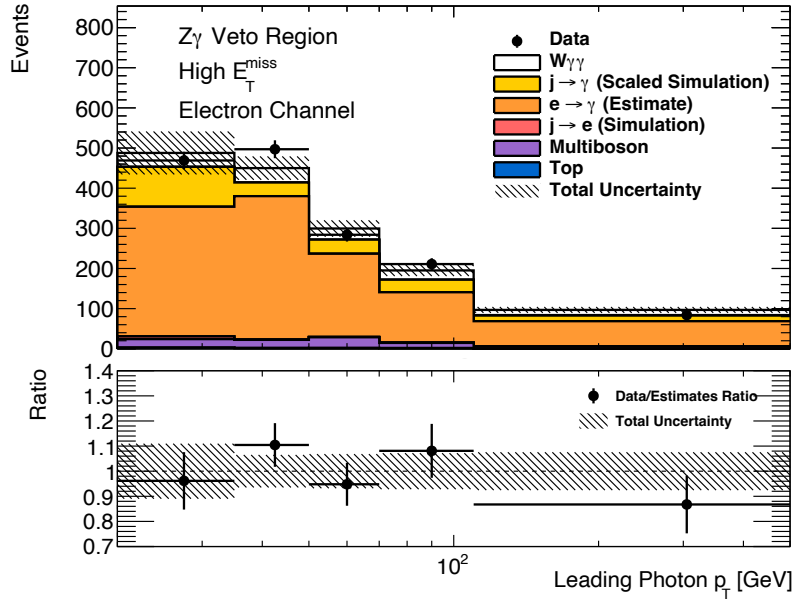


Figure 6.14: Leading photon p_T distribution for events in the $Z\gamma$ veto region at high E_T^{miss} used to validate the data-driven $e \rightarrow \gamma$ estimate. The number of events from the $e \rightarrow \gamma$ background estimate and from simulation is compared with data. The $e \rightarrow \gamma$ data-driven estimate includes statistical and systematic uncertainties described in Section 6.5.5.

both validation regions compared to data. The total estimated number of events in both validation regions is statistically compatible with the observed number of events in data. The $e \rightarrow \gamma$ fake factor estimates are shown with statistical and systematic uncertainties which are detailed in Section 6.5.5.

The $CR_{ee\gamma}$ and $CR_{\mu e\gamma}$ fake rate application regions can themselves contain misidentified leptons and photons. Indeed, the reconstructed photon in the application region can either be a prompt photon, an electron misidentified as a photon, or a jet misidentified as a photon. Events in the application region in which the photon is misidentified serve to estimate the number of events in which one photon is a misidentified electron and the other is either a prompt photon, a misidentified electron, or a misidentified jet. In other words, events with misidentified photons in the application region account for double $e \rightarrow \gamma$ misidentifications

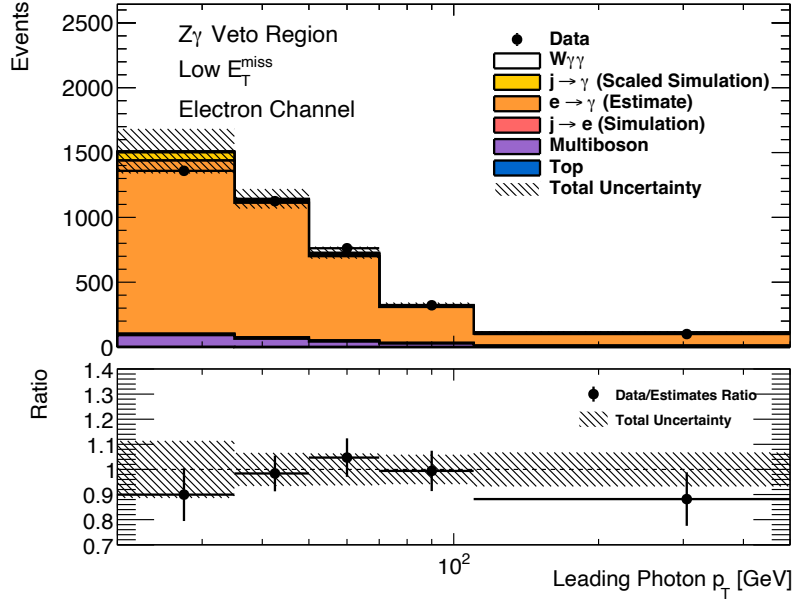


Figure 6.15: Leading photon p_T distribution for events in the $Z\gamma$ veto region at low E_T^{miss} used to validate the data-driven $e \rightarrow \gamma$ estimate. The number of events from the $e \rightarrow \gamma$ background estimate and from simulation is compared with data. The $e \rightarrow \gamma$ data-driven estimate includes statistical and systematic uncertainties described in Section 6.5.5.

	$Z\gamma$ high E_T^{miss}	$Z\gamma$ low E_T^{miss}
$e \rightarrow \gamma$ (simulation)	$954 \pm 50(stat)$	$2781 \pm 64(stat)$
$e \rightarrow \gamma$ (data-driven)	$1075 \pm 9(stat) \pm 84(syst)$	$3393 \pm 16(stat) \pm 289(syst)$
Other processes (simulation)	$455 \pm 56(stat)$	$424 \pm 35(stat)$
Total	$1529 \pm 101(stat + syst)$	$3817 \pm 292(stat + syst)$
Data	$1546 \pm 39(stat)$	$3667 \pm 61(stat)$

Table 6.3: Number of events predicted and observed in both $e \rightarrow \gamma$ validation regions. The number of $e \rightarrow \gamma$ events estimated from simulation and using the data-driven fake factor method are compared. In addition, the $e \rightarrow \gamma$ data-driven estimate and the simulated estimate from other processes are added and compared to data to validate the $e \rightarrow \gamma$ background fake factor estimation method.

in a single event, as well as mixed $e \rightarrow \gamma$ and $j \rightarrow \gamma$ misidentifications in a single event. However, the electron to which the fake rate is being applied to should be prompt and not a jet misidentified as an electron.

To study the truth type of the reconstructed electrons in the fake rate application region, the $e \rightarrow \gamma$ fake rate is calculated in simulated $Z + jets$ events and applied to simulated events in the $CR_{ee\gamma}$ and $CR_{\mu e\gamma}$ regions. This allows for an estimate of the number $e \rightarrow \gamma$ background event in simulated data using the fake factor method. In addition, truth information is also available for simulated events in the $W\gamma\gamma$ SR. As such, in addition to looking at the truth composition of the application region, a closure test can be performed by comparing the $e \rightarrow \gamma$ background from truth information in the $W\gamma\gamma$ SR (in reconstructed $e\gamma\gamma + E_T^{\text{miss}}$ events) with the $e \rightarrow \gamma$ estimate from the fake rate determined using and applied to simulated events in the application region (in reconstructed $ee\gamma + E_T^{\text{miss}}$ events). The truth information for events used in the $e \rightarrow \gamma$ fake factor estimate in simulation is compared with the $e \rightarrow \gamma$ background from truth-matched simulated events in the SR in Figure 6.16. Agreement between the $e \rightarrow \gamma$ background estimated from the fake rate applied to $ee\gamma + E_T^{\text{miss}}$ simulated events and the $e \rightarrow \gamma$ background from truth-matched $e\gamma\gamma + E_T^{\text{miss}}$ simulated events in the SR is good. In addition, it can be seen that there is a negligible amount of $j \rightarrow \ell$ background events in the $ee\gamma + E_T^{\text{miss}}$ application region, showing that the $e \rightarrow \gamma$ fake rate is not being applied to a significant amount of jets misidentified as electrons.

6.5.5 Systematic Uncertainties

The estimated number of events with an electron misidentified as a photon relies exclusively on data. Six separate sources of systematic uncertainty are considered, mostly to take into account some of the arbitrary choices that are made in the design of the method that may have an effect on the final estimated $e \rightarrow \gamma$ event yield. The sources of systematic uncertainty that are considered are listed here.

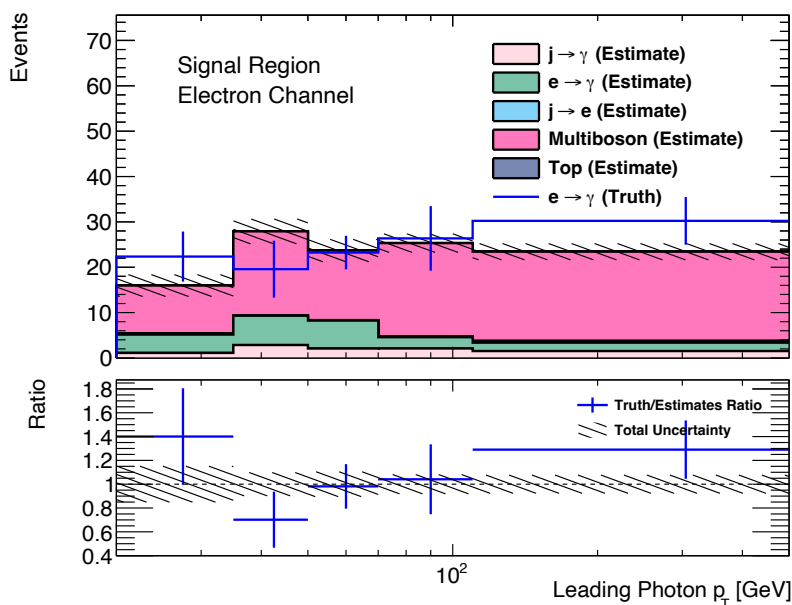


Figure 6.16: Cross-check comparing the estimated background from electrons misidentified as photons ($e \rightarrow \gamma$) using the $e \rightarrow \gamma$ fake rate determined using and applied to simulated events (in reconstructed $ee\gamma + E_T^{\text{miss}}$ events, labelled as "Estimate") to the background from $e \rightarrow \gamma$ events estimated from truth-matched simulation (in reconstructed $e\gamma\gamma + E_T^{\text{miss}}$ events, labeled as "Truth"). The stacked number of events labelled "Estimate" should agree with the "Truth" estimate, providing a closure test of the $e \rightarrow \gamma$ background estimation method in simulation. Statistical uncertainties on simulated data and systematic uncertainties on the $e \rightarrow \gamma$ fake factor estimate are included as described in Section 6.5.5.

Fake Rate Binning: The size and number of p_T and η bins used to estimate the $e \rightarrow \gamma$ fake rate are varied by separately adding and subtracting two bins from the nominal p_T and η binnings. These systematic variations were found to be negligible with an effect of less than 1% on the estimated number of $e \rightarrow \gamma$ background events.

Fitting Range: The range of the invariant mass values over which the fits are performed in the $CRee$ and $CRe\gamma$ regions of the *tag and probe* method is varied by ± 5 GeV on each side of the Z boson mass peak. The resulting uncertainty on the final $e \rightarrow \gamma$ estimate in the SR is approximately 1%.

Integration Range: The invariant mass range over which the fitted Z boson resonance is integrated is varied by ± 5 GeV. The resulting uncertainty on the final $e \rightarrow \gamma$ estimate in the SR is approximately 5%.

Background Estimate: The fits used to extract the number of signal events from a Z boson and the number of events from other background processes in the $CRee$ and $CRe\gamma$ regions are studied using simulated $Z + jets$ events. These simulated events are truth-matched to remove any background contributions from other processes. The fits are then performed to extract the signal Z boson contribution and the contribution from other background processes, which in this case should be zero. A comparison of these fits in both data and simulated and truth-matched Z events in a bin of *probe* photon p_T and $|\eta|$ is shown in Figure 6.17. It can be seen that the invariant mass fits used to extract the number of Z boson events overestimate the number of background events from other processes. The correct $e \rightarrow \gamma$ fake rate lies somewhere between the $e \rightarrow \gamma$ fake rate estimated in data with and without subtracting the estimated number of events from non- Z background processes. As such, the average of both estimates is taken as the $e \rightarrow \gamma$ fake rate and their difference is taken as a systematic uncertainty. The resulting

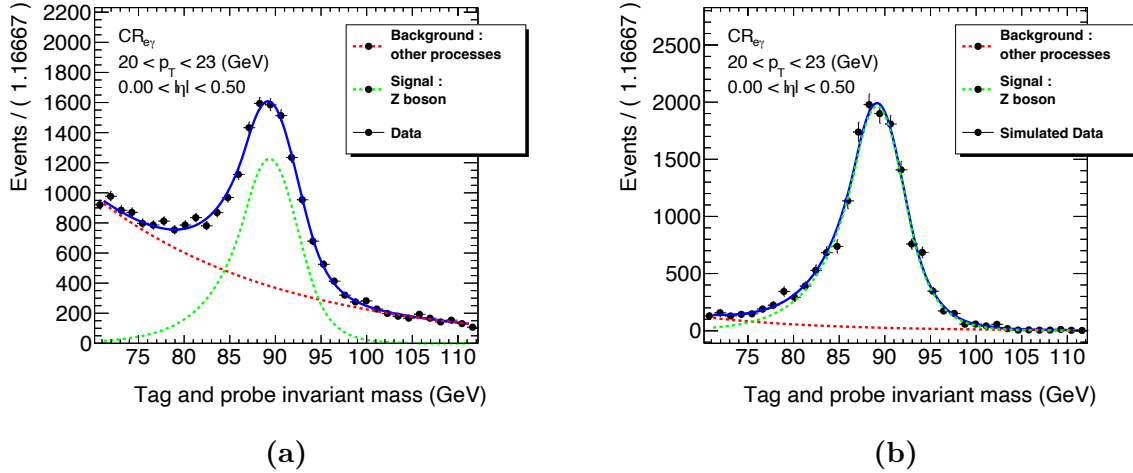


Figure 6.17: Example signal and background fits in (a) data and (b) truth-matched simulated $Z + jets$ events in a single $probe$ photon $|\eta|$ and p_T bin in $CRe\gamma$.

uncertainty on the final $e \rightarrow \gamma$ estimate in the SR is approximately 4%.

Energy Calibration: Events in the $CRe\gamma$ region are enriched in electrons misidentified as photons. As such, the photon calibration is incorrectly applied to the $probe$ object in the $CRe\gamma$ region, which is most likely a misidentified electron. Since the $e \rightarrow \gamma$ fake rate is applied to events with a reconstructed electron, a systematic uncertainty associated with the difference between the photon and electron energy scale is estimated. This is done by estimating the difference in the reconstructed Z boson mass in both the $CRee$ and $CRe\gamma$ regions. A 1% offset in the reconstructed photon's p_T with respect to the electron's p_T is observed. A systematic uncertainty is obtained by varying the photon's p_T in $CRe\gamma$ by $\pm 1\%$. The resulting uncertainty on the final $e \rightarrow \gamma$ estimate in the SR is approximately 3%.

For each systematic variation, the maximum relative variation of the $e \rightarrow \gamma$ fake rate in each p_T and $|\eta|$ bin is taken and symmetrized around its central value. A summary of each systematic variation on the $e \rightarrow \gamma$ fake rate is shown in Figure 6.18.

The final uncertainty on the estimated number of $e \rightarrow \gamma$ events is taken as the sum in

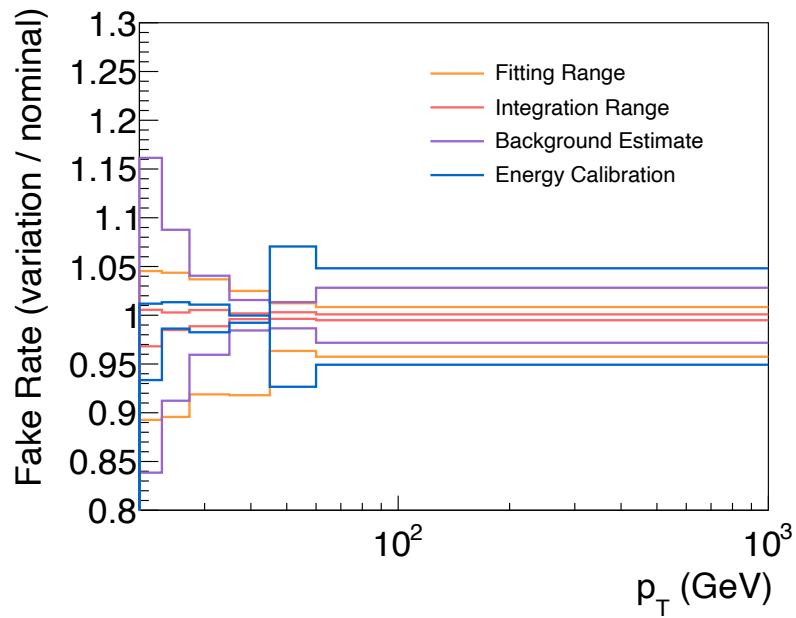


Figure 6.18: Relative changes to the $e \rightarrow \gamma$ fake rate from each systematic variation considered in the $e \rightarrow \gamma$ fake factor background estimation method.

		SR	$Z\gamma$ high E_T^{miss}	$Z\gamma$ low E_T^{miss}
Statistical Uncertainty		2%	1%	< 0.5%
Systematic Uncertainties	Fitting range	1%	1%	1%
	Integration Range	5%	6%	6%
	Energy Calibration	3%	2%	1%
	Background Estimate	4%	4%	5%
Total Uncertainty		7%	8%	9%

Table 6.4: Relative statistical, systematic, and total uncertainties on the estimated number of $e \rightarrow \gamma$ background events in the signal and $e \rightarrow \gamma$ validation regions.

quadrature of all systematic uncertainties, the statistical uncertainties on the invariant mass fit yields, and the statistical uncertainty associated with the number of events in $CR_{ee\gamma}$ and $CR_{e\mu\gamma}$ regions in which the fake rate is applied. The contribution from each source of uncertainty to the estimated number of $e \rightarrow \gamma$ background events in the SR and both $Z\gamma$ validation regions is shown in Table 6.4.

6.5.6 Signal and Control Region Estimates

The number of $e \rightarrow \gamma$ background events in the signal region is estimated to be $153 \pm 3(\text{stat}) \pm 11(\text{syst})$ based on the data-driven fake factor method, while it is estimated to be $191 \pm 25(\text{stat})$ from truth-matched simulation. The data-driven and simulated estimates are shown differentially in leading photon p_T in the SR for comparison in Figure 6.19. The data-driven estimates include the systematic uncertainties detailed in section 6.5.5. Agreement between the fake factor method and simulated $e \rightarrow \gamma$ background estimates is not expected. It can be seen that the total statistical and systematic uncertainties on the data-driven estimate are much smaller than the statistical uncertainties on the $e \rightarrow \gamma$ estimate from simulation.

The data-driven fake factor method is also used to estimate the $e \rightarrow \gamma$ background contributions in other regions of phase space. The data-driven $e \rightarrow \gamma$ estimate is performed

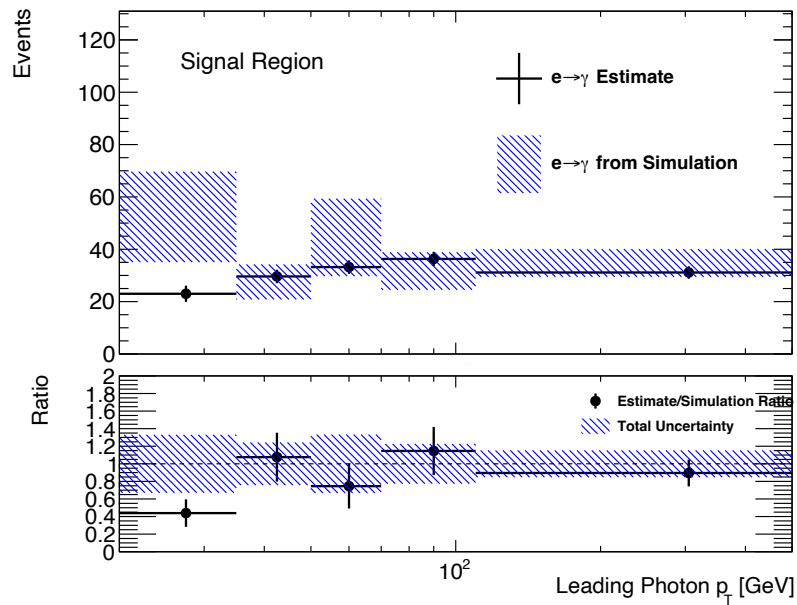


Figure 6.19: Differential $e \rightarrow \gamma$ background estimate in the Signal Region. The uncertainties on the $e \rightarrow \gamma$ background estimate include both statistical and systematic uncertainties associated with the fake factor method as described in Section 6.5.5, while uncertainties on the simulated $e \rightarrow \gamma$ estimate includes only statistical uncertainties.

in the CR_{TT} control region used in the 2D template fit estimate of the $j \rightarrow \gamma$ background described in Section 6.4. Since photons in the CR_{TT} control region are not required to pass any isolation cuts, the $e \rightarrow \gamma$ fake rate in this region is recalculated using *probe* photons with no isolation requirement. The new fake rate is then applied to the $\text{CR}_{ee\gamma}$ and $\text{CR}_{\mu e\gamma}$ application regions where the photons are selected without any isolation requirement.

The $e \rightarrow \gamma$ background is also estimated using the fake factor method in the CR_{Top} and VR_{Top} regions used to constrain and validate the background from processes with a top quark in their final state as described in Section 6.3. The $e \rightarrow \gamma$ fake rate for electrons in these regions is the same as in the SR. However, the $e \rightarrow \gamma$ fake rate application regions are adjusted to be compatible with the CR_{Top} and VR_{Top} regions.

6.6 Background from Jets Misidentified as Leptons

The hadronic fake lepton background, or the $j \rightarrow \ell$ background, comes from events in which a hadronic jet is misidentified as a lepton or a non-prompt lepton resulting from the decay of a heavy-flavour jet is misidentified as a prompt lepton. Similarly to the $j \rightarrow \gamma$ background, the $j \rightarrow \ell$ background is difficult to simulate due to the complexity of the interactions of hadronic showers with the calorimeter system and the numerous processes that can contribute to this kind of background. In addition, the rate of $j \rightarrow \ell$ misidentification is relatively small, resulting in an inefficient simulation requiring a computationally prohibitive number of generated events to attain a sufficiently small statistical uncertainty. This background represents approximately 3% of events in the SR. A data-driven fake factor method similar to the one used to estimate the number of $e \rightarrow \gamma$ background events is used to estimate the $j \rightarrow \ell$ background. Other data-driven techniques were explored, such as the one used in the ATLAS Run 1 $W\gamma\gamma$ analysis [107] and the matrix method described in Reference [111], though, due to limited statistics in the relevant control regions, the statistical uncertainties on the estimated number of $j \rightarrow \ell$

were too large and the methods did not converge.

6.6.1 Fake Factor Method

A data-driven approach similar to the one described in Section 6.5 is used to estimate the number of jets misidentified as leptons. First, the $j \rightarrow \ell$ fake rate ($F_{j \rightarrow \ell}$) is estimated in data. Then, the $j \rightarrow \ell$ background in the SR is estimated by applying the measured $j \rightarrow \ell$ fake rate to events in an application control region adjacent to the SR.

To estimate the $j \rightarrow \ell$ fake rate, two CRs enriched in leptons misidentified as jets are constructed. This is done using a Z boson *tag and probe* method in both the electron and muon decay channels of the Z boson. The electron and muon channels of the control region used to measure the $j \rightarrow \ell$ fake rate, called CR2_fake, are constructed by requiring two well measured *tags* used to reconstruct the Z boson, with a third opposite flavour lepton used as a *probe*. This selection criteria enhances the amount of jets misidentified as *probe* leptons given the large $Z + jets$ cross section when compared to possible prompt sources. Sources of prompt *probe* leptons in the CR2_fake region come almost exclusively from diboson events. The contribution from prompt leptons in the sample of *probe* leptons from diboson events in the CR2_fake control region is subtracted using simulated events.

Two sets of criteria are used for the *probe* leptons, a so-called *Tight* selection for *Signal* leptons as described in Section 5.3, and a so-called *Loose* (or *not-Tight*) set of criteria, where the lepton isolation and $|\sigma_{d_0}|$ requirements are inverted and required to fail. The *Loose* definition enhances the number of $j \rightarrow \ell$ background events since both inverted requirements select against misidentified jets. This is due to the fact that jets misidentified as leptons are expected to have more isolation energy due to the additional surrounding hadronic activity, and non-prompt leptons are expected to have displaced vertices due to the secondary decay vertices of heavy-flavour hadrons.

The rate at which misidentified jets or non-prompt leptons pass the *Tight* selection

criteria, i.e. the $j \rightarrow \ell$ fake rate, is estimated as:

$$F_{j \rightarrow \ell} = \frac{N_{\text{T}}^{\text{data}} - N_{\text{T}}^{\text{prompt,sim}}}{N_{\text{L}}^{\text{data}} - N_{\text{L}}^{\text{prompt,sim}}}, \quad (6.8)$$

where $N_{\text{T}}^{\text{data}}$ is the number of events from data in CR2_fake in which the *probe* lepton passes the *Tight* criteria, $N_{\text{T}}^{\text{prompt,sim}}$ the number of events from simulation in CR2_fake where the *probe* lepton is both prompt and passes the *Tight* criteria, and $N_{\text{L}}^{\text{data}}$ and $N_{\text{L}}^{\text{prompt,sim}}$ are the analogous numbers for *Loose probe* leptons. The electron and muon $j \rightarrow \ell$ fake rates are estimated in the CR2_fake control region channels in which the *probe* lepton is either an electron or a muon, respectively. A schematic diagram of the $j \rightarrow \ell$ fake rate estimation method is shown in Figure 6.20.

To obtain the number of $j \rightarrow \ell$ background events in the SR, the fake rate is applied to a region adjacent to the SR, labeled CR2, with all the same requirements but with the lepton isolation and $|\sigma_{d_0}|$ requirements inverted to match the selection for the *Loose probe* leptons in CR2_fake. The contribution from prompt *probe* leptons in the CR2 region is subtracted using truth matched simulation. The number of $j \rightarrow \ell$ events in the SR is given by:

$$N_{j \rightarrow \ell}^{\text{SR}} = F_{j \rightarrow \ell} \left(N_{\text{L}}^{\text{data,CR2}} - N_{\text{L}}^{\text{prompt,sim,CR2}} \right), \quad (6.9)$$

where $N_{\text{L}}^{\text{data,CR2}}$ is the number of events from data in CR2 and $N_{\text{L}}^{\text{prompt,sim,CR2}}$ is the number of events with a prompt *probe* lepton from simulation in CR2.

6.6.2 Fake Rate

The CR2_fake region used to estimate the $j \rightarrow \ell$ fake rate selects events with two same flavour opposite sign *Signal* leptons with an invariant mass within $\pm 10\%$ of the Z boson mass, accompanied by an opposite flavour *Baseline* lepton to avoid the ambiguity of which leptons are coming from the Z boson. The event must also pass the appropriate single lepton

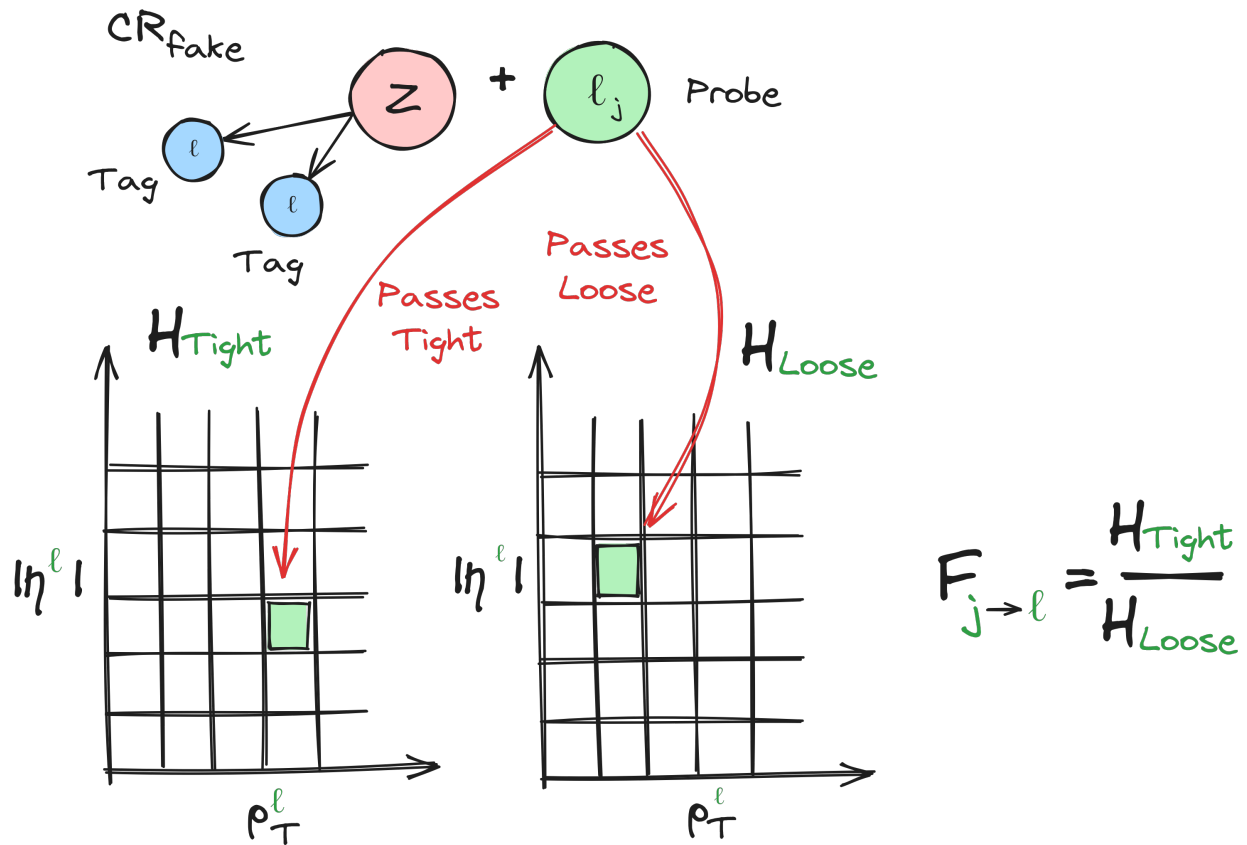


Figure 6.20: Schematic diagram describing the use of the *tag and probe* method to calculate the fraction of jets misidentified as leptons, $F_{j \rightarrow \ell}$, as a function of the object transverse momentum and pseudorapidity. The $F_{j \rightarrow \ell}$ fake rate is obtained by dividing the 2D histograms of the number of *probe* leptons which pass the *Tight* lepton requirement (H_{Tight}) by the number of *probe* leptons that pass the *Loose* requirement (H_{Loose}).

Object	Selection	
<i>Tag</i>	<u>Electron</u> $p_T > 27.3$ GeV <i>Tight</i> Identification $E_T^{\text{iso}} \Delta R=0.2/E_T < 0.06$ $p_T^{\text{iso}} R_{\text{max}}=0.2/p_T < 0.06$ $z_0 < 0.5$ & $ \sigma_{d_0} < 5$ $ \eta < 2.47$, excluding $1.37 < \eta < 1.52$	<u>Muon</u> $p_T > 27.3$ GeV <i>Medium</i> Identification $E_T^{\text{iso}} \Delta R=0.2/E_T < 0.15$ $p_T^{\text{iso}} R_{\text{max}}=0.3/p_T < 0.04$ $z_0 < 0.5$ & $ \sigma_{d_0} < 3$ $ \eta < 2.4$
	<u>Electron</u> $p_T > 25$ GeV <i>Medium</i> Identification $ \eta < 2.47$, excluding $1.37 < \eta < 1.52$	<u>Electron</u> $p_T > 25$ GeV <i>Medium</i> Identification $ \eta < 2.4$
<i>Event</i>	Two same flavour opposite sign <i>tags</i> <i>Tag</i> $m_{\ell\ell}$ within 10% of Z mass Opposite flavour <i>probe</i> $m_T^W < 40$ GeV & $E_T^{\text{miss}} < 40$ GeV Standard overlap removal <i>b</i> -tagging veto on jets with $p_T > 20$ GeV and $ \eta < 2.5$ JVT > 0.5 for jets with $20 < p_T < 60$ GeV and $ \eta < 2.4$	

Table 6.5: Table summarizing the object selection used to define the electron and muon channels of the CR2_fake region used to estimate the $j \rightarrow \ell$ fake rate.

triggers given the lepton flavour and year which are described in Section 5.2.2. Events with additional *Baseline* leptons, as they are described in Section 5.3, are vetoed. The same flavour opposite sign *tag* leptons are required to pass the *Tight* selection criteria with one of them being matched to its respective lepton trigger. The remaining *probe* lepton must pass the *Baseline* lepton selection and is used to calculate the fake efficiency as described in the previous section. In addition, events are required to have $E_T^{\text{miss}} < 40$ GeV and $m_T^W < 40$ GeV, where m_T^W is constructed using the *probe* lepton’s four momentum vector. This is done to reduce the contributions from WZ diboson events in the CR2_fake region. In addition, truth matched simulated diboson events are subtracted to account for the remaining contribution from events with a prompt *probe* lepton. A summary of the selection criteria used to form the CR2_fake region is given in Table 6.5.

To account for differences in fake rates due to detector effects and event kinematics, the $j \rightarrow \ell$ fake rate is estimated in bins of lepton p_T and $|\eta|$ in the electron channel and bins

of *probe* lepton p_T in the muon channel. The limited number of bins in the muon channel is mainly due to the limited number of events in the muon channel of the CR2_fake region. The electron and muon $j \rightarrow \ell$ fake rate estimates are shown in Figure 6.21. Only statistical uncertainties are shown.

6.6.3 Fake Rate Application

The $j \rightarrow \ell$ fake rate application region, CR2, has the same selection criteria as the SR but uses the *Loose* selection criteria for the leptons. In addition, a validation region called the $j \rightarrow \ell$ VR is obtained by inverting the SR E_T^{miss} and m_T^W requirements, thereby reducing the number of events with a prompt lepton from a W boson. A $j \rightarrow \ell$ fake rate application region is formed for the $j \rightarrow \ell$ VR by selecting for *Loose* leptons instead of *Tight* leptons. These regions are summarized in Figure 6.22.

6.6.4 Validation

A validation of the $j \rightarrow \ell$ data-driven estimate is done in the $j \rightarrow \ell$ Validation Region by comparing data to the $j \rightarrow \ell$ data-driven background estimate added to the other signal and background estimates. This is shown differentially in Figure 6.23 in both the electron and muon channels and in Table 6.6 for their respective one bin estimates. Uncertainties on the single bin and differential $j \rightarrow \ell$ background estimates include statistical uncertainties and systematic uncertainties described in Section 6.6.5. The simulated $W\gamma\gamma$, multiboson, and top quark contributions include statistical uncertainties only. The $e \rightarrow \gamma$ background contribution in this region is estimated using the data driven method described in Section 6.5.4 and includes both statistical and systematic uncertainties. In addition, the $j \rightarrow \gamma$ background contribution is estimated using simulated events and corrected using the same scale factor as the one used in the $e \rightarrow \gamma$ validation regions described in Section 6.5.4. Results show good agreement in both the one bin and binned estimates, though statistical

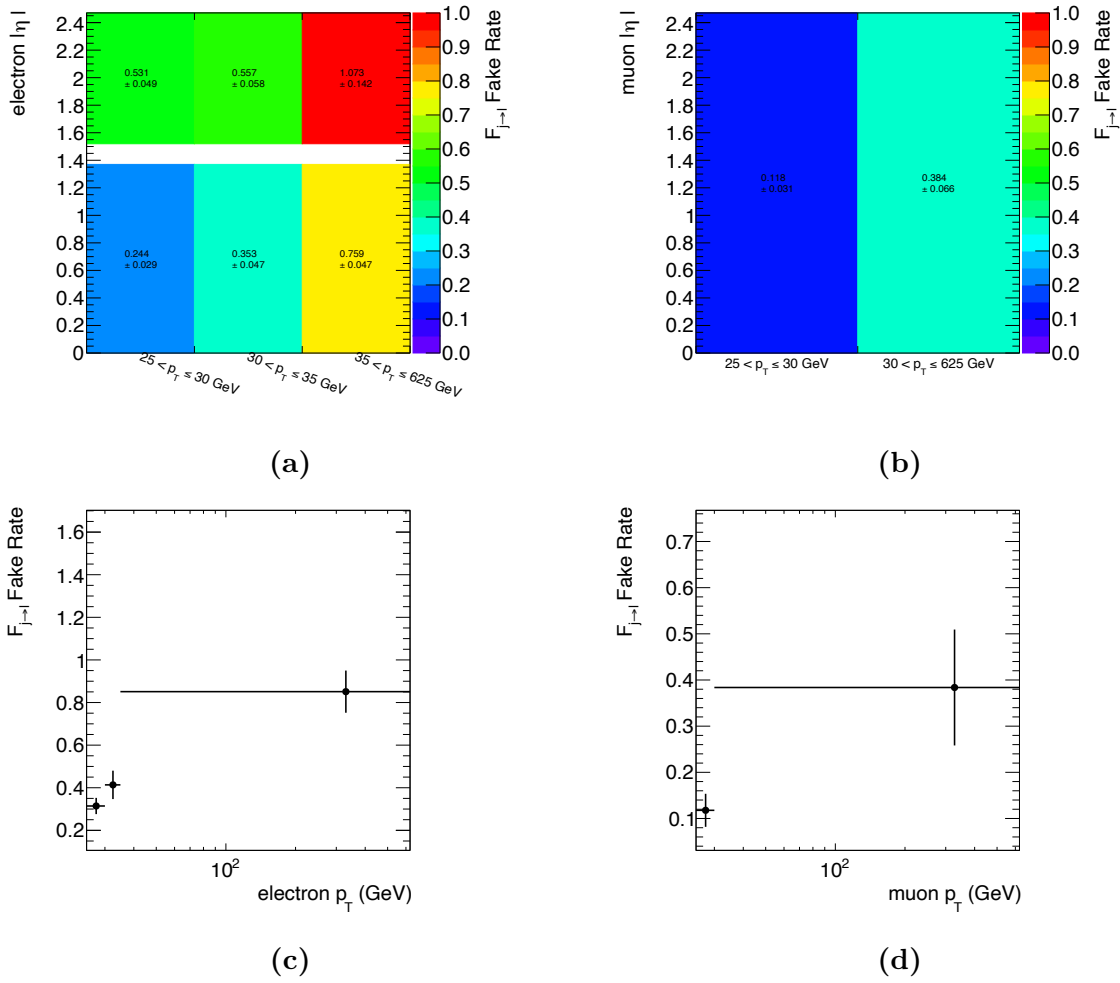
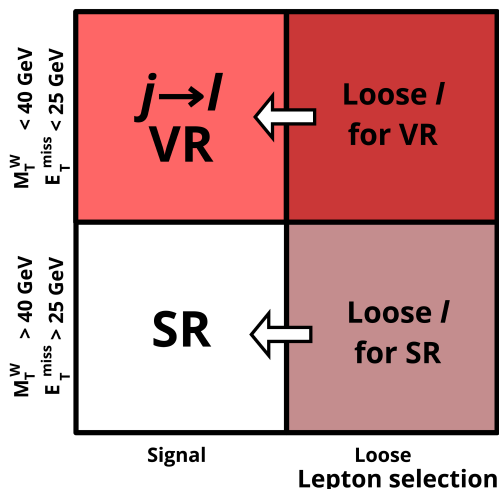


Figure 6.21: $j \rightarrow \ell$ fake rate estimates in the electron channel (left) and muon channel (right) in 2D and projected onto the object's p_T .



(a)

Figure 6.22: Schematic diagram summarizing the $j \rightarrow \ell$ Validation Region (VR) in relation to the Signal Region (SR), and their $j \rightarrow \ell$ fake rate application regions where the *Signal* lepton requirement is replaced with the *Loose* lepton requirement.

uncertainties are large due to the relatively small $j \rightarrow \ell$ fake rate.

The separate contributions of light-flavour jets misidentified as leptons and non-prompt leptons from heavy-flavour jets should be similar in the control regions used to estimate the fake efficiency (CR2_fake), the $j \rightarrow \ell$ VR, and the SR, assuming a difference in fake rate between fake and non-prompt leptons. Though statistical uncertainties are large, especially in the SR, there is statistical compatibility in simulation of both the fake rates and the ratios of $j \rightarrow \ell$ background events from light-flavour jets versus heavy-flavour jets in all three regions.

6.6.5 Systematic Uncertainties

The estimated number of events with a jet misidentified as a lepton relies both on data and simulation. Thus, several sources of systematic uncertainty are considered which are related

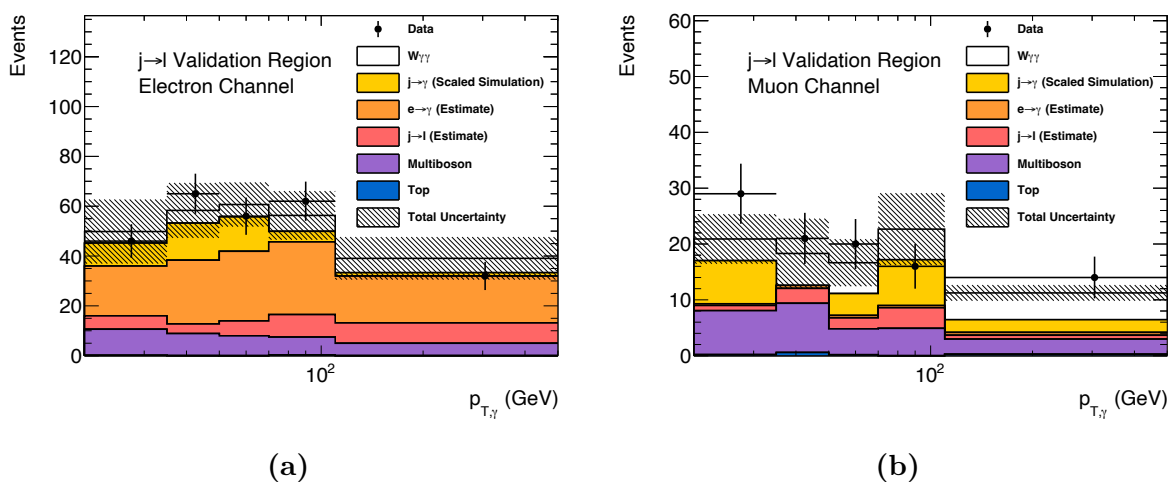


Figure 6.23: Leading photon p_T distributions in the (a) electron and (b) muon channels of the $j \rightarrow \ell$ Validation Region. The sum of the number of $j \rightarrow \ell$ events estimated with the fake factor method and the predicted number of events from processes with a prompt lepton is compared to data. The $j \rightarrow \ell$ background estimate includes statistical and systematic uncertainties, the $W\gamma\gamma$, multiboson, and top estimates include only statistical uncertainties, the $j \rightarrow \gamma$ and $e \rightarrow \gamma$ estimates include statistical and systematic uncertainties, and data includes only statistical uncertainties.

	$j \rightarrow \ell$ Validation Region	
	Electron Channel	Muon Channel
Data-driven $j \rightarrow \ell$ Estimate	$35_{-6}^{+6}(stat)_{-6}^{+6}(syst)$	$11_{-2}^{+2}(stat)_{-5}^{+5}(syst)$
Prompt ℓ Estimate (Simulation)	232 ± 7	80 ± 9
Total	267 ± 11	91 ± 11
Data	261 ± 16	100 ± 10

Table 6.6: Validation of the data-driven $j \rightarrow \ell$ background estimate in one bin. The $j \rightarrow \ell$ background is added to the prompt lepton estimate in the $j \rightarrow \ell$ Validation Region and compared to data in the electron and muon channels. The $j \rightarrow \ell$ estimate includes statistical and systematic uncertainties, the simulated signal, multiboson, and top quark components of the prompt photon estimate include only statistical uncertainties, the data-driven $j \rightarrow \gamma$ and $e \rightarrow \gamma$ components of the prompt lepton estimate include both statistical and systematic uncertainties, and data only includes statistical uncertainties.

to both the simulated diboson samples used in the CR2_fake region to estimate the $j \rightarrow \ell$ fake rate and the arbitrary choices made in the design of the $j \rightarrow \ell$ fake factor method.

The sources of uncertainty associated with the $j \rightarrow \ell$ fake factor method are described below. The fractional change in the value of the $j \rightarrow \ell$ fake rate due to each of these systematic variations is shown in Figure 6.24.

Impact Parameter Significance: The σ_{d_0} cut used to define the *Loose probe* leptons in the CR2_fake region is increased by 0.5 (the *Tight* lepton cut remains the same). The impact of this cut variation is shown to be negligible and is not included in the calculation of the total uncertainty.

E_T^{miss} Cut: The E_T^{miss} cut used to define the CR2_fake region is changed by $\pm 10\text{GeV}$. The cut's value represents an arbitrary choice made during the design of the fake factor method and the effect of varying the E_T^{miss} cut by $\pm 10\text{ GeV}$ is kept in the final estimate's systematic uncertainty. The resulting uncertainty on the estimated number of $j \rightarrow \ell$ events in the SR

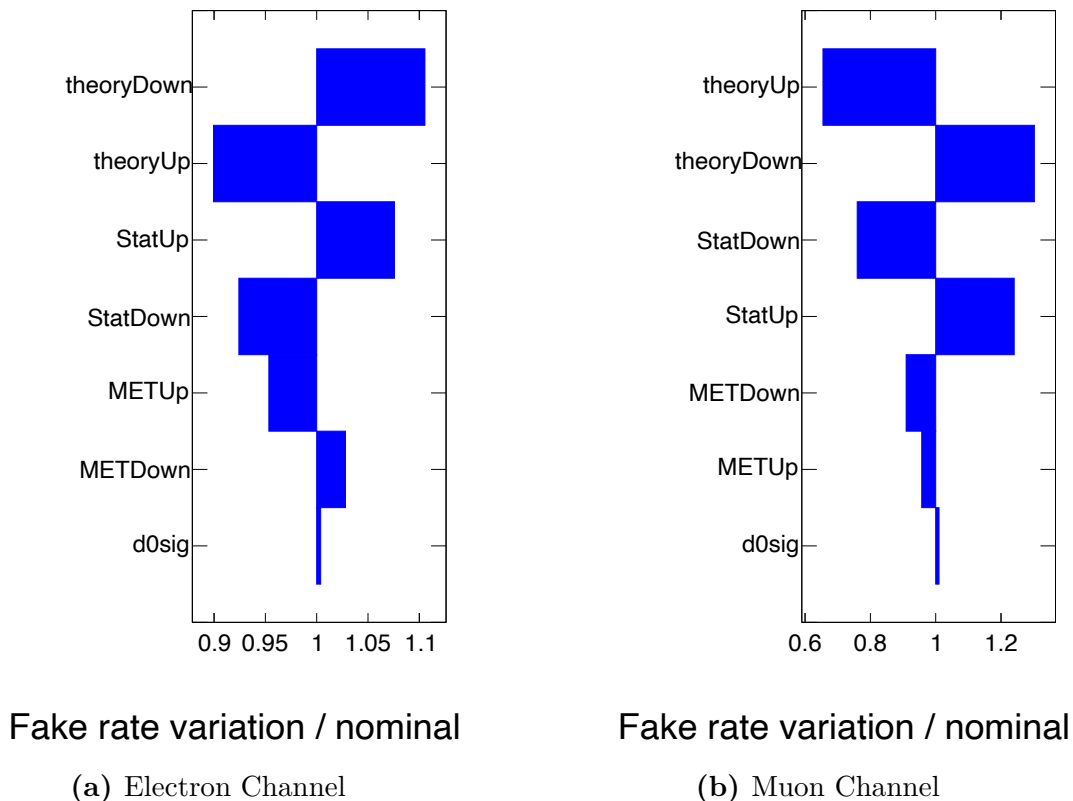


Figure 6.24: Fractional change of the total $j \rightarrow \ell$ fake rate resulting from different systematic variations ranked from largest (top) to smallest (bottom) and compared to statistical uncertainties (statUp and statDown).

is approximately 11% in the electron channel and 17% in the muon channel.

Theory Systematics: The effect of the theoretical systematic uncertainties on the subtracted simulated diboson background in the CR2_fake region are estimated. The procedure for estimating theoretical uncertainties on simulated samples is summarized in Section 7.2. The resulting uncertainty on the estimated number of $j \rightarrow \ell$ events in the SR is approximately 15% in the electron channel and 40% in the muon channel.

Region	Electron channel		Muon channel	
	$j \rightarrow \ell$ VR	SR	$j \rightarrow \ell$ VR	SR
Statistical Uncertainty	+18, -16%	+28, -24%	+21, -19%	+28%, -24%
E_T^{miss} Uncertainty	+11, -10%	+11, -10%	+17, -16%	+18, -16%
Theory Uncertainty	+14, -13%	+15, -14%	+45, -34%	+46%, -34%
Total Uncertainty	+25, -23%	+34, -30%	+52, -42%	+57, -45%

Table 6.7: Relative uncertainties on the estimated number of $j \rightarrow \ell$ background events from statistical and the systematic sources of uncertainty associated with the $j \rightarrow \ell$ fake factor method in the electron and muon channels of the Signal Region (SR) and $j \rightarrow \ell$ Validation Region (VR).

All uncertainties on the $j \rightarrow \ell$ fake rate relating to detector acceptance, efficiency, calibration, and resolution in simulation as they are described in Chapter 7 are also estimated. In addition, systematic uncertainties related to charge identification for leptons were also included. The cumulative effect of these systematic uncertainties was propagated to the final fit described in Chapter 8 and was shown to have no impact on the significance. Thus, these systematic uncertainties were found to have a negligible effect.

The systematic uncertainties that are kept in the final estimate are the theory uncertainties on the diboson sample and the effect of varying the E_T^{miss} cut by ± 10 GeV, in addition to the statistical uncertainties on the $j \rightarrow \ell$ fake rate estimates in the CR2_fake region and the statistical uncertainties from the CR2 application region. Their effects on the final single bin estimates in the electron and muon channels of the SR and in the $j \rightarrow \ell$ VR are shown in Table 6.7.

6.6.6 Signal Region Estimate

Results of the $j \rightarrow \ell$ background estimate in the SR are shown in Table 6.8 and compared to the $j \rightarrow \ell$ estimate from simulation, though no agreement is expected. Uncertainties on the

	Signal Region	
	Electron Channel	Muon Channel
Data-driven $j \rightarrow \ell$ Estimate	$25_{-6}^{+7}(stat)_{-4}^{+5}(syst)$	$9_{-2}^{+3}(stat)_{-4}^{+5}(syst)$
$j \rightarrow \ell$ from Simulation	16 ± 5	$< 0.5 \pm < 0.5$

Table 6.8: Total estimates of the $j \rightarrow \ell$ background in the electron and muon channels of the Signal Region from the data-driven fake factor method and the $j \rightarrow \ell$ estimate from truth-matched simulated events for comparison. The data-driven estimate includes both statistical and systematic uncertainties while the $j \rightarrow \ell$ estimate from simulation only includes statistical uncertainties.

$j \rightarrow \ell$ fake factor estimate include both statistical and systematic uncertainties as described in Section 6.6.5, while only statistical uncertainties are included for the $j \rightarrow \ell$ estimate from simulation.

6.7 Background from Pileup

In ATLAS, due to the absence of reconstructed tracks in the Inner Detector, the vertex of origin for unconverted photons is inferred from the properties of its associated clusters in the Electromagnetic Calorimeter. As a result, the uncertainty on the measured origin of a photon is larger than the average spacing between the multiple reconstructed vertices in an event. For this reason, no vertex requirement is placed on photons in the SR. This results in the possibility of selecting events in which one or both photons originate from a vertex different from the primary vertex. This type of background is called the pileup background since it largely originates from in-time pileup. This source of background represents approximately 1% of events in the SR. Simulated pileup events are overlaid onto all simulation samples as described in Section 6.1. However, because of the finite number of simulated events and the small probability for a pileup collision to produce one or more photons, this background

contribution is estimated using a data-driven method based on the method used in the ATLAS Run 2 $Z\gamma$ analysis [112].

The method takes advantage of differences in the distance from the primary vertex between pileup photons and photons originating from the primary vertex. The difference between the reconstructed longitudinal position of the photon (z_γ) and the longitudinal position of the primary vertex (z_{PV}) is denoted as Δz . The number of pileup photons is estimated separately for the leading and subleading photons using a subset of events of the SR with converted photons that have at least one track in the Inner Detector and a conversion radius of less than 400 mm. These photons have a more precise measurement of their longitudinal position of origin. The Δz distributions of $W\gamma\gamma$ simulated events in the SR for converted photons is shown in Figure 6.25, showing a relatively narrow spread of less than 400 μm . The longitudinal spread of the proton bunches at the LHC is expected to be Gaussian distributed around the origin with a spread of $\sigma = 35.5$ mm [112]. Since the longitudinal position of the pileup vertices is uncorrelated with the longitudinal position of the primary vertex, the distribution of the longitudinal positions of photons from pileup vertices is expected to be Gaussian distributed with $\sigma_{\Delta z} \approx \sqrt{2} \times 35.5 \approx 50.2$ mm. The number of photons from the primary vertex is estimated using simulated $W\gamma\gamma$ events and subtracted from data in order to obtain the fraction of pileup events in this subset of events of the SR. Since this fraction should not depend on whether a photon converts or not in the Inner Detector, it can be used to estimate the number of pileup events in the SR. In order to reduce the dependence on the modeling of photons originating from the primary vertex, this fraction is estimated in the tails of the Δz distribution at $\sigma_{\Delta z} > 50$ mm. This region is expected to contain a fraction of photons originating from pileup vertices of 32%.

The fractions of events with either the leading or subleading photon originating from pileup are estimated separately. Each is separately given by:

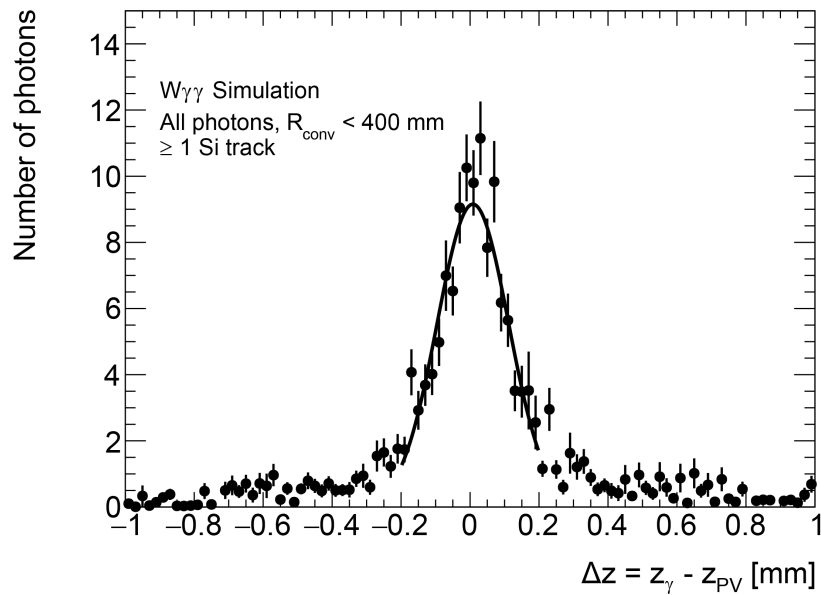


Figure 6.25: Difference in the longitudinal impact parameter between the primary vertex and the reconstructed origin of converted photons in the Signal Region in simulated signal events. Converted photons are required to have at least one silicon track and a conversion radius of less than 400 mm. The solid curve shows a Gaussian fit. Only statistical uncertainties are shown.

$$f_{PU} = \frac{N_{\text{data}, \geq 1\text{Si track}}^{|\Delta z| > 50\text{mm}} - N_{\text{single pp}, \geq 1\text{Si track}}^{|\Delta z| > 50\text{mm}}}{0.32 \times N_{\text{data}, \geq 1\text{Si track}}}, \quad (6.10)$$

where $N_{\text{data}, \geq 1\text{Si track}}^{|\Delta z| > 50\text{mm}}$ is the number of events in data in which the photon has $|\Delta z| > 50$ mm, $N_{\text{single pp}, \geq 1\text{Si track}}^{|\Delta z| > 50\text{mm}}$ is the number of events in simulation in which the photon originated from the primary vertex and has $|\Delta z| > 50$ mm, and $N_{\text{data}, \geq 1\text{Si track}}$ is the total number of events in data. Simulated $W\gamma\gamma$ events are normalized to data in the $-2 \text{ mm} < \Delta z < 2 \text{ mm}$ region and an additional factor of 1.48 ± 0.26 is applied to correct for mis-modelling in the tails, as determined by the $Z\gamma$ analysis by studying resonant $Z(\ell\ell\gamma)$ events [112]. The distributions for the number of events in data and simulation for the leading and subleading photons are shown in Figure 6.26, clearly showing an excess of events in the tails of the data distributions and indicating the presence of pileup photons. The pileup fraction f_{PU} for leading photons is determined to be 0.07 ± 0.03 , and 0.02 ± 0.04 for subleading photons, suggesting that most pileup events originate from $W\gamma$ events with an additional photon from a pileup vertex.

In order to avoid double counting the background from jets misidentified as photons that also originate from pileup, the photon purity for events in the sample of converted photons is estimated using a two dimensional side-band method similar to the one described in Reference [112]. The resulting measured photon purity is 0.22 ± 0.01 , where the uncertainty represents the statistical uncertainty. Taking into account the measured photon purity, the final number of events with a pileup photon in the SR is estimated to be 9_{-4}^{+5} , where the uncertainty represents the total statistical uncertainty.

6.8 Summary

A summary of the estimated number of signal and background events in the TopCR, TopVR, and SR is shown in Table 6.9. The uncertainties quoted in the table represent the total uncertainties which include the statistical and systematic components described in

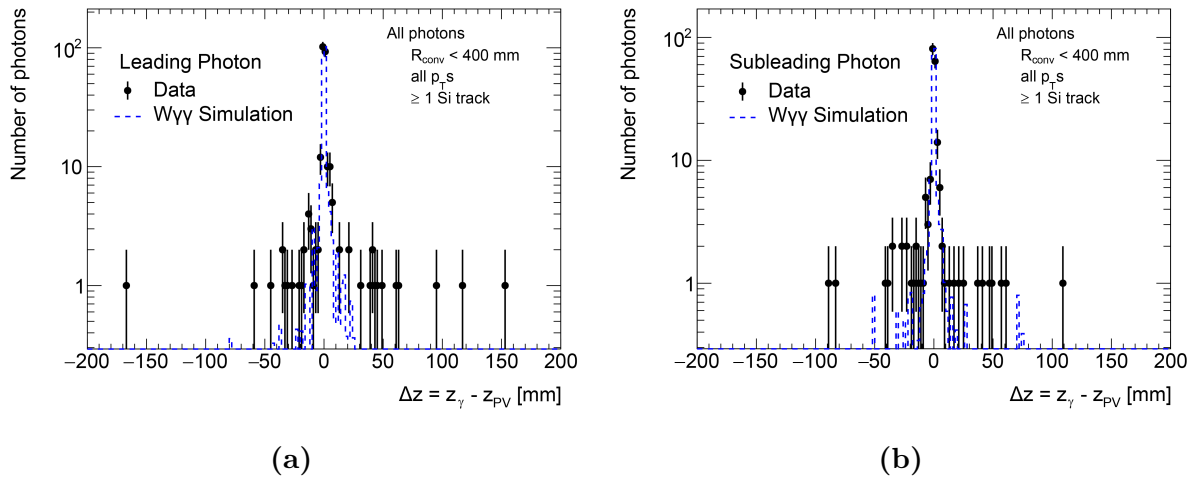


Figure 6.26: Difference in the longitudinal impact parameter between the primary vertex and the reconstructed origin of converted photons in the Signal Region for (a) the leading and (b) subleading photon. Converted photons are required to have at least one silicon track and a conversion radius of less than 400 mm. Uncertainties on events in data represent statistical uncertainties.

Source	TopCR	TopVR	SR
$W\gamma\gamma$	28 ± 5	4.3 ± 2.3	410 ± 60
$j \rightarrow \gamma$	47 ± 22	4.5 ± 2.4	420 ± 50
$e \rightarrow \gamma$	119 ± 9	15.6 ± 1.5	153 ± 11
Multiboson ($WH(\gamma\gamma)$, $WW\gamma$, $Z\gamma\gamma$)	5.8 ± 1.8	3.9 ± 1.3	76 ± 14
$j \rightarrow \ell$	–	–	35 ± 10
Top ($tt\gamma$, $tW\gamma$, $tq\gamma$)	161 ± 8	15.8 ± 1.7	35 ± 4
Pileup	–	–	10 ± 5
Total	359 ± 26	45 ± 4	$1\,130 \pm 60$
Data	333	36	1\,136

Table 6.9: Estimated signal and background event yields in the TopCR, TopVR, and Signal Region (SR). Estimates are shown before the likelihood fits described in Chapter 8. The uncertainties quoted in the table correspond to total uncertainties. Events from the “Multiboson” and “Top” backgrounds are estimated in simulation and contain only prompt leptons and photons. The $j \rightarrow \gamma$, $e \rightarrow \gamma$, $j \rightarrow \ell$, and pileup backgrounds are estimated using data-driven techniques. Event yields denoted with “–” correspond to backgrounds that are negligible.

this chapter and in Chapter 7. Estimates are shown prior to the likelihood fits described in Chapter 8. The estimated number of events in each region are in good agreement with the observed number of events in data. The dominant sources of uncertainty in the SR are from jets misidentified as photons and from the multiboson background. The next chapter describes the sources of systematic uncertainty considered in the $W\gamma\gamma$ measurement, other than those associated with the data-driven background estimates already described in this chapter.

Chapter 7

Systematic Uncertainties

In addition to statistical uncertainties on data and simulated event samples, several other sources of systematic uncertainty are considered in the $W\gamma\gamma$ analysis. Systematic uncertainties related to the data-driven methods used to estimate the background from misidentified objects are detailed in Chapter 6. This Chapter describes additional sources of systematic uncertainty considered in the analysis. These can be classified into two categories, experimental and theoretical systematic uncertainties. Most of the procedures used to evaluate experimental and theoretical systematic uncertainties and their potential grouping come from ATLAS recommendations made by dedicated working groups. All uncertainties are implemented as up and down variations representing 68% confidence intervals, meaning they can have asymmetric values. The effects of systematic variations on the physics objects and their properties in the analysis are propagated through the full analysis chain and result in up and down uncertainties on the estimated number of selected events. As described in Chapter 8, all uncertainties are implemented in the final significance and unfolding fits as nuisance parameters.

7.1 Experimental Uncertainties

This section describes the procedures used to evaluate systematic uncertainties associated with detector calibration, event triggering, and object reconstruction, identification, isolation, and vertex matching, as well as the uncertainty on the measured integrated luminosity.

7.1.1 Energy Scale and Resolution

This section describes the different sources of uncertainty affecting the energy scale and resolution of the different reconstructed objects in an event.

Electrons and Photons

Due to the similarity of their signatures in the ATLAS detector, the calibration of the energy scale and resolution of photons and electrons follow the same procedure [71]. Both the energy scale and resolution of electrons and photons are derived from simulated samples of single particles with no pileup. This is done separately for electrons, converted photons, and unconverted photons. A correction is then applied to account for differences between data and simulation. Systematic uncertainties associated with differences in the kinematic properties of $Z \rightarrow ee$ events in data and simulation are assigned to both electrons and photons as a function of their p_T and η . These uncertainties are estimated separately for electrons, converted photons, and unconverted photons. Converted photons tend to have a smaller systematic uncertainty associated to their energy calibration relative to unconverted photons due to the similarity of their shower development with prompt electrons.

The following sources of uncertainty affecting the energy scale of electrons and photons are considered:

- Uncertainties relating to the shift in measured energy due to pileup.

- Uncertainties on the calibration of the fraction of energy deposited by incident particles in the layers of the Electromagnetic Calorimeter.
- Uncertainties on the energy calibration of objects in the $1.4 < |\eta| < 1.6$ barrel/end cap transition region of the Electromagnetic Calorimeter.
- Uncertainties on the amount of material upstream of the Electromagnetic Calorimeter.
- Uncertainties on the liquid argon cell energy non-linearity.
- Uncertainties on the modelling of the electron and photon lateral shower shapes in the Electromagnetic Calorimeter.

The following sources of uncertainty affecting the energy resolution of electrons and photons are considered:

- Uncertainties associated to the fluctuations in the sampling of the electromagnetic showers and in the energy lost in the material upstream of the Electromagnetic Calorimeter.
- Uncertainties related to the electronic and pileup noise in the calorimeter readout.
- Uncertainties on the effects of non-uniformities in the response of the Liquid Argon Calorimeter.

Overall, the combined uncertainty on the electron and photon energy scale and resolution leads to a 0.2% uncertainty on the total estimated yield in the SR before the likelihood fits described in Chapter 8.

Muons

The muon momentum scale and resolution are estimated using $J/\Psi \rightarrow \mu\mu$ and $Z \rightarrow \mu\mu$ events in simulation [77]. Scale factors to correct for discrepancies between simulation and

data are calculated. Statistical uncertainties are considered in addition to systematic uncertainties associated to the fits of the Z and J/Ψ di-muon invariant mass distributions. The systematic uncertainties are obtained by varying the different parameters of the fitting procedure. In addition, an uncertainty related to the alignment of the Muon Spectrometer chambers is estimated using special ATLAS runs with the toroid magnet off. Overall, the uncertainty on the muon energy scale and resolution leads to a 0.1% uncertainty on the total estimated yield in the SR before the likelihood fits described in Chapter 8.

Jets

The jet energy scale calibration is done in several steps to correct for the jet energy, momentum, and mass measurements. The calibration procedure starts with a correction to remove excess energy from pileup. This is followed by a correction accounting for discrepancies between the kinematic properties of di-jet events in simulation and data. Finally, an *in situ* calibration is done to correct for remaining differences between simulation and data in well-measured reference objects such as Z bosons. There are 125 different contributions to the jet energy scale uncertainty in total [81].

The jet energy resolution is measured using jets recoiling against either a well defined reference object or another jet in both data and simulation. In regions of jet p_T where the resolution in data is larger than in simulation, the jet p_T in simulation is smeared to match data. Systematic uncertainties on the jet energy resolution are propagated through to the reconstructed physics objects in simulation.

Overall, the uncertainty on the jet energy scale and resolution leads to a 1.0% uncertainty on the total estimated yield in the SR before the likelihood fits described in Chapter 8.

Missing Transverse Energy

The missing transverse energy response and resolution are estimated by comparing data and simulation with the same event selections. Several different processes are considered in order to study the effects of the different physics objects that enter the so-called *soft* and *hard* terms of the E_T^{miss} calculation [88]. The *hard* term of the E_T^{miss} calculation comes from the reconstructed physics objects in the analysis event selection. As such, systematic uncertainties on the properties of these reconstructed objects are propagated through to the final E_T^{miss} estimate. In addition, systematic uncertainties on the E_T^{miss} *soft* term are considered. The soft term includes all charged particle tracks from the primary vertex that are not associated with any reconstructed object. Systematic uncertainties on the E_T^{miss} soft term are estimated by comparing data to simulation in $Z \rightarrow \mu\mu$ events. Overall, the uncertainty on the missing transverse energy response and resolutions leads to a 0.4% uncertainty on the total estimated yield in the SR before the likelihood fits described in Chapter 8.

7.1.2 Efficiencies

For all particles in the ATLAS detector, the trigger, reconstruction, identification, and isolation efficiencies in simulation are corrected to match data by computing correction factors that depend on the particle's kinematic properties, often its transverse momentum and pseudorapidity. Statistical and systematic uncertainties associated to these correction factors are accounted for and described in this section.

Electrons

For electrons, the efficiency correction factors are computed using a *tag-and-probe* method on known resonances such as the Z boson or J/Ψ meson decaying to two electrons [69]. The trigger, reconstruction, identification, and isolation correction factors are estimated using

$Z \rightarrow ee$ events, while $J/\Psi \rightarrow ee$ events are used to supplement the identification efficiency correction factors at low electron transverse energy in the range of $4.5 \text{ GeV} < E_T < 20 \text{ GeV}$. These correction factors include statistical uncertainties as well as systematic uncertainties obtained by varying the *tag-and-probe* selection requirements. In addition, a systematic uncertainty is obtained by varying how the background subtraction is performed. Overall, the uncertainty on the electron efficiencies leads to a negligible uncertainty on the total estimated yield in the SR before the likelihood fits described in Chapter 8.

Photons

Two methods are used to estimate photon trigger efficiencies [90]. The first, called the bootstrap method, relies on iteratively building the trigger efficiency from a sample of events selected using a lower level or unbiased trigger. The efficiency for the bootstrap sample of events is determined by comparing the number of events in the sample to the number of photons that pass offline reconstruction, isolation, and identification. To account for any biases, a systematic uncertainty is assigned based on the discrepancy between the efficiency measured in data and simulated events. In addition, the photon trigger efficiency is estimated using radiative $Z \rightarrow ll\gamma$ decays where the photon is produced as final state radiation off of one of the leptons from the Z boson decay. Statistical uncertainties are accounted for, and systematic uncertainties are obtained by varying the selection requirements on the Z boson decay products. Both methods show similar results for photons with transverse energies above 5 GeV.

The photon identification efficiency is estimated using three distinct methods [72]. All three methods correct for the mismodelling of photon shower shapes in simulation using control regions enriched in real photons. A systematic uncertainty associated to the modelling of the tails of the distribution is obtained by comparing the predictions from different simulation software packages. The first method estimates the photon identification efficiency in $Z \rightarrow ll\gamma$ events. Systematic uncertainties are assigned using a

closure test in simulation, with another systematic uncertainty associated to the use of different simulation software packages to assess modelling uncertainties. An additional systematic uncertainty is assigned to the invariant mass range used to reconstruct the Z boson decays. The second method relies on extrapolating the measured identification efficiencies from $Z \rightarrow ee$ events by modifying the electron shower shapes to resemble those of photons. Systematic uncertainties are estimated through a closure test in simulation. In addition, a systematic uncertainty is obtained by varying the parameters that go into the shower shape transformation. Finally, systematic uncertainties on the simulated $W + jets$ and multi-jet backgrounds that account for misidentified electrons in the reconstructed $Z \rightarrow ee$ events are considered. The final method for measuring the photon identification efficiency relies on a sample of inclusive photon production events in data. These events contain a mixture of prompt photons and jets misidentified as photons. A matrix method is used to extract the photon identification efficiency. The largest systematic uncertainty for this method comes from a closure test performed in simulation. The photon identification efficiencies estimated using all three methods agree within statistical and systematic uncertainties and are combined assuming their uncertainties are uncorrelated.

Photon isolation mismodelling in simulation is corrected for using a data-driven method involving fits to photon isolation energy distributions in regions dominated by real photons [72]. The photon isolation efficiency is then estimated with $Z \rightarrow ll\gamma$ events for photons with $10 \text{ GeV} < p_{\text{T}}^{\gamma} < 100 \text{ GeV}$, and with a sample of inclusive photons for photons with $25 \text{ GeV} < p_{\text{T}}^{\gamma} < 1.5 \text{ TeV}$. The isolation efficiency estimate using $Z \rightarrow ll\gamma$ events is similar to the method used for the photon identification efficiency estimate and the same sources of uncertainty are taken into account. Using the inclusive photon dataset, isolation energy efficiencies are estimated through fits to the photon isolation energy distributions in bins of photon p_{T} and η . Background from jets misidentified as photons is estimated using a 1D template fit method similar to the one described in Section 6.4. Alternate sets of photon identification criteria (different *LoosePrime* working points) are used in order to

estimate a systematic uncertainty related to the background estimate. In addition, uncertainties related to the isolation energy fits and signal leakage into the background templates are considered. Isolation efficiency measurements from the two methods in the overlap between $25 \text{ GeV} < p_T^\gamma < 100 \text{ GeV}$ are combined using a weighted average, and their uncertainties are assumed to be uncorrelated.

Overall, the uncertainty on the photon efficiencies leads to a 1.3% uncertainty on the total estimated yield in the SR before the likelihood fits described in Chapter 8.

Muons

The single muon trigger efficiencies are estimated using a *tag-and-probe* method with $Z \rightarrow \mu\mu$ events for muons with $p_T < 100 \text{ GeV}$. For muons with larger transverse momenta, $t\bar{t}$ and $W + jets$ events are used [91]. Statistical and systematic uncertainties are accounted for. The largest sources of uncertainty on the single muon trigger efficiency comes from the E_T^{miss} estimate in $t\bar{t}$ and $W + jets$ events and an uncertainty obtained by varying the muon quality working points.

The muon reconstruction, identification, isolation, and vertex association efficiencies are estimated using a *tag-and-probe* method with $Z \rightarrow \mu\mu$ and $J/\Psi \rightarrow \mu\mu$ events [77, 78]. Muon p_T and η dependent correction factors are derived to ensure that muon efficiencies in data and simulation match. Several sources of systematic uncertainty on the correction factors are considered. These include uncertainties on the background modelling, uncertainties on the extrapolation of efficiency correction factors to high energy muons, uncertainties associated to the smoothing procedure used for the invariant mass distributions of the reconstructed Z and J/Ψ resonances, and uncertainties on the cross section and luminosity estimates. Additional sources of systematic uncertainties specific to certain muon efficiency correction factors described in [78] are also taken into account.

Overall, the uncertainty on the muon efficiencies leads to a 0.4% uncertainty on the total estimated yield in the SR before the likelihood fits described in Chapter 8.

Jets

The efficiency of the jet-vertex-tagger (JVT) working point described in Section 4.5 is based on a multivariate discriminant tuned to reject jets from pileup. The JVT efficiency is estimated in $Z \rightarrow \mu\mu + jets$ events using a *tag-and-probe* method, where the jets are used as *probes* recoiling off of the reconstructed Z boson. Systematic uncertainties on the correction factors include an uncertainty on the modelling of the angular separation between the jet and the Z boson and an uncertainty based on discrepancies between the JVT efficiencies measured using different simulation software packages. Overall, the uncertainty on the jet JVT efficiency leads to a 1.0% uncertainty on the total estimated yield in the SR before the likelihood fits described in Chapter 8.

The efficiency for the b -tagging algorithm (described in Section 4.5.2) is estimated using $t\bar{t}$ events by selecting events with two leptons and two jets [86]. Four regions are formed that either enhance or suppress the b -jet contributions to the leading or subleading jet. The b -tagging efficiency and jet flavour compositions in all four regions are fit simultaneously. Statistical uncertainties are accounted for, in addition to systematic uncertainties from the detector calibration and simulation modelling. Overall, the uncertainty on the jet b -tagging efficiency leads to a 0.2% uncertainty on the total estimated yield in the SR before the likelihood fits described in Chapter 8.

7.1.3 Luminosity

The integrated luminosity measurement comes with its own experimental uncertainties described in [42]. A total uncertainty of 0.83% on the final luminosity measurement is taken into account in the final $W\gamma\gamma$ signal extraction and unfolding fits. The largest contribution to the luminosity measurement uncertainty comes from uncertainties related to the *van der Meer* scan calibration method [113]. In the *van der Meer* scan calibration method, the spatial distribution of protons in the LHC bunches is estimated by changing

the positioning of the proton beams relative to each other in the transverse plane. A measurement of the relative proton-proton interaction rate as a function of the separation between the beams is then performed to measure the shape and size of the interaction region. Overall, the uncertainty on the measured luminosity leads to a 0.3% uncertainty on the total estimated yield in the SR before the likelihood fits described in Chapter 8.

Pileup

Additional proton-proton pileup collisions are overlaid onto simulated events as described in Section 6.1. The number of pileup collisions per bunch crossing is reweighted to match the measured average number of interactions per bunch crossing over the course of the Run 2 data taking period shown in Figure 3.3. The statistical uncertainty on the reweighting procedure is taken into account as a systematic uncertainty in the final fit described in Chapter 8. Overall, the uncertainty on the pileup reweighting procedure leads to a 0.6% uncertainty on the total estimated yield in the SR before the likelihood fits described in Chapter 8.

7.2 Theoretical Uncertainties

In addition to statistical uncertainties on the simulation samples due to the limited number of events that are generated, several other sources of systematic uncertainty are considered. These account for the limited accuracy of the perturbative and non-perturbative calculations that go into the full simulation chain described in Section 6.1. The treatment of theoretical uncertainties on simulation samples is based on recommendations made by the ATLAS Physics Modelling Group and adopted by most ATLAS analyses. Overall, the uncertainties on the theoretical modelling in simulation lead to a 1.2% uncertainty from the simulated signal events and 1.1% from the simulated background events on the total estimated yield in the SR before the likelihood fits described in Chapter 8.

7.2.1 Parton Distribution Functions

Uncertainties arising from the Parton Distribution Functions (PDFs) include both theoretical and experimental uncertainties. The PDF4LHC group provides recommended recipes to estimate systematic uncertainties arising from the use of PDFs in simulation [114]. The uncertainties associated with PDFs leads to a 1.3% uncertainty on the total estimated number of signal $W\gamma\gamma$ events in the SR before the likelihood fits described in Chapter 8.

7.2.2 Strong Coupling Constant

The value of the strong coupling constant α_S and its uncertainty are determined through a global fit to an ensemble of hard scattering data [115]. As described in Section 6.1, the value of the strong coupling constant is used and fully correlated across many stages of the simulation chain. The uncertainty on α_S is propagated to the final number of estimated events in simulation by varying its value up and down by a fixed amount. The uncertainty on the strong coupling constant leads to a 0.9% uncertainty on the total estimated number of signal $W\gamma\gamma$ events in the SR before the likelihood fits described in Chapter 8.

7.2.3 Renormalization and Factorization Scales

Missing higher order terms in the perturbative QCD calculations of the matrix elements of simulated processes are evaluated by varying the unphysical renormalization and factorization scales independently by factors of 0.5 and 2, giving 7 possible variations (including nominal) [116]. The up and down uncertainties associated to the choice of renormalization and factorization scale in simulation is taken as the largest up and down variations of the 7 possible variations. The uncertainty associated to the renormalization and factorization scales leads to an 11% uncertainty on the total estimated number of signal $W\gamma\gamma$ events in the SR before the likelihood fits described in Chapter 8.

7.3 Summary of Uncertainties

A summary of the systematic uncertainties and their effect on the total estimated yield in the analysis SR before the likelihood fits described in Chapter 8 is shown in Table 7.1. The largest systematic uncertainty comes from the data-driven background estimates described in Chapter 6. The next largest sources of uncertainty comes from the uncertainties on the combined photon trigger, reconstruction, identification, and isolation efficiencies. The third and fourth largest uncertainties come from the theoretical uncertainties on the signal and background estimates in simulation, respectively. As described in Chapters 8 and 9, all sources of uncertainty are taken into account in the fits performed to determine the expected and observed statistical significance as well as the cross section measurement of the $W\gamma\gamma$ process.

Source of Uncertainty	Uncertainty on Yield (%)
Data-Driven Backgrounds	4.5
Photon Efficiencies	1.3
Signal Theoretical Uncertainties	1.2
Background Theoretical Uncertainties	1.1
Jet Energy Scale and Resolution	1.0
Jet JVT	1.0
Pileup Reweighting	0.6
Missing Transverse Energy	0.4
Muon Efficiencies	0.4
Luminosity	0.3
Electron and Photon Scale and Resolution	0.2
b -tagging Efficiency	0.2
Muon Energy Scale and Resolution	0.1
Electron Efficiencies	0.0

Table 7.1: Systematic uncertainties on the total predicted event yield in the Signal Region before the final likelihood fit. Uncertainties from individual sources within a category are added in quadrature.

Chapter 8

Statistical Model

This chapter presents the statistical model used to extract the $W\gamma\gamma$ signal significance and the fiducial cross section. This model is constructed using the signal and background estimates along with their associated statistical and systematic uncertainties. It is based on a Frequentist interpretation of statistics. The model is used to measure the expected and observed $W\gamma\gamma$ signal significance with respect to the background only hypothesis in the Signal Region (SR). In addition, in order to extract a fiducial cross section, the same statistical model is used to unfold the measurement into a truth-level phase space. This is done by essentially deconvolving the detector efficiency and acceptance effects from the detector-level measurement in a process called *unfolding*. An overview of the methods presented in this chapter can be found in Reference [8], with a more in-depth review in Reference [117].

8.1 Signal Significance Extraction

The probability to observe data \mathbf{x} given a hypothesis H is labeled as $P(\mathbf{x}|H)$. For a measured and fixed set of data points, the probability is called the likelihood, and is labeled as $\mathcal{L}(H)$. The likelihood is a function of the hypothesis model parameters $\boldsymbol{\theta}$ and is usually written as

$\mathcal{L}(\boldsymbol{\theta})$.

In the $W\gamma\gamma$ analysis, the model parameters are one parameter of interest (p.o.i.) and several Nuisance Parameters (NPs). The signal strength μ is the p.o.i. and is defined as the ratio of the fitted signal cross section to the signal cross section predicted by the Standard Model. The NPs defined in the statistical model can be grouped into three categories. The $\boldsymbol{\alpha}$ NPs represent the systematic, experimental, and theoretical uncertainties on the predicted number of signal and background events from simulation and from data-driven methods. The $\boldsymbol{\gamma}$ NPs represent the statistical uncertainties on the simulated background estimates. Finally, the τ NP describes the overall normalization scale factor for the top background.

Events belonging to the CRTop region are split into three bins of leading photon p_T , while events in the SR are grouped into one single bin. Each bin is treated as an independent counting experiment. The likelihood function $\mathcal{L}(\boldsymbol{\theta})$ for bin i is represented by a Poisson distribution that depends on the observed number of events n_i , the expected number of signal events $S_i(\boldsymbol{\alpha})$, and the expected number of background events $B_i(\boldsymbol{\alpha}, \boldsymbol{\gamma}, \boldsymbol{\tau})$. The total likelihood function $\mathcal{L}(\boldsymbol{\theta})$ is constructed by multiplying the likelihood functions $\mathcal{L}_i(\boldsymbol{\theta})$ for each individual bin i :

$$\mathcal{L}(\mu, \boldsymbol{\alpha}, \boldsymbol{\gamma}, \boldsymbol{\tau}) = \prod_{i=1}^{n_{\text{bins}}} \mathcal{L}_i(\mu, \boldsymbol{\alpha}, \boldsymbol{\gamma}, \boldsymbol{\tau}) = \prod_{i=1}^{n_{\text{bins}}} P(n_i | \mu S_i(\boldsymbol{\alpha}) + B_i(\boldsymbol{\alpha}, \boldsymbol{\gamma}, \boldsymbol{\tau})), \quad (8.1)$$

where P is the Poisson distribution:

$$P(k|\lambda) = \frac{\lambda^k e^{-\lambda}}{k!}, \quad (8.2)$$

where k is an integer representing the number of observed events and λ is the number of expected events.

The significance represents the probability of obtaining the observed number of events or a more extreme deviation from the background-only hypothesis. As such, the theoretical uncertainties on the estimated number of $W\gamma\gamma$ signal events from simulation are not included

in the likelihood used to extract the $W\gamma\gamma$ significance, but are included in the fit used to measure the $W\gamma\gamma$ cross section described in the next section.

The nuisance parameters $\boldsymbol{\alpha}$, representing the systematic, experimental, and theoretical uncertainties, are individually constrained using a Gaussian probability density function:

$$\mathcal{L}_\alpha(\boldsymbol{\alpha}) = \prod_{j=1}^{n_\alpha} G(\alpha_j|0, 1), \quad (8.3)$$

where n_α corresponds to the number of $\boldsymbol{\alpha}$ nuisance parameters. Here, G represents a normalized Gaussian distribution:

$$G(y|m, s) = \frac{1}{\sqrt{2\pi s^2}} e^{-\frac{(y-m)^2}{2s^2}}, \quad (8.4)$$

where y is the independent variable, m is the mean, and s the standard deviation. The choice of using a Gaussian distribution is motivated by the fact that most experimental uncertainties originate from secondary measurements and can be interpreted as representing a 68% confidence interval.

Theoretical uncertainties and certain systematic uncertainties associated with the data-driven background estimates cannot however be interpreted within a frequentist framework as representing a 68% confidence interval since they are not the outcomes of previous measurements. For example, this includes the theoretical uncertainties obtained by varying the factorization and renormalization scales for signal and background estimates from simulation. In these cases, the choice of describing the NPs as Gaussian constraints can be interpreted as Bayesian constraints with a constant prior. Experimental uncertainties are fully correlated from bin to bin across the different regions of phase space and across the different simulated processes. Other uncertainties such as the theoretical uncertainties are instead considered to be uncorrelated across processes. Certain systematic uncertainties associated with the data-driven backgrounds are fully correlated across the

SR and CRTop regions. These include the systematic uncertainties associated with the $e \rightarrow \gamma$ and $j \rightarrow \ell$ background estimates. However, the portion of the uncertainty that comes from the limited statistics in the fake rate application regions for the $e \rightarrow \gamma$ and $j \rightarrow \ell$ background estimates is uncorrelated from bin to bin and across regions. The uncertainty on the $j \rightarrow \gamma$ background is considered fully uncorrelated between CRTop and the SR due to the different methods used in estimating them, as described in Section 6.4.

The γ NPs representing the statistical uncertainties on the simulated event samples are uncorrelated across the different simulated processes and across bins. In each bin, the total statistical uncertainty is calculated as the sum in quadrature of the statistical uncertainty from each simulated sample. These statistical uncertainties are Poisson distributed and are constrained in the likelihood function with the following term:

$$\mathcal{L}_\gamma(\boldsymbol{\gamma}) = \prod_{l=1}^{n_{\text{bins}}} P'(B_l^\gamma | \gamma B_l^\gamma), \quad (8.5)$$

where B_l^γ denote the backgrounds which are estimated directly in simulation. The symbol P' is the Poisson distribution defined with the Gamma function in the denominator (instead of a factorial) since simulated events have non-integer event weights:

$$P'(k|\lambda) = \frac{\lambda^k e^{-\lambda}}{\Gamma(k)}, \quad (8.6)$$

where $\Gamma(z)$ is the Gamma function:

$$\Gamma(z) = \int_0^\infty t^{z-1} e^{-t} dt. \quad (8.7)$$

The total likelihood is given by:

$$\mathcal{L}(\boldsymbol{\mu}, \boldsymbol{\alpha}, \boldsymbol{\gamma}, \boldsymbol{\tau}) = \prod_{i=1}^{n_{\text{bins}}} P(n_i | \mu S_i(\boldsymbol{\alpha}) + B_i(\boldsymbol{\alpha}, \boldsymbol{\gamma}, \boldsymbol{\tau})) \prod_{j=1}^{n_\alpha} G(\alpha_j | 0, 1) \prod_{l=1}^{n_{\text{bins}}} P'(B_l^\gamma | \gamma B_l^\gamma). \quad (8.8)$$

The likelihood function parameters are estimated using the using the Maximum Likelihood Estimator (MLE) method, which consists in finding the values of all the parameters θ that maximize the likelihood function such that:

$$\frac{\partial \mathcal{L}}{\partial \theta_i} = 0. \quad (8.9)$$

In order to test whether or not the measured value of the signal strength μ constitutes an observation, the profile likelihood ratio test statistic is used. For a signal strength μ and NPs ν , $\hat{\mu}$ and $\hat{\nu}$ are defined as their respective values which maximize $\mathcal{L}(\mu, \nu)$. These are called the unconditional maximum likelihood estimators. In addition, $\hat{\nu}$ are defined as the values of the NPs that maximize $\mathcal{L}(\mu, \nu)$ for fixed μ . These are called the conditional maximum likelihood estimators. From these variables, the profile likelihood ratio is constructed as:

$$\lambda = \frac{\mathcal{L}(\mu, \hat{\nu})}{\mathcal{L}(\hat{\mu}, \hat{\nu})}. \quad (8.10)$$

The profile likelihood ratio tends to a value of 1 when the observed data is close to the Standard Model prediction. To quantify the compatibility between the signal strength μ and the measured data, a test statistic is defined as:

$$t(\mu) = \begin{cases} -2\ln(\lambda(\mu)), & \text{if } \mu > 0 \\ 0, & \text{if } \mu \leq 0, \end{cases} \quad (8.11)$$

since the signal strength should be greater or equal to 0. A larger value of the test statistic $t(\mu)$ in this case signifies poorer agreement with background only hypothesis. As such, the p -value, or the probability of observing data \mathbf{x} of equal or lesser compatibility with the background only hypothesis, is then given by:

$$p = \int_{t_{\text{obs}}}^{\infty} f(t|\mu) dt, \quad (8.12)$$

where $f(t|\mu)$ is the probability density function of t for a given μ . According to Wilk's theorem [118], the distribution for the test statistic $t(\mu)$ tends to the χ^2 distribution in the large statistics limit. The p -value is usually converted to a significance \mathcal{Z} , which represents the number of standard deviations of a Gaussian distribution:

$$\mathcal{Z} = \Phi^{-1}(1 - p), \quad (8.13)$$

where Φ^{-1} is the inverse cumulative distribution of the standard Gaussian probability distribution. The threshold for discovery in particle physics is, by convention, established as $\mathcal{Z} = 5\sigma$, which corresponds to a p -value of 2.87×10^{-7} .

The likelihood function described in this section is used to extract the expected and observed significance of the $W\gamma\gamma$ process. The results from these two fits are presented in the next chapter, Chapter 9.

8.2 Fiducial Cross Section

In addition to the two likelihood fits done to extract the expected and observed signal significance of the $W\gamma\gamma$ process, a third likelihood fit is performed to extract the $W\gamma\gamma$ fiducial cross section. This third likelihood fit is detailed in this chapter. In order to obtain a measurement of the fiducial cross section of the $pp \rightarrow W\gamma\gamma$ process, the ATLAS detector efficiency and acceptance need to be deconvoluted from the observed signal strength. In other words, this is done to determine how many truth-level events (before the detector simulation) are expected given an observed number of detector-level events.

The first step consists in defining a fiducial phase space for the cross section measurement. The truth-level fiducial selection is chosen to be close to the detector-level selection to avoid extrapolating too far into regions of phase space not covered by the detector measurement. The truth selection makes use of so-called *dressed* leptons, which are electrons and muons that

Truth-Level Fiducial Selection
1 <i>dressed</i> electron or muon with $p_T^\ell > 25$ GeV and $ \eta^\ell < 2.47$
2 photons with $p_T^\gamma > 20$ GeV, $ \eta^\gamma < 2.37$, and $E_T^{\text{iso,truth}} _{\Delta R < 0.4} - 0.032 \cdot E_T < 6.53$ GeV
$\Delta R_{\gamma\gamma} > 0.4$ and $\Delta R_{\ell\gamma} > 0.4$
$E_T^{\text{miss}} > 25$ GeV and $m_T^W > 40$ GeV
$n_{b\text{jets}}=0$

Table 8.1: Summary of the truth-level selection criteria defining the region of phase space used to measure the fiducial cross section of the $pp \rightarrow W\gamma\gamma$ process.

are recombined at truth-level with all of their radiated photons within a cone of $\Delta R = 0.1$.

To construct a truth-level selection close to the detector-level selection, an isolation cut for photons at truth-level is estimated that is comparable to the isolation cut at detector-level. The truth versus reconstructed isolation energy for photons, $E_T^{\text{iso,truth}}$ and $E_T^{\text{iso,reco}}$ respectively, in simulated $W\gamma\gamma$ events is plotted in bins of truth photon p_T as shown in Figure 8.1. It can be seen that the truth isolation energy is on average larger than the reconstructed isolation energy for photons. This is due to the fact that a fraction of the truth isolation energy comes from the underlying event and pileup which is accounted for and subtracted in the reconstructed isolation energy as described in Section 4.2.3. A linear fit is performed to extract the $E_T^{\text{iso,truth}}$ cut value corresponding to the isolation cut applied at detector-level of $E_T^{\text{iso,reco}}|_{\Delta R < 0.4} - 0.022 \cdot E_T < 2.45$ GeV. The values of $E_T^{\text{iso,truth}}$ found in each bin of truth photon p_T are then plotted with their uncertainties as a function of truth photon p_T as shown in Figure 8.2. A linear fit is done to extract the p_T -dependent truth isolation energy cut of $E_T^{\text{iso,truth}}|_{\Delta R < 0.4} - 0.032 \cdot E_T < 6.53$ GeV.

The truth-level fiducial selection is summarized in Table 8.1. After having defined the fiducial phase space for the cross section measurement, the next step consists in deconvoluting the detector efficiency and acceptance from the selected signal events. This is done using

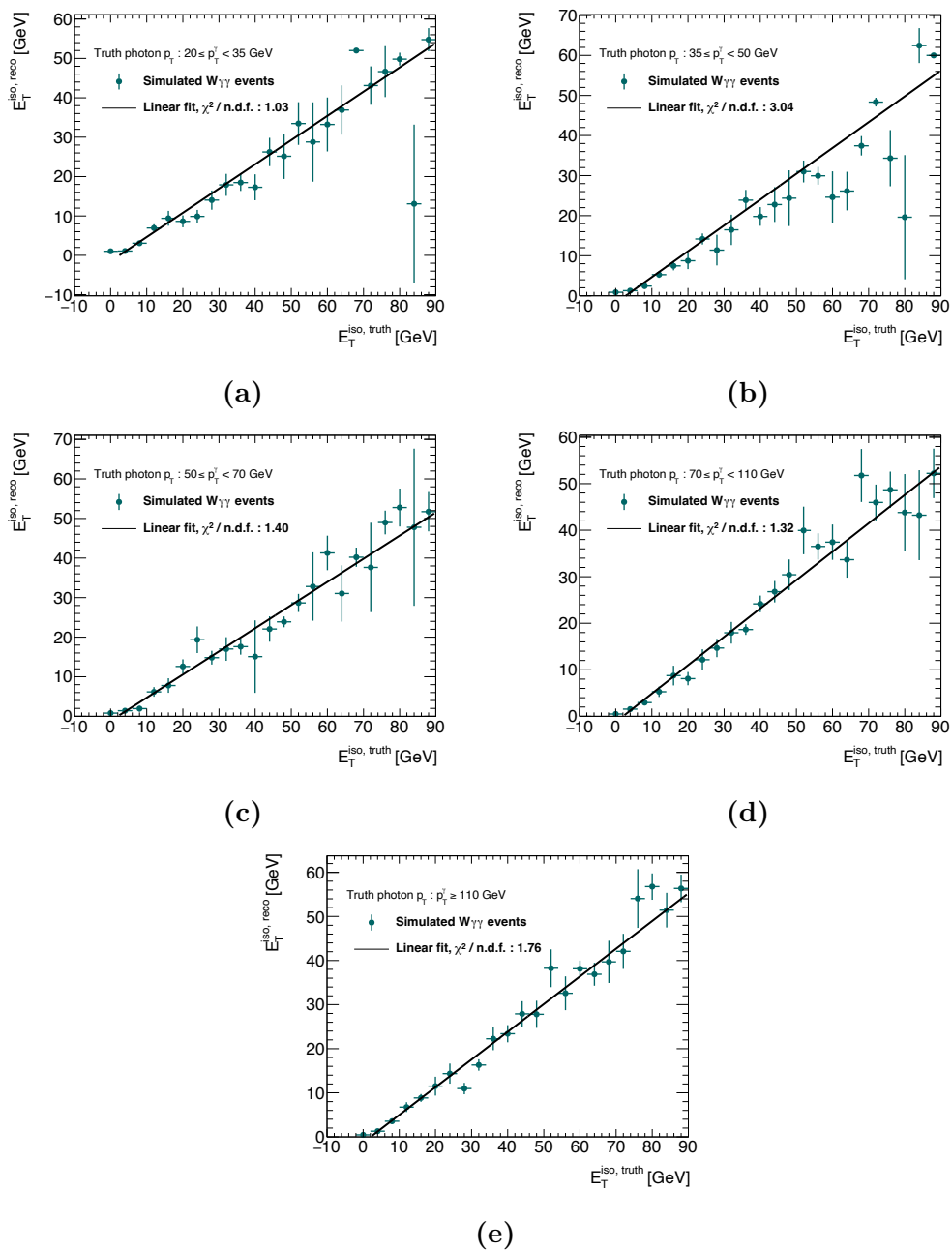


Figure 8.1: Reconstructed photon isolation energy ($E_T^{\text{iso, reco}}$) as a function of truth photon isolation energy ($E_T^{\text{iso, truth}}$) in bins of truth photon p_T in simulated $W\gamma\gamma$ events satisfying the truth-level fiducial selection requirements without the photon isolation requirement. A linear fit is shown overlaid in black.

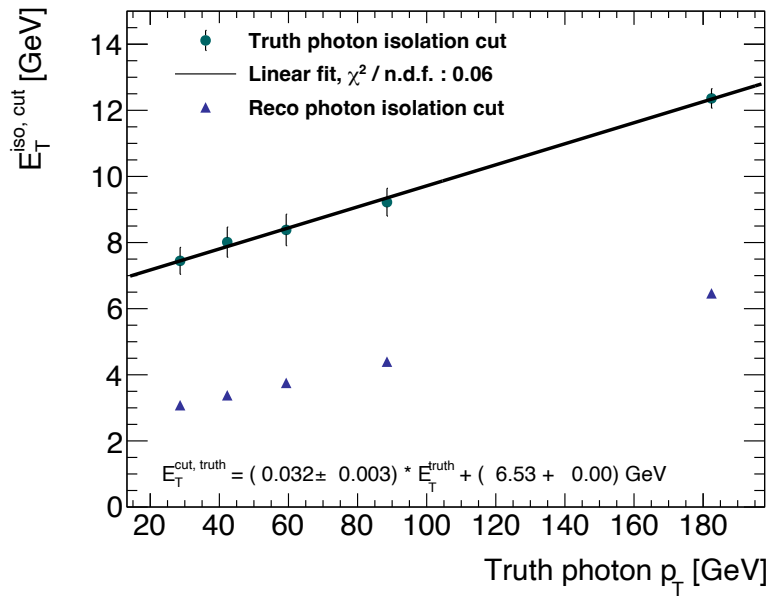


Figure 8.2: Value of the truth isolation energy cut equivalent to the reconstructed isolation energy cut as a function of truth photon p_T . A linear fit is shown overlaid in black, with the fitted parameter values shown with their uncertainties at the bottom of the figure. The values of the reconstructed isolation energy cut used at the detector level ($E_T^{\text{iso, reco}} |_{\Delta R < 0.4} - 0.022 \cdot E_T < 2.45 \text{ GeV}$) are represented by the purple triangles.

an unfolding correction factor C which is defined as the ratio of the expected number of reconstructed $W\gamma\gamma$ signal events in the SR (N_{reco}) to the number of $W\gamma\gamma$ signal events satisfying the truth-level fiducial selection (N_{truth}):

$$C = \frac{N_{\text{reco}}}{N_{\text{truth}}}. \quad (8.14)$$

The measured fiducial cross section is defined to be the production cross section of the $pp \rightarrow W\gamma\gamma$ process for events in which the W boson decays to either an electron/neutrino pair or a muon/neutrino pair. While events selected at detector-level include events in which the W boson decays to a tau/neutrino pair and the tau lepton subsequently decays leptonically, these events are not part of the fiducial cross section measurement definition. The measured fiducial cross section for the electrons and muon decay channels of the W boson is given by:

$$\sigma_{\text{fid}}^{e+\mu} = \frac{N^{\text{data}} - N_{\text{reco}}^{\tau} - N_{\text{reco}}^{\text{bkg}}}{C^{e+\mu} \mathcal{L}}, \quad (8.15)$$

where $C^{e+\mu} = N_{\text{reco}}^{e+\mu}/N_{\text{truth}}^{e+\mu}$ is the correction factor for the combined electron and muon decay channels of the W boson, not including electrons and muons from $W \rightarrow \tau\nu_{\tau}$ decays where the τ subsequently decays leptonically. In addition, N^{data} is number of events measured in data, N_{reco}^{τ} is the estimated number of $W(\rightarrow \tau\nu_{\tau})\gamma\gamma$ events at detector-level where the τ subsequently decays leptonically, and $N_{\text{reco}}^{\text{bkg}}$ is the estimated number of events at detector-level from all background sources. The number of $W \rightarrow \tau\nu_{\tau}$ events at detector-level can be written as:

$$N_{\text{reco}}^{\tau} = \sigma_{\text{fid}}^{\tau} C^{\tau} \mathcal{L}, \quad (8.16)$$

where $C^{\tau} = N_{\text{reco}}^{\tau}/N_{\text{truth}}^{\tau}$ and $\sigma_{\text{fid}}^{\tau}$ is the fiducial cross section for the $pp \rightarrow W(\rightarrow \tau\nu_{\tau})\gamma\gamma$ process. Assuming lepton universality, then $\sigma_{\text{fid}}^{e+\mu} = 2\sigma_{\text{truth}}^{\tau}$, where $\sigma_{\text{fid}}^{e+\mu}$ is the truth-level cross

section for the electron and muon decay channels of the W boson, while $\sigma_{\text{truth}}^\tau$ is the truth-level cross section for the tau decay channel of the W boson. Consequently, $N_{\text{truth}}^{e+\mu} = 2N_{\text{truth}}^\tau$. Equation 8.15 can then be rewritten and rearranged as:

$$\sigma_{\text{fid}}^{e+\mu} = \frac{N^{\text{data}} - N_{\text{reco}}^{\text{bkg}}}{C^{e+\mu} \mathcal{L}} - \frac{\frac{1}{2} \sigma_{\text{fid}}^{e+\mu} C^\tau \mathcal{L}}{C^{e+\mu} \mathcal{L}}, \quad (8.17)$$

$$\sigma_{\text{fid}}^{e+\mu} \left(1 + \frac{C^\tau}{2C^{e+\mu}} \right) = \frac{N^{\text{data}} - N_{\text{reco}}^{\text{bkg}}}{C^{e+\mu} \mathcal{L}}, \quad (8.18)$$

$$\sigma_{\text{fid}}^{e+\mu} = \frac{N^{\text{data}} - N_{\text{reco}}^{\text{bkg}}}{\left(C^{e+\mu} + \frac{1}{2} C^\tau \right) \mathcal{L}}. \quad (8.19)$$

Finally, since $C^\tau = N_{\text{reco}}^\tau / N_{\text{truth}}^\tau = N_{\text{reco}}^\tau / \frac{1}{2} N_{\text{truth}}^{e+\mu}$,

$$\sigma_{\text{fid}}^{e+\mu} = \frac{N^{\text{data}} - N_{\text{reco}}^{\text{bkg}}}{C \mathcal{L}}, \quad (8.20)$$

where $C = \frac{N_{\text{reco}}^{e+\mu+\tau}}{N_{\text{truth}}^{e+\mu}}$. As such, while $W \rightarrow \tau\nu_\tau$ decays are included in the detector-level selection when the τ decays leptonically, these events are not included in the truth-level selection. This is done in order to unfold and obtain a truth-level cross section for the combined electron and muon decay channels of the W boson in the $pp \rightarrow W\gamma\gamma$ process. In what follows, N_{reco} is used as shorthand for $N_{\text{reco}}^{e+\mu+\tau}$ and N_{truth} is used as shorthand for $N_{\text{truth}}^{e+\mu}$.

Care must be taken in the calculation of the statistical uncertainty of the unfolding correction factor C . There is overlap between the events that pass the truth-level selection and the detector-level selection. As such, the statistical uncertainties on events that appear in both the numerator and denominator of the correction factor are fully correlated. However, events that pass the truth-level and detector-level selections have different event weights. This is due to the fact that events that pass the truth-level selection are not subject to any detector efficiency or acceptance scale factors, unlike detector-level events.

To address this, the statistical uncertainties on N_{truth} and N_{reco} are propagated to C through a bootstrapping procedure assuming Gaussian distributed statistical uncertainties. This is done by resampling the uncertainty distributions of the events in the numerator and the denominator from separate, uncorrelated distributions for the events that are non-overlapping, while sampling from a common distribution for events that are overlapping. A different scaling is then applied to the numerator and denominators to correct for the different event weights. The resulting uncertainty is the standard deviation of 10,000 bootstrap samples.

All statistical, experimental, theoretical, and data-driven uncertainties are propagated through the correction factor calculation. In addition, as opposed to the signal significance extraction fit, theoretical systematic uncertainties on the signal simulation samples are also accounted for in the unfolding on both N_{reco} and N_{truth} . Any correlations between the uncertainties on the numerator and denominator of the correction factor C are fully accounted for.

The correction factor is computed to be $C = 0.210 \pm 0.004$ using the Sherpa NLO simulation, including statistical uncertainties only. The correction factor was also estimated using the signal $W\gamma\gamma$ MadGraph NLO simulation samples, showing good agreement within statistical uncertainties with the nominal correction factor obtained using Sherpa.

While the $W(\rightarrow \tau\nu_\tau)\gamma\gamma$ contribution is not included in the truth-level fiducial phase space definition, it still contributes to signal-like events at detector-level. As such, it must still be allowed to float in the fit along with the unfolded $W(\rightarrow e\nu_e/\mu\nu_\mu)\gamma\gamma$ contributions with respect to the signal strength μ . The same signal strength is used due to lepton universality and the fact that the kinematic properties of tau leptons are otherwise well-modelled in simulation. In the unfolding likelihood fit, the $\mu S_i(\boldsymbol{\alpha})$ term in the SR in Equation 8.8 becomes:

$$\mu S_i(\boldsymbol{\alpha}) = \mu (N_{\text{reco}}(\boldsymbol{\alpha}))_i = \mu \left(N_{\text{reco}}(\boldsymbol{\alpha}) \times \frac{\sigma_{\text{truth}}^{e+\mu} \mathcal{L}}{N_{\text{truth}}(\boldsymbol{\alpha})} \right)_i = \mu (C(\boldsymbol{\alpha}) \sigma_{\text{truth}}^{e+\mu} \mathcal{L})_i. \quad (8.21)$$

Maximizing this new likelihood function results in an unfolded signal strength μ . This unfolded signal strength μ is multiplied by the predicted cross section $\sigma_{\text{truth}}^{e+\mu}$ to obtain the measured fiducial cross section $\sigma_{\text{meas}}^{e+\mu}$. The results of the unfolded likelihood fit are presented in the next chapter, Chapter 9, along with the results from the expected and observed signal significance likelihood fits described in the previous section.

Chapter 9

Results

In this chapter, the results of the three likelihood fits of the $W\gamma\gamma$ analysis statistical model described in Chapter 8 are presented. These fits are performed to extract the expected and observed signal significance of the $W\gamma\gamma$ process and obtain a measurement of the unfolded $W\gamma\gamma$ fiducial cross section.

Three separate likelihood scans are performed. The first is the expected likelihood fit which is performed as described in Section 8.1 using pseudo-data (prior to the unblinding of the SR), giving an expected signal strength and significance. Note that data in all other regions is unblinded for the expected results presented here. Pseudo-data, also called *Asimov* data, is taken to be the predicted number of signal and background events in the SR. Asimov data is given a statistical uncertainty of \sqrt{n} for n predicted events. As such, the expected signal strength μ obtained from a likelihood fit to this pseudo-data should be exactly one. In practice, the fitted value of the signal strength is not exactly one since the fit includes real data in the CRTop region which is predicted to be made up of approximately 8% signal events. The observed likelihood fit is performed the same way as the expected likelihood fit but using the unblinded data in the SR. Finally, the unfolded likelihood fit is performed as described in Section 8.2 to extract the fiducial cross section.

	Expected	Observed	Unfolded
μ	$1.01^{+0.17}_{-0.16}$	$1.01^{+0.17}_{-0.16}$	$1.01^{+0.18}_{-0.17}$
τ	$0.83^{+0.21}_{-0.25}$	$0.83^{+0.21}_{-0.25}$	$0.83^{+0.21}_{-0.25}$

Table 9.1: Best fit values of the signal strength (μ) and top normalization factor (τ) obtained from the expected, observed and unfolded likelihood fits.

The value of the negative log likelihood with respect to its minimum value ($-\Delta\ln(\mathcal{L})$) as a function of the signal strength μ is shown in Figure 9.1 for the expected, observed, and unfolded likelihood fits. The corresponding fitted signal strengths and top background normalization values are summarized in Table 9.1. Since CRTop is ublinded in all three fits and signal in CRTop is not unfolded to truth-level in the unfolding likelihood fit, the top background normalization factor is the same in all three fits. In addition, the negative log likelihood scans and the values of their respective extracted signal strengths are very similar for the expected and observed significance fits due to the similarity between prediction and data prior to the observed significance fit in the SR. The negative log likelihood scan for the unfolding fit is slightly wider than the ones obtained for for the expected and observed significance fits, giving a slightly larger uncertainty on the extracted unfolded signal strength. This is expected due to the additional inclusion of the unfolding correction factor and its additional associated uncertainties as described in Section 8.2.

The observed pre- and post-fit event yields for the signal and background estimates in each of the bins in the CRTop, VRTop, and SR regions are shown in Figure 9.2 for the observed significance likelihood fit. Only the SR and CRTop regions are included in the observed significance likelihood fit. The best-fit value of the top normalization factor is used to estimate the number of background events from processes with a top quark in their final state in VRTop and the SR. A comparison of the number of observed and predicted events in the VRTop region is used to validate the top background estimate in the SR. Good agreement between the number of observed and predicted events is seen in all regions

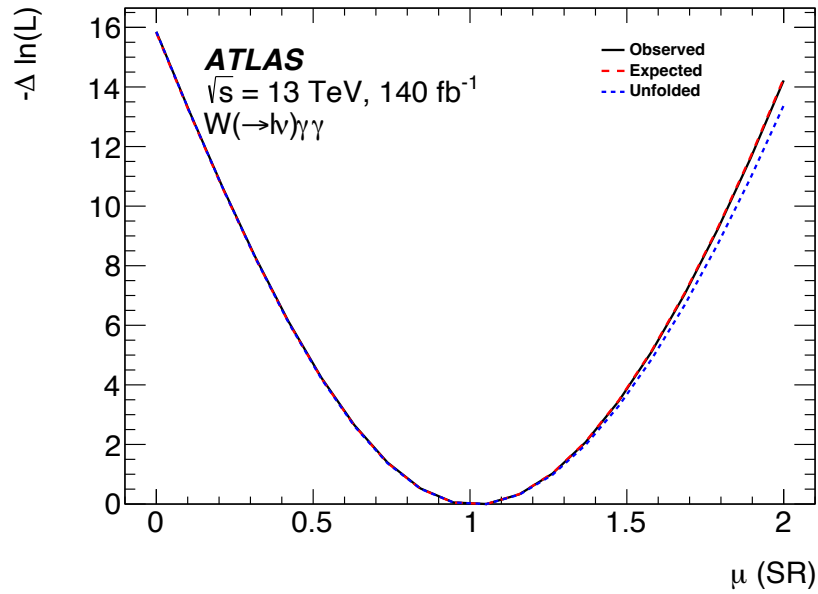


Figure 9.1: Scan of the negative log likelihood with respect to its minimum value, $-\Delta \ln(L)$, as a function of the signal strength μ for the observed, expected, and unfolded likelihood fits.

Source	CRTop	VRTop	SR
$W\gamma\gamma$	28 ± 5	4.3 ± 2.3	410 ± 60
$j \rightarrow \gamma$	42 ± 20	4.5 ± 2.4	420 ± 50
$e \rightarrow \gamma$	120 ± 9	15.7 ± 1.5	155 ± 11
Multiboson ($WH(\gamma\gamma)$, $WW\gamma$, $Z\gamma\gamma$)	5.2 ± 1.7	4.2 ± 1.2	76 ± 13
$j \rightarrow \ell$	–	–	35 ± 10
Top ($tt\gamma$, $tW\gamma$, $tq\gamma$)	136 ± 32	14.0 ± 2.9	30 ± 7
Pileup	–	–	10 ± 5
Total	332 ± 18	43 ± 5	$1\,136 \pm 34$
Data	333	36	1\,136

Table 9.2: Estimated signal and background yields in the CRTop, VRTop, and SR regions, as well as their sums, compared with the observed number of events in data. Values are shown after the observed signal significance likelihood fit. The uncertainties quoted in the table correspond to total uncertainties. Events from the “Multiboson” and “Top” backgrounds are estimated from simulation and contain only prompt leptons and photons. Event yields denoted with “–” correspond to sources of background that are negligible. The $tt\gamma$ background is scaled by the normalization factor τ obtained in CRTop and the $W\gamma\gamma$ prediction is scaled by the signal strength μ

post-fit. In addition, the ratio of the number of events predicted pre-fit to the number of events predicted post-fit is close to 1, indicating that good agreement between the predicted and observed number of events is also seen pre-fit. The post-fit total event yields and the uncertainties on the fitted number of signal and background events in CRTop, VRTop, and the SR are shown in Table 9.2.

An expected and observed statistical significance of 5.6σ is achieved, passing the threshold needed to claim first observation of the $pp \rightarrow W\gamma\gamma$ process. The inclusive fiducial cross section for $W (\rightarrow e\nu_e) \gamma\gamma$ and $W (\rightarrow \mu\nu_\mu) \gamma\gamma$ events in proton-proton collisions is measured to be $\sigma_{\text{fid}} = 13.8 \pm 1.1(\text{stat})_{-2.0}^{+2.1}(\text{syst}) \pm 0.1(\text{lumi})$ fb, statistically consistent with the predictions from both the Sherpa and Madgraph NLO simulation samples, as shown in Figure 9.3.

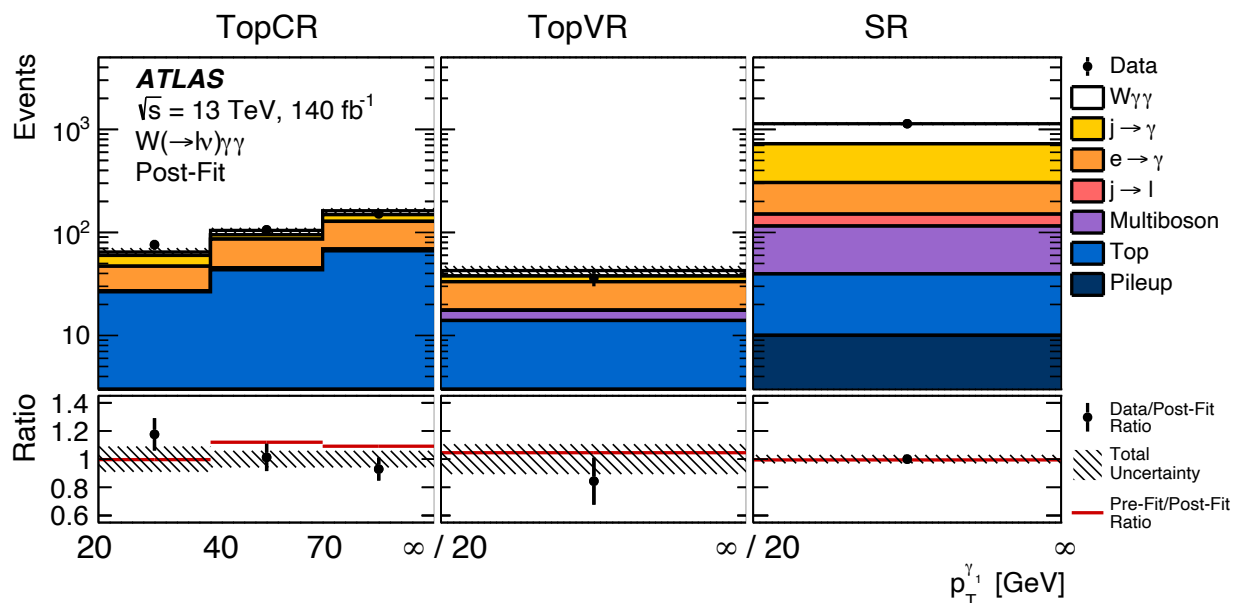


Figure 9.2: Number of observed and predicted events in the CRTop, VRTop, and SR regions before (pre-fit) and after (post-fit) the likelihood fit used to calculate the observed signal significance. The error bars on data indicate the size of the statistical uncertainty. The bottom panel shows the ratio of the observed to the predicted post-fit yield (black points) and the ratio of the predicted pre-fit to post-fit yield (solid red line) for each region. The uncertainty band includes both the statistical and systematic uncertainties obtained from the fit. The $t\bar{t}\gamma$ background is scaled by the normalization factor τ obtained in CRTop and the $W\gamma\gamma$ prediction is scaled by the signal strength μ . Pileup and $j \rightarrow \ell$ background contributions in CRTop and VRTop are negligible.

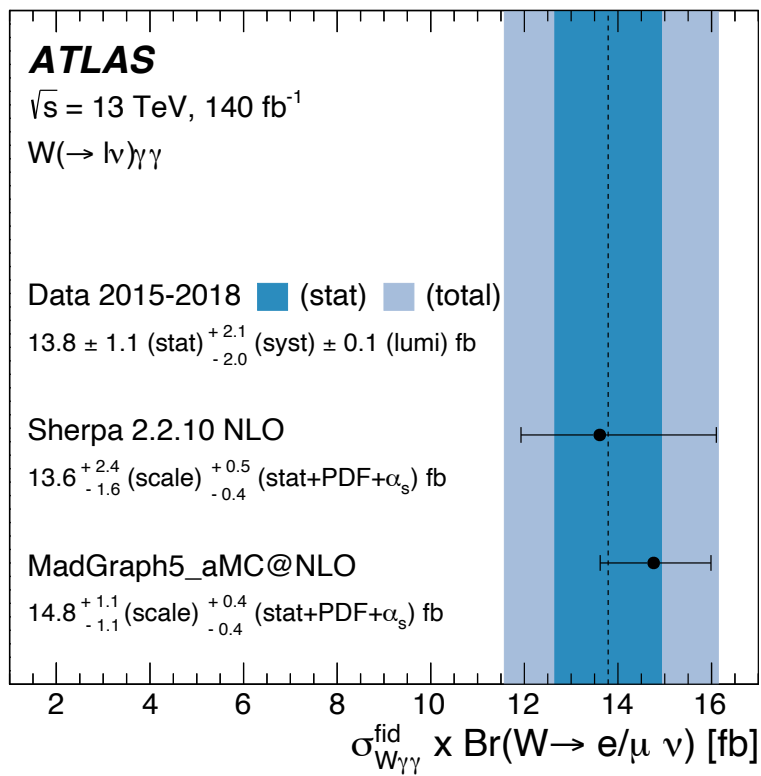


Figure 9.3: The measured inclusive fiducial $W(\rightarrow e\nu_e/\mu\nu_\mu)\gamma\gamma$ cross section compared with both the Sherpa and MadGraph signal event generator predictions.

The relative contributions of the different sources of uncertainty grouped by category on the unfolding fit are shown in Table 9.3. These are calculated from the correlation matrix of the unfolding fit. The relative contribution of a group of systematic uncertainties is obtained by fixing all of the nuisance parameters in a given group to their best-fit values and then performing a conditional MLE unfolding fit. The resulting total uncertainty is then subtracted in quadrature from the total uncertainty obtained from the nominal unconditional MLE unfolding fit. It can be seen in Table 9.3 that the uncertainty on the $j \rightarrow \gamma$ background is the dominant source of uncertainty, followed by the statistical uncertainty on data. While it seems that the analysis is limited by its systematic uncertainty, additional data has the potential to greatly reduce the uncertainty on the $j \rightarrow \gamma$ background. This is due to the fact that the uncertainty on the $j \rightarrow \gamma$ background mainly comes from the limited amount of statistics in the *LoosePrime* control regions used in the 2D template fit method described in Section 6.4. The third largest source of uncertainty is from the experimental uncertainties on the photon efficiencies, and the fourth largest is from the combined uncertainties on the other data-driven background estimates.

The relative contributions to the total uncertainty of the top 18 individual sources of systematic uncertainty are shown in Figure 9.4. It can be seen that the uncertainty on the $j \rightarrow \gamma$ background has the largest impact on the measured fiducial cross section, followed by the theory uncertainty on the $Z\gamma\gamma$ multiboson background, the uncertainty on the photon identification efficiency, and the uncertainty on the photon isolation efficiency. In addition, Figure 9.4 shows the pulls of the nuisance parameters (NPs) from their nominal pre-fit values. Pulls quantify the deviation of a NP's best-fit value $\hat{\theta}$ from their nominal value θ_0 in terms of their pre-fit uncertainty $\Delta\theta$. A NP's pull is given by the following relation:

$$(\hat{\theta} - \theta_0) / \Delta\theta. \quad (9.1)$$

As such, pull values should be close to zero with an uncertainty of approximately ± 1 . Values

Source of uncertainty	Impact [%]
$j \rightarrow \gamma$ data-driven background estimate	12
Photon efficiency	4.5
Other data-driven background estimates	3.5
Background theoretical uncertainties	3.0
Simulation statistical uncertainties	2.7
Signal theoretical uncertainties	2.6
Jet efficiency and calibration	2.4
Top normalization	2.3
Pileup reweighting	1.6
Muon efficiency and calibration	1.4
E_T^{miss} calibration	1.3
Luminosity	1.0
Electron and photon calibration	0.7
Flavour tagging efficiency	0.6
Systematic	15
Statistical	8.3
Total	17

Table 9.3: Major sources of uncertainty and their relative contribution to the total uncertainty on the measured fiducial cross section. Systematic uncertainty sources that contribute less than 0.1% are not shown. Efficiency uncertainties include, where applicable, uncertainties on data-simulation agreement due to reconstruction, trigger selection, identification, isolation, and vertex-matching.

that differ significantly from 0 could be an indication of a NP being over-constrained due to the mismodelling of a signal or background contribution. All NP pulls in the expected and observed significance likelihood fits as well as the unfolding likelihood fit are within a statistically acceptable range.

It can be seen from the ranking of the relative impacts of the systematic uncertainties on the measured fiducial cross section in Table 9.3 and Figure 9.4 that the precision of the $W\gamma\gamma$ cross section measurement is mainly limited by the uncertainties on the reducible sources of background, the photon identification and isolation efficiencies, and the theoretical modelling of the irreducible sources of background.

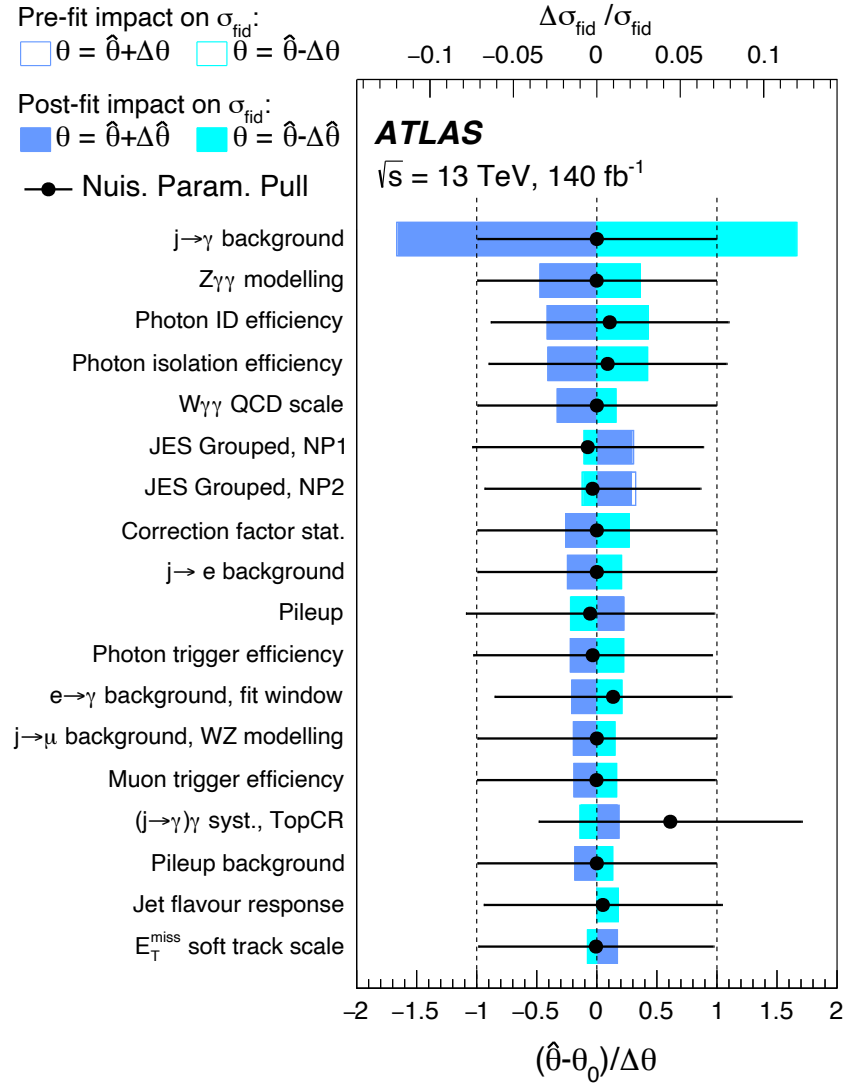


Figure 9.4: Relative contribution to the total uncertainty ($\Delta\sigma_{\text{fid}}/\sigma_{\text{fid}}$, top axis) of the 18 most important systematic uncertainties on the fitted fiducial cross section shown pre-fit (empty boxes) and post-fit (filled boxes). The impacts of both the up (dark blue) and down (light blue) variations of the systematic uncertainties are shown. The systematic uncertainties are listed in decreasing order of their post-fit impact on the fitted fiducial cross section. The black dots represent the pull values ($(\hat{\theta} - \theta_0) / \Delta\theta$, bottom axis) of each nuisance parameter, where θ_0 and $\hat{\theta}$ are the pre- and post-fit values, respectively, and $\Delta\theta$ and $\Delta\hat{\theta}$ are their pre- and post-fit uncertainties, respectively. The black lines represent the post-fit NP uncertainty normalized to the pre-fit uncertainty.

Chapter 10

Summary and Outlook

This thesis presents the results of a search for the $pp \rightarrow W\gamma\gamma$ process predicted by the Standard Model of Particle Physics. An analysis was done using a dataset consisting of 140 fb^{-1} of proton-proton collision at a center of mass energy of 13 TeV. The data was recorded by the ATLAS detector at the Large Hadron Collider at CERN during the Run 2 data taking period between 2015 and 2018. An expected and observed signal significance of 5.6σ was achieved, constituting the first observation of the $pp \rightarrow W\gamma\gamma$ process. An unfolded cross section measurement was performed to obtain an inclusive fiducial cross section for $W(\rightarrow e, \nu_e)\gamma\gamma$ and $W(\rightarrow \mu, \nu_\mu)\gamma\gamma$ events in proton-proton collisions of $\sigma_{\text{fid}} = 13.8 \pm 1.1(\text{stat})_{-2.0}^{+2.1}(\text{syst}) \pm 0.1(\text{lumi}) \text{ fb}$, in good agreement with the leading Standard Model predictions at NLO obtained using the Sherpa and MadGraph simulation packages.

A signal region was constructed to select $W\gamma\gamma$ events in which the W boson decays to either an electron or a muon accompanied by its respective neutrino. The tau channel decays of the W boson where the tau lepton subsequently decays leptonically were included in the detector-level selection but not in the truth-level selection. This was done to define a fiducial phase space used to measure the unfolded fiducial cross section of the $pp \rightarrow W(\rightarrow e\nu_e/\mu\nu_\mu)\gamma\gamma$ process. The reducible sources of background from hadronic jets

misidentified as photons, electrons misidentified as photons, hadronic jets misidentified as leptons, and photons from pileup vertices were estimated using data-driven techniques. The irreducible sources of background from multiboson processes and processes involving a top quark were estimated in simulation. In addition, the background from processes involving a top quark in their final state was constrained in a control region in a simultaneous fit with the signal region. Likelihood fits were performed to extract the expected and observed statistical significance of the $W\gamma\gamma$ process. A third likelihood fit was done to extract the measured fiducial cross section using a detector- to truth-level unfolding correction factor. The largest systematic uncertainty on the measured fiducial cross section comes from the uncertainty on the estimated of the number of events with a hadronic jet misidentified as a photon, the largest source of background in the analysis. While the measurement is limited by its systematic uncertainty, more data in the control regions used to estimate the background from hadronic jets misidentified as photons has the potential to greatly reduce its uncertainty.

The natural next step for the $W\gamma\gamma$ analysis is the measurement of a differential cross section, for which most of the analysis framework is already in place. In addition, a differential cross section measurement would allow for limits to be set on anomalous quartic gauge coupling operators in the context of effective field theories. A differential $W\gamma\gamma$ cross section measurement could then be included in a combination of ATLAS measurements that are sensitive to certain effective field theory operators in a so-called *global fit*.

Additional data that is being collected during the ongoing Run 3 at the Large Hadron Collider at a higher center of mass energy could greatly improve the precision of this measurement. Furthermore, this new larger dataset is opening the door to the study of exceptionally rare processes such as the $WH(\rightarrow \gamma\gamma)$ production, for which the $W\gamma\gamma$ process would be a background. Consequently, the insights derived from the measurement presented in this thesis will surely be invaluable to other measurements in the context of future analyses using the ATLAS detector.

In conclusion, this measurement provides a new test of the Standard Model with the first observation of the $W\gamma\gamma$ process, opening up new opportunities to explore the electroweak sector in search of hints of new physics. In addition, it provides the first insights into a process that will be an important background to future measurements at the Large Hadron Collider. Finally, the $W\gamma\gamma$ analysis has contributed to the development of analysis techniques that will be important for realizing the full physics potential of the ATLAS experiment in the years to come.

Bibliography

- [1] ATLAS Collaboration. *ATLAS LAr Calorimeter Phase-II Upgrade: Technical Design Report*. ATLAS-TDR-027; CERN-LHCC-2017-018. 2017. URL: <https://cds.cern.ch/record/2285582>.
- [2] ATLAS Collaboration. “Observation of a new particle in the search for the Standard Model Higgs boson with the ATLAS detector at the LHC”. In: *Phys. Lett. B* 716 (2012), p. 1. DOI: 10.1016/j.physletb.2012.08.020. arXiv: 1207.7214 [hep-ex].
- [3] CMS Collaboration. “Observation of a new boson at a mass of 125 GeV with the CMS experiment at the LHC”. In: *Phys. Lett. B* 716 (2012), p. 30. DOI: 10.1016/j.physletb.2012.08.021. arXiv: 1207.7235 [hep-ex].
- [4] C. P. Burgess and G. D. Moore. *The standard model: A primer*. Cambridge University Press, Dec. 2006. ISBN: 978-0-511-25485-7, 978-1-107-40426-7, 978-0-521-86036-9.
- [5] D. J. Griffiths. *Introduction to elementary particles; 2nd rev. version*. Physics textbook. New York, NY: Wiley, 2008.
- [6] M. E. Peskin and D. V. Schroeder. *An Introduction to quantum field theory*. Reading, USA: Addison-Wesley, 1995. ISBN: 978-0-201-50397-5.
- [7] Wolchover, N. and Velasco, S. and Reading-Ikkanda, L. *A New Map of All the Particles and Forces*. <https://www.quantamagazine.org/a-new-map-of-the->

- standard - model - of - particle - physics - 20201022/. [Online; accessed 5-February-2023]. 2023.
- [8] Particle Data Group et al. “Review of Particle Physics”. In: *Prog. Theor. Exp. Phys.* 2020.8 (2020), p. 083C01. DOI: 10.1093/ptep/ptaa104.
- [9] E. Noether. “Invariant variation problems”. In: *Transport theory and statistical physics* 1.3 (1971), pp. 186–207.
- [10] M. Gell-Mann. “The interpretation of the new particles as displaced charge multiplets”. In: *Nuovo Cim.* 4.S2 (1956), pp. 848–866. DOI: 10.1007/BF02748000.
- [11] K. Nishijima. “Charge Independence Theory of V Particles*”. In: *Progress of Theoretical Physics* 13.3 (Mar. 1955), pp. 285–304. ISSN: 0033-068X. DOI: 10.1143/PTP.13.285. eprint: <https://academic.oup.com/ptp/article-pdf/13/3/285/5425869/13-3-285.pdf>. URL: <https://doi.org/10.1143/PTP.13.285>.
- [12] P. A. M. Dirac. “The quantum theory of the emission and absorption of radiation”. In: *Proceedings of the Royal Society of London. Series A, Containing Papers of a Mathematical and Physical Character* 114.767 (1927), pp. 243–265.
- [13] A. Ali, J. Lange Sören, and S. Stone. “Exotics: Heavy pentaquarks and tetraquarks”. In: *Progress in Particle and Nuclear Physics* 97 (2017), pp. 123–198. ISSN: 0146-6410. DOI: <https://doi.org/10.1016/j.pnpnp.2017.08.003>. URL: <https://www.sciencedirect.com/science/article/pii/S0146641017300716>.
- [14] Y. L. Dokshitzer. “Calculation of the Structure Functions for Deep Inelastic Scattering and $e^+ e^-$ Annihilation by Perturbation Theory in Quantum Chromodynamics.” In: *Sov. Phys. JETP* 46 (1977), pp. 641–653.
- [15] V. N. Gribov and L. N. Lipatov. “Deep inelastic $e p$ scattering in perturbation theory”. In: *Sov. J. Nucl. Phys.* 15 (1972), pp. 438–450.

- [16] G. Altarelli and G. Parisi. “Asymptotic Freedom in Parton Language”. In: *Nucl. Phys. B* 126 (1977), pp. 298–318. DOI: 10.1016/0550-3213(77)90384-4.
- [17] NNPDF Collaboration et al. “Parton distributions with LHC data”. In: *Nucl. Phys. B* 867 (2013), p. 244. DOI: 10.1016/j.nuclphysb.2012.10.003. arXiv: 1207.1303 [hep-ph].
- [18] T. Gleisberg et al. “Event generation with SHERPA 1.1”. In: *JHEP* 02 (2009), p. 007. DOI: 10.1088/1126-6708/2009/02/007. arXiv: 0811.4622 [hep-ph].
- [19] S. S. Satapathy et al. “Higgs in Quark Gluon Plasma”. In: *DAE Symp. Nucl. Phys.* 64 (2019). Ed. by Yogesh K. Gupta et al., pp. 746–747.
- [20] N. Cabibbo. “Unitary Symmetry and Leptonic Decays”. In: *Phys. Rev. Lett.* 10 (1963), pp. 531–533. DOI: 10.1103/PhysRevLett.10.531.
- [21] M. Kobayashi and T. Maskawa. “CP Violation in the Renormalizable Theory of Weak Interaction”. In: *Prog. Theor. Phys.* 49 (1973), pp. 652–657. DOI: 10.1143/PTP.49.652.
- [22] UA1 Collaboration. “Experimental Observation of Isolated Large Transverse Energy Electrons with Associated Missing Energy at $\sqrt{s} = 540$ GeV”. In: *Phys. Lett. B* 122 (1983), pp. 103–116. DOI: 10.1016/0370-2693(83)91177-2.
- [23] UA1 Collaboration. “Experimental Observation of Lepton Pairs of Invariant Mass Around 95-GeV/c² at the CERN SPS Collider”. In: *Phys. Lett. B* 126 (1983), pp. 398–410. DOI: 10.1016/0370-2693(83)90188-0.
- [24] CDF Collaboration. “Observation of top quark production in $\bar{p}p$ collisions”. In: *Phys. Rev. Lett.* 74 (1995), pp. 2626–2631. DOI: 10.1103/PhysRevLett.74.2626. arXiv: hep-ex/9503002.

- [25] D0 Collaboration. “Observation of the Top Quark”. In: *Phys. Rev. Lett.* 74 (14 Apr. 1995), pp. 2632–2637. DOI: 10.1103/PhysRevLett.74.2632. URL: <https://link.aps.org/doi/10.1103/PhysRevLett.74.2632>.
- [26] *Standard Model Summary Plots October 2023*. Tech. rep. All figures including auxiliary figures are available at <https://atlas.web.cern.ch/Atlas/GROUPS/PHYSICS/PUBNOTES/ATL-PHYS-PUB-2023-039>. Geneva: CERN, 2023. URL: <http://cds.cern.ch/record/2882448>.
- [27] SNO Collaboration. “Measurement of the Rate of $\nu_e + d \rightarrow p + p + e^-$ Interactions Produced by 8B Solar Neutrinos at the Sudbury Neutrino Observatory”. In: *Phys. Rev. Lett.* 87 (7 July 2001), p. 071301. DOI: 10.1103/PhysRevLett.87.071301. URL: <https://link.aps.org/doi/10.1103/PhysRevLett.87.071301>.
- [28] I. Brock and T. Schörner-Sadenius. *Physics at the Terascale*. John Wiley & Sons, 2011.
- [29] O. J. P. Éboli and M. C. Gonzalez-Garcia. “Classifying the bosonic quartic couplings”. In: *Phys. Rev. D* 93.9 (2016), p. 093013. DOI: 10.1103/PhysRevD.93.093013. arXiv: 1604.03555 [hep-ph].
- [30] O. J. P. Éboli, M. C. Gonzalez-Garcia, and M. Martines. “Bounds on quartic gauge couplings in HEFT from electroweak gauge boson pair production at the LHC”. In: *Phys. Rev. D* 109 (3 Feb. 2024), p. 033007. DOI: 10.1103/PhysRevD.109.033007. URL: <https://link.aps.org/doi/10.1103/PhysRevD.109.033007>.
- [31] CMS Collaboration. “Observation of $WW\gamma$ production and search for $H\gamma$ production in proton-proton collisions at $\sqrt{s} = 13$ TeV”. In: *Phys. Rev. Lett.* 132.12 (2024), p. 121901. DOI: 10.1103/PhysRevLett.132.121901. arXiv: 2310.05164 [hep-ex].

- [32] ATLAS Collaboration. “Observation of $WZ\gamma$ Production in pp Collisions at $\sqrt{s}=13$ TeV with the ATLAS Detector”. In: *Phys. Rev. Lett.* 132.2 (2024), p. 021802. DOI: 10.1103/PhysRevLett.132.021802. arXiv: 2305.16994 [hep-ex].
- [33] ATLAS Collaboration. *Observation of $W\gamma\gamma$ triboson production in proton–proton collisions at $\sqrt{s} = 13$ TeV with the ATLAS detector*. 2024. DOI: <https://doi.org/10.1016/j.physletb.2023.138400>. arXiv: 2308.03041 [hep-ex]. URL: <https://www.sciencedirect.com/science/article/pii/S0370269323007335>.
- [34] Lyndon R Evans and Philip Bryant. “LHC Machine”. In: *JINST* 3 (2008). This report is an abridged version of the LHC Design Report (CERN-2004-003), S08001. DOI: 10.1088/1748-0221/3/08/S08001. URL: <https://cds.cern.ch/record/1129806>.
- [35] ATLAS Collaboration. “The ATLAS Experiment at the CERN Large Hadron Collider”. In: *JINST* 3 (2008), S08003. DOI: 10.1088/1748-0221/3/08/S08003.
- [36] CMS Collaboration. “The CMS experiment at the CERN LHC. The Compact Muon Solenoid experiment”. In: *JINST* 3 (2008). Also published by CERN Geneva in 2010, S08004. DOI: 10.1088/1748-0221/3/08/S08004. URL: <https://cds.cern.ch/record/1129810>.
- [37] ALICE Collaboration. “The ALICE experiment at the CERN LHC. A Large Ion Collider Experiment”. In: *JINST* 3 (2008). Also published by CERN Geneva in 2010, S08002. DOI: 10.1088/1748-0221/3/08/S08002. URL: <https://cds.cern.ch/record/1129812>.
- [38] LHCb Collaboration. “The LHCb Detector at the LHC”. In: *JINST* 3 (2008). Also published by CERN Geneva in 2010, S08005. DOI: 10.1088/1748-0221/3/08/S08005. URL: <https://cds.cern.ch/record/1129809>.

- [39] E. Mobs. “The CERN accelerator complex - August 2018. Complexe des accélérateurs du CERN - Août 2018”. In: (2018). General Photo. URL: <https://cds.cern.ch/record/2636343>.
- [40] S. Dailler. “Cross section of LHC dipole.” AC Collection. Legacy of AC. Pictures from 1992 to 2002. 1999. URL: <https://cds.cern.ch/record/842530>.
- [41] ATLAS Collaboration. *Public ATLAS Luminosity Results for Run-2 of the LHC*. <https://twiki.cern.ch/twiki/bin/view/AtlasPublic/LuminosityPublicResultsRun2>. [Online; accessed 06-November-2023]. 2023.
- [42] ATLAS Collaboration. “Luminosity determination in pp collisions at $\sqrt{s} = 13$ TeV using the ATLAS detector at the LHC”. In: *Eur. Phys. J. C* 83 (2023), p. 982. DOI: 10.1140/epjc/s10052-023-11747-w. arXiv: 2212.09379 [hep-ex].
- [43] C. Grupen, A. Böhrer, and L. Smolik. *Particle detectors*. Cambridge monographs on particle physics, nuclear physics, and cosmology. Cambridge: Cambridge Univ. Press, 1996. URL: <https://cds.cern.ch/record/306826>.
- [44] J. Pequeno and P. Schaffner. “How ATLAS detects particles: diagram of particle paths in the detector”. 2013. URL: <https://cds.cern.ch/record/1505342>.
- [45] ATLAS Collaboration. *ATLAS Inner Detector: Technical Design Report, Volume 1*. ATLAS-TDR-4; CERN-LHCC-97-016. 1997. URL: <https://cds.cern.ch/record/331063>.
- [46] ATLAS Collaboration. *ATLAS Inner Detector: Technical Design Report, Volume 2*. ATLAS-TDR-5, CERN-LHCC-97-017. 1997. URL: <https://cds.cern.ch/record/331064>.
- [47] ATLAS Collaboration. *ATLAS Pixel Detector: Technical Design Report*. ATLAS-TDR-11; CERN-LHCC-98-013. 1998. URL: <https://cds.cern.ch/record/381263>.

- [48] ATLAS Collaboration. *ATLAS Insertable B-Layer: Technical Design Report*. ATLAS-TDR-19; CERN-LHCC-2010-013. 2010. URL: <https://cds.cern.ch/record/1291633>.
- [49] ATLAS Collaboration. *Track Reconstruction Performance of the ATLAS Inner Detector at $\sqrt{s} = 13$ TeV*. ATL-PHYS-PUB-2015-018. 2015. URL: <https://cds.cern.ch/record/2037683>.
- [50] ATLAS Collaboration. *ATLAS Liquid Argon Calorimeter: Technical Design Report*. ATLAS-TDR-2; CERN-LHCC-96-041. 1996. URL: <https://cds.cern.ch/record/331061>.
- [51] ATLAS Collaboration. “Electron and photon energy calibration with the ATLAS detector using LHC Run 1 data”. In: *Eur. Phys. J. C* 74 (2014), p. 3071. DOI: 10.1140/epjc/s10052-014-3071-4. arXiv: 1407.5063 [hep-ex].
- [52] ATLAS Collaboration. *ATLAS Tile Calorimeter: Technical Design Report*. ATLAS-TDR-3; CERN-LHCC-96-042. 1996. URL: <https://cds.cern.ch/record/331062>.
- [53] ATLAS Collaboration. *ATLAS Muon Spectrometer: Technical Design Report*. ATLAS-TDR-10; CERN-LHCC-97-022. CERN, 1997. URL: <https://cds.cern.ch/record/331068>.
- [54] G. Avoni et al. “The new LUCID-2 detector for luminosity measurement and monitoring in ATLAS”. In: *JINST* 13.07 (2018), P07017. DOI: 10.1088/1748-0221/13/07/P07017.
- [55] ATLAS Collaboration. “Operation of the ATLAS trigger system in Run 2”. In: *JINST* 15 (2020), P10004. DOI: 10.1088/1748-0221/15/10/P10004. arXiv: 2007.12539 [hep-ex].
- [56] ATLAS Collaboration. *ATLAS Level-1 Trigger: Technical Design Report*. ATLAS-TDR-12; CERN-LHCC-98-014. 1998. URL: <https://cds.cern.ch/record/381429>.

- [57] ATLAS Collaboration. *ATLAS High-Level Trigger, Data Acquisition and Controls: Technical Design Report*. ATLAS-TDR-16; CERN-LHCC-2003-022. 2003. URL: <https://cds.cern.ch/record/616089>.
- [58] ATLAS Collaboration. “The ATLAS Simulation Infrastructure”. In: *Eur. Phys. J. C* 70 (2010), p. 823. DOI: 10.1140/epjc/s10052-010-1429-9. arXiv: 1005.4568 [physics.ins-det].
- [59] ATLAS Collaboration. *Athena*. Version 22.0.1. 2019. DOI: 10.5281/zenodo.2641997. URL: <https://doi.org/10.5281/zenodo.2641997>.
- [60] M. Elsing et al. “The ATLAS Tier-0: Overview and operational experience”. In: *Journal of Physics: Conference Series* 219.7 (Apr. 2010), p. 072011. DOI: 10.1088/1742-6596/219/7/072011. URL: <https://dx.doi.org/10.1088/1742-6596/219/7/072011>.
- [61] ATLAS Collaboration. “Performance of the ATLAS track reconstruction algorithms in dense environments in LHC Run 2”. In: *Eur. Phys. J. C* 77 (2017), p. 673. DOI: 10.1140/epjc/s10052-017-5225-7. arXiv: 1704.07983 [hep-ex].
- [62] T. Cornelissen et al. “The new ATLAS track reconstruction (NEWT)”. In: *Journal of Physics: Conference Series* 119.3 (July 2008), p. 032014. DOI: 10.1088/1742-6596/119/3/032014. URL: <https://dx.doi.org/10.1088/1742-6596/119/3/032014>.
- [63] R. Frühwirth. “Application of Kalman filtering to track and vertex fitting”. In: *NIM-A* 262.2 (1987), pp. 444–450. ISSN: 0168-9002. DOI: [https://doi.org/10.1016/0168-9002\(87\)90887-4](https://doi.org/10.1016/0168-9002(87)90887-4). URL: <https://www.sciencedirect.com/science/article/pii/0168900287908874>.
- [64] T. G. Cornelissen et al. *Updates of the ATLAS Tracking Event Data Model (Release 13)*. Tech. rep. All figures including auxiliary figures are available at <https://atlas.web.cern.ch/Atlas/GROUPS/PHYSICS/PUBNOTES/ATL-SOFT->

- PUB-2007-003. Geneva: CERN, 2007. URL: <https://cds.cern.ch/record/1038095>.
- [65] ATLAS Collaboration. *Vertex Reconstruction Performance of the ATLAS Detector at $\sqrt{s} = 13$ TeV*. ATL-PHYS-PUB-2015-026. 2015. URL: <https://cds.cern.ch/record/2037717>.
- [66] ATLAS Collaboration. “Reconstruction of primary vertices at the ATLAS experiment in Run 1 proton–proton collisions at the LHC”. In: *Eur. Phys. J. C* 77 (2017), p. 332. DOI: 10.1140/epjc/s10052-017-4887-5. arXiv: 1611.10235 [hep-ex].
- [67] W. Lampl et al. *Calorimeter Clustering Algorithms: Description and Performance*. ATL-LARG-PUB-2008-002. 2008. URL: <https://cds.cern.ch/record/1099735>.
- [68] ATLAS Collaboration. “Topological cell clustering in the ATLAS calorimeters and its performance in LHC Run 1”. In: *Eur. Phys. J. C* 77 (2017), p. 490. DOI: 10.1140/epjc/s10052-017-5004-5. arXiv: 1603.02934 [hep-ex].
- [69] ATLAS Collaboration. “Electron reconstruction and identification in the ATLAS experiment using the 2015 and 2016 LHC proton–proton collision data at $\sqrt{s} = 13$ TeV”. In: *Eur. Phys. J. C* 79 (2019), p. 639. DOI: 10.1140/epjc/s10052-019-7140-6. arXiv: 1902.04655 [physics.ins-det].
- [70] ATLAS Collaboration. *Improved electron reconstruction in ATLAS using the Gaussian Sum Filter-based model for bremsstrahlung*. ATLAS-CONF-2012-047. 2012. URL: <https://cds.cern.ch/record/1449796>.
- [71] ATLAS Collaboration. “Electron and photon energy calibration with the ATLAS detector using 2015–2016 LHC proton–proton collision data”. In: *JINST* 14 (2019), P03017. DOI: 10.1088/1748-0221/14/03/P03017. arXiv: 1812.03848 [hep-ex].

- [72] ATLAS Collaboration. “Electron and photon performance measurements with the ATLAS detector using the 2015–2017 LHC proton–proton collision data”. In: *JINST* 14 (2019), P12006. DOI: 10.1088/1748-0221/14/12/P12006. arXiv: 1908.00005 [hep-ex].
- [73] M. Cacciari and G. P. Salam. “Pileup subtraction using jet areas”. In: *Phys. Lett. B* 659.1 (2008), pp. 119–126. ISSN: 0370-2693. DOI: <https://doi.org/10.1016/j.physletb.2007.09.077>. URL: <https://www.sciencedirect.com/science/article/pii/S0370269307011094>.
- [74] ATLAS Collaboration. *Expected Performance of the ATLAS Experiment - Detector, Trigger and Physics*. 2009. arXiv: 0901.0512 [hep-ex]. URL: <https://arxiv.org/abs/0901.0512>.
- [75] ATLAS Collaboration. “Measurement of the photon identification efficiencies with the ATLAS detector using LHC Run 2 data collected in 2015 and 2016”. In: *Eur. Phys. J. C* 79 (2019), p. 205. DOI: 10.1140/epjc/s10052-019-6650-6. arXiv: 1810.05087 [hep-ex].
- [76] J. Saxon. “Discovery of the Higgs Boson, Measurements of its Production, and a Search for Higgs Boson Pair Production”. Presented 13 06 2014. Pennsylvania U., 2014. URL: <https://cds.cern.ch/record/1746004>.
- [77] ATLAS Collaboration. “Muon reconstruction performance of the ATLAS detector in proton–proton collision data at $\sqrt{s} = 13$ TeV”. In: *Eur. Phys. J. C* 76 (2016), p. 292. DOI: 10.1140/epjc/s10052-016-4120-y. arXiv: 1603.05598 [hep-ex].
- [78] ATLAS Collaboration. “Muon reconstruction and identification efficiency in ATLAS using the full Run 2 pp collision data set at $\sqrt{s} = 13$ TeV”. In: *Eur. Phys. J. C* 81 (2021), p. 578. DOI: 10.1140/epjc/s10052-021-09233-2. arXiv: 2012.00578 [hep-ex].

- [79] ATLAS Collaboration. “Jet reconstruction and performance using particle flow with the ATLAS Detector”. In: *Eur. Phys. J. C* 77 (2017), p. 466. DOI: 10.1140/epjc/s10052-017-5031-2. arXiv: 1703.10485 [hep-ex].
- [80] Matteo Cacciari, Gavin P. Salam, and Gregory Soyez. “The anti- k_t jet clustering algorithm”. In: *JHEP* 04 (2008), p. 063. DOI: 10.1088/1126-6708/2008/04/063. arXiv: 0802.1189 [hep-ph].
- [81] ATLAS Collaboration. “Jet energy scale and resolution measured in proton–proton collisions at $\sqrt{s} = 13$ TeV with the ATLAS detector”. In: *Eur. Phys. J. C* 81 (2021), p. 689. DOI: 10.1140/epjc/s10052-021-09402-3. arXiv: 2007.02645 [hep-ex].
- [82] ATLAS Collaboration. *Tagging and suppression of pileup jets with the ATLAS detector*. ATLAS-CONF-2014-018. 2014. URL: <https://cds.cern.ch/record/1700870>.
- [83] ATLAS Collaboration. *Optimisation and performance studies of the ATLAS b-tagging algorithms for the 2017-18 LHC run*. ATL-PHYS-PUB-2017-013. 2017. URL: <https://cds.cern.ch/record/2273281>.
- [84] ATLAS Collaboration. *Secondary vertex finding for jet flavour identification with the ATLAS detector*. ATL-PHYS-PUB-2017-011. 2017. URL: <https://cds.cern.ch/record/2270366>.
- [85] ATLAS Collaboration. *Topological b-hadron decay reconstruction and identification of b-jets with the JetFitter package in the ATLAS experiment at the LHC*. ATL-PHYS-PUB-2018-025. 2018. URL: <https://cds.cern.ch/record/2645405>.
- [86] ATLAS Collaboration. “ATLAS b-jet identification performance and efficiency measurement with $t\bar{t}$ events in pp collisions at $\sqrt{s} = 13$ TeV”. In: *Eur. Phys. J. C* 79 (2019), p. 970. DOI: 10.1140/epjc/s10052-019-7450-8. arXiv: 1907.05120 [hep-ex].

- [87] ATLAS Collaboration. E_T^{miss} performance in the ATLAS detector using 2015–2016 LHC pp collisions. ATLAS-CONF-2018-023. 2018. URL: <https://cds.cern.ch/record/2625233>.
- [88] ATLAS Collaboration. “Performance of missing transverse momentum reconstruction with the ATLAS detector using proton–proton collisions at $\sqrt{s} = 13$ TeV”. In: *Eur. Phys. J. C* 78 (2018), p. 903. DOI: 10.1140/epjc/s10052-018-6288-9. arXiv: 1802.08168 [hep-ex].
- [89] ATLAS Collaboration. *Reconstruction, Energy Calibration, and Identification of Hadronically Decaying Tau Leptons in the ATLAS Experiment for Run-2 of the LHC*. ATL-PHYS-PUB-2015-045. 2015. URL: <https://cds.cern.ch/record/2064383>.
- [90] ATLAS Collaboration. “Performance of electron and photon triggers in ATLAS during LHC Run 2”. In: *Eur. Phys. J. C* 80 (2020), p. 47. DOI: 10.1140/epjc/s10052-019-7500-2. arXiv: 1909.00761 [hep-ex].
- [91] ATLAS Collaboration. “Performance of the ATLAS muon triggers in Run 2”. In: *JINST* 15 (2020), P09015. DOI: 10.1088/1748-0221/15/09/p09015. arXiv: 2004.13447 [physics.ins-det].
- [92] A. Buckley et al. “General-purpose event generators for LHC physics”. In: *Physics Reports* 504.5 (2011), pp. 145–233.
- [93] B.R. Webber. “A QCD model for jet fragmentation including soft gluon interference”. In: *Nuclear Physics B* 238.3 (1984), pp. 492–528. ISSN: 0550-3213. DOI: [https://doi.org/10.1016/0550-3213\(84\)90333-X](https://doi.org/10.1016/0550-3213(84)90333-X). URL: <https://www.sciencedirect.com/science/article/pii/055032138490333X>.
- [94] B. Andersson et al. “Parton fragmentation and string dynamics”. In: *Phys. Rept.* 97 (1983), pp. 31–145. DOI: 10.1016/0370-1573(83)90080-7.

- [95] S. Agostinelli et al. “GEANT4 – a simulation toolkit”. In: *Nucl. Instrum. Meth. A* 506 (2003), p. 250. DOI: 10.1016/S0168-9002(03)01368-8.
- [96] J. Alwall et al. “The automated computation of tree-level and next-to-leading order differential cross sections, and their matching to parton shower simulations”. In: *JHEP* 07 (2014), p. 079. DOI: 10.1007/JHEP07(2014)079. arXiv: 1405.0301 [hep-ph].
- [97] S. Alioli et al. “A general framework for implementing NLO calculations in shower Monte Carlo programs: the POWHEG BOX”. In: *JHEP* 06 (2010), p. 043. DOI: 10.1007/JHEP06(2010)043. arXiv: 1002.2581 [hep-ph].
- [98] E. Bothmann et al. “Event generation with Sherpa 2.2”. In: *SciPost Phys.* 7.3 (2019), p. 034. DOI: 10.21468/SciPostPhys.7.3.034. arXiv: 1905.09127 [hep-ph].
- [99] T. Gleisberg and S. Höche. “Comix, a new matrix element generator”. In: *JHEP* 12 (2008), p. 039. DOI: 10.1088/1126-6708/2008/12/039. arXiv: 0808.3674 [hep-ph].
- [100] F. Cascioli, P. Maierhöfer, and S. Pozzorini. “Scattering Amplitudes with Open Loops”. In: *Phys. Rev. Lett.* 108 (2012), p. 111601. DOI: 10.1103/PhysRevLett.108.111601. arXiv: 1111.5206 [hep-ph].
- [101] F. Buccioni et al. “OpenLoops 2”. In: *Eur. Phys. J. C* 79.10 (2019), p. 866. DOI: 10.1140/epjc/s10052-019-7306-2. arXiv: 1907.13071 [hep-ph].
- [102] A. Denner, S. Dittmaier, and L. Hofer. “COLLIER: A fortran-based complex one-loop library in extended regularizations”. In: *Comput. Phys. Commun.* 212 (2017), pp. 220–238. DOI: 10.1016/j.cpc.2016.10.013. arXiv: 1604.06792 [hep-ph].
- [103] S. Schumann and F. Krauss. “A parton shower algorithm based on Catani–Seymour dipole factorisation”. In: *JHEP* 03 (2008), p. 038. DOI: 10.1088/1126-6708/2008/03/038. arXiv: 0709.1027 [hep-ph].

- [104] T. Sjöstrand, S. Mrenna, and P. Skands. “A brief introduction to PYTHIA 8.1”. In: *Comput. Phys. Commun.* 178 (2008), pp. 852–867. DOI: 10.1016/j.cpc.2008.01.036. arXiv: 0710.3820 [hep-ph].
- [105] S. Mrenna and P. Skands. “Automated parton-shower variations in PYTHIA 8”. In: *Phys. Rev. D* 94 (2016), p. 074005. DOI: 10.1103/PhysRevD.94.074005. arXiv: 1605.08352 [hep-ph].
- [106] ATLAS Collaboration. “Measurement of the isolated diphoton cross section in pp collisions at $\sqrt{s} = 7$ TeV with the ATLAS detector”. In: *Phys. Rev. D* 85 (2012), p. 012003. DOI: 10.1103/PhysRevD.85.012003. arXiv: 1107.0581 [hep-ex].
- [107] ATLAS Collaboration. “Evidence of $W\gamma\gamma$ Production in pp Collisions at $\sqrt{s} = 8$ TeV and Limits on Anomalous Quartic Gauge Couplings with the ATLAS Detector”. In: *Phys. Rev. Lett.* 115 (2015), p. 031802. DOI: 10.1103/PhysRevLett.115.031802. arXiv: 1503.03243 [hep-ex].
- [108] A. D. Bukin. “Fitting function for asymmetric peaks”. In: (Nov. 2007). arXiv: 0711.4449 [physics.data-an].
- [109] S. Das. *A simple alternative to the Crystal Ball function*. 2016. arXiv: 1603.08591 [hep-ex].
- [110] K. Cranmer. “Kernel estimation in high-energy physics”. In: *Computer Physics Communications* 136.3 (2001), pp. 198–207. ISSN: 0010-4655. DOI: [https://doi.org/10.1016/S0010-4655\(00\)00243-5](https://doi.org/10.1016/S0010-4655(00)00243-5). URL: <https://www.sciencedirect.com/science/article/pii/S0010465500002435>.
- [111] ATLAS Collaboration. “Tools for estimating fake/non-prompt lepton backgrounds with the ATLAS detector at the LHC”. In: *JINST* 18 (2023), T11004. DOI: 10.1088/1748-0221/18/11/T11004. arXiv: 2211.16178 [hep-ex].

- [112] ATLAS Collaboration. “Measurement of the $Z(\rightarrow \ell^+ \ell^-) \gamma$ production cross-section in pp collisions at $\sqrt{s} = 13$ TeV with the ATLAS detector”. In: *JHEP* 03 (2020), p. 054. DOI: 10.1007/JHEP03(2020)054. arXiv: 1911.04813 [hep-ex].
- [113] S. van der Meer. *Calibration of the effective beam height in the ISR*. Tech. rep. Geneva: CERN, 1968. URL: <https://cds.cern.ch/record/296752>.
- [114] J. Butterworth et al. “PDF4LHC recommendations for LHC Run II”. In: *J. Phys. G* 43 (2016), p. 023001. DOI: 10.1088/0954-3899/43/2/023001. arXiv: 1510.03865 [hep-ph].
- [115] A. D. Martin et al. “Uncertainties on α_S in global PDF analyses and implications for predicted hadronic cross sections”. In: *Eur. Phys. J. C* 64 (2009), pp. 653–680. DOI: 10.1140/epjc/s10052-009-1164-2. arXiv: 0905.3531 [hep-ph].
- [116] ATLAS Collaboration. *Multi-boson simulation for 13 TeV ATLAS analyses*. ATL-PHYS-PUB-2016-002. 2016. URL: <https://cds.cern.ch/record/2119986>.
- [117] O. Behnke et al. *Data analysis in high energy physics: a practical guide to statistical methods*. Weinheim: Wiley-VCH, 2013. DOI: 10.1002/9783527653416. URL: <https://cds.cern.ch/record/1517556>.
- [118] S. S. Wilks. “The Large-Sample Distribution of the Likelihood Ratio for Testing Composite Hypotheses”. In: *Annals Math. Statist.* 9.1 (1938), pp. 60–62. DOI: 10.1214/aoms/1177732360.

List of Acronyms

aQGC	anomalous Quartic Gauge Couplings.
aTGC	anomalous Triple Gauge Couplings.
BC	Bunch Crossing.
BCM	Beam Conditions Monitor.
BSM	Beyond the Standard Model.
CCA	Connected Component Analysis.
CERN	Conseil Européen pour la Recherche Nucléaire.
CKM	Cabibbo–Kobayashi–Maskawa.
CP	Charge Parity.
CR	Control Region.
CSC	Cathode Strip Chamber.
DGLAP	Dokshitzer–Gribov–Lipatov–Altarelli–Parisi.
EFT	Effective Field Theory.
EM	electromagnetic.
EMB	Electromagnetic Barrel.
EMEC	Electromagnetic End-Cap.
EW	Electroweak.
FCal	Forward Calorimeter.
FPGA	Field Programmable Gate Array.

FSR	Final State Radiation.
GRL	Good Runs List.
GSF	Gaussian-Sum Filter.
HEC	Hadronic End-Cap.
HLT	High Level Trigger.
IBL	Insertable B-Layer.
ID	Inner Detector.
IP	Interaction Point.
ISR	Initial State Radiation.
JVT	jet-vertex-tagger.
L1	Level 1.
LAr	Liquid Argon.
LH	Likelihood.
LHC	Large Hadron Collider.
LINAC2	Linear Accelerator 2.
LO	Leading Order.
LP	Loose Prime.
LUCID2	LUMinosity Cherenkov Integrating Detector 2.
MC	Monte Carlo.
MDT	Monitored Drift Tube.
ME	Matrix Element.
MET	Missing Transverse Energy.
MIP	Minimum Ionizing Particle.
MLE	Maximum Likelihood Estimator.
MS	Muon Spectrometer.
NLO	Next-to Leading Order.

NN	Neural Network.
NP	Nuisance Parameter.
PDF	Parton Distribution Function.
PMG	Physics Modelling Group.
PMT	Photomultiplier Tube.
p.o.i.	parameter of interest.
PS	Proton Synchrotron.
PV	Primary Vertex.
QCD	Quantum Chromodynamics.
QED	Quantum Electrodynamics.
QFT	Quantum Field Theory.
RF	Radio Frequency.
RMS	Root Mean Square.
RPC	Resistive Plate Chamber.
SCT	Semiconductor Tracker.
SM	Standard Model.
SPS	Super Proton Synchrotron.
SR	Signal Region.
SUSY	Supersymmetry.
TDAQ	Trigger and Data Acquisition.
TGC	Thin Gap Chamber.
TRT	Transition Radiation Tracker.
v.e.v.	vacuum expectation value.
VR	Validation Region.

List of Figures

2.1	Summary of the Standard Model elementary particles and their properties.	6
2.2	The interaction vertex of Quantum Electrodynamics.	11
2.3	The interaction vertices of Quantum Chromodynamics	12
2.4	Example Parton Distribution Function	14
2.5	Schematic diagram of a proton-proton collision.	15
2.6	Sketch of the Higgs potential.	17
2.7	The interaction vertices of Electroweak theory.	18
2.8	The interaction vertices of the Higgs boson.	19
2.9	Summary of the Standard Model production cross section measurements of different processes by the ATLAS Collaboration.	21
2.10	Feynman diagrams of Fermi's effective interaction and the Standard Model diagram for β decay.	23
2.11	Example $W\gamma\gamma$ Feynman diagrams.	25
3.1	Schematic diagram of the CERN accelerator complex.	28
3.2	Cross section of the LHC at the location of a dipole magnet.	30
3.3	Distribution of the mean number of interactions per bunch crossing during Run 2.	32
3.4	Schematic diagram of the ATLAS detector and its sub-detectors.	33

3.5	Schematic diagram showing how different types of particles interact with each subsystem of the ATLAS detector.	37
3.6	Schematic diagram of the ATLAS Inner Detector.	39
3.7	Schematic diagram of the ATLAS solenoid and toroid magnet systems.	40
3.8	Schematic diagram showing the multiple layers of each of the Inner Detector sub-detectors.	42
3.9	Schematic diagram of the ATLAS calorimeter system.	43
3.10	Schematic diagram of the Electromagnetic Barrel layers and their segmentation.	45
3.11	Schematic diagram of the Tile Calorimeter optical readout.	46
3.12	Schematic diagram of the ATLAS Muon Spectrometer.	47
3.13	Integrated luminosity over the course of the Run 2 data taking period.	51
4.1	Schematic diagram of a track's parameters.	55
4.2	Schematic drawing of the path of an electron in the ATLAS detector.	58
4.3	Electron reconstruction efficiency as a function of electron E_T	60
4.4	Schematic of the electron calorimeter-based isolation energy calculation.	63
4.5	Efficiency to reconstruct converted photons as a function of true photon E_T	65
4.6	Schematic depiction of the different calorimeter-based variables used for photon identification.	67
4.7	Tight photon identification efficiency for unconverted and converted prompt photons as a function of photon E_T	68
4.8	Combined muon reconstruction and identification efficiencies for the <i>Medium</i> identification working point.	71
4.9	Schematic diagram highlighting the differences in the kinematic properties of a b -jet.	76
4.10	The missing transverse energy resolution as a function of the true missing transverse energy.	78

5.1	Diagram summarizing the process of selecting events from both data and simulation.	81
5.2	Diphoton invariant mass $m_{\gamma\gamma}$ in the Signal Region before the $Z\gamma$ veto requirement.	89
5.3	Distributions of the $Z\gamma$ veto variables using simulated $e\nu\gamma\gamma$ and $ee\gamma\gamma$ events in the Signal Regions.	91
5.4	Signal Region cutflow.	92
5.5	$W\gamma\gamma$ event display, electron channel.	93
5.6	$W\gamma\gamma$ event display, muon channel.	94
6.1	Schematic diagram summarizing the CRTop and VRTop regions	103
6.2	Estimated composition of the CRTop and VRTop regions.	103
6.3	Example of a 1D template fit to toy data of the isolation energy distributions of prompt photons and jets misidentified as photons in an extended Signal Region.	106
6.4	Schematic diagram of the control regions and their relation to the Signal Region used in the $j \rightarrow \gamma$ background estimate.	107
6.5	One-dimensional fits to the photon isolation energy distributions.	110
6.6	Two-dimensional photon isolation energy distribution templates.	111
6.7	One-dimensional projections of the leading and subleading photon isolation energy distributions from the 2D template fit in the CR_{TT} region.	112
6.8	Distributions of the reconstructed invariant mass in CR_{ee}	118
6.9	Distributions of the reconstructed invariant mass in $CR_{e\gamma}$	119
6.10	Schematic diagram of $e \rightarrow \gamma$ fake rate estimate.	121
6.11	Nominal $e \rightarrow \gamma$ fake rate with statistical uncertainties as a function of p_T and $ \eta $	122

6.12 Schematic diagram summarizing the $e \rightarrow \gamma$ validation region in relation to the Signal Region and their respective fake rate application regions.	123
6.13 Truth-matched type of reconstructed photon pair in the electron channel of the $Z\gamma$ Veto Region at Low and High E_T^{miss} and the Signal Region.	126
6.14 Validation of the $e \rightarrow \gamma$ data-driven estimate as a function of leading photon p_T in the $Z\gamma$ veto region at high E_T^{miss}	127
6.15 Validation of the $e \rightarrow \gamma$ data-driven estimate as a function of leading photon p_T in the $Z\gamma$ veto region at low E_T^{miss}	128
6.16 Truth composition of the $e \rightarrow \gamma$ Signal Region estimate.	130
6.17 Example invariant mass fits in data and in truth matched simulated $Z + jets$ events in $CR e\gamma$	132
6.18 Relative changes to the $e \rightarrow \gamma$ fake rate from each systematic variation considered in the $e \rightarrow \gamma$ fake factor background estimation method.	133
6.19 Differential $e \rightarrow \gamma$ background estimate in the Signal Region.	135
6.20 Schematic diagram of $j \rightarrow \ell$ fake rate estimate.	139
6.21 $j \rightarrow \ell$ fake rate estimates in the electron and muon channels.	142
6.22 Schematic diagram summarizing the regions used in the $j \rightarrow \ell$ background estimate.	143
6.23 Differential validation of the data-driven $j \rightarrow \ell$ background in the $j \rightarrow \ell$ Validation Region.	144
6.24 Systematic uncertainties on the $j \rightarrow \ell$ fake rate.	146
6.25 Difference in the longitudinal impact parameter between the primary vertex and the origin of converted photons in simulated events in the Signal Region.	150
6.26 Difference in the longitudinal impact parameter between the primary vertex and the reconstructed origin of converted photons in data in the Signal Region.	152

8.1	Reconstructed photon isolation energy as a function of truth photon isolation energy in bins of truth photon E_T	173
8.2	Truth isolation energy cut equivalent to a the reconstructed isolation energy cut as a function of truth photon E_T	174
9.1	Scan of the negative log likelihood with respect to the minimum negative log likelihood of the signal strength and the top normalization for the observed, expected, and unfolded fits.	181
9.2	Data, and pre- and post-fit yields for CRTop as a function of leading photon p_T , and for VRTop and SR each as a single bin.	183
9.3	The measured inclusive fiducial $W(\rightarrow e\nu_e/\mu\nu_\mu)\gamma\gamma$ cross section.	184
9.4	Impact of the systematic uncertainties on the fitted fiducial cross section. . .	188

List of Tables

5.1	Summary of the <i>Preselect</i> , <i>Baseline</i> , and <i>Signal</i> selection requirements for electrons, muons, and jets.	85
5.2	Summary of the Loose Prime (LP) and <i>Tight</i> identification working points used in the analysis.	87
5.3	Summary of the Signal Region selection criteria.	90
6.1	Summary of the signal and background simulation samples.	100
6.2	Table summarizing the event selection for CR_{ee} and $CR_{e\gamma}$	117
6.3	One bin validation of the $e \rightarrow \gamma$ background estimate in the $Z\gamma$ veto region at high and low E_T^{miss}	128
6.4	Relative statistical, systematic, and total uncertainties on the estimated number of $e \rightarrow \gamma$ background events in the signal and $e \rightarrow \gamma$ validation regions.	134
6.5	Table summarizing the CR2_fake selections	140
6.6	One bin validation of the data-driven $j \rightarrow \ell$ background in the $j \rightarrow \ell$ Validation Region.	145
6.7	Systematic uncertainties on the $j \rightarrow \ell$ background estimates.	147
6.8	Total estimates of the data-driven $j \rightarrow \ell$ background in the Signal Region.	148
6.9	Estimated signal and background event yields in the TopCR, TopVR, and Signal Region.	153

7.1	Summary of the effect of all systematic uncertainties on total event yield in the Signal Region before the final likelihood fit.	165
8.1	Summary of the truth-level selection criteria defining the region of phase space used to measure the fiducial cross section of the $pp \rightarrow W\gamma\gamma$ process.	172
9.1	Signal strengths and top normalization factors from the expected, observed and unfolded likelihood fits.	180
9.2	Estimated signal and background yields in the CRTop, VRTop, and SR.	182
9.3	Major sources of uncertainty and their impacts on the measured fiducial cross section.	186